الجمهورية الجزائرية الديمقراطية الشعبية
People's Democratic republic of Algeria
وزارة التعليم العالي و البحث العلمي
Ministry of Higher Education and Scientific Research
جامعة عبد الحميد بن باديس – مستغانم
Abdelhamid Ibn Badis University – Mostaganem
كلية العلوم و التكنولوجيا
Faculty of Sciences and Technology
قسم هندسة الطرائق
Department of Process Engineering

N° D'ORDRE : D……..GP/2025

THÈSE

Présenté pour obtenir le **diplôme**

DE DOCTORAT LMD 3ème cycle

Filière: Génie des Procédés

Spécialité : Génie des Procédés des Matériaux

Par

Mme. SMATI Sabrina

X-ray diffraction and molecular modelling of the structural properties of an aromatic compound with biological

Soutenue le **:…../…../ 2025** **Devant le jury composé de:**

Mr. GHEZZAR Mouffok Redouane	Président	Professeur	Université de Mostaganem
Mme. YAHIAOUI Salem	Examinateur	Professeur	ENS Mostaganem
Mme. DRISSI Mokhtaria	Examinatrice	Professeur	Université de Tiaret
Mr. SAIDJ Merzouk	Examinateur	MCA	Université de Mostaganem
Mr. BOUKABCHA Nourdine	Directeur de thèse	Professeur	Université de Chlef
Mme. MENAD Karima	Co-directrice de thèse	MCA	Université de Mostaganem
Mr. CHOUAIH Abdelkader	Invité	Professeur	Université de Mostaganem
Mr. MEGROUSS Youcef	Invité	Professeur	Université de Chlef

ANNEE UNIVERSITAIRE : 2024/2025

الجمهورية الجزائرية الديمقراطية الشعبية
People's Democratic republic of Algeria
وزارة التعليم العالي و البحث العلمي
Ministry of Higher Education and Scientific Research
جامعة عبد الحميد بن باديس – مستغانم
Abdelhamid Ibn Badis University – Mostaganem
كلية العلوم و التكنولوجيا
Faculty of Sciences and Technology
قسم هندسة الطرائق
Department of Process Engineering

N° D'ORDRE : D……..GP/2025

THÈSE

Présenté pour obtenir le **diplôme**

DE DOCTORAT LMD 3ème cycle

Filière: Génie des Procédés

Spécialité : Génie des Procédés des Matériaux

Par

Mme. SMATI Sabrina

Etude par diffraction X et modélisation moléculaire des propriétés Structurales d'un composé aromatique d'activité biologique

Soutenue le **:…../…../ 2025** **Devant le jury composé de:**

Mr. GHEZZAR Mouffok Redouane	Président	Professeur	Université de Mostaganem
Mme. YAHIAOUI Salem	Examinateur	Professeur	ENS Mostaganem
Mme. DRISSI Mokhtaria	Examinatrice	Professeur	Université de Tiaret
Mr. SAIDJ Merzouk	Examinateur	MCA	Université de Mostaganem
Mr. BOUKABCHA Nourdine	Directeur de thèse	Professeur	Université de Chlef
Mme. MENAD Karima	Co-directrice de thèse	MCA	Université de Mostaganem
Mr. CHOUAIH Abdelkader	Invité	Professeur	Université de Mostaganem
Mr. MEGROUSS Youcef	Invité	Professeur	Université de Chlef

ANNEE UNIVERSITAIRE : 2024/2025

Acknowledgment

This thesis would not have been possible without the support, guidance, and encouragement of numerous individuals to whom I am deeply indebted.

First and foremost, I would like to express my sincere gratitude to my thesis supervisor, Pr. **BOUKABCHA Nourdine**, Professor at the University of Chlef, for his exceptional guidance, continuous support, and patience throughout the course of this research. His profound expertise, insightful suggestions, and unwavering encouragement have been the cornerstone of my progress and have inspired me to achieve my best.

I would also like to express my heartfelt thanks to my co-supervisor, **Dr. Karima MENAD**, Associate Professor A at the University of Mostaganem, for her valuable support, constructive feedback, and guidance throughout this research.

I would also like to extend my heartfelt thanks to the esteemed members of the examination committee: **Pr. Mouffok Redouane GHEZZAR**, President, Professor at the University of Mostaganem, **Pr. Salem YAHIAOUI**, Examiner, Professor at ENS Mostaganem, **Pr. Mokhtaria DRISSI**, Examiner, Professor at the University of Tiaret, and **Dr. Merzouk SAIDJ**, Examiner, Associate Professor A at the University of Mostaganem, for graciously accepting to evaluate this thesis. Their thorough review, thoughtful comments, and constructive criticism have greatly enriched this work.

My deepest appreciation goes to the invited professors: **Pr. Abdelkader CHOUAIH**, Professor at the University of Mostaganem, and **Pr. Youcef MEGROUSS**, Professor at the University of Chlef, for their interest in my research and their valuable remarks that have contributed to enhancing the quality of this thesis.

A special thanks to **Pr. Yusuf ATALAY**, Professor at the University of Sakarya, Turkey, for welcoming me into his lab and offering me the opportunity to collaborate and gain invaluable experience.

Finally, to all those who contributed to this thesis, either directly or indirectly, I offer my sincere thanks and appreciation.

Dedication

I dedicate this work to my parents, for being the foundation of everything I am today. For their endless sacrifices, for always showing me what hard work and love truly mean, and for supporting me even when the journey wasn't clear. They've been my guiding light, my biggest cheerleaders, and the ones who taught me to never settle. A special thanks to my mom for her unwavering support, her patience, and for always believing in me. Without her, I wouldn't be where I am today. I dedicate this to her for everything she has given me and for always encouraging me to reach higher.

I dedicate this work to my husband, for being my rock and constant source of strength. His love, support, and belief in me have carried me through every challenge. He's my partner in every sense of the word through the highs and lows, he's been there every step of the way, cheering me on, lifting me up, and reminding me that together, we can face anything. His patience, determination, and unwavering faith in me have been a driving force throughout this journey. This work is as much his as it is mine.

I dedicate this work to my friends, for being my constant support system, my laughter, and my light in dark times. They've celebrated my victories, helped me through my struggles, and never once let me feel alone in this journey. They've shown me the power of true friendship unselfish, loyal, and full of love. To the ones who've listened when I needed to vent, who've celebrated my wins with me, and who've always been by my side, this is for you. You are the family I chose, and I'm forever grateful

This one is for all of you

Last but not least, I wanna thank me

I wanna thank me for believing in me

I wanna thank me for doing all this hard work

I wanna thank me for having no days off

I wanna thank me for, for never quitting

TABLE OF CONTENT

List of abbreviations

NMR	Nuclear Magnetic Resonance
$CDCl_3$	Deuterated Chloroform
RNA	Ribonucleic Acid
DNA	Deoxyribonucleic Acid
NLO	Nonlinear Optics
FDA	Food and Drug Administration
UV	Ultraviolet
ppm	Parts per Million
TMS	Tetramethylsilane
DFT	Density Functional Theory
LDA	Local Density Approximation
GGA	Generalized Gradient Approximation
LSDA	Local Spin Density Approximation
EMBIT	(E)-3-(3-(2-Methoxyphenyl)-4-Methylthiazol-2(3H)-ylidene) Benzo [4,5] imidazole[1,2-c] thiazole-1(3H)-thione
XRD	X-ray Diffraction
NCI	Non-Covalent Interaction
RDG	Reduced Density Gradient
IR	Infrared Spectroscopy
TLC	Thin-Layer Chromatography
Rf	Retention Factor
SC-XRD	Single-Crystal X-ray Diffraction
hkl	Miller Indices
INS	Instruction File
CCDC	Cambridge Crystallographic Data Centre
PED	Potential Energy Distribution
HOMO	Highest Occupied Molecular Orbital
LUMO	Lowest Unoccupied Molecular Orbital
DMSO	Dimethyl Sulfoxide
CPCM	Conductor-like Polarizable Continuum Model
MEP	Molecular Electrostatic Potential
NBO	Natural Bond Orbital

LOL	Localized Orbital Locator
ELF	Electron Localization Function
NPA	Natural Population Analysis
ICT	Intramolecular Charge Transfer
LP	Lone Pair
FMO	Frontier Molecular Orbital
DOS	Density of States
GCRD	Global Conceptual Reactivity Descriptors
ADMET	Absorption, Distribution, Metabolism, Excretion, and Toxicity
IOP	Input Output Parameters
ROCK	Rotation about Bonds
PASS	Prediction of Activity Spectra of Substances
Pa	Probability of Activity
Pi	Probability of Inactivity
RCSB	Research Collaboratory for Structural Bioinformatics
BBB	Blood-Brain Barrier
GI Penetration	Gastrointestinal Penetration

TABLES LIST

LIST OF FIGURES

General Introduction

Heterocyclic compounds have become a prevailing trend in contemporary research due to their exceptional versatility and broad applications across various scientific and industrial domains, notably in medicinal chemistry [1-4], corrosion prevention [5,6], and in optics [7-9]. Among these, thiazoles have attracted significant attention for their remarkable utility in diverse fields. The thiazole ring, characterized by the presence of nitrogen and sulfur atoms, exhibits unique chemical and biological properties, establishing it as a vital structural motif in medicinal chemistry. Thiazoles have shown considerable potential as antitumor [10,11], antimicrobial [12,13], antifungal [14], antioxidant [15], anti-inflammatory [16], and antimalarial agents [17].

One noteworthy thiazole derivative is (E)-3-(3-(2-Methoxyphenyl)-4-Methylthiazol-2(3H)-ylidene) Benzo [4,5] imidazole[1,2-c] thiazole-1(3H)-thione abbreviated as EMBIT, stands out as a promising compound with applications in nonlinear optical NLO materials and therapeutics. Its complex structure combines thiazole, imidazole, and methoxyphenyl groups, enhancing its electronic properties and reactivity creating a synergistic effect thereby increasing its potential in advanced material science and pharmaceutical development [18].

The primary goal of this study is to explore the structural properties of the newly synthesized bioactive compound EMBIT using a combination of X-ray diffraction (XRD) and molecular modeling techniques. By integrating the insights from both XRD and molecular modeling, this study aims to achieve a detailed understanding of EMBIT's molecular properties, electronic distribution, and chemical behavior. These findings will not only enhance the interpretation of experimental data but will also guide future modifications of EMBIT to optimize its applications in medicinal chemistry and material science.

The main objectives of this thesis are to gain a comprehensive understanding of EMBIT's structure, reactivity, and potential applications. First, we aim to investigate the compound's crystalline structure, molecular geometry, and intermolecular interactions through XRD, along with the analysis through FT-IR and NMR spectroscopy. This will provide valuable information on bond lengths, angles, molecular arrangement, and functional groups, offering a precise picture of EMBIT's solid-state structure.

In parallel, molecular modeling using Density Functional Theory (DFT) at the B3LYP/6-311G++(d,p) level will be employed to explore EMBIT's electronic structure, vibrational frequencies, reactive sites, and geometry. Additionally, DFT calculations will help in determining the energy gap, global chemical reactivity descriptors, and molecular electrostatic potential (MEP). These theoretical analyses will predict key electronic properties, such as frontier molecular orbitals (FMOs), molecular electrostatic potential (MEP), and nonlinear

optical (NLO) responses, shedding light on the compound's reactivity and its potential use in various advanced materials.

Additionally, this research evaluates EMBIT's pharmacological potential, focusing on its biological activity, toxicity, and pharmacokinetic properties. The study will investigate how EMBIT interacts with biological targets, assessing its feasibility as a therapeutic agent. Furthermore, we will explore potential structural modifications that could improve the pharmacokinetic properties and biological efficacy of EMBIT derivatives.

Beyond its biomedical applications, this work will also investigate EMBIT's role in nonlinear optical (NLO) materials. By leveraging its unique electronic properties and molecular architecture, this study will evaluate its potential for use in advanced material science and optoelectronic applications.

The thesis was structured as follow:

Chapter 1 provides a general overview of thiazole-based compounds, highlighting their importance in drug design, material science, and NLO applications. It discusses the significance of thiazole derivatives and sets the context for the study of EMBIT.

Chapter 2 focuses on the experimental and computational methods used to elucidate EMBIT's molecular structure, including X-ray diffraction, infrared and NMR spectroscopy, and Density Functional Theory (DFT) calculations. These techniques are employed to confirm the compound’s structure.

In Chapter 3, the synthesis and detailed characterization of EMBIT by Xray, NMR and, FT-IR were presented, with a focus on combining experimental and theoretical analysis of EMBIT Structure.

Chapter 4 presents a theoretical analysis using molecular modeling techniques, which complement the experimental findings and provide further insight into the electronic properties, reactivity.

Finally, Chapter 5 explores the EMBIT’s applicability in NLO and places special emphasis on the biological activity of EMBIT, exploring deeper its interactions with relevant biological targets, as well as its toxicity and pharmacokinetic profiles. The chapter also discusses the structural modifications of EMBIT derivatives and their impact on improving the compound’s pharmacokinetic properties.

Finally, the conclusion summarizes the key findings and suggests directions for future research.

References:

[1] E. Kabir, M.Uzzaman, A review on biological and medicinal impact of heterocyclic compounds , *Res Chem 4:100606(2022),* https://doi.org/10.1016/j.rechem.2022.100606

[2] P. Singh et al, Recent Progresses in Development of Heterocyclic Compounds for Epilepsy Treatment: Key Research Highlights from 2019–2024, *Chem. Biodiversity e202401620 (2024).*https://doi.org/10.1002/cbdv.202401620

[3] A. M. Fahim, E. H. I. Ismael, H. E. M. Tolan, Numerous Heterocyclic Compounds with an Isonicotinic Moiety have Been Studied for Their Synthesis, Antibacterial, Anticancer, Docking Simulation, and DFT Characteristics. *Polycyclic Aromatic Compounds*, *44*(9): 5707–5748(2023), https://doi.org/10.1080/10406638.2023.2266549

[4] H.E. Hashem, S. Ahmad, A., Kumer, *et al,* In silico and in vitro prediction of new synthesized N-heterocyclic compounds as anti-SARS-CoV-2, *Sci Rep* 14: 1152 (2024). https://doi.org/10.1038/s41598-024-51443-7

[5] A. S. Al-Kiey, R.A. Mohamed-Ezzat, S. Dacrory , Eco-friendly anti-corrosion performance of chitosan modified with fused heterocyclic compound on mild steel in acidic medium , *Int. J. Biol. Macromol* 263(1) : 130133(2024) https://doi.org/10.1016/j.ijbiomac.2024.130133

[6] Sheetal, A.K. Singh, S. Thakur, B. Pani, M. Singh, Heterocyclic compounds as corrosion inhibitors for iron alloys in various industrial processes: A review, *J. Ind. Eng. Chem. 130(25):141-177(2024)* , https://doi.org/10.1016/j.jiec.2023.10.005

[7] M.G. Abu-Taweel, S.S.Alharthi, , H.M. Al-Saidi, A.O. Babalghith, , M.M Ibrahim, S. Khan,. Heterocyclic Organic Compounds as a Fluorescent Chemosensor for Cell Imaging Applications: A Review, *Crit Rev Anal Chem54*(7):2538–2553(2023). https://doi.org/10.1080/10408347.2023.2186695

[8] N.A.M Daud, Impact of Homocyclic and Heterocyclic Rings of Chalcones on Charge Transfer Behaviour: A Nonlinear Optical Study, *Chem. Phys. Impact. 8:100565(2024)* https://doi.org/10.1016/j.chphi.2024.100565

[9] R. Iftikhar, F.Z. Khan, N. Naeem, Recent synthetic strategies of small heterocyclic organic molecules with optoelectronic applications: a review. *Mol Divers* 28:271–307 (2024) https://doi.org/10.1007/s11030-022-10597-0

[10] M. K. Abdalla, S.A. H. Mandour, K. M. Wahdan, H.A. El-Ghamry, New nanometric metal complexes based on thiazole derivative as potential antitumor and antimicrobial agents: Full structural elucidation, docking simulation and biological activity studies, *J. Mol. Liq. 401:124665(2024)* https://doi.org/10.1016/j.molliq.2024.124665

[11] A. Bin-Muhsinah et al , Chemoselective synthesis, X-ray structure study, Hirshfeld surface analysis, antitumor, and antimicrobial activities of new Thiophene and Thiazole derivatives , J. Mol. Struct. 1316 :139083(2024) https://doi.org/10.1016/j.molstruc.2024.139083

[12] H. Liu et al, Current Development of Thiazole-Containing Compounds as Potential Antibacterials against Methicillin-Resistant Staphylococcus aureus, *ACS Infect. Dis*. 10(2):350–370(2024) https://doi.org/10.1021/acsinfecdis.3c00647

[13] A. Khamitova, Thiadiazole and Thiazole Derivatives as Potential Antimicrobial Agents, *Mini-Rev. Med. Chem.* 24(5):531-545 (*2024)* https://doi.org/10.2174/1389557523666230713115947

[14] G.Shanbhag, M. Naik , D.Wagh, , S. Autkar, , M. V. Hagalavadi, , U. Wachendorff, J. Pabba, A. Klausener, Synthesis and antifungal activity of novel piperidinyl thiazole derivatives. *Pest Manag Sci.* (2024) https://doi.org/10.1002/ps.8431

[15] M.Z. Alamshany ,N.Y. Tashkandi ,I.M.M. Othman , A versatile precursor for one-pot synthesis of novel azo-thiazole and thiazole scaffolds as prospective antimicrobial and antioxidant agents , *J. Chin. Chem. Soc*. 71(10) :1309-1323(2024) https://doi.org/10.1002/jccs.202400173

[16] H. K.Narasimhamurthy , T.R. Swaroop , K.S. Rangappa , A review on progress of thiazole derivatives as potential anti-inflammatory agents , *Eur J Med Chem Rep. (12) 100225(2024)* https://doi.org/10.1016/j.ejmcr.2024.100225

[17] T. Kalita et al, A Review on Synthetic Thiazole Derivatives as an Antimalarial Agent, *Curr. Drug. Discov. Technol.* 21(5): e240124226141 (2024) https://doi.org/10.2174/0115701638276379231223101625

[18] A. Petrou, M. Fesatidou, A. Geronikaki, Thiazole Ring—A Biologically Active

Scaffold, *Molecules*. 26 (11) (2021) 3166, https://doi.org/10.3390/molecules26113166

Chapter I

Generalities on Thiazoles

I.1 Introduction:

Heterocyclic compounds play a crucial role in various industries, including pharmaceuticals, catalytic ligands, fine chemicals, and agrochemicals [1]. These compounds are essential due to their structural diversity and versatility, allowing them to be applied in a broad spectrum of chemical processes. Recent research has increasingly focused on the study of heterocyclic compounds that contain nitrogen, sulfur, or a combination of both heteroatoms. Notable examples include pyrrole, thiophene, and thiazole, each of which has been the subject of extensive investigation for its unique properties and potential applications [2,3]. Thiazole, in particular, is a significant member of the azole heterocyclic family. Azoles, as a class of heterocyclic compounds, hold a prominent place in modern medicinal chemistry due to their wide-ranging applications in drug design and discovery [4,5]. The presence of nitrogen and sulfur in thiazole makes it a small but highly important heterocycle. Its structure and chemical properties have made it a subject of considerable interest in research, especially in the development of medicinally valuable compounds. Thiazole has garnered attention for its role in the development of pharmaceutically important molecules. It has been found to possess several medicinal properties, making it highly versatile in different therapeutic areas. Thiazole and its derivatives have been studied extensively for their anti-inflammatory [6], antibacterial [7], and antifungal [8] properties, demonstrating their potential in treating a variety of diseases and infections. Additionally, thiazole-based compounds have found applications as corrosion inhibitors [9], protecting industrial settings, and in heavy metal detection [10], contributing to environmental monitoring and safety.

In this first chapter, we offer a comprehensive overview of thiazoles, examining their structure, properties, and applications. A significant part of this discussion will focus on the various derivatives of thiazoles, with special attention given to thiazolines and thiazolidines. These derivatives are of particular interest due to their unique chemical characteristics and potential applications, which have made them key subjects in ongoing research.

I.2 Structure of Thiazoles:

Thiazoles are heterocyclic molecules featuring a five-membered ring structure composed of three carbon atoms, one nitrogen atom at position 3, and one sulfur atom at position 1. These compounds are commonly referred to as 1,3-thiazoles. [11]. They have a planar, aromatic structure characterized by significant π-electron delocalization, which imparts a high degree of aromaticity. This aromatic nature is evident from the chemical shifts of protons observed in NMR spectroscopy [12].

Structurally, thiazoles are sulfur-containing derivatives of azoles, with their framework first described by Hantzsch and Weber in 1887 [13].

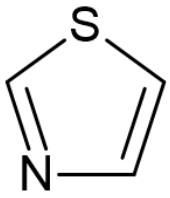

Fig. 1.1 Thiazole ring

The thiazole structure can be understood as a resonance hybrid of several canonical forms. Additional resonance structures are possible due to the involvement of sulfur's d-orbitals, further contributing to the molecule's stability [12].

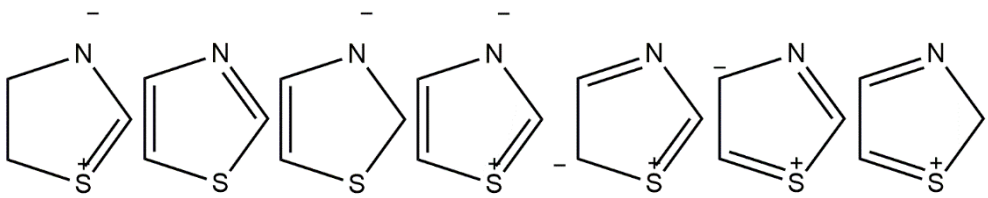

Fig. 1.2. Resonant structure of thiazole

The structure of thiazole rings was initially studied by correlating the ^{13}C and ^{1}H NMR coupling constants with interorbital and internuclear angles to deduce bond angles and C-H bond lengths. Metzger [14],[15] utilized these correlations, while bond lengths of C-C, C-N, and C-S were determined using bond orders calculated by the Hückel molecular orbital (HMO) method [16]. Comprehensive geometric parameters were later established through microwave spectroscopy studies of thiazole and its isotopically labeled isomers [17]. Early explorations of the infrared spectra and vibrational assignments of thiazole and its derivatives were conducted by Chouteau [18].

I.3 Physico-chemical proprieties of thiazole:

Thiazole is a pale-yellow, flammable compound with a pyridine-like odor. It has a boiling point of 116–118°C and a pKa of 2.5 for its conjugate acid. The compound has a density of 1.2 g/cm³ and shows good solubility in ether and alcohol, though it is only slightly soluble in water. Thiazole has an ionization potential of 9.50 eV and a dipole moment of 1.61 Dand in terms of spectral data, the UV spectrum of thiazole ring in ethanol shows absorption at 207.5 nm (ε = 3.41) and 233.0 nm (ε = 3.57). The ^{1}H NMR spectrum recorded in $CDCl_3$ reveals chemical shifts at 8.88, δ 7.41, and δ 7.98 ppm for

the C2–H proton, for the C3–H proton, and for the C4–H proton respectively. The ^{13}C NMR spectrum shows shifts at δ 153.6 ppm for C2, δ 143.3 ppm for C4, and δ 119.6 ppm for C5[11B], [19]

I.4 Synthesis:

Numerous synthetic methods have been developed to create these compounds. The foundation for thiazole synthesis was laid by *Hantzsch* in 1887 **Fig. I.3.,** who pioneered early techniques that have influenced subsequent research **[13].** The *Hantzsch* synthesis, despite being over a century old, is the most commonly used method for synthesizing thiazole derivatives. It involves condensing a compound with both heteroatoms on the same carbon with another compound that has a halogen and a carbonyl group on adjacent carbons. Various nucleophiles like thioamides, thioureas, and thiocarbamates can be used in this reaction **[12].**

A variation of the *Hanstzch* method **Fig. I.4** uses thiourea with 1,2-dichloro-1-ethoxyethane to synthesize 2-aminothiazole **[20]-[21].** *The Cook–Heilbron* method involves the reaction of aminonitriles with carbon disulfide to produce 2,4-disubstituted 5-aminothiazoles Fig. I.5. **[22].** The *Robinson–Gabriel* method **Fig. I.6**. uses acyl aminocarbonyl compounds and phosphorus pentasulfide for cyclization to form thiazoles **[23].** More recently, in 2003, *G. Sarodnick* and his team contributed innovative techniques that continue to shape modern thiazole synthesis shown in. **[24].** while thiazole can also be synthesized by reducing 2-methylthiothiazole, **Fig. I.7. [25]** *Sheldrake et al*. **Fig.8.** introduced a novel method for synthesizing 5-arylthiazoles. Their methodology includes the reaction of N,N-diformylaminomethyl aryl ketones with phosphorus pentasulfide and triethylamine in a chloroform medium, efficiently yielding 5-arylthiazoles in high quantities **[26]** Tang et al., **Fig. I. 9** Additionally, a copper-catalyzed [3+1+1] condensation of oximes, anhydrides, and potassium thiocyanate has been reported **[27].** Wang et al. **Fig. I.10** introduced a green oxidative synthesis of thiazoles using aldehydes, amines, and sulfur in the presence of molecular oxygen **[28].** Meanwhile, Lingaraju et al. **Fig. I.11** developed a method for synthesizing 4,5-disubstituted thiazoles through base-induced cyclization of active methylene isocyanides. **[29]** *Sanz-Cervera* **Fig.I.12** synthesized thiazoles from protected glycine intermediates reacting with *Lawesson's* reagent **[30],** and *Miura et al.* reported the synthesis of 2,5-disubstituted thiazoles using rhodium (II) catalysis **Fig. I.13 [31] Fig.I.14**. Microwave-assisted synthesis of thiazoles has also been explored, with *Chinnajara and Rajalakshmi* synthesizing hydrazinyl thiazole derivatives under microwave irradiation with excellent yield and purity **[32]. Fig. I.15.** Other recent approaches include Kiran et al.'s synthesis of 4-methylthio-5-acylthiazoles and 4-ethoxycarbonyl-5-acylthiazoles through the cyclization of tosylmethyl isocyanide with α-oxodithioesters **[33].** Additionally, Mamidala et al. developed a

method for preparing coumarin-based thiazole derivatives by reacting thiocarbohydrazide, aldehydes, and α-halocarbonyl coumarins under microwave heating Fig. I.16. [34] These efforts have been complemented by the work of numerous other research groups, who have collectively advanced the synthesis of thiazole derivatives, ensuring their ongoing importance in chemical and pharmaceutical research [35-37]

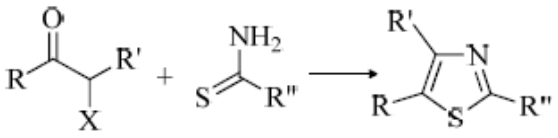

Fig. 1.3 Hantzsch synthesis equation

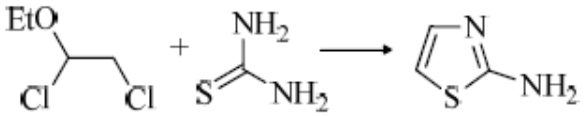

Fig. 1.4. Synthesis of 2-aminothiazole from thiourea and 1,2-dichloro-1-ethoxyethane.

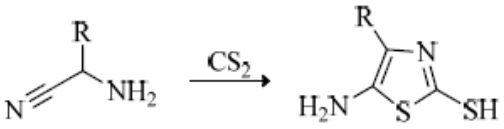

Fig. 1.5. Cook–Heilbron thiazole synthesis.

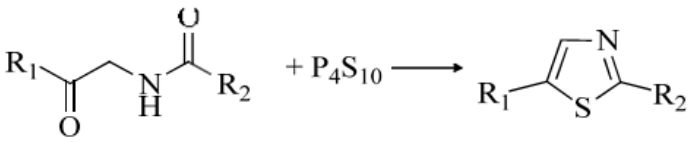

Fig. 1.6. Robinson–Gabriel thiazole synthesis

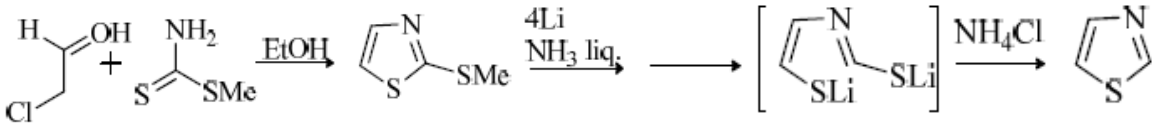

Fig. 1.7. Sarodnick thiazole synthesis

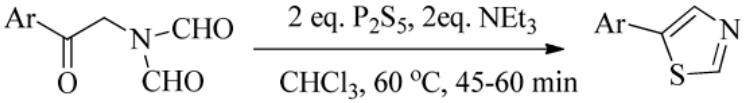

Fig. 1.8. Sheldrake et al. *synthesis*

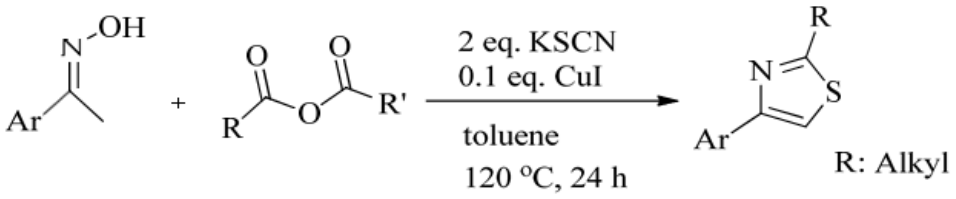

Fig. 1.9. Tang et al Synthesis

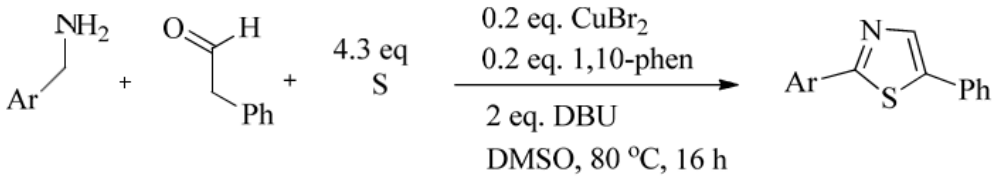

Fig. 1.10. Wang et al..

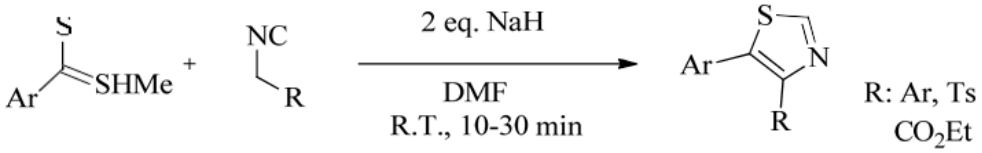

Fig. 1.11. *Lingaraju et al. synthesis*

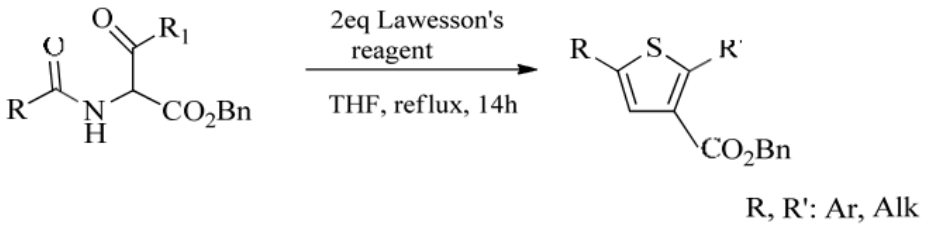

Fig. 1.12. *Sanz-Cervera synthesis*

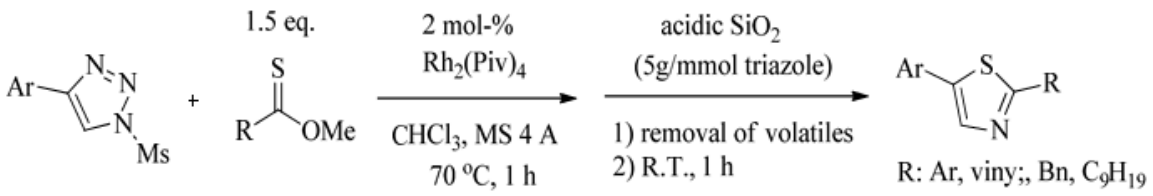

Fig. 1.13. *Miura et al synthesis*

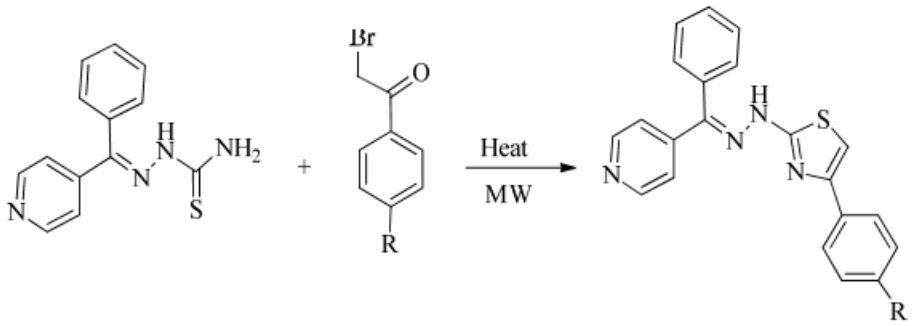

Fig. 1.14. *Chinnajara and Rajalakshmi synthesis*

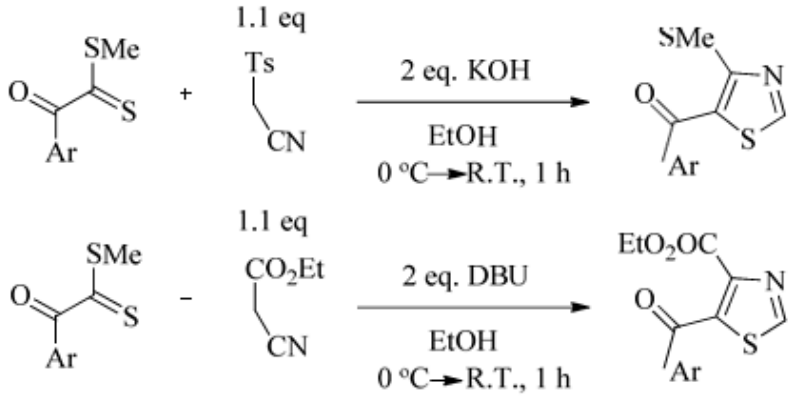

Fig.1.15. *Kiran et al synthesis*

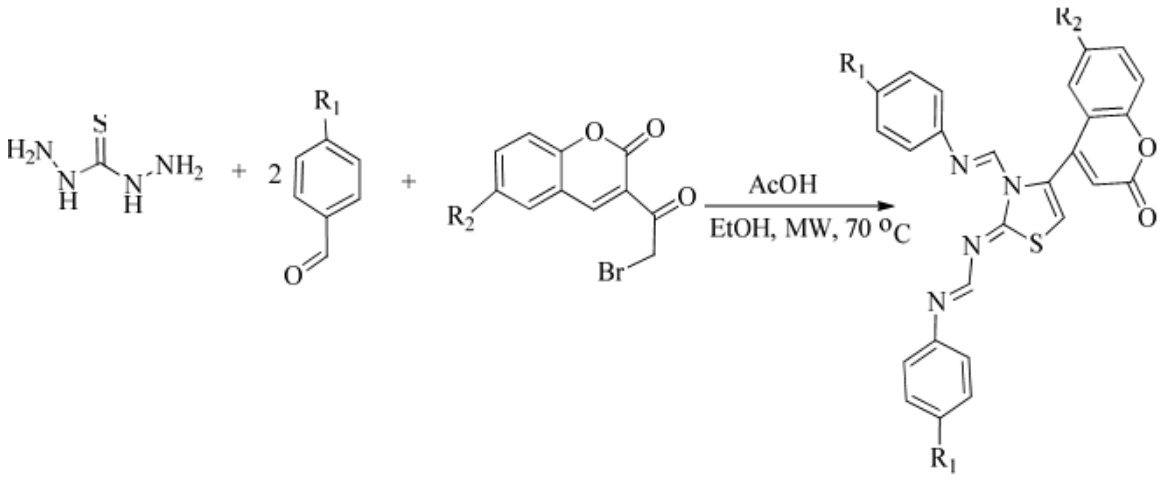

Fig. 1.16. Mamidala et al synthesis

I.5 Thiazole derivatives:

Thiazole has two important derivatives: thiazoline and thiazolidine. Thiazoline is an unsaturated compound where the carbon-sulfur double bond in thiazole is replaced by a single bond, Thiazolidine, on the other hand, is a saturated derivative, where the ring structure is fully saturated with single bonds, Both derivatives are used in various chemical and pharmaceutical applications,

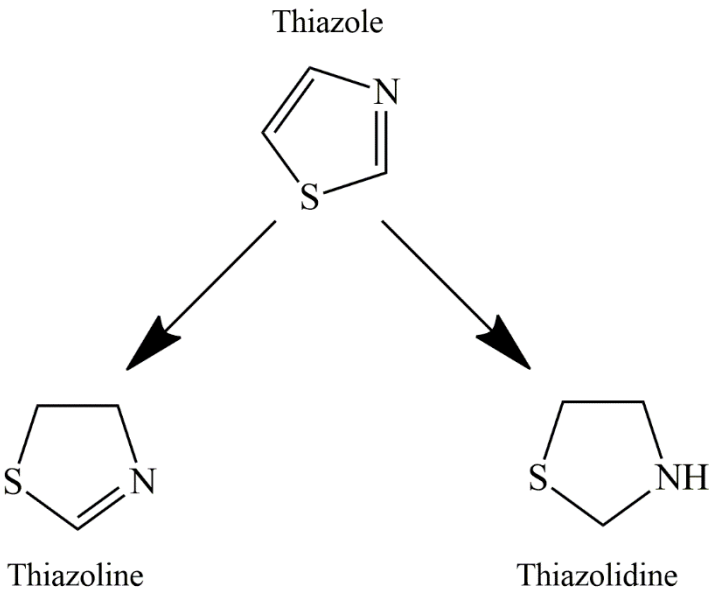

Fig I.17. thiazole derivatives

I.5.1 Thiazolines:

Thiazolines are sulfur-containing organic compounds featuring a five-membered ring structure with four carbon atoms and one sulfur atom, which can also incorporate a nitrogen atom as a substituent. **Fig I.17 .** Thiazolines possess a broad range of applications, making them highly valuable in both organic and medicinal chemistry. They are frequently found in bioactive natural compounds of peptide origin **[38].** A key feature of these compounds is their presence in various biologically active molecules, including certain antibiotics and natural products **[39]**. Thiazolines contribute to conformational stability and strengthen interactions with proteins, RNA, and DNA by acting as recognition sites **[38].** Additionally, they play a crucial role in the synthesis of pharmaceuticals and biologically active natural compounds, such as micacocidin, known for its antibacterial properties **[39,41].** as well as flavor and food chemistry **[42]**

I.5.2 Thiazolidines

Thiazolidines, or tetrahydrothiazoles, are thiazole derivatives that belong to the family of heterocyclic organic compounds. These molecules are characterized by a thioether group at position 1 and an

amine group at position 3 within a saturated five-membered ring [43,44]. Although thiazolidine, its basic structure is frequently found in many natural products and pharmaceutical compounds. Substituted derivatives of thiazolidine are particularly recognized for their remarkable anticancer properties [45-47]. Beyond their anticancer effects, these derivatives also exhibit various biological activities, including antifungal, herbicidal, antioxidant, and antiviral properties [48-54]. This diversity of activities underscores the importance of thiazolidines in the development of new therapies and pharmaceutical applications.

I.6 Thiazoles applications:

I.6.1 Nonlinear optical propriety:

Organic second-order nonlinear optical (NLO) materials have garnered significant attention over the past two decades due to their numerous advantages, including ultrafast response times, broad operational bandwidths, low driving voltages, tunable molecular structures, and large electro-optic coefficients These properties make organic NLO materials highly promising for a wide range of applications, such as optical switches, sensors, and telecommunication devices. The design of materials with enhanced second-order NLO efficiency has become a key area of focus, driven by their potential in optical signal processing, data storage, and sensors, especially within rapidly evolving photonic-based industries [55-67]. as well as their ability to enhance molecular hyperpolarizability [68] Furthermore, derivatives containing thiazole moieties stand out for their enhanced photochromic properties, making them promising candidates for second-order NLO applications [69] Notably, the incorporation of a thiazole ring into these derivatives results in a significant increase in NLO response, further underscoring their potential [70]

I.6.2 Biological activity:

Thiazole derivatives have garnered significant attention in medicinal chemistry due to their versatile pharmacological properties. These compounds have been reported to exhibit a wide array of therapeutic effects. Thiazole plays a crucial role in numerous natural products that are biologically significant. One prominent example is the thiazolium ring found in vitamin B1 [71] (thiamine), an essential nutrient for instance, they are known for their antidiabetic potential, . Additionally, thiazole derivatives have been investigated for their central nervous system (CNS) depressant properties [72]. Furthermore, their analgesic effects [73] make them valuable in pain management. In the field of infectious diseases, thiazole derivatives have demonstrated antifilarial activity [74], which is significant in combating parasitic infections. They also possess notable antifungal and antibacterial properties, making them effective against a range of microbial infections [75]. Moreover, these

derivatives show potential as anthelmintic agents, and have been investigated for their antitumoral activity, showing promise in cancer **[76].** Overall, the broad spectrum of activities exhibited by thiazole derivatives makes them important candidates for the development of new therapeutic agents. The thiazole scaffold is a key component in over 18 FDA-approved drugs. A prominent example is cefiderocol, the first siderophore antibiotic approved by the FDA in 2019 under the brand name Fetroja® . This thiazole derivative exhibits potent activity against a wide range of multi-drug-resistant Gram-negative bacteria, including *Pseudomonas aeruginosa* (*P. aeruginosa*), and is prescribed for complicated urinary tract infections when alternative treatments are ineffective **[77–79].** Another noteworthy example is alpelisib, marketed as Piqray®, which also received FDA approval in 2019 for the treatment of certain forms of breast cancer. Breast cancer remains one of the most prevalent and life-threatening diseases worldwide and is the second leading cause of cancer-related mortality, particularly in less developed regions [80].

Table I.1.Examples of Thiazole-Based Drugs and Their Therapeutic Functions

Structure	Name (function)
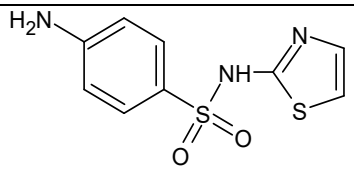	Sulfathiazole (antimicrobial drug) **[81]**
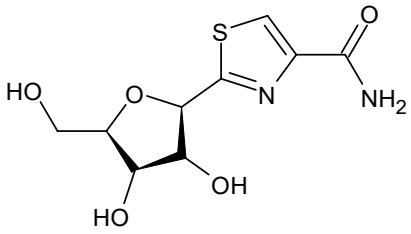	bleomycine and tiazofuri (antineoplastic drug) **[81]**
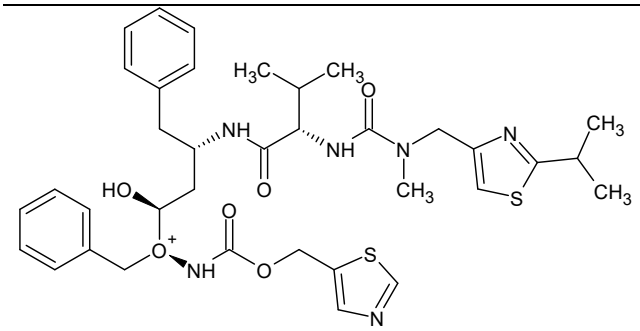	Ritonavir (antiretroviral drug) **[81]**

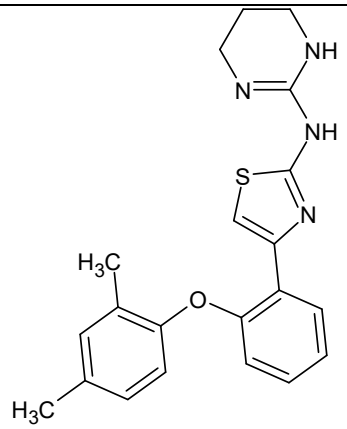	abafungin (antifungal drug) [81]
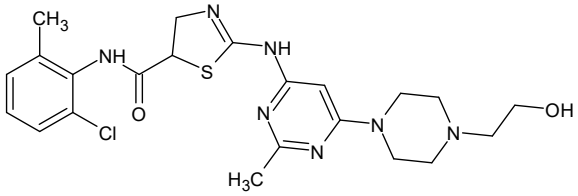	Dasatinib (antileukimia) [19]
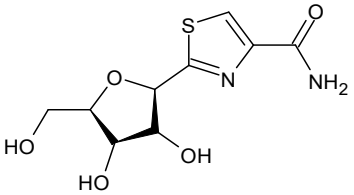	Thaizofurin (antritumor) [19]
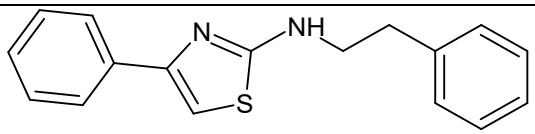	Fentiziole (immunomodulator) [19]
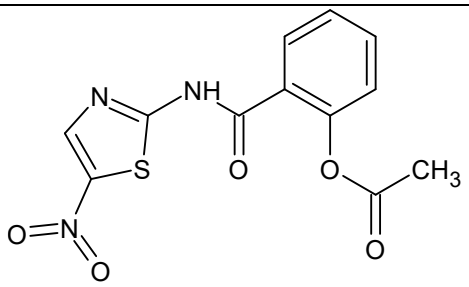	Nitazoxanide (antiparasitic) [19]

I.7 Conclusion:

Thiazoles, as a vital class of heterocyclic compounds, hold a prominent position in various fields due to their structural versatility and unique properties. Their significance is underscored by their applications in pharmaceuticals, agrochemicals, and industrial processes, demonstrating their indispensable role in modern science and technology. The combination of nitrogen and sulfur within the thiazole ring confers a diverse range of chemical and biological activities, making thiazole derivatives highly sought-after in medicinal chemistry.

In this chapter, we conducted a comprehensive bibliographic study on thiazole synthesis, its derivatives, and their wide-ranging applications. Special emphasis was placed on their role in non-linear optical NLO applications and biological activities. Thiazole-based compounds have shown significant promise in NLO materials, which are critical in the advancement of photonic technologies. Additionally, their diverse biological activities, including anti-inflammatory, antibacterial, and antifungal properties, highlight their therapeutic potential in addressing various health challenges.

Additionally, we reported the latest research trends in the study of thiazoles, capturing recent advancements in their synthesis, functionalization, and emerging applications. This includes innovative approaches in NLO material design and cutting-edge discoveries in their biological activity profiles. These recent trends highlight the dynamic nature of thiazole research and the continued exploration of their potential in addressing modern scientific and technological challenges.

By exploring the synthesis, properties, and applications of thiazoles, along with their derivatives, and incorporating the latest research developments, this chapter provides a comprehensive understanding of their importance in various scientific domains. The insights gained from this study not only highlight the current state of research but also pave the way for future investigations aimed at harnessing the full potential of these versatile heterocycles.

References:

[1] A.I.Meyers,Heterocycles in Organic Synthesis,Wiley,(1974).

[2] A.R. Katritzky, C.A Ramsden, E.F.V. Scriven et al, Comprehensive Heterocyclic Chemistry III, Five-membered Rings with One Heteroatom together with their Benzo and other Carbocyclic-fused Derivatives, Elsevier, Ltd. Vol.3. (2008)

[3] A.R. Katritzky, C.A Ramsden, E.F.V. Scriven et al, Comprehensive Heterocyclic Chemistry III; Five-membered Rings with Two Heteroatoms, each with their Fused Carbocyclic Derivatives., Elsevier, Ltd Vol. 4. (2008)

[4] P.C. Sharma, K.K. Bansal, A. Deep, M. Pathak, Benzothiazole derivatives as potential anti-infective agents, Curr. Top. Med. Chem. 17 (2): 208-237, (2017)

[5] P.C. Sharma, A. Saini, K.K. Bansal, Synthesis of some thiazole clubbed heterocycles as possible antimicrobial and anthelmintic agents, Indian J. Heterocycl. Chem. 25 (3-4): 303-310 (2016)

[6] R.G. Kalkhambkar, G.M. Kulkarni, H.Shivkumar , R. R. Nagendra, Synthesis of novel triheterocyclic thiazoles as anti-inflammatory and analgesic agents, *Eur J Med Chem*; 42(10): 1272 - 1276. (2007)

[7] A.M. Khalil, M.A. Berghot, M.A. Gouda, Synthesis and antibacterial activity of some new thiazole and thiophene derivatives, *Eur J Med Chem* 44(11): 4434–4440. (2009)

[8] M.M. Ghorab, A.I. El-Batal, Synthesis of some new Thiazole derivatives antifungal activity and ultrastructure changes of some mycotoxin producing fungi, *Boll Chim Farm*141 (2):110- 7. (2002)

[9] A. S. Fouda, E. Abdel-Latif, H. M. Helal, and A. El-Hossiany, Synthesis and Characterization of Some Novel Thiazole Derivatives and Their Applications as Corrosion Inhibitors for Zinc in 1 M Hydrochloric Acid Solution, *Russ. J. Electrochem* 57(2): 159–171(2021), **https://doi.org/10.1134/S1023193521020105.**

[10] M. A. M. Alhamami, J. S. Algethami, and S. Khan, A Review on Thiazole Based Colorimetric and Fluorimetric Chemosensors for the Detection of Heavy Metal Ions, *Crit Rev Anal Chem* :1–25 (2023), **https://doi.org/10.1080/10408347.2023.2197073.**

[11] T. Eicher, S. Hauptmann, A.Speicher , The Chemistry of Heterocycles: Structure, Reactions, Syntheses, and Applications Ed 2, (2003), Wiley-VCH Verlag & Co. KGaA, Germany.

[12] R. RAHMANI, "Analyse par diffraction X et calcul théorique des propriétés structurales des composés organiques à transfert de charges," X-ray Diffraction Analysis and Theoretical Calculation of the Structural Properties of Charge Transfer Organic Compounds, Ph.D. Thesis, Abdelhamid Ibn Badis University, Mostaganem, (2017).

[13] A. Hantzsch, J. H. Weber, Ueber Verbindungen des Thiazols (Pyridins der Thiophenreihe)," Berichte der deutschen chemischen Gesellschaft, 20(2): 3118–3132 (1887), doi: 10.1002/cber.188702002200.

[14] Metzger J V, Z. Chem., 9, 99, 1969; Chem. Abstr., 70, 105567, 1969".

[15] Metzger JV, Thiazole and its derivatives part one (The Chemistry of heterocyclic compounds 34 (1979), John Wiley & Sons, Inc, USA. 10.1002/9780470187081

[16] J. A. Braun, J. V. Metzger, Bull. Soc. Chim. France, 503, 1967; Chem. Abstr., 67, 11446, 1967.

[17] L. Nygaard, E. Asmussen, J.H. Høg et al, Microwave spectra of isotopic thiazoles. molecular structure and 14N quadrupole coupling constants of thiazole, *J. Mol. Structure.* 8:225- 233(1971) ".

[18] J. Chouteau, G. Davidovics, J. Metzger, and A. Bonzom, Sur le spectre infrarouge de l'amino-2 thiazole, du méthyl-4 amino-2 thiazole et de leurs dérivés NN dialcoylés—II. Etude á l'état liquide—Essai d'interprétation générale, Spectrochim. Act. 22(4) : 719–735(1966), **https://doi.org/10.1016/0371-1951(66)80102-9.**

[19] J.R. Vishnu, S. Arun, N. Mahendra , P. Ramendra , The Chemistry of Heterocycles Chapter 5 - Five-Membered Heterocycles , *Nomenclature and Chemistry of Three-to-Five Membered Heterocycles 149-478 (2019)* , **https://doi.org/10.1016/B978-0-08-101033-4.00005-X**

[20] A.I.Vogel, A.R. Tatchell, B.S. Furnis, A.J. Hannaford, P.W.G. Smith, Vogel's Textbook of Practical Organic Chemistry 5:1151–1154 (1989) Harlow Longman, London, UK,

[21] W.K. Warburton, Arylthiazathiolium Salts and o-aminoaryl Thiols—The Herz Reaction. *Chem. Rev*.57: 1011–1020 (1957)

[22] A.H. Cook, I. Heilbron, S.F. MacDonald, A.P. Mahadevan, Studies in the Axole Xeries. Part XII. Some Thiamlopyrimidines. *J. Chem. Soc*. 1064-1068. (1949), https://doi.org/10.1039/JR9490001064

[23] S. Gabriel, Eine Synthese von Oxazolen und Thiazolen. I. Eur. J. of Inor. Chem;43(1):134-138 (1910), **https://doi.org/10.1002/cber.19100430117**

[24] G. Sarodnick, M. Heydenreich, T.Linker , E. Kleinpeter, Quinoxalines. Part 12- Synthesis and structural study of 1-(thiazol-2-yl)-1H-pyrazolo[3,4-b] quinoxalines—the dehydrogenative cyclization with hydroxylamine hydrochloride, Tetrahedron 59(33):6311–6321(2003) , **https://doi.org/10.1016/S0040-4020(03)01024-X**

[25] L. Brandsma, R.L.P. Jong, H.D. Ver Kruijsse, An Efficient Synthesis of 1, 3-Thiazole. Synthesis **1985**, 1985, 948–949, **https://doi.org/10.1055/s-1985-31396**

[26] P.W. Sheldrake, M.Matteucci, E. McDonald, Facile Generation of a Library of 5-Aryl-2-arylsulfonyl-1,3-thiazoles. *Synlett* 460–462(2006), **https://doi.org/10.1055/s-2006-926243**

[27] X. Tang, J. Yang, Zhu, Z. M. Zheng, W. Wu, H. Jiang, Access to Thiazole via Copper-Catalyzed [3+1+1]-Type Condensation Reaction under Redox-Neutral Conditions. *J. Org. Chem*. 81:11461–11466. (2016), https://doi.org/10.1021/acs.joc.6b02124

[28] X. Wang, X. Qiu, J.Wei, J. Liu, S. Song, W. Wang, N. Jiao, Cu-Catalyzed Aerobic Oxidative Sulfuration/Annulation Approach to Thiazoles via Multiple Csp3-H Bond Cleavage. *Org. Lett*. 20:2632–2636(2018), **https://doi.org/10.1021/acs.orglett.8b00840**

[29] G.S. Lingaraju, T.R. Swaroop, A.C.Vinayaka, K.S.S.Kumar, M.P.Sadashiva, K.S. Ragappa, An Easy Access to 4,5-DisubstitutedThiazoles via Base-Induced Click Reaction of Active Methylene Isocyanides with Methyl Dithiocarboxylates. *Synthesis*, 44,1373–1379 (2012), **https://doi.org/10.1021/10.1055/s-0031-1290762**

[30] J.F.Sanz-Cervera, R.Blasco, J. Piera, M. Cynamon, I.Ibáñez, M.Murguía, S. Fustero, Solution versus Fluorous versus Solid- Phase Synthesis of 2,5-Disubstituted 1,3-Azoles. Preliminary Antibacterial Activity Studies. *J. Org. Chem*. 74(23):8988–8996(2009), **https://doi.org/10.1021/jo9016265**

[31] T.Miura, Y.Funakoshi, Y. Fujimoto, J. Nakahashi, M. Murakami, Facile Synthesis of 2,5-Disubstituted Thiazoles from Terminal Alkynes, Sulfonyl Azides and Thionoesters. *Org. Lett.*17:2454–2457 (2015), **https://doi.org/10.1021/acs.orglett.5b00960**

[32] D.Chinnaraja, R Rajalakshmi, A facile, solvent and catalyst free, microwave assisted one pot synthesis of hydrazinyl thiazole derivatives. *J. Saudi Chem. Soc,*19:200–206 (2015), **https://doi.org/10.1016/j.jscs.2014.05.001**

[33] K.R. Kiran, T.Swaroop, N. Rajeev, S.Anil, J. Rangappa, M. Sadashiva, Cyclization of Active Methylene Isocyanides with -Oxodithioesters Induced by Base: An Expedient Synthesis of 4-Methylthio/Ethoxycarbonyl-5-acylthiazoles. *Synthesis*. 52:1103–1112(2020), **https://doi.org/10.1055/s-0039-1690821**

[34] S.Mamidala, S. R Peddi, R.K.Aravilli, P.C. Jilloju, V.Manga,; R.R. Vedula, Microwave irradiated one pot, three component synthesis of a new series of hybrid coumarin based thiazoles: Antibacterial evaluation and molecular docking studies. *J. Mol.Struct.* 1225:129114(2021), **https://doi.org/10.1016/j.molstruc.2020.129114**

[35] M.T. Bogert, H.B. Corbitt, Researches on thiazoles. X. The synthesis of some 2-phenylbenzothiazole arsonic acids, *Chemistry.* 11:768-772(1925), **https://doi.org/10.1073/pnas.11.12.768**

[36] P. Wipf, S.Venkatraman , A new thiazole synthesis by cyclocondensation of thioamides and alkynyl(aryl)iodonium reagents. *J Org Chem.* 61(23):8004-8005(1996), **https://doi.org/10.1021/jo961681c.**

[37] Y. Izumisawa, H.Togo , Preparation of α-Bromoketones and Thiazoles from Ketones with NBS and Thioamides in Ionic Liquids. *Green Sustain Chem.* 1(3):54-62(2011), **doi:10.4236/gsc.2011.13010.**

[38] S. Kumar et al, Recent advances in the synthesis and utility of thiazoline and its derivatives, *RSC Adv.* 14: 902-953(2024), **https://doi.org/10.1039/D3RA06444A**

[39] S. Carmeli, R. E. Moore, G. M. L. Patterson, T. H. Corbett and F. A. T. Valeriote, Unusual Cytotoxic Alkaloids from the Blue-Green Alga Scytonema Mirabile, *J. Am. Chem. Soc.* 112(22): 8195–8197(1990), **https://doi.org/10.1021/ja00178a070.**

[40] A. Ino, A. Murabayashi, Synthetic Studies of Thiazoline and Thiazolidine-Containing Natural Products—1. Phosphorus Pentachloride-Mediated Thiazoline Construction Reaction, *Tetrahedron*. 55(34):1027110282(1999), https://doi.org/10.1016/S0040-4020(99)00582-7

[41] A. Ino, Y. Hasegawa and A. Murabayashi, Synthetic Studies of Thiazoline and Thiazolidine-Containing Natural Products — 2. Total Synthesis of the Antimycoplasma Antibiotic Micacocidin, *Tetrahedron*. 55(34):1028310294(1999), **https://doi.org/10.1016/S0040-4020(99)00583-9**

[42] G. M. Leod, J. M. Ames, Effect of Water on the Production of Cooked Beef Aroma Compounds,*J. Food Sci.* 52(1): 42–45(1987), **https://doi.org/10.1111/J.1365-2621.1987.TB13968.X**

[43] A.G.M. Al-sehemi, Preparation and Structure Studies of Thiazolidine and Bisthiazolidine Derivatives. *J. King Saud.* Univ.21(1):79-88(2009)

[44] V. Viswanathan, N.S. Rao, R. Raghunathan, D. Velmurugan,Crystal structures of two substituted thiazolidine derivatives, Acta *cryst. E research commun 72(8)*1126-1129(2016). **doi:10.1107/S2056989016011336.**

[45] M.S.A. El-Gaby, Z.H. Ismail, S.M. Abdel-Gawad et al, Synthesis of Thiazolidine and Thiophene Derivatives for Evaluation as Anticancer Agents, *Phosphorus Sulfur Silicon Relat*. 184(10):2645-2654(2009). **https://doi.org/10.1080/10426500802561096**

[46] F.E. Onen-Bayram, I. Durmaz, D. Scherman et al., A novel thiazolidine compound induces caspase-9 dependent apoptosis in cancer cells. *Bioorganic Med Chem.* 20(17):5094- 5102(2012). **https://doi.org/10.1016/j.bmc.2012.07.016**

[47] E. Ami, K. Nakahara, A. Sato, J.T. Nguyen, K. Hidaka, Y.Hamada, S.Nakatani , T.Kimura , Y.Hayashia , Y. Kisoa, Synthesis and antiviral property of allophenylnorstatine-based HIV protease inhibitors incorporating D-cysteine derivatives as P2/P3 moieties, *Bioorg. Med. Chem. Lett* 17: 4213-4217(2007), **https://doi.org/10.1016/j.bmcl.2007.05.039**

[48] Y. Pandey, P.K. Sharma, N.Kumar , A. Singh, Biolgical activities of thiazolidine - A review. *Int J PharmTech Res*. 3(2):980-985 (2011)

[49] D.S. Abid, N.L. Shihab, F.S..Kamounah, Research Article Synthesis, characterization and structure activity relationship analysis of N- acetyl-2-substituted phenyl thiazolidine-4-carboxylic acids derivatives as neuraminidase inhibitors, J. Chem. Pharm. Res. 6(11):845-854. (2014)

[50] N.C. Desai, K.M. Rajpara, V.V. Joshi, Microwave induced synthesis of fluorobenzamidescontaining thiazole and thiazolidine as promising antimicrobial analogs. *J Fluor Chem*. 145:102-111 (2013), **https://doi.org/10.1016/j.jfluchem.2012.10.012.**

[51] M.H. Shih, Y.Y. Xu, Y.S. Yang, G.L.A. Lin, Facile Synthesis and Antimicrobial ActivityEvaluation of Sydnonyl-Substituted Thiazolidine Derivatives. *Molecules*. 20:6520-6532(2015). **https://doi.org/10.3390/molecules20046520.**

[52] X.Xua, X. Qianb, L.Zhong, Synthesis and fungicidal activity of fluorine-containingphenylimino-thiazolidines derivatives, *J. Fluor. Chem.,* 126:297- 300(2005)
https://doi.org/10.1016/J.JFLUCHEM.2004.03.004

[53] G.Li., X. Qian, J. Cui, Q. Huang, D. Cui, R. Zhang, F. Liu, Synthesis and herbicidal activitiesof fluorine-containing 3-pyridylmethyl-2-phenyliminothiazolidine derivatives, J. Fluor. Chem., 127 :182-186(2006)

[54] E.S.A.K. Soares et al, Effect of new thiazolidine derivatives LPSF/GQ-02 and LPSF/GQ-16 on atherosclerotic lesions in LDL receptor-deficient mice (LDLR-/-). *Cardiovasc. Pathol.* 22(1):81-90(2013). https://doi.org/10.1016/j.carpath.2012.05.006

[55] S.Vitaliy, Synthesis, Polymerization Ability, Nonlinear Optical Properties of Methacrylic Monomers and Polymers with Benzylidene Moiety. 2007;1(3):131-135. https://doi.org/10.23939/chcht01.03.131

[56] S.Vitaliy,et al, Nonlinear optical properties of thiazolidinone derivatives. *Opt Mater* 31(3):554-557(2009). https://doi.org/10.1016/j.optmat.2007.10.019.

[57] N. Benhalima, K. Toubal, A. Chouaih, G. Chita, S. Maggi, A. Djafri, F. Hamzaoui, Synthesis and Molecular Structure Investigation by DFT and X-Ray Diffraction of ARNO. *J. Chem. Crystallogr.* 41: 1729-1736 (2011). https://doi.org/10.1007/s10870-011-0165-9

[58] L. R. Dalton, P. A. Sullivan and D. H. Bale, Electric Field Poled Organic Electro-Optic Materials: State of the Art and Future Prospect, *Chem. Rev* 110: 25–55. (2010), https://doi.org/10.1021/cr9000429

[59] L. Dalton, Advances in Polymer Science, *Springer*, Berlin Heidelberg, (2002)

[60] J. Luo et al, Facile Synthesis of Highly Efficient Phenyltetraene-Based Nonlinear Optical Chromophores for Electrooptics, Org. *Lett*. 8 :1387–1390 (2006), https://doi.org/10.1021/ol060178b

[61] S.-K. Kim et al, Side-chain electro-optic polymer modulator with wide thermal stability ranging from -46°C to 95°C for fiber-optic gyroscope applications,*Appl. Phys. Lett.,* 2005, 87, 061112. https://doi.org/10.1063/1.2009807

[62] L.R. Dalton, D. Lao, B.C. Olbricht, S. Benight, D.H. Bale, J.A. Davies, T.Ewy, S.R. Hammond , P.A. Sullivan, Theory-inspired development of new nonlinear optical materials and their integration into silicon photonic circuits and devices, *Opt. Mater.* 32, 658–6682 (2010) ,https://doi.org/10.1016/j.optmat.2009.02.002

[63] H.C. Song, M.C. Oh, S.W. Ahn, W.H. Steier, H.R. Fetterman,C. Zhang, Flexible low-voltage electro-optic polymer modulators, *Appl. Phys. Lett*. 82:4432–4434(2003). https://doi.org/10.1063/1.1586474

[64] F. Liu, S. Chen, S. Mo, G. Qin, C. Yu, W. Zhang, W.-J. Shi, P. Chen, H. Xu and M. Fu, J. Synthesis of novel nonlinear optical chromophores with enhanced electro-optic activity by introducing suitable isolation groups into the donor and bridge. *Mater. Chem.* C, 2019, 7, 8019–8028. https://doi.org/10.1039/C9TC01658A

[65] M. Balakrishnan, M. Faccini, M. B. J.Diemeer, W. Verboom, Driessen, A. Reinhoudt, D. N.; Leinse, A. Photodefinable electro-optic polymer for high-speed modulators, *Electron Lett* 42 (2006)

[66] S. K Kim, Y. C Hung. B. J Seo, K. Geary, W. Yuan, B. Bortnik, Fetterman, H. R.; Wang, C.; Steier, W. H.; Zhang, C. Antioxidant and anti-inflammatory compounds isolated from Acer tegmentosum. *Appl Phys Lett* 87(061112):1-2. (2005) **https://doi.org/10.5897/JMPR11.1421**

[67] S. Park, J. J Ju, S. K Park, M. H Lee, J. Y. Do, Thermal relaxation trimming for enhancement of extinction ratio in electro-optic polymer Mach-Zehnder modulators, *Appl Phys Lett* 86, (071102): 1-3(2005), **https://doi.org/10.1063/1.1864236**

[68] C.W. Dirk, H.E. Katz, M.L. Schilling, L.A. King. Use of thiazole rings to enhance molecular second-order nonlinear optical susceptibilities, *Chem Mat* 2(6):700-705 (1990) **https://doi.org/10.1021/cm00012a020**

[69] M. Manuela M. Raposo, Synthesis and characterization of novel diazenes bearing pyrrole, thiophene, and thiazole heterocycles as efficient photochromic and nonlinear optical (NLO) materials, 91(1): 62-73(2011), **https://doi.org/10.1016/j.dyepig.2011.02.012**

[70] L.K. Zaitri , S.M. Mekelleche , Nonlinear optical activity of imino-dyes with furan, thiophene or thiazole moieties as π-conjugated bridge: a computational investigation , Mol. Phys. 118(18) (2020) , **https://doi.org/10.1080/00268976.2020.1761471.**

[71] A. Qureshi, Short Review on Thiazole Derivative, *J Drug Deliv Therapeut* 9(4) (2019) **https://doi.org/10.22270/jddt.v9i4-A.3701**

[72] Pattan SR, Suresh CH, Pujar VD, Reddy VVK, Rasal VP, Koti BC. Synthesis and antidiabetic activity of 2-amino [5'(4sulphonylbenzylidine)- 2,4-thiazolidinedione]-7-chloro-6-flourobenzothiazole. *Indian J Chem Sect* B 44: 2404-8. (2005)

[73] M.S. Pingle, Synthesis and biological activity of 4H-pyrimido [2,1-b] benzothiazole-8-substituted-2-thiomethyl-3-cyano-4ones. *Indian J Heterocyc. Chem* 12(4):343-346 (2003)

[74] Y. Kumar, R. Green, Wise DS, Wotring LL, Townsend LB. Synthesis of 2,4-disubstituted thiazoles and selenazoles as potential antifilarial and antitumour agents. 2- arylamido and 2-alkylamido derivatives of 2- amino-4(isothiocyanatomethyl)thiazole and 2- amino-4-(isothiocyanomethyl)selenazole. *J Med Chem* 1993; 36: 3849-52.

[75] S. Rollas, S.G. Kucukguzel. Biological activites of hydrazone derivatives. *Molecules* 12:1910-39 (2007), **https://doi.org/10.3390/12081910.**

[76] A.A. Havan, N.R Pai, Synthesis and antimicrobial screening of 5arylidine-2-imino-4 -thiazolidinones. *Arkivoc* 14:14855 (2007)

[77] J.J. Choi, M.W. McCarthy, Cefiderocol: A novel siderophore cephalosporin. *Expert Opin. Investig. Drugs* 27:193–197. (2018)

[78] T. Aoki, H.Yoshizawa, K.Yamawaki, K. Yokoo, J. Sato, S. Hisakawa, Y. Hasegawa, H. Kusano, M. Sano, H. Sugimoto et al. Cefiderocol (S-649266), A new siderophore cephalosporin exhibiting potent activities against Pseudomonas aeruginosa and other gram-negative pathogens including multi-drug-resistant bacteria: Structure activity relationship. *Eur. J. Med. Chem*. 155:847–868. (**2018**), **https://doi.org/10.1016/j.ejmech.2018.06.014**

[79] S. Portsmouth, D van Veenhuyzen, R.Echols, M.Machida, ; J.C.A. Ferreira, M.Ariyasu, P. Tenke, T.D. Nagata, Cefiderocol versus imipenem-cilastatin for the treatment of complicated urinary tract infections caused by Gram-negative uropathogens: A phase 2, randomised, double-blind, non-inferiority trial. *Lancet Infect. Dis* 18:1319–1328(2018)

[80] M.Ghoncheh, Z.Pournamdar, H.Salehiniya, Incidence and Mortality and Epidemiology of Breast Cancer in the World. *Asian Pac. J. Cancer Prev.* 17, 43–46 (2016).

[81] Sukinah H. Ali , Abdelwahed R. Sayed , Review of the synthesis and biological activity of thiazoles ,Synthetic Commun. 51(2021) **https://doi.org/10.1080/00397911.2020.1854787**

Chapter II

Fundamental Concepts

of Computational Methods

II.1 Importance of computational methods in chemistry:

Classical computational methods have become vital tools in many fields. These simulations allow us to interpret experimental results, validate physical models, and better understand system properties. However, the complexity of realistic models often limits their ability to guide the design of new materials or compounds. Since quantum computers are designed to efficiently simulate quantum systems, they may provide deeper insights into the models we use today, as well as the ability to simulate more complex and realistic models. Computational and experimental methods complement each other, enhancing understanding and increasing efficiency. As quantum hardware continues to develop, it is expected that quantum simulations might eventually become accurate enough to corroborate experimental results [1]. Quantum algorithms can address a range of chemistry-related problems, but the primary focus is on calculating the low-lying energy levels of chemical systems, known as the electronic structure, this energy levels is essential for predicting reactivity, identifying stable molecular configurations, and determining optical properties.[2].

II.2 Quantum mechanics:

Quantum mechanics serves as the foundation for modern chemistry, suggesting that this theory could potentially predict the behavior of any chemical compound. However, this is not entirely true. As Dirac pointed out in 1929, " The precise application of these laws results in equations that are too complex to be solved". *Dirac 1929* [3], The complexity of a quantum system's wavefunction increases exponentially with the number of particles, making exact solutions computationally expensive or even infeasible for most systems. To address this, a wide range of approximation methods such as Hartree-Fock, density functional theory (DFT), and post-Hartree-Fock approaches, have been developed to make quantum chemical calculations more practical and accessible.

II.3 X-ray diffraction:

X-ray diffraction is an essential technique for probing molecular structures, offering unparalleled precision in structural analysis. Its evolution has made it the foremost method for determining structures in chemistry, when a sample is exposed to X-rays, these rays interact with the material's electrons, generating a diffraction pattern caused by the scattering of X-rays by the electron clouds surrounding the atoms. This pattern reveals crucial details about the atomic arrangement within the material. In this section, we begin by outlining the X-ray diffractometer used in our experiments, highlighting its key features and operational principles. Following this, we will delve

into the methods for processing the raw diffraction data and applying necessary corrections to the intensities. These corrected intensities are critical for accurately determining the structure of the compound under study, allowing for precise resolution and refinement of its molecular configuration.

In a crystal, atomic distances are typically on the angstrom scale, meaning the radiation used for diffraction experiments has wavelengths between 0.5 and 2 Å. X-rays, as electromagnetic waves, interact with the electrons of atoms in the material, and two types of interactions can be observed in single crystals [4] The first is inelastic interaction, where the X-ray photon's wavelength changes as it transfers some or all of its energy to the material, leading to phenomena such as absorption and the Compton effect. In absorption, the photons give up all their energy to the atoms, while in the Compton effect, the photons are deflected from their original path, losing part of their energy. The second type is elastic interaction, where the photons are deflected without any change in their energy. This conservation of wavelength in the scattering process, known as Thomson scattering, causes diffraction. The scattered waves can interfere with one another, producing diffraction peaks in specific directions.

II.3.1 Bragg law:

According to Bragg's analysis [5], lattice planes hkl in crystals are considered to be layered. A distance d separates these layers, as shown in **Fig. II.1.**, and the impact of X-rays or incident light on these atomic planes results in reflection [6]. At the lattice planes, the angle between the incident radiation and the corresponding diffracted radiation remains unchanged. For a diffracted ray to be observed at a certain angle to the incident radiation, Bragg's law must be satisfied:

$$n\lambda = 2d_{hkl} \sin \theta_{hkl} \qquad \textbf{(II.1)}$$

where:

n: integer called the order of diffraction;

λ: wavelength;

d_{hkl}: interplanar distance (the distance between two lattice planes of the (hkl) family);

θ_{hkl}: The Bragg angle is defined as half of the angle formed between the incident radiation and the diffracted radiation.

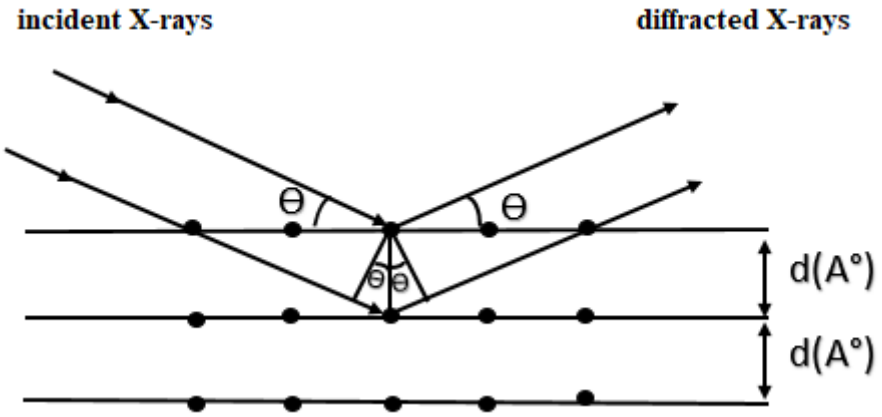

Fig. II.1. Illustration of an X-ray diffraction pattern.

Detection of diffracted X-rays is achieved using a diffraction pattern, Which is composed of Bragg spots. Specifically, a shorter interplanar distance (d) corresponds to a higher $sin\ \theta$ value, and consequently, a larger θ. As a result, diffraction from closely spaced lattice planes occurs at greater angles. This large reflection angle enables a more detailed detection of electron density, corresponding to higher resolution in diffraction data. The intensity of the diffraction peak reveals information about the atomic number and atomic positions within the unit cell, while its position provides insights into the unit cell's size and shape [7]. In a perfect crystal, an infinite number of lattice planes can generate diffraction in accordance with Bragg's condition. However, in real crystals, imperfections and natural limitations on diffraction generally exist, which can vary from one crystal to another

II.3.2 Scattering factor:

The scattering intensity from an atom is determined by summing the scattering contributions from all its electrons, which is referred to as the atomic scattering factor. This factor is influenced by the atom's chemical composition, the diffraction angle 2θ, and the X-ray wavelength.

For each pseudo-atom, the electron distribution, which moves with the nucleus without distortion, is described at a point $\overrightarrow{r_1}$ in relation to the positions of the nuclei within the scattering system by:

$$\rho(\vec{r},\vec{R}) = \sum\sum_{K,l}(\vec{r} - \overrightarrow{R_{k,l}}) \qquad \textbf{(II.2)}$$

R denotes the set of instantaneous coordinates of the nuclei, and $R_{K,l}$ represents the position vector of nucleus K within lattice l The scattering factor for the pseudo-atom k is then given by:

$$f_k(\vec{H}) = \int_K^R K,l\ \rho_k(\vec{r}_K)e^{-2\pi ihr_K}dv \qquad \textbf{(II.3)}$$

II.3.3 Structure Factor:

The structure factor (*F*) quantifies the amplitude of the electric field generated by electrons when subjected to incident X-rays. It represents the total sum of the amplitudes scattered by all atoms (*fj*) within a unit cell. Mathematically, the structure factor is expressed as:

$$\boldsymbol{F = \sum_{j=1}^{N} f_j\, e^{i\varphi}} \qquad \textbf{(II.4)}$$

N represents the total number of atoms present within a unit cell,

Since the structure factor Fis influenced by the atomic scattering factor, fj and these atoms must be located on lattice planes such that their diffraction conforms to Bragg's law, F will also depend on the hkl planes. This is why the structure factor is indexed by hkl, giving F(hkl).

Thus, the structure factor can be written in terms of the atomic coordinates (x_j,y_j,z_j)as follows:

$$F(hkl) = \sum_{j=1}^{N} f_j\, e^{i2\pi(hxj+kyj+lzj)} \qquad \textbf{(II.5)}$$

II.3.4 Integrated Intensity:

When X-rays interact with matter, the crystal lattice points generate coherent sources, and the scattered waves interfere with each other to form diffraction peaks at specific orientations. The diffraction angle (Bragg angle) is utilized to calculate the intensity I_{hkl} of these peaks. The magnitude of the structure factor F_{hkl} is derived from this measured intensity, commonly referred to as the integrated intensity.

The integrated intensity from an X-ray diffraction experiment is expressed in terms of the structure factor. The below formula can be simplified if the components [A] and [E] are equal to unity. This principle applies to a small crystal or to a mosaic crystal composed of crystallites that are somewhat disorientated.

$$\frac{I_{hkl}}{I_0} = \lambda^3 r_0^2 \frac{V}{V_c^2} \frac{1}{\omega} [L][P][A][T][E]|\overrightarrow{F_{hkl}}|^2 \qquad \textbf{(II.6)}$$

I_0: the intensity of the incident beam;

λ : wavelength ;

r_0: classical radius of the electron;

V_c: volume of the unit cell;

V: volume of the diffracting sample;

ω : angular scanning speed (rotation of the crystal around the ω axis);

[P]: polarization factor.

[A]: factor accounting for absorption effects.

[E]: factor accounting for extinction effects.

[T]: Debye-Waller factor, arising from the fact that atoms vibrate around their average position.

[L]: geometric factor, called the Lorentz factor, which depends on how the integrated intensity was measured.

The above formula can be simplified if the components [A] and [E] are equal to one. This principle applies to a small-sized crystal or a mosaic crystal composed of somewhat misoriented crystallites.

II.3.4.2 Intensity corrections:

II.3.4.2.1 Lorentz Corrections (L):

Diffraction takes place when a node of the reciprocal lattice intersects the reflection sphere (Ewald sphere). The intensity of the corresponding reflection increases proportionally if a reciprocal lattice point remains in the diffracting position for an extended period. Since the duration for different lattice points to cross the Ewald sphere varies based on the intensity recording method and the positions of reciprocal lattice nodes, a correction factor is required. This is where the Lorentz correction is applied.

The duration a reciprocal lattice point stays in a diffracting position is influenced by two factors: the location of the reciprocal lattice nodes and the speed at which they traverse the reflection sphere. In this context, the crystal is rotated around an axis perpendicular to the plane formed by the incident and diffracted beams. Assuming the crystal, and consequently the reciprocal lattice, rotates at a constant angular velocity ω, and if V_n represents a component of the linear velocity of the reciprocal lattice point along the radius of the reflection sphere, the Lorentz factor (L) can be defined accordingly..

The Lorentz factor **[8] Fig. II.2.** corresponds to an angular correction applied to any hkl reflection to account for the differences in the speeds V_n at which the hkl nodes pass through the reflection sphere. This correction ensures that the varying times during which different nodes remain in the diffracting position are properly adjusted for, resulting in accurate intensity measurements.

$$L = \omega / V_n \lambda = 1 / \sin 2\theta \qquad \textbf{(II.7)}$$

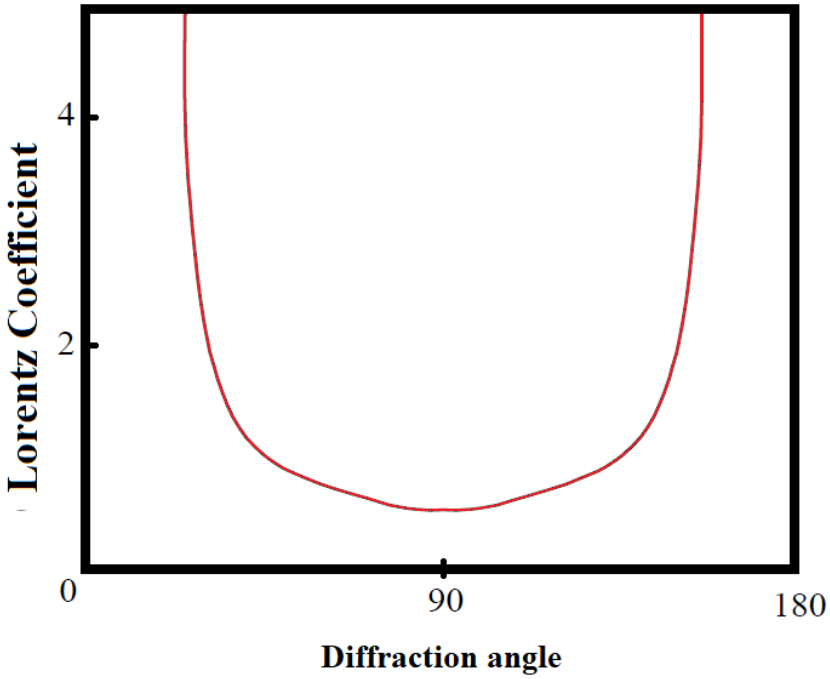

Fig. II.2. Lorentz Factor

II.3.4.2.2 Correction de polarisation (P) :

The X-rays diffracted by the crystal planes are partially polarized, This results in a decrease in the intensity of the reflected beam. The phenomenon is dependent only on the diffraction angle and is corrected by a factor that accounts for this effect. Specifically, X-rays with electric vectors parallel to the plane scatter without any loss of intensity, whereas those with electric vectors perpendicular to the plane experience intensity changes depending on the angle of diffraction. This correction factor, denoted as (P), varies between 0.5 and 1, depending on the scattering angle.

$$P = \frac{1}{2}(1 + cos^2 2\theta) \qquad \text{(II.8)}$$

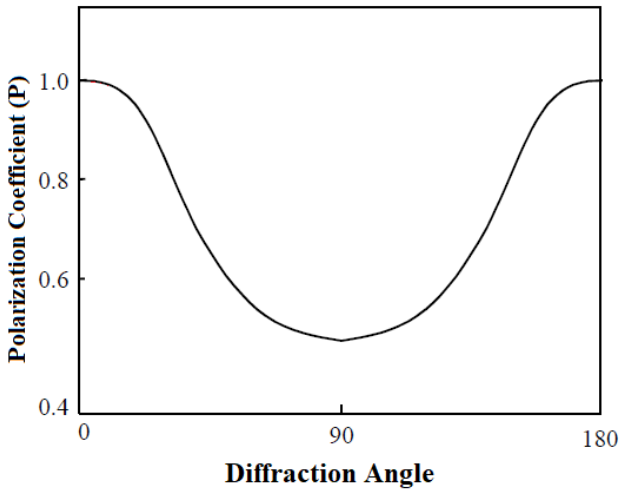

Fig. II.3 Polarisation factor

II.3.4.2.3 Absorption Correction:

As X-rays pass through a material of any shape (e.g., a crystal of thickness (l), they are partially transmitted and partially absorbed. The fractional decrease dI in the intensity I of X-ray beam as it traverses a homogenous material is experimentally observed to be proportional to the distance traveled l Hence, in differential form:

$$-\frac{dI}{I} = \mu . dl \qquad \text{(II.9)}$$

In this case, μ the constant of proportionality, is referred to as the linear absorption coefficient. This coefficient is influenced by the material's properties, its density, and the wavelength of the X-rays. Integrating the equation above results in:

$$I = I_0 e^{-\mu l} \qquad \text{(II.10)}$$

where I_0 is the intensity of the incident X-ray beam, and I is the intensity of the X-ray beam after passing through a thickness l. The linear absorption coefficient μ is proportional to the material's density ρ, and μ/ρ represents a material-specific constant that is independent of its physical state. This constant is often listed for various characteristic wavelengths used in X-ray diffraction. The equation above can be modified and rewritten as:

$$I = I_0 e^{-\left(\frac{\mu}{\rho}\right)\rho . l} \qquad \text{(II.11)}$$

$$\frac{\mu}{\rho} = k\lambda^3 Z^3 \qquad \text{(II.12)}$$

where k is a constant that varies for each branch of the curve,, and Z represents the atomic number of the absorber. As a result, short-wavelength X-rays possess high penetrating ability and are commonly known as "hard" X-rays .in contrast to long-wavelength X-rays, which are easily absorbed and referred to as "soft." The term $e^{-\left(\frac{\mu}{\rho}\right)\rho.l}$ is called the absorption correction. The length of the path thus makes a difference, which is why the ideal shape of a crystal would be spherical.

II.3.4.2.4 Extinction Correction (E)

Crystallographic planes cause reflections when the primary X-ray beam passes through a crystal. This theory assumes that the crystal has a degree of imperfection, which overlooks the possibility that reflections can be scattered successively along the crystal. However, in certain crystal samples, the diffracted beam can indeed be diffracted successively. This secondary diffraction leads to a reduction in the intensity of the affected reflections. There are two main extinction processes:

- Primary Extinction: As the beam passes through the crystal, its intensity decreases due to successive reflections along the crystallographic planes

- Secondary Extinction: This occurs when the beam passes through different domains of perfect crystals that make up the single crystal. Here, the crystal is considered as a mosaic structure

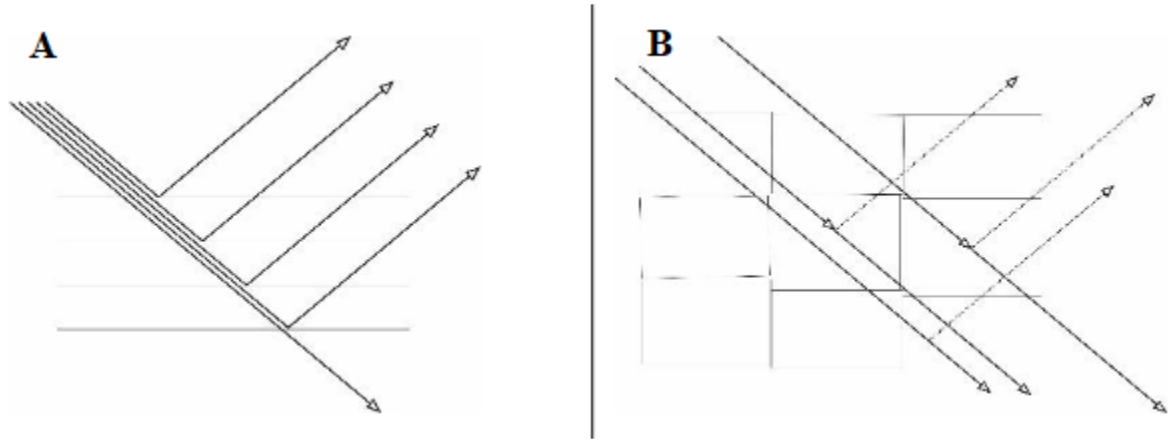

Fig. II.4. Diagrams of the three extinction processes occurring in crystals. a) primary extinction, where the beam is progressively extinguished as it passes through the crystal. c) secondary extinction due to mosaicity.

II.4 UV visible absorption spectroscopy:

UV visible absorption spectroscopy is a very common method in the laboratory. It is based on the property of molecules to absorb light radiation of a specific wavelength. The useful UV-visible wavelength range extends from 800 to 10 nm. This type of spectroscopy is very useful for studying

the electronic structures of unsaturated molecules and for measuring the extent of their conjugation. The UV-visible spectrophotometer is used to measure the absorbance of a homogeneous solution at a given wavelength or over a given spectral region. When the quantum of energy is absorbed, there are electronic transitions from the bonding molecular orbital to the unfilled anti-bonding molecular orbital. This produces an electronic spectrum. The absorption band, observed in the UV-visible range, is characterized by its position in wavelength λmax (nm) and by its intensity linked to the molar extinction coefficient ε max.

II.5 Infrared spectroscopy:

Infrared spectroscopy is a diagnostic method for determining the nature of chemical bonds present in a molecule **[9].** Experience shows that certain vibration frequencies, known as 'group frequencies', are characteristic of the presence of a chemical group in the molecule under study. The mechanical theory of vibrations enables the prediction of group frequencies based on the approximate values of various types of force constants **[10].** Infrared spectroscopy is therefore a very powerful characterization tool for identifying molecular groups and obtaining a wealth of microscopic information about their conformation and possible interactions **[11].** During this analysis, the sample is subjected to electromagnetic radiation in the central infrared wavelength range (2.5 µm < λ < 50 µm). The electric field induced by the electromagnetic wave can interact with a dipole moment of a molecular entity present in the material. When the field frequency coincides with the vibration frequency of an eigenmode of the molecule, the interaction created causes certain bonds to vibrate and the energy of the corresponding exciting wave to be absorbed. The frequency of absorbed radiation is influenced by the type of bonds, the masses of the atoms involved, and the surrounding environment.

II.6 Nuclear magnetic resonance spectroscopy

Nuclear magnetic resonance (NMR) spectroscopy exploits the magnetic properties of specific atomic nuclei, such as the hydrogen nucleus ^{1}H and that of the carbon nucleus ^{13}C.

Because of their nuclear spin, which is a rotating charge that makes them resemble tiny magnets, atomic nuclei can all exhibit nuclear magnetic moments. The latter can take on several orientations when subjected to an external magnetic field. These different orientations represent different energy levels: low energy, when the magnetic moment is parallel and in the same direction as the external magnetic field, and higher energy, when the direction is opposite.

The external field has a proportional effect on the energy difference, ΔE, between the two states. Radiation of frequency (ν) with: ΔE = hν can be absorbed to cause the transition from a low level to a high level. The nucleus is considered to be in resonance at the moment of transition.

When an external magnetic field is applied to a molecule, it affects the nuclear spins and causes the electrons to flow around the proton in a direction perpendicular to the field. An internal magnetic field is therefore present. This field is added to the external field and is called the unshielding phenomenon, whereas if it opposes the external field, it is called the shielding phenomenon. The absorption peaks move further to the right of the field.

spectrum as the shielding intensity increases, and vice versa in the case of de-shielding. The degree of shielding or unshielding is therefore determined by the proton's environment, the chemical structure of the compound and, most importantly, the existence of π or free electrons.

Chemical shifts are measured in parts per million (ppm) relative to a standard reference compound. Tetramethylsilane (TMS) was chosen as the reference compound. Chemically, it is inert and does not react with the compounds analysed. Its symmetrical molecular structure comprises four methyl groups (CH3) attached to a central silicon atom and its spectrum shows a single peak resulting from this symmetry, which facilitates identification and integration. On the NMR scale, its proton signals appear as a single, sharp peak at 0 ppm. This indicates that all other signals in the spectrum are referenced to the TMS peak.

II.7 Molecular modeling:

In the field of research and the development of new chemical substances, the role of molecular modeling has become increasingly significant.This technique allows for the examination of chemical properties and reactions, as well as the manipulation of structural models in both two-dimensional and three-dimensional representations. By utilizing theoretical computational methods, molecular modeling enables the determination of a molecule's geometry and atomic configuration, as well as its physicochemical characteristics. This approach not only conserves time and resources by eliminating the need to synthesize and evaluate less promising compounds but also enhances the understanding of molecular mechanisms, which can lead to major advancements in areas like pharmacology and materials science.

Modeling a molecule involves determining the spatial positions of its atoms and calculating the energy of the resulting configuration. The most accurate structure corresponds to the one with the lowest achievable energy.

Different approaches are utilized in molecular modeling, each tailored to specific needs. Classical mechanics methods, which are computationally efficient, are ideal for handling large molecular systems. They allow for the analysis of complex structures like proteins or polymers without requiring extensive computational power.

II.7.1 Quantum Chemistry Calculation Methods:

On the other hand, quantum methods including ab initio, semi-empirical, and density functional theory (DFT) are used to calculate the electronic properties of smaller systems with great precision. These methods, while more computationally demanding, provide detailed insights into the electronic structure and reactivity of molecules. The use of quantum approaches in this study is due to their ability to accurately predict electronic properties, which are crucial for understanding molecular behavior. These methods are based on solving the time-independent Schrödinger equation, which not only determines the system's energy but also reveals other important properties such as molecular energies, thermochemical properties, atomic charges, and IR and Raman spectra. By employing these quantum methods, researchers can achieve a deeper understanding of molecular systems, leading to more accurate predictions and potentially significant advancements in various fields.

II.7.1.1 Schrodinger equation:

The Schrödinger equation describes the time evolution of a system composed of N particles at the atomic and molecular level, defined by their spatial position. It is represented by a wave function. $\Psi(\vec{r_1}, \vec{r_2}, \dots \vec{r_n}, t)$ and is expressed as follows:

$$\hat{H}\Psi(\vec{r_1}, \vec{r_2}, \dots \vec{r_n}, t) = i\,\hbar\frac{\partial}{\partial t}\Psi(\vec{r_1}, \vec{r_2}, \dots \vec{r_n}, t) \quad \textbf{(II.13)}$$

$$\hat{H} = -\frac{h^2}{2m}\nabla^2 + V(\vec{r_1}, \vec{r_2}, \dots \vec{r_n}, t) \quad \textbf{(II.14)}$$

$\Psi(\vec{r_1}, \vec{r_2}, \dots \vec{r_n}, t)$ The wave function of the particle at position $\vec{r}$ and time t

$\hat{H}$:Hamiltonian operator;

$V(\vec{r_1}, \vec{r_2}, \dots \vec{r_n}, t)$: the potential energy in which the particle is located at position $\vec{r}$ and time t

i: the imaginary unit;

ħ: the reduced Planck constant $\hbar = \frac{h}{2\pi} = 1.11265.\ 10^{-34}\ J^{1}C^{2}m^{-1}$

∇^2: the Laplacian operator $\nabla_K^2 = \frac{\partial^2}{\partial X_K^2} + \frac{\partial^2}{\partial Y_K^2} + \frac{\partial^2}{\partial Z_K^2}$

This equation is known as the time-dependent Schrödinger equation. It is a second-order differential equation that includes time-dependent derivatives, and solving it in its general form poses a significant challenge.

In certain simplified cases, such as for isolated atoms or molecules, where external factors like time-invariant fields and strong gravitational forces are neglected, and interactions between electrons and nuclear spins are considered negligible, the forces governing the system's behavior are time-independent. In other words, the particles experience a potential energy that depends solely on their spatial coordinates and remains constant over time in the absence of external perturbations. The solutions for $\Psi(\overrightarrow{r_1}, \overrightarrow{r_2}, \ldots \overrightarrow{r_n}, t)$ can be expressed as:

$$\Psi(\overrightarrow{r_1}, \overrightarrow{r_2}, \ldots \overrightarrow{r_n}, t) = \frac{\partial}{\partial t} \Psi(\overrightarrow{r_1}, \overrightarrow{r_2}, \ldots \overrightarrow{r_N}, t) e^{-iEt/\hbar} \quad \textbf{(II.15)}$$

Where E represents the total energy of the system associated with the wave function $\Psi(\overrightarrow{r_1}, \overrightarrow{r_2}, \ldots \overrightarrow{r_n}, t)$ which is obtained by solving the time-independent Schrödinger equation:

$$\hat{H}\Psi(\vec{r}, \overrightarrow{R}) = E\psi(\vec{r}, \vec{R}) \quad \textbf{(II.16)}$$

The Hamiltonian for a system composed of N nuclei and n electrons can also be expressed as:

$$H = -\frac{\hbar^q}{2m_e}\Sigma_k^n \nabla_k^2 - \Sigma_k^n \Sigma_A^N \frac{z_A e^2}{4\pi\varepsilon_0 r_{kA}} + \frac{1}{2}\Sigma_k^n \Sigma_{k\neq L}^n \frac{e^2}{4\pi\varepsilon_0 r_{kL}} - \frac{\hbar^2}{2}\Sigma_A^N \frac{1}{M_A}\nabla_A^2 + \frac{1}{q}\Sigma_A^N \Sigma_B^N \frac{z_A z_B}{4\pi\varepsilon_0 R_{AB}} \quad \textbf{(II.17)}$$

$$H = T_e + V_{ne} + V_{ee} + T_n + V_{nn} \quad \textbf{(II.18)}$$

Where e and m_e are the charge and mass of the electron, respectively;

M_A is the mass of nucleus A;

r_{kA} is the distance between the k^{th} electron and the L^{th} nucleus;

r_{kL} is the distance between the k^{th} electron and the L^{th} electron;

R_{AB} is the distance between nuclei A and B, with charges Z_A and Z_B respectively;

ε_0 is the vacuum permittivity constant, where $4\pi\ \varepsilon_0 = 1.11265.\ 10^{-10}$, $j^{-1}C^2m^{-1}$.

The expression for the Hamiltonian consists of five terms:

- ✓ Kinetic energy of the electrons T_e;
- ✓ Attraction energy between electrons and nuclei V_{ne};
- ✓ Electrostatic repulsion energy between electrons V_{ee};
- ✓ Kinetic energy of the nuclei T_n;
- ✓ Electrostatic repulsion energy between the nuclei V_{nn}.

The Schrödinger equation can only be solved exactly for the hydrogen atom and hydrogen-like ions. For multi-electron systems, approximation methods are necessary to solve the Schrödinger equation approximately.

II.7.1.1.1 Born-Oppenheimer Approximation:

The Born-Oppenheimer approximation [12] relies on the fact that the mass of a nucleus is much greater than that of an electron. This makes it possible to disregard the motion of the nuclei relative to the electrons. Consequently, we consider that the electrons move in a potential created by fixed nuclei. In this context, the kinetic energy of the nuclei is zero $T_n = 0$, and the Coulombic energy V_{nn} due to the repulsion between nuclei becomes a constant.

At this point, we transition from solving the Schrödinger equation for a system with N electrons and M nuclei to solving the equation for a system with N electrons interacting with the potential of the nuclei

The Hamiltonian then includes only the following electronic contributions:

$$H_{él} = -\frac{1}{2}\sum_i \nabla_i^2 - \sum_i \sum_A \frac{Z_A}{R_{Ai}} + \sum_{i<j} \frac{1}{r_{ij}} \qquad \textbf{(II.19)}$$

$$H_n = -\frac{1}{2}\sum_A \frac{\nabla_A^2}{M_A} + \sum_{i<j} \frac{1}{r_{ij}} + \sum_{A<B} \frac{Z_A Z_B}{R_{AB}} \qquad \textbf{(II.20)}$$

Now we need to solve the Schrödinger equation for $H_{él}$ to determine the electronic energy $E_{él}$ and the corresponding wave function $\Psi_{él}$:

$$H_{él}\Psi = E_{él}\Psi \qquad \textbf{(II.21)}$$

Despite these simplifications, solving this equation remains extremely challenging because for a system with n electrons, it depends on $3n$ spatial coordinates. This is why it is often coupled with the Hartree approximation [12], which further simplifies the problem.

II.7.1.1.2 Orbital Approximation:

The electronic wave function, denoted by Ψ_e or simply Ψ, is a function of the coordinates of the electrons within the system. In 1928, Douglas Hartree [13] developed the orbital approximation, which is based on the idea of separating the multi-electron wave function Ψ (1, 2,2n) into a product of 2n electron wave functions. Each one-electron wave function corresponds to a single electron in the system depending only on the coordinates of one electron and is often referred to as a "molecular orbital," leading to:

$$\Psi\ (1,\ 2,2n) = \Phi_1(1).\Phi_2(2)\ \ldots\ \Phi_{2n}(\Sigma_n)\ \cdot = \Pi_{i=1}^{2}\Phi i(i) \qquad \textbf{(II.22)}$$

Where:

- i designates the i orbital.
- 2n is generally considered as the practical number of electrons.
- $\Psi$is a function of 2n) ×3variables since each electron is described by three spatial coordinates in three-dimensional space.

What characterizes the orbital approximation is the assumption that the behavior of each electron in the system can be considered independently of the other electrons; this is why it is also referred to as the "independent electron approximation." In this framework, each electron is under the influence of the other electrons within the system, but on average. In other words, electron iii does not interact with the other electrons directly, but rather with an average potential generated by them.

However, poly-electronic systems cannot be described solely using the wave function represented in the previous equation as it is impossible to distinguish one electron from another when they occupy the same quantum state. To fully describe a poly-electronic system, it is essential to consider the indistinguishability of electrons and the Pauli exclusion principle, which asserts that two identical fermions (particles with half-integer spin, such as electrons) cannot occupy the same quantum state simultaneously.

Incorporating these principles into the description of a poly-electronic system involves ensuring that the total wave function of the system adheres to the antisymmetry requirement with respect to the permutation of the electrons' coordinates in both position and spin space.This antisymmetry guarantees that two electrons cannot occupy the same quantum state, in accordance with the Pauli exclusion principle [14]. For example, the permutation of two electrons results in:

$$\Psi(1,\ 2,\ldots,i,\ldots,k,\ldots,2n) = -\Psi(1,2,\ldots,k,\ldots,i,\ldots,2n) \qquad \textbf{(II.23)}$$

However, these principles are not adhered to in Hartree's formulation of the wave function. In this approach, each electron is considered to occupy a single spin-orbital, without accounting for the fact that electrons with the same spin and energy must avoid occupying the same quantum state.

More advanced methods, such as Hartree-Fock theory, introduce a generalization of the wave function called the "Slater determinant," to account for the indistinguishability of electrons and the Pauli exclusion principle. This determinant consists of n spin-orbitals [15,16], where 2n corresponds to the number of electrons in the system.

$$\Psi(1,2,\dots 2n) = \frac{1}{\sqrt{2n!}} = \begin{vmatrix} \phi_1 X_1 & \phi_2 X_1 & \dots & \phi_{2n} X_{2n} \\ \phi_1 X_2 & \phi_2 X_2 & \dots & \phi_{2n} X_{2n} \\ \dots & \dots & \dots & \dots \\ \phi_2 X_{2n} & \phi_2 X_{2n} & \dots & \phi_{2n} X_{2n} \end{vmatrix} \quad \text{(II.24)}$$

Where:

- The variables X_i represent the coordinates in both space and spin.
- $\frac{1}{\sqrt{2n!}}$is the normalization factor.
- $\Phi_i(Xi)$ are the orthonormal spin orbitals.

The antisymmetric nature of the Slater determinant plays a critical roleWhen the positions of two electrons are exchanged, it corresponds to swapping two rows (or columns) of the determinant, which leads to a change in the order of the spin-orbitals. Consequently, the overall sign of the determinant changes, ensuring that the total wave function conforms to the antisymmetric condition.

Moreover, the spin-orbitals Φ_i must be distinct from one another; this condition is essential for the proper functioning of the Slater determinant. In fact, attempting to evaluate the determinant with two identical rows (or columns) (i.e., two identical spin-orbitals) yields a determinant with a value of zero. Therefore, it is essential that each spin-orbital constitutes a unique quantum state to avoid the annihilation of the determinant.

II.7.1.2 Hartree-Fock Approximation:

In 1927, Hartree proposed a method to calculate approximate multi-electron wave functions by expressing them as products of one-electron wave functions [13]. Each electron corresponds to an orbital, and the total wave function is written as a product of orthogonal one-particle wave functions:

$$\Psi=\psi_1(r1)\cdot\psi_2(r2)\cdot\psi_3(r3)\cdots\psi_N(rN) \quad \text{(II.25)}$$

In 1930, Fock showed that Hartree's method does not adhere to the antisymmetry principle of the wave function [17]. According to the Pauli exclusion principle, two electrons cannot occupy the same quantum state at the same time.

The Hartree-Fock method [18] provides an approximate solution to the Schrödinger equation for a quantum system with *n* electrons and *N* nuclei, where the multi-electron wave function Ψ_{HF} is expressed as a Slater determinant composed of one-electron spin orbitals, which respects the antisymmetry of the wave function:

$$\boldsymbol{\psi(X_1, X_2, X_3, \ldots, X_N)} = \frac{1}{\sqrt{N!}}\begin{vmatrix} \boldsymbol{\psi_1(X_1)} & - & \boldsymbol{\psi_N(X_1)} \\ - & - & - \\ - & - & - \\ \boldsymbol{\psi_1(X_N)} & - & \boldsymbol{\psi_N(X_N)} \end{vmatrix} \quad \text{(II.26)}$$

Were

$$\psi j(x)=\phi j(rj)\alpha j(\zeta j)$$

is the spin variable $(\pm\frac{1}{2})$and the spin functions are orthonormal:

$$\int\alpha*(\zeta i)\alpha(\zeta j)\, d\tau=\delta(\zeta i,\zeta j)$$

This formulation ensures that the wave function remains antisymmetric with respect to the exchange of any two electrons, in accordance with the requirements of quantum mechanics and the Pauli exclusion principle.

II.7.1.3 Theory of Density Functional Theory (DFT):

The core idea of Density Functional Theory DFT is to express the energy of a multi-electron system based on the electronic density, thus replacing the wave function for energy calculations. The advantage of this approach is that the electron density is a physical observable and depends on only three variables (x, y, z), regardless of the number of particles in the system, making it independent of the system's size. In contrast, the wave function for a system with N electrons depends on 4N variables: 3N spatial coordinates and N spin coordinates, resulting in greater complexity as the number of variables increases.

The objective of DFT is to find a functional (that is, a function dependent on another function) that relates density and energy. A relatively simple expression for the total energy, independent of the

wave function, can be expressed in terms of the one-particle reduced density matrix $[\gamma 1\left(\overrightarrow{r_1}, \overrightarrow{r_1'}\right)]$ and its diagonal part, $\rho 1(\overrightarrow{r_1})$ called the classical density , together with the diagonal term of the two-particle matrix $\rho_2\left(\overrightarrow{r_1}, \overrightarrow{r_1'}\right)$:

$$E = \int \left[-\frac{1}{2}\nabla^2\gamma_1\left(\overrightarrow{r_1}, \overrightarrow{r'_1}\right)\right]_{\overrightarrow{r_1}=\overrightarrow{r r_1}} d\overrightarrow{r_1} - \Sigma_A \int \frac{z_A}{r_{1A}}\rho_1(\overrightarrow{r_1})\, d\overrightarrow{r_1} + \iint \frac{\rho(\overrightarrow{r_1},\overrightarrow{r_2})}{r_{12}} \overrightarrow{d_{r_1}}, \overrightarrow{d_{r_2}} \qquad \textbf{(II.27)}$$

The foundational principles of DFT, establishing the possibility of calculating properties of a system using electronic density, were established in 1964 by Hohenberg and Kohn [19] and later by Kohn and Sham [20].

II.7.1.3.1 Hohenberg-Kohn Theorem:

The Hohenberg-Kohn formulation aims to simplify the expression for energy and establish density functional theory (DFT) as an exact theory for many-body systems. Hohenberg and Kohn demonstrate that the electron density $\rho(r)$ is the sole function needed to obtain all electronic properties of a system in its ground state. The electron density also determines the number of electrons nnn in the system through the condition:

$$n=\int \rho(r)\, dr \qquad \textbf{(II.27)}$$

where $\rho(r)$ denotes the electron density and r represent the coordinates of the electrons refers to the electron coordinates. The electron density is defined by:

$$\rho(r)=\int |\Psi(r)|^2\, dr \qquad \textbf{(II.28)}$$

with Ψ being the electronic wave function, the solution to the electronic Schrödinger equation:

$$H\Psi=[T+V_{Ne}+V_{ee}]\ \Psi=E\Psi \qquad \textbf{(II.29)}$$

In practice, the electron-nucleus attraction term V_{Ne} is often replaced by an external potential V_{ext} that encompasses V_{Ne} as well as various external perturbations (such as electric fields, etc.).

The total electron density can be expressed in terms of spin densities ρ_α and ρ_β

$$\rho(r)=\rho_\alpha(r)+\rho_\beta(r) \qquad \textbf{(II.30)}$$

The electronic energy is thus a functional of the density, expressed as:

$$E[\rho] \text{ where } \rho= (\rho_\alpha, \rho\beta) \qquad \textbf{(II.31)}$$

This energy, expressed in terms of density functional, is decomposed into three parts:

$$E[\rho]=T[\rho]+E_{Ne}[\rho]+E_{ee}[\rho] \quad \textbf{(II.32)}$$

where:

- $T[\rho]$ respresents the kinetic energy.
- $E_{Ne}[\rho]$ is the energy of the electron-nucleus interaction.
- $E_{ee}[\rho]$ is the energy of the electron-electron interactions, which can also be split into two terms: a Coulomb term $J[\rho]$ and an exchange term $K[\rho]$.

The electron-nucleus interaction $E_{Ne}[\rho]$ and the Coulomb interaction term $J[\rho]$ are given by the following expressions:

$$E_{Ne}[\rho]=\sum a \int \frac{z_a \rho(r)}{|R_a - r|} d^3r \quad \textbf{(II.33)}$$

and

$$J[\rho]=\frac{1}{2}\iint \frac{\rho(r)\rho(r\prime)}{|r-r\prime|} d^3r\, d^3r\, r\,' \quad \textbf{(II.34)}$$

The energy $E_{Ne}[\rho]$ is obtained from the potential $V_{Ne}(r)$:

$$E_{Ne}[\rho]=\int \rho(r) V_{Ne}(r)\, d^3r \quad \textbf{(II.35)}$$

An alternative formulation was later established by Kohn and Sham to determine the other terms in the expression for $E[\rho]$.

II.7.1.3.2 Kohn-Sham Approach:

The success of Density Functional Theory (DFT) is largely attributed to the approach proposed by Kohn and Sham (KS) [19] in 1965. The idea was to consider a gas of n non-interacting electrons defined by their orbitals $\phi_i(r)$. The electronic density is given by the relation:

$$\rho(r)=\sum_i^N | \phi i(r) |^2 \quad \textbf{(II.36)}$$

Kohn and Sham' The kinetic energy $T_s[\rho]$ in the non-interacting electron system is given by:

$$T[\rho]= \sum_i^N \langle \phi i | \frac{\rho^2}{\rho} | \phi i \rangle \quad \textbf{(II.37)}$$

This leads to a system of Schrödinger equations for the non-interacting electrons, which takes the form:

$$[\frac{\rho^2}{2}+V_{eff}(r)]\phi i=\varepsilon_i \phi_i \quad \textbf{(II.38)}$$

where $V_{eff}(r)$ is the mean field created by the electron gas and experienced by any given electron. The total energy of this system is:

$$E_S[\rho]=T_s[\rho]+E_{Ne}[\rho] \quad \textbf{(II.39)}$$

In reality, the electrons do interact with each other, and the energy $E_S[\rho]$ is not the total energy. Similar to the Hartree-Fock method, this energy corresponds to 99% of the energy of independent electron gas, but it is necessary to include a term for electron-electron interaction (just as the Hartree-Fock method does not include electronic correlation).

To incorporate electron interaction into the energy equation, we can rewrite it as a function of $T_S[\rho]$ and $J_S[\rho]$:

$$E[\rho]=(T[\rho]-T_S[\rho]) +T_S[\rho]+E_{Ne}[\rho]+(E_{ee}[\rho]-J[\rho]) +J[\rho] \quad \textbf{(II.40)}$$

This simplifies to:

$$E[\rho]=T_S[\rho]+E_{Ne}[\rho]+J[\rho]+E_{XC}[\rho]$$

where $E_{XC}[\rho]$ is the energy containing all the correlation of interacting electrons:

$$E_{XC}[\rho]=(T[\rho]-T_S[\rho]) +(E_{ee}[\rho]-J[\rho])$$

Here, $T[\rho]-T_S[\rho]$ isthe kinetic correlation corresponding to the difference between the exact kinetic energy of correlated electrons and the kinetic energy of a non-interacting electron system. Similarly, $E_{ee}[\rho]-J[\rho]$ represents an exchange term and a correlation energy.

With:$V_{XC}(r) = \frac{dE_{XC}[\rho]}{d\rho(r)}$ the exchange-correlation potential, the system of equations to solve can be written as:

$$[\frac{\rho^2}{2} + VNe(r) + \int \frac{\rho(r\prime)}{|r-r\prime|} d^3r' + V_{XC}(r)]\phi i(r) = \varepsilon i\phi i(r)] \quad \textbf{(II.41)}$$

Finally, we can define the Kohn-Sham Hamiltonian, h_{KS}

$h_{KS}\phi i=\varepsilon i\phi i$

Combining this equation with the relation for electronic density gives us the Kohn-Sham equations. This last equation will be minimized using the variational principle.

There is a similarity in the treatment of Kohn-Sham and Hartree-Fock. The difference between these two methods arises from the term V_{XC}, which should allow DFT to obtain the exact energy, thus accounting for all correlations. This is not the case in the HF method, where configuration

interactions are not described. However, the Kohn-Sham method cannot be evaluated analytically due to the difficulty in calculating its integrals.

II.7.1.4 Exchange and Correlation Functional:

The challenge in evaluating Kohn-Sham's methods lies in determining a valid exchange-correlation term applicable to all systems [20]. Consequently, the accuracy of DFT depends on the approximation made for this term. Numerous approximations have emerged, varying in their effectiveness at describing the exchange-correlation term, with the most popular being the Local Density Approximation (LDA) [21] and the Generalized Gradient Approximation (GGA) [22].

II.7.1.4.1 Local Density Approximation (LDA):

The effectiveness of density functional theory relies on the principle that the exchange-correlation energy can be corrected by applying the exact functional for a homogeneous electron gas, where both the electronic density and wave function are considered locally constant. The exchange-correlation functional is expressed as:

$$E_{XC}^{LDA}[\rho] = \int \rho(r)\varepsilon_{XC}(\rho(r))\, d_r \qquad \textbf{(II.42)}$$

Here, $\varepsilon_{XC}(\rho(r))$ represents the exchange-correlation energy per particle of the uniform electron gas with density $\rho(r)$. Moreover$\varepsilon_{XC}(\rho(r))$can be viewed as the sum of an exchange contribution and a correlation contribution:

$$\varepsilon_{XC}(\rho(r)) = \varepsilon_X(\rho(r)) + \varepsilon_C(\rho(r)) \qquad \textbf{(II.43)}$$

The exchange energy for a homogeneous electron gas, denoted by S (after Slater), is known exactly:

$$\varepsilon_{XC}(\rho(r)) = -\frac{3}{4}\left(\frac{3\rho(r)}{\pi}\right)^{1/3} \qquad \textbf{(II.44)}$$

For the correlation energy $\varepsilon_X\rho(r)$, no exact analytical form is known.

II.7.1.4.2 Introduction of Spin Term (LSDA):

The Local Spin Density Approximation (LSDA) introduces the concept of spin into the LDA approximation. The electronic density is divided into two populations: ρ(↑) for spin-up and ρ(↓) for spin-down. The energy then becomes:

$$E_{XC}^{LSDA}[\rho\downarrow,\rho\uparrow] = \int \varepsilon_{XC}^{hom}(\rho\downarrow(r),\rho\uparrow(r),\rho(r))\,d^3r$$

The advantage of this approximation is that it allows for the description of systems placed in an external magnetic field and enables access to susceptibility. LSDA is applicable to both systems with slowly varying electronic density and those with rapidly varying density, making it more frequently used than LDA. However, it still tends to overestimate binding energies and gives too low gaps for semiconductors and insulating compounds [23].

II.7.1.4.3 Generalized Gradient Approximation (GGA):

An improvement in the precision of the LDA method involves the use of a non-uniform electron gas. In this context, the functional describing exchange-correlation no longer depends solely on the electronic density but also on the density's derivatives. In GGA methods, the first derivative of the density is introduced as a variable in the functional describing exchange-correlation. GGA methods allow the exchange-correlation term to depend on higher-order derivatives of the electronic density as well.

It is generally written in the form:

$$E_{XC}^{GGA} = \int (\rho(\vec{r})\varepsilon_{XC}(\rho(\vec{r}),\nabla\rho(\vec{r})))\,d\vec{r} \qquad \text{(II.45)}$$

A significant limitation of the LDA approximation lies in the exchange part. An improved formulation was proposed:

$$E_X = E_X^{LDA} - \int F(S(\vec{r}))\rho^{\frac{4}{3}}(\vec{r})\,d\vec{r} \qquad \text{(II.46)}$$

where

$$S(\vec{r}) = \frac{|\nabla\rho(\vec{r})|}{\rho^{\frac{4}{3}}(\vec{r})}$$

Notable functions include those proposed by Becke (B88) [24], Perdew (PW86) [25], and Handy and Cohen (OPTX) [26].

II.7.1.4 B88 Exchange Functional:

The B88 exchange functional is based on dimensional analysis and the correct asymptotic behavior of the exchange energy density:

$$F^{B88}(S) = \frac{\beta S^2}{1+6\beta sinh^{-1}(S)}) \quad \text{(II.47)}$$

where β=0.042 This parameter is empirically determined through a least-squares analysis of the exchange energies of six rare gas atoms (from He to Rn).

The Perdew-Wang (PW91) functional [27] is derived from a modification of this functional to satisfy certain scaling conditions.

II.7.1.5 PW86:

This functional is based on an analysis of the gradient expansion of the exchange-correlation hole around its LSDA form:

$$F^{PW86}(S) = [1 + 1.296\left(\frac{S}{P}\right)^2 + 14\left(\frac{S}{P}\right)^4 + 0.2\left(\frac{S}{P}\right)^6]\frac{1}{15} \quad \text{(II.48)}$$

where P= $(24\pi^2)^{1/3}$. The Perdew, Burke, and Ernzerhof (PBE) functional [28] is a modification of this functional. Notably, neither PW86 nor PBE contains empirical parameters.

II.7.1.6Hybrid Functionals:

A third class of functionals, commonly used today, is known as hybrid functionals. These add a certain percentage of the Hartree-Fock exchange energy $E_X^{GGA}E_X^{HF}$ can be calculated exactly and the percentage is empirical. The most well-known of these is B3LYP [29] (with "3" indicating three parameters), but variations like B3PW91, O3LYP, and PBE also exist. The total exchange-correlation energy of B3LYP can be represented by the following equation [30]:

$$E_{XC}^{B3LYP} = (1-a)E_X^{LSDA} + aE_{XC} \quad + bE_X^{B88} + cE_C^{LYP} + (1-c)E_C^{LSDA} \quad \text{(II.49)}$$

with a=0.2, b=0.72, and c=0.81.

These parameters are semi-empirical quantities determined by fitting the formation heats of a standard set of molecules. This functional provides remarkably accurate results across a wide range of systems.

II.8 Conclusion:

In this chapter, we have provided a comprehensive overview of the fundamental concepts required to understand structure resolution techniques based on experimental X-ray diffraction analysis. X-ray diffraction is a cornerstone method in structural chemistry and materials science, enabling the determination of the atomic and molecular structure of crystalline substances with high precision. In addition to the experimental aspects of X-ray diffraction, we have explored the theoretical framework underlying the approximations used in solving the Schrödinger equation. This equation is central to quantum mechanics and serves as a foundational tool for calculating the electronic structure of multi-particle systems. The chapter discusses various approximation methods, each tailored to balance computational efficiency with the desired level of accuracy. These include techniques such as Hartree-Fock theory, density functional theory (DFT). Furthermore, this chapter emphasizes the integration of experimental and computational approaches. By combining high-quality X-ray diffraction data with advanced theoretical and computational methods

References:

[1] S. McArdle, S. Endo, A. Aspuru-Guzik, S.C. Benjamin, X. Yuan, Quantum computational chemistry, *Rev. Mod. Phys.* 92(2020) 015003, https://doi.org/10.1103/RevModPhys.92.015003

[2] T. Helgaker, S. Coriani, P. Jrgensen, K. Kristensen, J. Olsen, and K. Ruud, *Chem. Rev.* 112 (1):543(2012), https://doi.org/10.1021/cr2002239

[3] P. Dirac, Quantum mechanics of many-electron systems, Proc. *R. Soc. A* 123:714 (1929)

[4] N. Boukabcha, Study of the Structural Properties of Poly-Substituted Organic Compounds "Étude des propriétés structurales des composés organiques poly-substitués". PhD thesis, University of Mostaganem, Process Engineering: Materials Science, (2017).

[5] A. Authier, Dynamical theory of X ray diffraction, in: Int. Tables Crystallography., *International Union of Crystallography, Chester, England*. 534-551(2006). http://dx.doi.org/10.1107/97809553602060000569

[6] E.S. Ameh, A review of basic crystallography and x ray diffraction applications, *Int. J. Adv.Manuf. Technol*. 105:3289-3302(2019) . https://doi.org/10.1007/s00170 019 04508 1.

[7] M. Lee, X Ray Diffraction for Materials Research, Apple Academic Press,:*Apple Academic Press* 302 (2016) New York. https://doi.org/10.1201/b19936.

[8] C. Giacovazzo, H.L. Monaco, D. Viterbo, F. Scordari, G. Gilli, G. Zanotti, M. Catti, C. Giacovazzo, P. Paufler, Fundamentals of Crystallography. International Union of Crystallography, *Cryst. Res. Technol.* 28:370-370 (1993). https://doi.org/10.1002/crat.2170280318,

[9] W. BRÜGEL, An Introduction to Infrared Spectroscopy, *Methuen & Co. Ltd*., (1962).

[10] G. HERZBERG, Molecular Spectra and Molecular Structure. In Infrared and Raman Spectra of Polyatomic Molecules, D. Van Nostrand Company Inc., (1945).

[11] R. T. CONLEY, Infrared Spectroscopy, Alin and Bacon Inc., (1966).

[12] Lovenberg, Iron-Sulfur Proteins, Molecular Properties, *W. Lovenberg 2(*1973) Academic press, New York – London

[13] D.R. Hartree, The Wave Mechanics of an Atom with a Non-Coulomb Central Field. Part I. Theory and Methods, *Math. Proc. Cambridge Philos. Soc.* 24(1):89-110(1928). https://doi.org/10.1017/S0305004100011919.

[14] W. Pauli, The Connection Between Spin and Statistics, *Phys. Rev.* 58:716-722 (1940).

https://doi.org/10.1103/PhysRev.58.716.

[15] J.C. Slater, Statistical Exchange Correlation in the Self Consistent Field, *Adv. Quant. Chem 6:* 1-92(1972). https://doi.org/10.1016/S0065 3276(08)60541 9.

[16] J.C. Slater, Cohesion in Monovalent Metals, *Phys. Rev.* 35:509-529(1930). https://doi.org/10.1103/PhysRev.35.509.

[17] V.Fock, Naherungsmethode zur Losung des quantenmechanischen Mehrkorperproblems. *Zeitschrift für Physik* 61 :126-148. (1930)

[18] J.L. Rivail, Eléments de chimie quantique à l'usage des chimistes 2 (1999).

[19] W. Kohn, L. J. Sham, Self-Consistent Equations Including Exchange and Correlation Effects, *Phys. Rev*., 140 :1133(1965) , https://doi.org/10.1103/PhysRev.140.A1133

[20] K. Mathivon, Phd thesis, university Paris-est (2013).

[21] P.Dirac, Note on Exchange Phenomena in the Thomas Atom. *Math. Proc. Cambridge Philos. Soc.* 26:376-385(1930) http://dx.doi.org/10.1017/S0305004100016108

[22] J. P. Perdew, J. A. Chevory, S. H. Vosko, K. A. Jackson, M. A. Perderson, D. J. Singh and C. Fiolhais, Atoms, molecules, solids, and surfaces: Applications of the generalized gradient approximation for exchange and correlation, *phys Rev*. B 46:6671. 1992

[23] D.Berbouche, Etude théorique et modélisation des quelques molécules biologiques actives, PhD thesis , University Mohamed Khider, Biskra Algeria (2014).

[24] A.D. Becke, Density-functional exchange-energy approximation with correct asymptotic behavior, *Phys. Rev*. A 38 :3098-1988, https://doi.org/10.1103/PhysRevA.38.3098

[25] J. P. Perdew, Y. Wang, Accurate and simple density functional for the electronic exchange energy: Generalized gradient approximation, *Phys. Rev*. B 33 :8800(1986)

[26] N. C. Handy, A. J. Cohen, Left-right correlation energy, *Mol. Phys*. 99:403-412 (2001) , https://doi.org/10.1080/00268970010018431

[27] J. P. Perdew, Y. Wang, Accurate and simple analytic representation of the electron-gas correlation energy, *Phys. Rev*. B 45:244 (1992), https://doi.org/10.1103/PhysRevB.45.13244

[28] J. P. Perdew, K. Burke, M. Ernzerhof, Generalized Gradient Approximation Made Simple, *Phys. Rev. Lett*. 77:3865(1996), http://dx.doi.org/10.1103/PhysRevLett.77.3865

[29] P. J. Stephens, F. J. Devlin, C. F.Chabalowski, M. J. J. Frish, Ab Initio Calculation of Vibrational Absorption and Circular Dichroism Spectra Using Density Functional Force Fields, Phys. *Chem*.98(45): 11623 (1994)

[30] F. Jensen, Introduction to Computational Chemistry, *John Wiley & Sons*, Ltd, (2007).

Chapter III

Structural and Spectroscopic Analysis

III.1. Introduction

The structural elucidation of organic compounds is a cornerstone of chemical research, providing critical insights into their geometry, bonding, and intermolecular interactions. In this chapter, the compound (E)-3-(3-(2-Methoxyphenyl)-4-Methylthiazol-2(3H)-ylidene) Benzo [4,5] imidazole[1,2-c] thiazole-1(3H)-thione (EMBIT) is comprehensively analyzed using a combination of experimental and computational approaches to ensure a thorough understanding of its molecular and crystal structure, as well as its electronic and spectroscopic properties.

The chapter begins with the synthesis and isolation of EMBIT, followed by its structural determination using single-crystal X-ray diffraction XRD. This technique provides precise information about the atomic arrangement, bond lengths, and angles, forming the basis for a detailed analysis of the compound's geometry.

To complement the experimental findings, molecular modeling techniques are utilized to visualize the optimized geometry of EMBIT and analyze its stability. These computational tools enhance our understanding of the conformational preferences and interactions within the molecule. The structural analysis includes a geometrical evaluation of bond lengths, angles, and planarity, alongside an in-depth study of hydrogen bonding interactions, which play a crucial role in crystal packing. Furthermore, Hirshfeld surface analysis is conducted to visualize intermolecular contacts and interaction regions within the crystal lattice. Non-Covalent Interaction NCI and Reduced Density Gradient RDG analyses are used to explore the nature and strength of non-covalent interactions, crucial for understanding the compound's stability and properties. These computational tools provide detailed visualization of interaction regions and their contributions to the molecular framework.

Finally Spectroscopic analyses both experimentally and theoretically play a key role in confirming the structure and functional groups of EMBIT. The Infrared (IR) spectrum highlights characteristic vibrational frequencies, such as the C=S, C=N, and C=C stretches, which confirm the presence of thiazole and benzimidazole moieties. The Nuclear Magnetic Resonance (NMR) spectra, both ^{1}H and ^{13}C, provide detailed insights into the chemical environment of hydrogen and carbon atoms, confirming the compound's connectivity and functional groups. Additionally, UV-Vis spectroscopy is employed to study the electronic transitions, offering valuable information about the compound's conjugated system and light absorption properties.

This integrated approach, combining experimental spectroscopy, X-ray crystallography, and theoretical modeling, offers a comprehensive understanding of the structure, interactions, and properties of EMBIT, paving the way for its potential applications in various fields.

III.2 Synthesis Process of (E)-3-(3-(2-Methoxyphenyl)-4-Methylthiazol-2(3H)-ylidene) Benzo [4,5] imidazole[1,2-c] thiazole-1(3H)-thione (EMBIT) :

(E)-3-(3-(2-Methoxyphenyl)-4-methylthiazol-2(3H)-ylidene) benzo [4,5] imidazole[1,2-c] thiazole-1(3H)-thione (EMBIT) was synthesized in the Laboratory of Organic Applied Synthesis (LSOA), Department of Chemistry, Faculty of Sciences, University of Oran 1 Ahmed Ben Bella, by *Dr. Abdelmadjid Benmohamed,* it's representing a significant advancement in the development of heterocyclic compounds. Such compounds are of great interest due to their potential applications in medicinal and pharmaceutical chemistry, particularly for their diverse biological activities. This process involves a straightforward, stepwise approach, ensuring high efficiency and satisfactory yields. The methodology includes the formation of a thiazolium salt as an intermediate, followed by a condensation reaction to produce the target compound. Careful monitoring and purification techniques ensure the synthesis of a pure and well-characterized final product. Shown in **Fig III.1.** and detailed steps are outlined below:

1. Formation of Thiazolium Salt (2) :
    - 3-(2-Methoxyphenyl)-4-methylthiazole-2-thione (1) was mixed with methyl iodide.
    - Acetone was used as the solvent.
    - The reaction was carried out at room temperature for 30 minutes.
2. Condensation Reaction:
    - The thiazolium salt (2) was reacted with thiazole[3,4-a] benzimidazole-1-thione (3).
    - The reaction was performed in acetone under basic conditions at room temperature.
3. Reaction Monitoring :
    - The progress of the reaction was monitored using Thin Layer Chromatography (TLC).
    - A solvent system of chloroform and ethanol in an 8:2 ratio was used.

4. Isolation of Product :

    - After 24 hours, the reaction mixture was filtered to collect the product.
    - The collected product was washed with acetone to remove impurities.

5. Drying and Recrystallization:

    - The filtered product was dried.
    - The dried product was recrystallized using ethanol to obtain the final compound.

6. Final Product :

    - The process yielded a brown solid as the final product, produced in satisfactory yield.

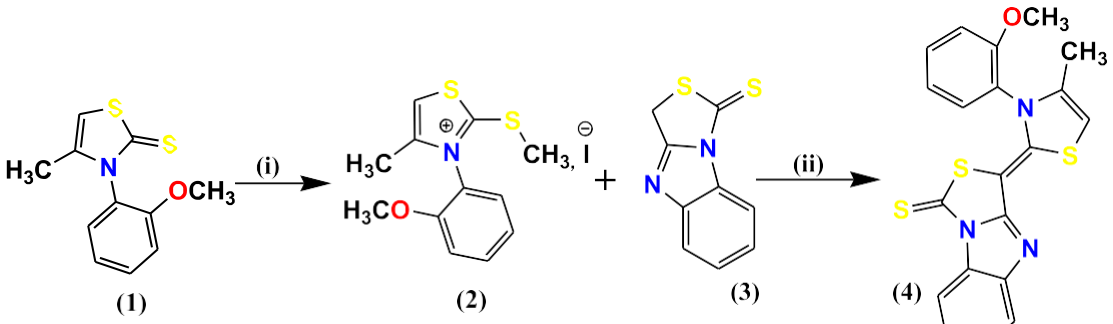

Condition and reagent: (i)CH_3I, Acetone, 25°C; **(ii)**Acetone, 25°C

Fig III.1. Synthesis Process scheme

III.3 Results:

III.3.1. Physical Characteristics:

The compound (E)-3-(3-(2-Methoxyphenyl)-4-Methylthiazol-2(3H)-ylidene) Benzo [4,5] imidazole[1,2-c]thiazole-1(3H)-thione (EMBIT) is a heterocyclic organic compound with distinct physical properties that reflect its stability and structural complexity. With a molar mass of 409.55 g/mol, it is synthesized as a brown solid with a yield of 71%.

The compound exhibits a high melting point exceeding 260 °C, indicative of its thermal robustness. During chromatographic analysis, EMBIT demonstrates an Rf value of 0.7 in chloroform, reflecting its moderate mobility and compatibility with this solvent system. Its characteristic brown color and well-defined properties make it a notable subject for further chemical investigations.

These physical attributes highlight EMBIT's potential for use in a variety of research applications, are enlisted in the Table III.1:

Table III.1: physical Properties of EMBIT

Nature:	Heterocyclic organic compound
Molar mass:	409.55 g/mol
Yield (%):	71% (brown solid)
Melting point:	> 260 °C
Rf:	0.7 (in chloroform)
Color:	Brown

III.3.2 Spectroscopic Data:

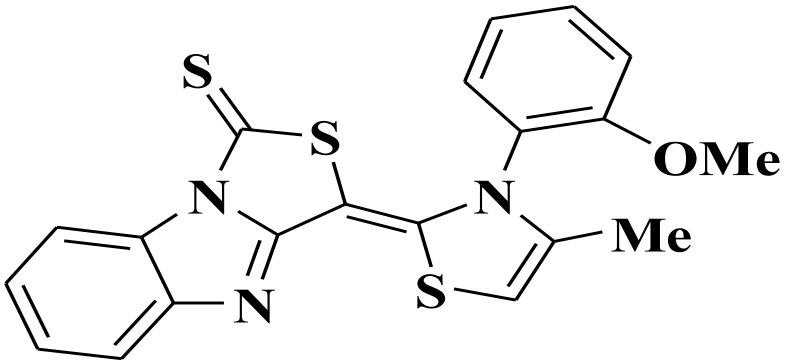

Fig III.2. EMBIT structure

IR (ν cm^{-1}):1289 (C=S), 1520 (C=C), 1610 (C=N).

RMN 1H (300 MHz, CDCl3) δ(PPM) J(Hz):1,90 (s, 3H, CH3thia); 3,84 (s, 3H, OMe); 6,39 (s, 1H, C-H, thia); 7,12 (q, 3H, benzimidazole, J=6,76, J=16,07); 7,34 (m, 2H, thia); 7,73 (m, 2H, thia); 8,65 (d, 1H, benzimidazole, J=7,46).

RMN 13C (75 MHz, CDCl3):14,01 (CH3); 56,14 (O-CH3); 98,06 (Cbenzi=Cthia); 102,41; 113,11; 113,81; 118,50; 121,28; 121,97; 123,05; 129,90; 130,82; 130,92; 133,57; 138,40; 151,14; 156,65 (Cthia=Cbenzi); 170,53 (C-OMe); 181,53 (C=S).

III.4 Structural determination of the compound EMBIT by single-crystal X-ray diffraction

Single-crystal X-ray diffraction remains the reference technique for characterizing small molecules in the solid state. For an appropriate crystalline sample, this method provides a

complete three-dimensional image of the atomic positions that make up the molecules, along with the geometric features of their interactions with other molecules in the solid.

The compound EMBIT, was characterized using X-ray diffraction. The experimental three-dimensional structure of EMBIT was derived from X-ray diffraction analysis of a single crystal at room temperature. Once the structure was resolved and refined, we were able to identify atomic distances, bond angles, torsion angles, and various other structural parameters.

III.4.1Single-crystal X-ray diffraction

Single-crystal X-ray diffraction (SC-XRD) data **Table III.2** were collected at 293(2) K using a STOE IPDS 2 diffractometer **Fig III.3** with monochromatic Mo-Kα radiation (λ = 0.71073 Å). The crystal belongs to the monoclinic system and is characterized by a particular space group. P 21/n, had unit cell dimensions of a = 10.6513(4) Å, b = 13.4438(6) Å, c = 13.0539(5) Å, β = 95.581(3) °, and a unit cell volume of 1860.38(13) Å³. Data were corrected for absorption using the integration method (X-RED32, Stoe & Cie, 2002), with T_{min} and T_{max} values of 0.898 and 0.936, respectively. A total of 12,728 reflections were measured, of which 5,309 were independent (R_{int} = 0.047), and 3,143 were observed with I > 2σ(I). The final refinement yielded an R-factor of 0.040 and a wR(F^2) of 0.096 with a goodness of fit (S) of 0.89, using 244 refinement parameters. Maximum and minimum residual electron densities were 0.27 and -0.17 eÅ^{-3}, respectively.

Table III.2: Crystal data of EMBIT

Molecular weight	409.53 g.mol $^{-1}$
Temperature	293(2)K
Radiation wavelength	0.71073 Å
Crystal System	Monoclinic
Space group	P 2_1/n
a	10.6513(4) Å
b	13.4438(6) Å
c	13.0539(5) Å
α	90°
β	95.581(3) °
γ	90°
V	1860.38(13)Å^3
Z	4
Radiation type	Mo *Kα*
Density	1.462 g.cm^{-3}
Crystal size	0.38 × 0.28 × 0.18 mm
μ	0.414 mm^{-1}
Data collection	
Diffractometer	STOE IPDS 2

Absorption correction	Integration (X-RED32; Stoe & Cie, 2002)
F(000)	848
T_{min}, T_{max}	0.898, 0.936
Reflections	-8<h<15, -19<k< 19, -18<l<18
Number of measured, independent, and observed [I > 2s(I)] reflections	12728, 5309, 3143
R_{int}	0.047
$(\sin \theta/\lambda)_{max}$ ($Å^{-1}$)	0.703
R [F2 > 2s(F2)], wR(F2), S	0.040, 0.096, 0.89
Refinement parameters	244
$\Delta\rho_{max}$, $\Delta\rho_{min}$	0.27, − 0.17

Fig III.3 STOE IPDS II diffractometer.

III.4.1.1 Key Criteria for Single-Crystal Selection:

The development of new materials generally requires a thorough physical study of the solid state, which can only be achieved using single-crystal samples. A suitable single crystal was selected using an optical microscope. This allowed us to view the crystal from different angles and to detect any defects that might interfere with the X-ray diffraction. For an optimal study, the desired single crystal must meet several specific criteria:

- A satisfactory diffracting volume to ensure efficient X-ray analysis;
- A small enough volume to minimize absorption effects;
- The ability to be placed in the homogeneous part of the beam for consistent exposure;
- Maximum homogeneity to avoid inconsistencies in data collection;
- The most isotropic shape to ensure uniformity in all directions.

To fulfill all these conditions, the crystal should have average dimensions of less than 0.5 mm. This ensures precise structural data and a more reliable understanding of the material's properties.

III.4.1.2 Determining the number of molecules in a mesh (Z):

The number of molecules present in one unit cell (Z) is calculated using the following expression:

$$Z = \frac{mass\ of\ the\ unit\ cell}{mass\ of\ the\ molecule}$$

Where :

$$Z = \frac{\rho \cdot V \cdot N}{M}$$

M: Molecular mass

V: Volume of the unit cell

N: Avogadro's number

ρ: Density

The volume of the unit cell can be calculated using:

$$V = abc\sqrt{1 - \cos^2 a - \cos^2 \beta - \cos^2 \gamma + 2\ cos\alpha\ cos\beta\ cos\gamma}$$

The linear parameters a, b, c and angular parameters α, β, γ are given in Table X

- **V** = 1860.38 Å³
- **M** = 409.53 g/mol
- **Z**=4

III.4.1. 3 Determination of the Space Group:

The space group can be determined either by manually examining the filename.hkl file or directly using the WINGX software **[1]:**

- By directly examining the filename.hkl file, a careful examination of the filename.hkl file allows you to:
- Search for systematic extinctions on hkl due to the lattice types A, B, C, I, F, or R

- Search for systematic extinctions due to glide planes and screw axes.

Knowing the rules for systematic extinctions, the International Tables for Crystallography [2] can be used to propose one or more space groups.

This examination revealed the following systematic extinction conditions: hkl: no condition

The space group is therefore: $P2_1/n$

- x, y, z
- -x+1/2, y+1/2, -z+1/2
- -x, -y, -z
- x-1/2, -y-1/2, z-1/2

III.4.1.4 Structural Resolution Procedure:

The structure of the molecule was determined using the ShelxS program [3], integrated within the WinGX software suite [1]. This procedure involves generating two key files: EMBIT.HKL, which contains the measured reflection data, and EMBIT.INS, which holds the molecule's crystallographic information along with the necessary instructions for structure resolution.

Running the ShelxS [3] the EMBIT.ins instruction file (input file) Fig.III.4 contains, in this order, the following information:

- TITL: Title assigned of the studied structure
- CELL: Wavelength (λ) and the parameters of the unit cell (a, b, c; α, β, γ).
- ZERR: Number of molecules in the unit cell and the errors associated with each parameter.
- LATT: Type of lattice (Center-symmetry (+), non-center-symmetry (−)).
- SYMM: Symmetry map generated by the different symmetry elements of the considered group.
- SFAC: Type of atoms contained in the unit cell. The order of their introduction is important; the first atom will be numbered 1, the second atom will be numbered 2, and so on.

- UNIT: Number of atoms in the unit cell; the specified order must be respected.
- HKLF: Miller indices

```
TITL shelxt_a.res in P2(1)/n
CELL  0.71073  10.6513  13.4438  13.0539   90.000   95.581   90.000
ZERR     4.00   0.0004   0.0006   0.0005    0.000    0.003    0.000
LATT   1
SYMM  1/2 - X, 1/2 + Y, 1/2 - Z
SFAC  C    H    N    O    S
UNIT  80 60 12 4 12
HKLF    4
END
```

Fig.III.4 INS file of EMBIT compound

ShelxS[3] facilitates the mapping of electron density distributions within the molecule, with the peaks corresponding to atomic positions. After removing parasitic electron density peaks, the true electron density distribution was visualized **Fig III.5** using the Mercury software **[4],** providing a clear representation of the molecule's atomic structure.

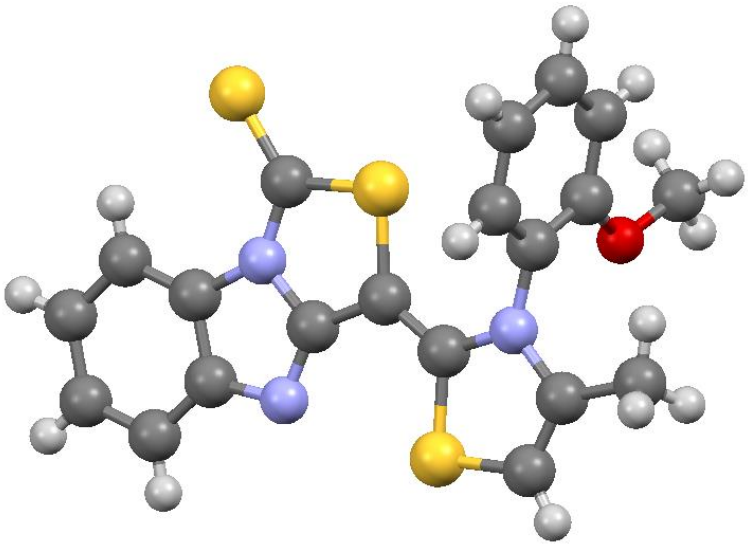

Fig III.5 EMBIT structure visualization by Mercury program [4]

III.4.1.5 Structural refinement:

After resolving the structure of the studied compound, Structural refinement is a crucial step in X-ray diffraction analysis, aimed at enhancing the precision and accuracy of the obtained molecular model. After the initial structure resolution, the model must be adjusted to minimize

discrepancies between observed and calculated diffraction intensities, a refinement of the various structural parameters was performed using the ShelXS program [3], applying the least squares method to |F2|.The ShelxL [5] program was used for the refinement of the molecular structure. This program requires the preparation of two distinct files. The first file, named EMBIT.HKL, contains the intensities of the reflections along with the corresponding Miller indices. The second file, named EMBIT.INS, includes the atomic coordinates obtained during the structural resolution, as well as the instructions needed to refine the structure. The preparation of these files is an essential step to ensure the accuracy of the molecular structure refinement. With the ShelxL program [5], it is thus possible to obtain a detailed molecular structure containing precise information about the geometry of the atoms and bonds. This step of refining the structural parameters allowed us to improve the accuracy of the structure and, most importantly, to obtain more reliable values for the various structural parameters, including interatomic distances, bond angles, and temperature factors.

$$\Sigma w||F_{Oi}|-|F_{Ci}||^2$$

The equation connecting the observed structure factors F_{Oi} and the calculated structure factors F_{Ci} involves a weighting parameter ω. This weighting is applied to give more importance to the most significant reflections. The refinement process is carried out using 3,143 observed reflections.

The structure factor is expressed using the following formula:

$$F(hkl)= \sum_{j=1}^{N} f_j \exp\left[-2\left(hx_j + ky_j + lz_j\right)\right] \exp[-2\pi^2 (U_{11}h^2 + U_{22}k^2 + U_{33}l^2 + 2U_{12}hk + 2U_{13}hl + 2U_{23}kl)]$$

the structure factor equation can indeed be expressed in terms of multiple variables, where each atom contributes a set of parameters. For N atoms, the total number of variables is 9N because each atom is associated with:

- **3 positional parameters**: xj,yj,zj (the fractional coordinates).
- **6 thermal parameters**: U_{ij} (the components of the anisotropic thermal displacement parameters).

Thus, for N atoms, you would have 3N+6N=9N variables. To solve for these variables, a system of 9N equations is required. The resolution procedure involves refining the parameters successively and individually, starting with the scale factor (K), followed by the atomic positions (x_j, y_j, and z_j), and then the thermal displacement parameters (U_{ij}). The refinement of

isotropic and anisotropic thermal parameters, along with the positioning of hydrogen atoms using Fourier series, resulted in a final reliability factor of 4.35%. However, the hydrogen atoms were positioned theoretically using the "HFIX" instruction due to the difficulty of experimentally determining their positions, as they have very few electrons. Additionally, the relatively low reliability factor and the consistency of the various variable parameters throughout the refinement cycles confirm the accuracy of the obtained structure. Following the resolution and refinement process, the final structure of the studied compound is presented in. **Fig.III.6**, including the hydrogen atoms This structure has been deposited at the Cambridge Crystallographic Data Centre under the access number CCDC 1898125.

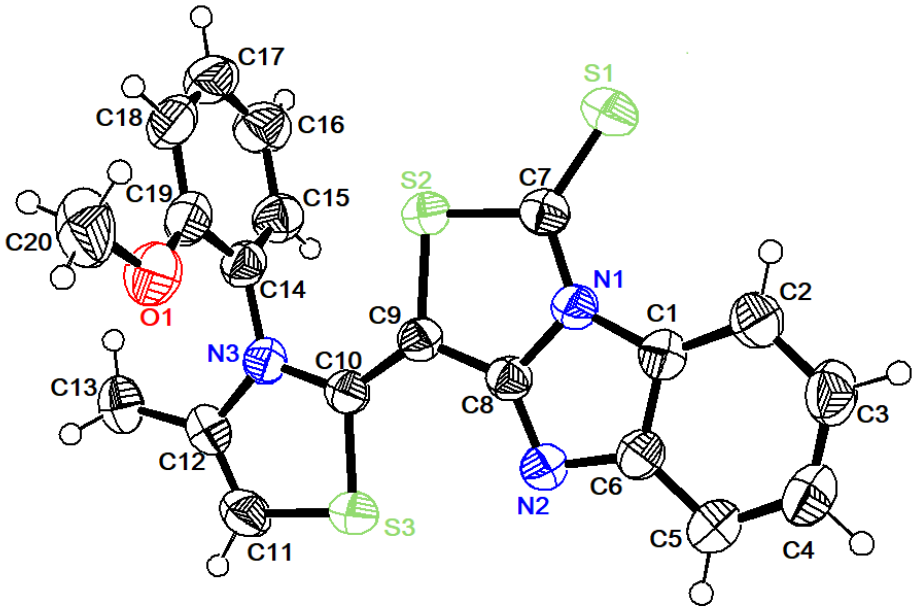

Fig.III.6 labeled structure of EMBIT

Table III.3 Fractional atomic coordinates along with isotropic or equivalent isotropic displacement parameters (Å^2)

	x	*y*	*z*	*U*iso*/*U*eq
S2	0.57616 (5)	0.43795 (3)	0.76738 (3)	0.04720 (12)
S3	0.65575 (5)	0.41297 (4)	0.44214 (3)	0.05141 (13)
S1	0.38553 (6)	0.34047 (4)	0.88860 (4)	0.05867 (15)
N1	0.42391 (15)	0.30854 (10)	0.69015 (10)	0.0414 (3)
N3	0.75098 (15)	0.52109 (10)	0.58964 (11)	0.0434 (3)
N2	0.45582 (15)	0.28612 (10)	0.52284 (11)	0.0446 (3)
O1	0.93715 (16)	0.45558 (12)	0.72922 (12)	0.0702 (4)
C8	0.49136 (17)	0.33479 (11)	0.60814 (12)	0.0402 (4)
C9	0.58393 (17)	0.40830 (12)	0.63642 (12)	0.0407 (4)

C10	0.66162 (17)	0.44905 (12)	0.57002 (12)	0.0403 (4)
C1	0.33706 (18)	0.23587 (12)	0.65327 (13)	0.0443 (4)
C6	0.35992 (17)	0.22370 (12)	0.55044 (13)	0.0437 (4)
C7	0.45344 (19)	0.35543 (12)	0.78225 (13)	0.0448 (4)
C14	0.77209 (19)	0.56799 (13)	0.68908 (14)	0.0468 (4)
C12	0.81454 (19)	0.54862 (13)	0.50525 (15)	0.0495 (4)
C2	0.2457 (2)	0.18448 (14)	0.69879 (15)	0.0566 (5)
H2A	0.231304	0.195134	0.767060	0.068*
C11	0.7732 (2)	0.49716 (15)	0.42118 (15)	0.0577 (5)
H11	0.804476	0.505761	0.357692	0.069*
C15	0.6959 (2)	0.64619 (14)	0.71222 (15)	0.0562 (5)
H15	0.634440	0.670240	0.662937	0.067*
C5	0.2888 (2)	0.15371 (13)	0.49046 (15)	0.0539 (5)
H5	0.301928	0.143389	0.421854	0.065*
C4	0.1990 (2)	0.10066 (15)	0.53614 (17)	0.0627 (6)
H4A	0.152055	0.052949	0.497690	0.075*
C19	0.8671 (2)	0.53248 (15)	0.76060 (15)	0.0535 (5)
C13	0.9154 (2)	0.62539 (16)	0.51795 (18)	0.0648 (6)
H13A	0.878876	0.688536	0.532349	0.097*
H13B	0.956285	0.630076	0.455752	0.097*
H13C	0.976161	0.607110	0.573958	0.097*
C18	0.8813 (2)	0.57613 (18)	0.85715 (16)	0.0670 (6)
H18	0.944017	0.553800	0.906340	0.080*
C3	0.1763 (2)	0.11604 (16)	0.63760 (18)	0.0662 (6)
H3	0.113293	0.079724	0.665121	0.079*
C16	0.7113 (3)	0.68833 (16)	0.80845 (18)	0.0707 (6)
H16	0.660093	0.740849	0.824884	0.085*
C17	0.8030 (3)	0.65228 (18)	0.88037 (17)	0.0721 (7)
H17	0.812200	0.680014	0.945934	0.087*
C20	1.0396 (3)	0.4191 (2)	0.7994 (2)	0.0935 (9)
H20A	1.084216	0.368200	0.766189	0.140*
H20C	1.006712	0.392007	0.859334	0.140*
H20B	1.096202	0.472794	0.819333	0.140*

Table III.4 Atomic displacement parameters (Å^2)

	U^{11}	U^{22}	U^{33}	U^{12}	U^{13}	U^{23}
S2	0.0509 (3)	0.0530 (2)	0.0376 (2)	−0.0052 (2)	0.00374 (18)	−0.00385 (18)
S3	0.0557 (3)	0.0588 (3)	0.0406 (2)	−0.0035 (2)	0.00926 (19)	−0.0056 (2)
S1	0.0656 (4)	0.0686 (3)	0.0438 (2)	−0.0022 (3)	0.0157 (2)	0.0014 (2)
N1	0.0435 (9)	0.0430 (7)	0.0375 (7)	−0.0010 (6)	0.0036 (6)	0.0003 (6)
N3	0.0394 (9)	0.0462 (7)	0.0439 (7)	−0.0025 (6)	0.0013 (6)	0.0022 (6)
N2	0.0438 (9)	0.0493 (8)	0.0407 (7)	−0.0013 (7)	0.0030 (6)	−0.0023 (6)
O1	0.0540 (10)	0.0835 (10)	0.0700 (9)	0.0136 (8)	−0.0089 (7)	0.0075 (8)
C8	0.0411 (10)	0.0428 (8)	0.0367 (8)	0.0018 (7)	0.0036 (7)	0.0017 (6)
C9	0.0400 (10)	0.0444 (8)	0.0374 (8)	0.0004 (7)	0.0018 (7)	−0.0008 (7)
C10	0.0379 (10)	0.0434 (8)	0.0391 (8)	0.0043 (7)	0.0022 (7)	0.0005 (7)
C1	0.0442 (10)	0.0413 (8)	0.0468 (9)	0.0000 (7)	0.0010 (7)	0.0034 (7)
C6	0.0418 (10)	0.0423 (8)	0.0463 (9)	0.0006 (7)	−0.0002 (7)	0.0008 (7)
C7	0.0472 (11)	0.0449 (8)	0.0423 (9)	0.0067 (8)	0.0041 (7)	0.0018 (7)
C14	0.0470 (11)	0.0475 (9)	0.0453 (9)	−0.0095 (8)	0.0019 (8)	0.0010 (7)
C12	0.0443 (11)	0.0508 (10)	0.0547(11)	0.0007 (8)	0.0121 (8)	0.0051 (8)
C2	0.0618 (14)	0.0552 (10)	0.0532(11)	−0.0084 (10)	0.0073 (9)	0.0061 (9)
C11	0.0601 (14)	0.0652 (11)	0.0505(11)	−0.0021 (10)	0.0195 (9)	0.0012 (9)

C15	0.0642 (14)	0.0477 (10)	0.0562(11)	−0.0025 (9)	0.0041 (10)	−0.0034 (8)
C5	0.0562 (13)	0.0509 (10)	0.0527(11)	−0.0028 (9)	−0.0039 (9)	−0.0037 (8)
C4	0.0650 (15)	0.0532 (11)	0.0671(13)	−0.0128 (10)	−0.0074 (11)	−0.0008 (10)
C19	0.0471 (12)	0.0587 (11)	0.0535(11)	−0.0093 (9)	−0.0014 (9)	0.0049 (9)
C13	0.0558 (14)	0.0644 (12)	0.0755(14)	−0.0100 (10)	0.0131 (11)	0.0066 (10)
C18	0.0613 (15)	0.0846 (15)	0.0521(11)	−0.0239 (12)	−0.0096 (10)	0.0041 (11)
C3	0.0644 (16)	0.0611 (12)	0.0726(14)	−0.0190 (11)	0.0043 (11)	0.0109 (10)
C16	0.0862 (19)	0.0569 (12)	0.0701(14)	−0.0107 (12)	0.0127 (13)	−0.0145 (10)
C17	0.0830 (19)	0.0805 (15)	0.0531(12)	−0.0322 (14)	0.0077 (12)	−0.0147 (11)
C20	0.0528 (15)	0.135 (2)	0.0906(18)	0.0176 (16)	−0.0017 (13)	0.0427 (17)

III.5 Structural determination of the EMBIT compound using molecular modeling:

Molecular modeling is a powerful computational technique that allows researchers to investigate the structure and properties of molecules at the atomic level. By employing methods such as crystallography, scientists can gain insights into the geometric properties and shapes of crystals, which play a crucial role in understanding various material characteristics. Recent advancements in theoretical calculation methods, particularly ab initio techniques and

Density Functional Theory DFT have significantly enhanced our ability to model and predict atomic positions within lattices, interatomic distances, bond angles, and torsion angles with remarkable accuracy.

These theoretical approaches are essential for elucidating molecular structures, and the careful selection of appropriate calculation methods is vital for obtaining results that closely align with experimental observations. In the realm of molecular modeling, DFT, particularly with the B3LYP functional, has emerged as a prominent choice due to its efficacy in accounting for electron correlation, making it one of the most reliable methods in quantum chemistry.

To facilitate accurate modeling, a well-defined basis set is crucial. For example, the 6-311G++(d,p) basis set is commonly utilized, where "6" denotes the number of Gaussian primitives used to describe the core orbitals of heavy atoms (excluding hydrogen). This basis set consists of three Gaussian functions for valence electrons, along with additional functions for the electrons furthest from the nucleus. The inclusion of "d" and "p" denotes the use of polarization orbitals, which improve the accuracy of the calculations.

Overall, molecular modeling, particularly through methods like DFT/B3LYP/6-311G++(d,p), using Gaussian 09 software [6] , is exceptionally well-suited for studying organic molecules. It provides reliable predictions for optimized bond angles, bond lengths, and molecular geometry, as well as accurate spectral analysis. These capabilities not only aid in understanding molecular

behavior but also drive innovation in fields such as drug discovery, materials science, and biochemical research

III.5.1 Structural analysis:

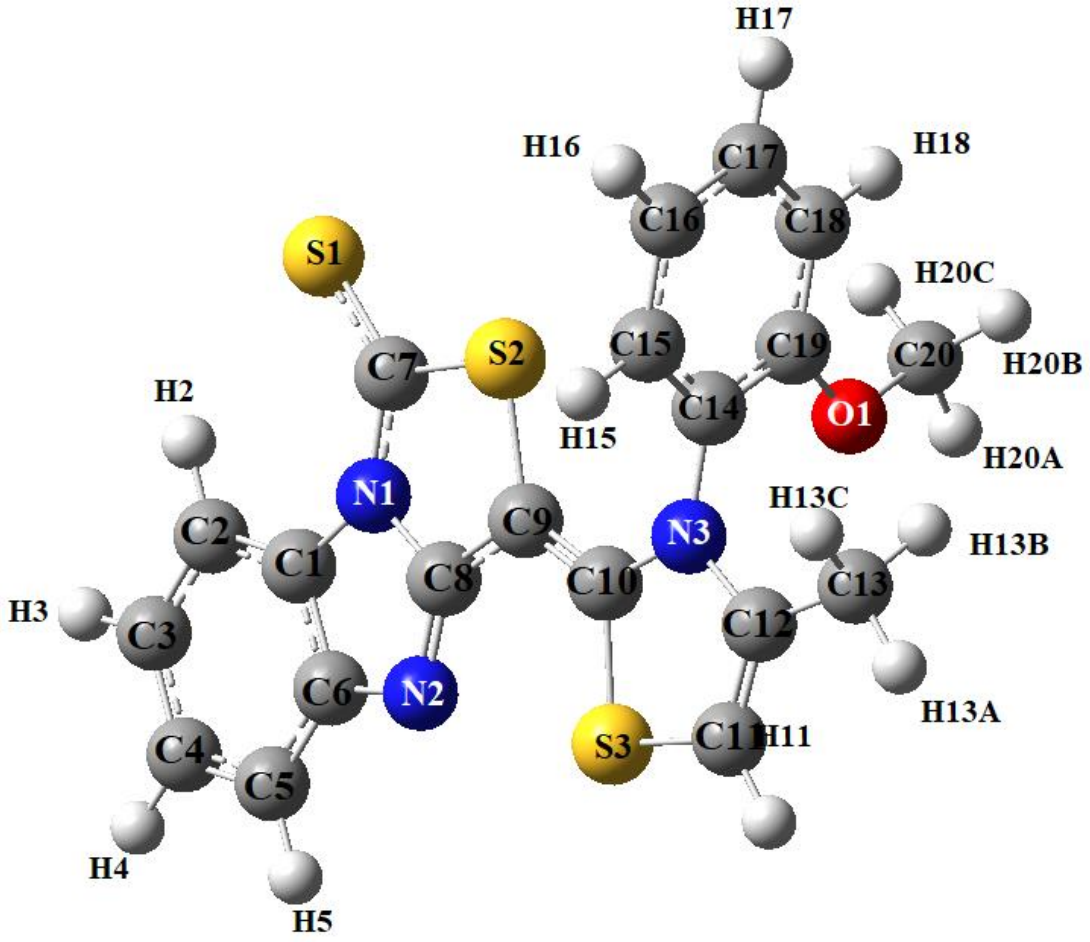

Fig.III.7 Optimized structure of EMBIT B3LYP / 6-311G++(d,p)

III.5.1.1 Interatomic distances:

Table III.5, provides a detailed comparison X-ray diffraction values and DFT with the B3LYP/6-311G++(d,p) level of theory bond lengths analysis of the EMBIT compound, showing a strong correlation between experimental X-ray diffraction and theoretical DFT values, with minor variations. The C–C bond lengths in the two benzene rings are consistent with literature values [7], with the experimental lengths slightly shorter. For example, the C1–C2 bond, the shortest among aromatic C–C bonds, measures 1.375 Å experimentally and 1.388 Å theoretically. Shorter bond lengths observed for N1–C1, N3–C10, and N2–C8 compared to aromatic C–C bonds can be attributed to the influence of nitrogen's smaller atomic size and higher electronegativity, which increase ionic character and pull bonding electrons closer [8,9]. The average C–S bond lengths, approximately 1.75 Å for both experimental and theoretical

data, are in excellent agreement with literature values [10], demonstrating accurate modeling of sulfur-carbon interactions. These observations affirm the reliability of DFT in reproducing the molecular geometry of EMBIT, Overall, the EMBIT compound's bond lengths from DFT align well with experimental X-ray data, validating the method's effectiveness in structural analysis.

Table III.5. measured and computed bond lengths of EMBIT

Bond length	X-Ray	DFT/B3LYP/6-311G++(d,p)
S2–C7	1.740 (2)	1.776
S2–C9	1.7652 (17)	1.792
S3–C11	1.728 (2)	1.756
S3–C10	1.7337 (17)	1.766
S1–C7	1.639 (2)	1.651
N1–C7	1.367 (2)	1.370
N1–C8	1.391 (2)	1.409
N1–C1	1.398 (2)	1.402
N3–C10	1.365 (2)	1.382
N3–C12	1.398 (2)	1.407
N3–C14	1.441 (2)	1.435
N2–C8	1.315 (2)	1.309
N2–C6	1.396 (2)	1.393
O1–C19	1.361 (3)	1.353
O1–C20	1.441 (3)	1.427
C8–C9	1.419 (2)	1.422
C9–C10	1.370 (2)	1.378
C1–C2	1.375 (3)	1.388
C1–C6	1.397 (3)	1.418
C6–C5	1.399 (2)	1.395
C14–C15	1.379 (3)	1.391
C14–C19	1.393 (3)	1.408
C12–C11	1.335 (3)	1.342
C12–C13	1.487 (3)	1.494
C2–C3	1.384 (3)	1.395
C15–C16	1.373 (3)	1.392
C5–C4	1.375 (3)	1.392
C4–C3	1.385 (3)	1.402
C19–C18	1.385 (3)	1.397
C18–C17	1.373 (4)	1.394
C16–C17	1.376 (4)	1.391

III.5.1.2 bond angles:

The bond angle analysis of the EMBIT compound in Table III.6 comparing measured and computed values, highlights strong consistency between experimental X-ray and theoretical DFT B3LYP/6-311G++(d,p) values, with most angles showing deviations of less than 1 degree,

indicating the reliability of DFT calculations for angular geometry prediction. The experimental bond angles involving sulfur atoms, such as C7–S2–C9, 94.05° and 93.58° respectively, and C11–S3–C10, 90.59° and 90.36° respectively, closely align with theoretical values. Angles around nitrogen atoms, such as C7–N1–C8, 117.90° and 117.76° respectively, and N3–C10–C9, 128.20° and 128.37° respectively, also show excellent agreement, although theoretical values slightly underestimate angles involving aromatic rings and nitrogen by approximately 1–2°, may be due to substitution effect **[11-13]**

For aromatic rings, angles within benzene rings deviate minimally from the ideal 120 degrees. For instance, C16–C15–C14 measures 119.6° and 120.45° respectively, while C15–C16–C17 measures 119.5° and 119.15° respectively. Notable differences include angles influenced by substitutions, such as C2–C1–N1, 132.43° and 133.02° respectively, and N1–C7–S1, 127.28° and 128.37° respectively, where deviations of about 1 degree are observed. Bond angles involving sulfur and bridging atoms, like S1–C7–S2, 124.82° and 123.76° respectively, remain consistent, with differences less than 1 degree.Angles involving oxygen atoms, such as O1–C19–C18, 125.53° and 124.93° respectively, and O1–C19–C14, 116.25° and 116.16° respectively, also align closely between experimental and theoretical data. Overall, the DFT approach effectively models the angular geometry of the EMBIT compound

Table III.6 : X-Ray vs DFT/B3LYP/6-311G++(d,p) bond angles of EMBIT

Bond angles	X-Ray	DFT/B3LYP/6-311G++(d,p)
C7–S2–C9	94.05 (8)	93.58
C11–S3–C10	90.59 (9)	90.36
C7–N1–C8	117.90 (15)	117.76
C7–N1–C1	135.48 (16)	136.05
C8–N1–C1	106.62 (13)	106.18
C10–N3–C12	114.99 (15)	114.75
C16–C15–C14	119.6 (2)	120.45
C4–C5–C6	117.88 (19)	118.13
C10–N3–C14	121.63 (15)	123.18
C12–N3–C14	123.30 (15)	121.91
C8–N2–C6	103.78 (14)	104.75
C19–O1–C20	118.1 (2)	118.84
N2–C8–N1	113.43 (15)	113.40
N2–C8–C9	134.60 (16)	133.77
N1–C8–C9	111.97 (14)	112.81
C10–C9–C8	124.14 (15)	123.37
C10–C9–S2	127.65 (13)	128.66
C8–C9–S2	108.20 (12)	107.95
N3–C10–C9	128.20 (15)	128.37
N3–C10–S3	109.78 (13)	109.57
C9–C10–S3	122.01 (13)	122.05
C2–C1–C6	123.60 (16)	122.82
C2–C1–N1	132.43 (17)	133.02
C6–C1–N1	103.97 (16)	104.14
N2–C6–C1	112.20 (14)	111.51
N2–C6–C5	129.03 (18)	129.02
C1–C6–C5	118.77 (18)	119.45
N1–C7–S1	127.28 (15)	128.37
N1–C7–S2	107.88 (13)	107.86
S1–C7–S2	124.82 (11)	123.76
C15–C14–C19	121.26 (18)	120.43
C15–C14–N3	119.16 (16)	120.17
C19–C14–N3	119.56 (17)	119.38
C11–C12–N3	111.36 (17)	112.42
C11–C12–C13	128.91 (19)	127.28
N3–C12–C13	119.72 (17)	120.28
C1–C2–C3	116.44 (19)	116.67
C12–C11–S3	113.27 (15)	112.86
C5–C4–C3	122.08 (19)	121.52
O1–C19–C18	125.53 (19)	124.93
O1–C19–C14	116.25 (17)	116.16
C18–C19–C14	118.2 (2)	118.90
C17–C18–C19	120.1 (2)	119.98

C2–C3–C4	121.2 (2)	121.37
C15–C16–C17	119.5 (2)	119.15
C18–C17–C16	121.2 (2)	121.05

III.5.1.3 torsion angles:

The torsion angles of the EMBIT compound reveal a combination of planarity and slight deviations from ideal configurations. Most torsion angles are close to 0° or 180°, indicating nearly planar arrangements between specific atoms, such as in the C6–N2–C8–N1 and C6–N2–C8–C9 bonds, with only minor variations between experimental and theoretical values. For example, the C7–N1–C8–C9 torsion angle deviates slightly (0.6° experimental, −0.08° theoretical), reflecting small alterations in the molecular structure. Some torsion angles, such as C10–N3–C14–C15 (−83.2° experimental, 94.53° theoretical), These discrepancies between the experimental (X-ray) and theoretical (DFT) results likely arise from the different environments in which the measurements were obtained, as the X-ray diffraction data represents the solid-state molecule, while the DFT calculations describe the molecule in the gas phase **[14].** Despite these differences, the overall agreement between the experimental and theoretical data suggests that the compound maintains a stable molecular structure with only minor torsional distortions. **[15]**

Table III.7 experimental and theoretical torsion angles of EMBIT

Torsion angles	X-Ray	DFT/B3LYP/6-311G++(d,p)
C6–N2–C8–N1	−0.40 (19)	0.02
C6–N2–C8–C9	179.24 (19)	-179.66
C7–N1–C8–N2	−179.68 (14)	-179.84
C1–N1–C8–N2	0.11 (19)	-0.03
C7–N1–C8–C9	0.6 (2)	-0.08
C1–N1–C8–C9	−179.61 (14)	179.72
N2–C8–C9–C10	1.8 (3)	1.00
N1–C8–C9–C10	−178.51 (16)	-178.69
N2–C8–C9–S2	−179.74 (17)	-179.78
N1–C8–C9–S2	−0.10 (17)	0.52
C7–S2–C9–C10	178.06 (17)	178.52
C7–S2–C9–C8	−0.28 (13)	-0.63
C12–N3–C10–C9	−179.12 (17)	-178.82
C14–N3–C10–C9	−2.2 (3)	-3.11
C12–N3–C10–S3	0.28 (19)	1.48
C14–N3–C10–S3	177.17 (12)	177.19
C8–C9–C10–N3	178.53 (16)	179.58
S2–C9–C10–N3	0.4 (3)	0.54
C8–C9–C10–S3	−0.8 (2)	-0.77
C1–N1–C7–S2	179.51 (16)	179.86
C9–S2–C7–N1	0.58 (13)	0.58
C9–S2–C7–S1	−178.19 (13)	-179.51
C10–N3–C14–C15	−83.2 (2)	94.53
C12–N3–C14–C15	93.4 (2)	-90.05
C10–N3–C14–C19	95.6 (2)	-86.48
C12–N3–C14–C19	−87.8 (2)	88.92
C10–N3–C12–C11	0.0 (2)	-1.41
C14–N3–C12–C11	−176.86 (17)	-177.18
C10–N3–C12–C13	−179.05 (17)	178.46
C14–N3–C12–C13	4.1 (3)	2.69
C6–C1–C2–C3	1.4 (3)	-0.00
N1–C1–C2–C3	−179.58 (19)	-179.92
N3–C12–C11–S3	−0.2 (2)	0.64
C13–C12–C11–S3	178.67 (18)	-179.22
C10–S3–C11–C12	0.35 (17)	0.15
C19–C14–C15–C16	−1.8 (3)	0.55
N3–C14–C15–C16	176.93 (18)	179.53
N2–C6–C5–C4	179.80 (18)	179.94
S2–C9–C10–S3	−178.88 (10)	-179.81
C11–S3–C10–N3	−0.34 (13)	-0.91
C11–S3–C10–C9	179.10 (16)	179.37
C7–N1–C1–C2	0.8 (3)	-0.28
C8–N1–C1–C2	−178.9 (2)	179.95
C7–N1–C1–C6	179.97 (18)	179.78

C8–N1–C1–C6	0.24 (18)	0.02
C8–N2–C6–C1	0.56 (19)	-0.00
C8–N2–C6–C5	−178.87 (18)	-179.94
C2–C1–C6–N2	178.73 (17)	-179.95
N1–C1–C6–N2	−0.50 (19)	-0.01
C2–C1–C6–C5	−1.8 (3)	-0.00
N1–C1–C6–C5	179.00 (15)	179.92
C8–N1–C7–S1	177.95 (14)	179.70
C1–N1–C7–S1	−1.8 (3)	-0.02
C8–N1–C7–S2	−0.79 (18)	-0.40
C1–C6–C5–C4	0.4 (3)	0.01
C6–C5–C4–C3	1.2 (3)	-0.00
C20–O1–C19–C18	−3.6 (3)	-6.81
C20–O1–C19–C14	177.6 (2)	173.18
C15–C14–C19–O1	−179.50 (18)	179.30
N3–C14–C19–O1	1.7 (3)	0.32
C15–C14–C19–C18	1.7 (3)	-0.69
N3–C14–C19–C18	−177.08 (17)	-179.67
O1–C19–C18–C17	−178.7 (2)	-179.68
C14–C19–C18–C17	0.0 (3)	0.31
C1–C2–C3–C4	0.2 (3)	0.01
C5–C4–C3–C2	−1.6 (4)	-0.01
C14–C15–C16–C17	0.3 (3)	-0.04
C19–C18–C17–C16	−1.4 (4)	0.19
C15–C16–C17–C18	1.3 (4)	-0.33

III.5.2 Hydrogen bonds:

Intermolecular contacts play a crucial role in understanding how molecules interact within different environments. The EMBIT experimental analysis enlisted in **Table III.8** show that the title compound forms several possible hydrogen bonds and **Fig.III.8** show crystal packing of the title compound assessed with mercury program **[04],** which contribute to its molecular interactions and stability. The first hydrogen bond is C2–H2A···S3 with a bond distance of 3.65 Å and an angle of 140°, indicating a moderate interaction between the hydrogen atom on C2 and the sulfur atom on S3. The second hydrogen bond, C3–H3···S2, is slightly longer at 3.89 Å, with an angle of 171°, suggesting a nearly linear arrangement between the donor and acceptor atoms, which enhances the strength of this interaction. The C15–H15···N2 hydrogen bond (3.44 Å, 154°) shows a moderate angle, reflecting a significant interaction between the hydrogen of C15 and the nitrogen of N2. Lastly, the C17–H17···H2 interaction (3.28 Å, 111°) is characterized by a weaker interaction due to the low angle, but still contributes to the molecular structure. Based on the results obtained, it can be concluded that specific carbon

atoms (C2, C15, and C17) demonstrate donor properties, while S2, S3, N2, and H2 exhibit characteristics of acceptors.

The symmetry codes provided indicate the positions of the acceptors relative to the donor atoms, further clarifying the spatial arrangements of these hydrogen bonds within the molecular lattice. Specifically, the symmetry codes (i), (ii), (iii), and (iv) correspond to different rotational and translational positions of the acceptors, ensuring the correct alignment of the hydrogen bond network within the crystal structure.

Table III.8 EMBIT Hydrogen Bond Predicted Experimentally

D–H···A	D–H (Å)	H···A(Å)	D···A(Å)	D–H···A (°)
C2–H2*A*···S3^{i}	0.93	2.89	3.65	140
C3 H3···S2 ^{ii}	0.93	2.97	3.89	171
C15–H15···N2^{iii}	0.93	2.59	3.44	154
C17 H17···H2 ^{iv}	0.93	2.84	3.28	111

Symmetry codes : (i) x-1/2,-y+1/2, +z+1/2, (ii) -x+1/2,+y+1/2,-z+1/2+1 (iii) -x+1,-y,-z+1 (iv) -x+1/2+1,+y-1/2,-z+1/2+1

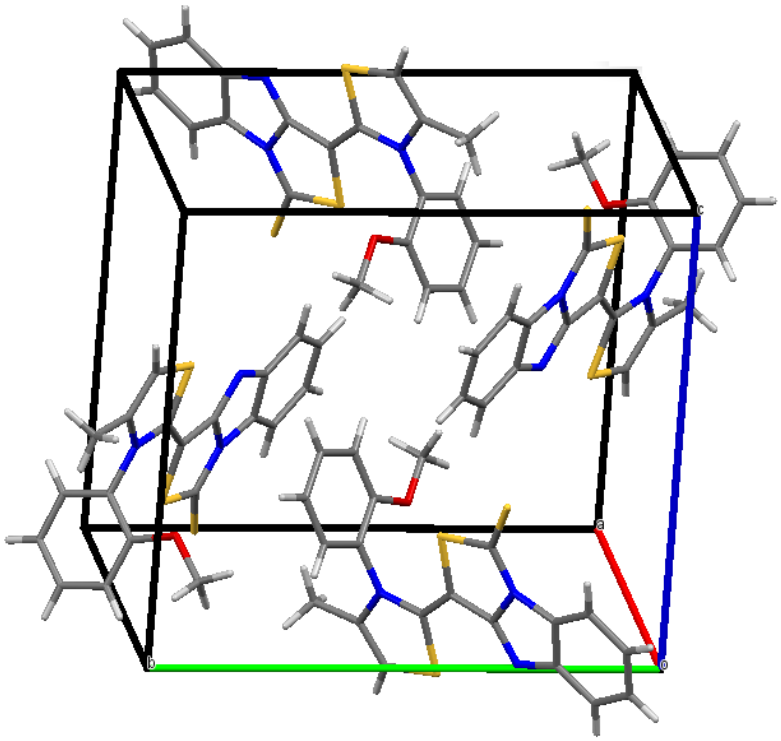

Fig.III.8 Crystal packing of EMBIT

III.5.3 Hirshfeld Surface Analysis:

Hirshfeld surface analysis, conducted using Crystal Explorer [16] Fig.III.9, provided detailed visualizations of the molecule's surface and its interactions. Key features such as d_{norm}, d_i, d_e, curvedness, fragment patches, and the shape index were displayed Fig.III.10. These features offer valuable insights into the molecular structure and bonding of the compound.

The shape index surface was used to identify complementary cavities and bumps, representing areas where two molecular surfaces interact. The curvedness maps highlighted large green patches indicating relatively flat areas interrupted by dark blue edges, reflecting regions of high positive curvature [17,18] The d_i value represents the distance from the Hirshfeld surface to the nearest nucleus within the surface, while d_e measures the distance to the nearest nucleus outside the surface.. The d_{norm} value, which combines both di and de, displays intermolecular interactions by color-coding distances: red for shorter than van der Waals radii, white for equal to van der Waals radii, and blue for greater than van der Waals radii.

The latter determines the distances from the surface to the outer d_e and inner d_i nuclei. internal (di). The distances of the di and de contacts have to be normalised as d_{norm}. The internal and external radii and dnorm on the surface are related by the following formula [19]

$$d_{norm} = \frac{d_i - r_i^{vdw}}{r_i^{vdw}} + \frac{d_e - r_e^{vdw}}{r_e^{vdw}}$$

Fingerprint analysis further clarified the contributions of different molecular interactions to the Hirshfeld surface of EMBIT in Fig III.11. The analysis is presented in a 2D fingerprint diagram, where di and de values are combined. The diagram reveals a pair of spikes at the bottom left, representing short di and de values, with the top spike corresponding to the donor atom and the lower spike [20]to the acceptor atom. The hydrogen-hydrogen (H-H) interaction stands out with the highest contribution to the Hirshfeld surface, highlighting its significant role in stabilizing the crystal structure. [20,21]

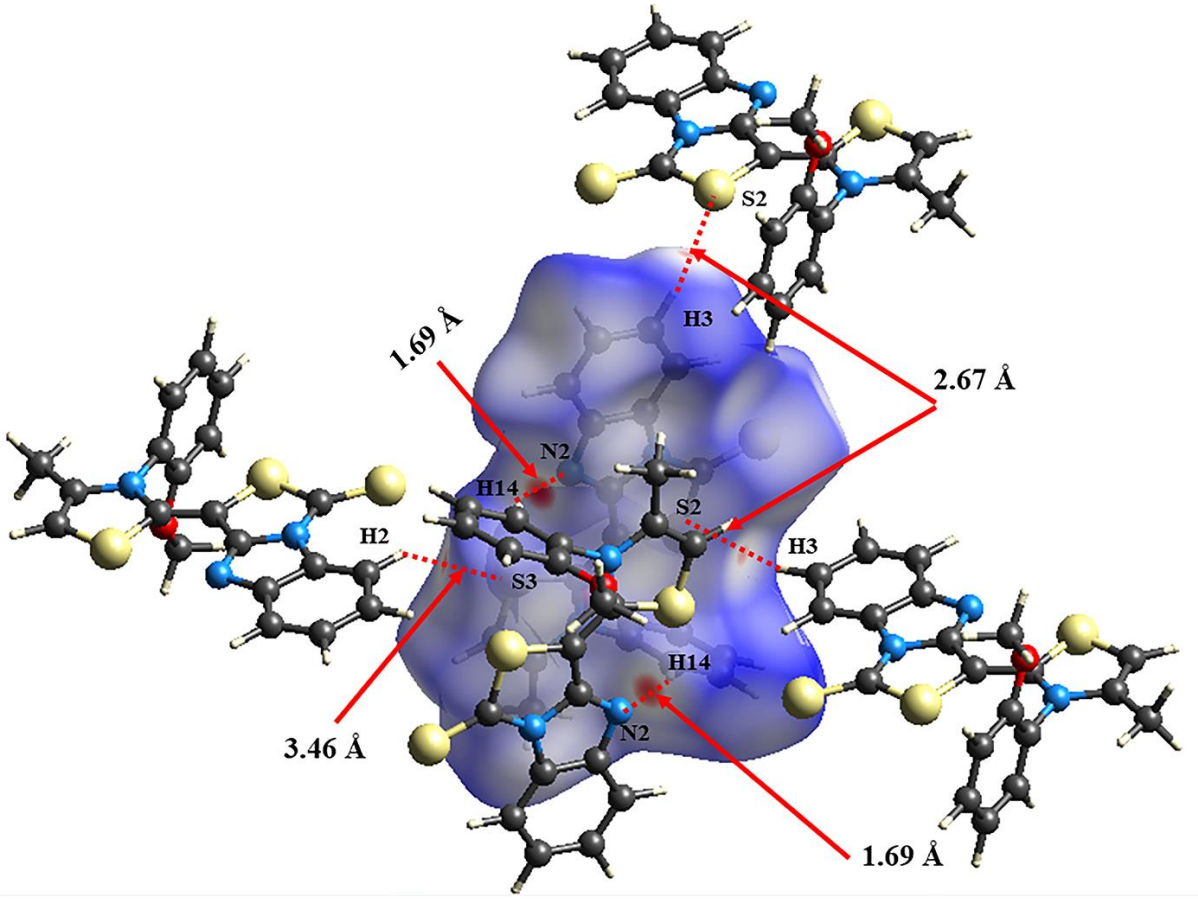

Fig.III.9 d_{norm} surface of EMBIT

The d_{norm} mapped surface analysis revealed red patches, indicating areas of strong molecular bonding. Among the intermolecular interactions, the shortest was between N2...H14/H14...N2, with a distance of 1.69 Å, suggesting a strong nitrogen-hydrogen bond. This interaction contributed significantly to the Hirshfeld surface. Another notable interaction, S2...H3/H3...S2, occurred at 2.67 Å, reflecting a strong sulfur-hydrogen bond. The broadest interaction, S3...H2/H2...S3, at 3.46 Å, indicated a weaker, though still notable, bond. The weakest interactions, contributing less than 5% to the Hirshfeld surface, involved H... O/O...H, C...C, C... S/S...C, C... N/N...C, S...S, and N...N.

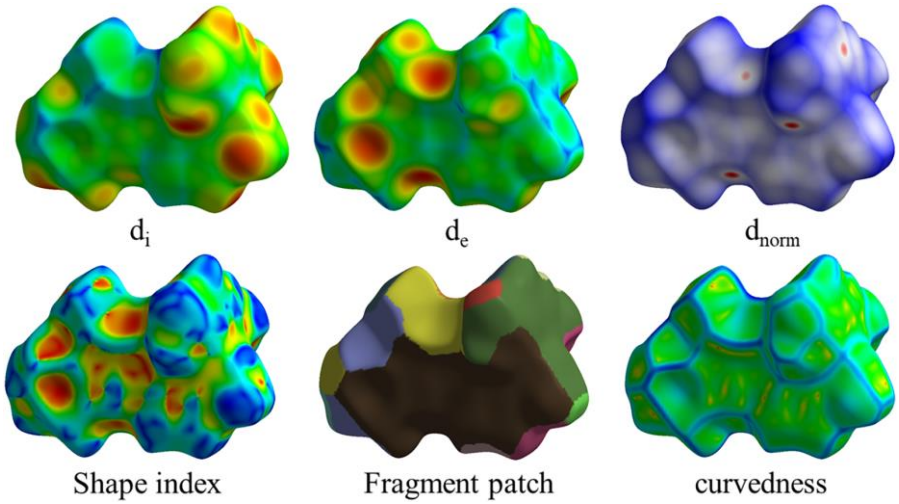

Fig.III.10 different representation of surface analysis by crystal explorer

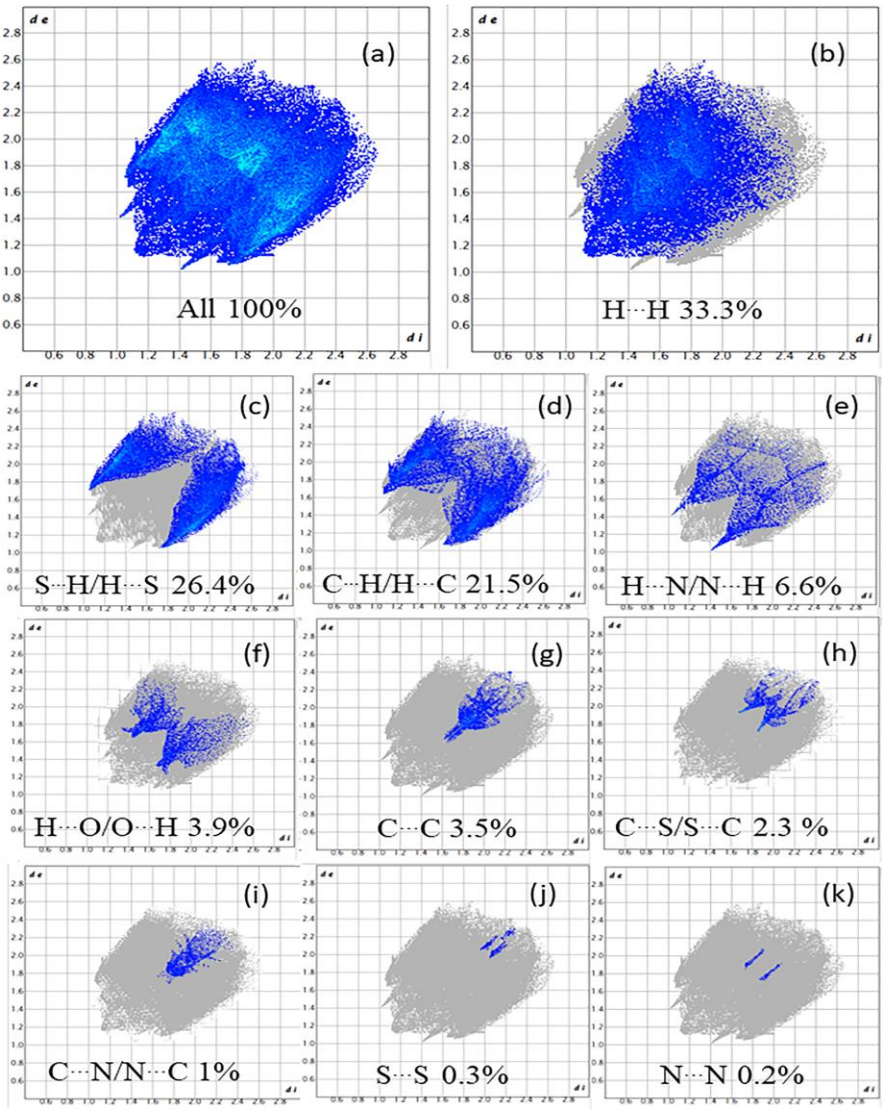

Fig III.11 fingerprints of all the intermolecular contribution

III.5.4 Reduced gradient density and non- covalent bond analysis:

Johnson et al [22] introduced the Reduced Density Gradient (RDG) technique, which is based on electron density and it's based on the electron density and its first derivative. The RDG function is given by the following equation:

$$RDG\ (r) = \frac{1|\nabla\rho(r)|}{2(3\pi 2)^{1/3}\rho(r)^{4/3}}$$

r is the coordinate vector. This method is also key to understanding noncovalent interactions (NCI). The RDG analysis was conducted with the Multiwfn program [23], visualized using the VMD software [24] and the 2D scatter graph was plotted using Gnuplot [25] Lambda 2 values, illustrated in the 2D scatter plot are important for assessing the nature of intermolecular forces Fig.III.12 .a . A lambda 2 value greater than zero indicates a repulsive interaction, meaning the molecules are pushing away from each other. Conversely, a lambda 2 value below zero suggests a significant attractive force between the molecules, indicating a strong affinity. When lambda 2 is near zero, Van der Waals interactions dominate, indicating weak, non-covalent forces such as dispersion forces, dipole-dipole interactions, and hydrogen bonding.

RDG analysis was applied to investigate the intrinsic molecular interactions within the EMBIT compound Fig.III.12. b. Using an isosurface threshold of 0.5, the electron density within the molecule was visualized and quantified. The results from both the 2D scatter plot and the 3D isosurface rendering revealed that the compound does not contain strong hydrogen bonds. Instead, red patches appeared, indicating steric effects, particularly around the central regions of the aromatic rings. These areas are characterized by significant electronic density, contributing to steric repulsion. Moreover, Van der Waals interactions were observed between various atom pairs in the compound, including H2 and S1, N2 and S3, O1 and N3, H15 and H13, H17 and H20, and S2 and H12. These interactions highlight the presence of Van der Waals forces between these atoms. In summary, the lambda 2 values provide insights into the nature of molecular interactions, while RDG analysis with a 0.5 iso surface threshold shows the lack of strong hydrogen bonds, the presence of steric effects, and the involvement of Van der Waals forces between various atom pairs. This emphasizes the complexity of intermolecular forces in the EMBIT compound.

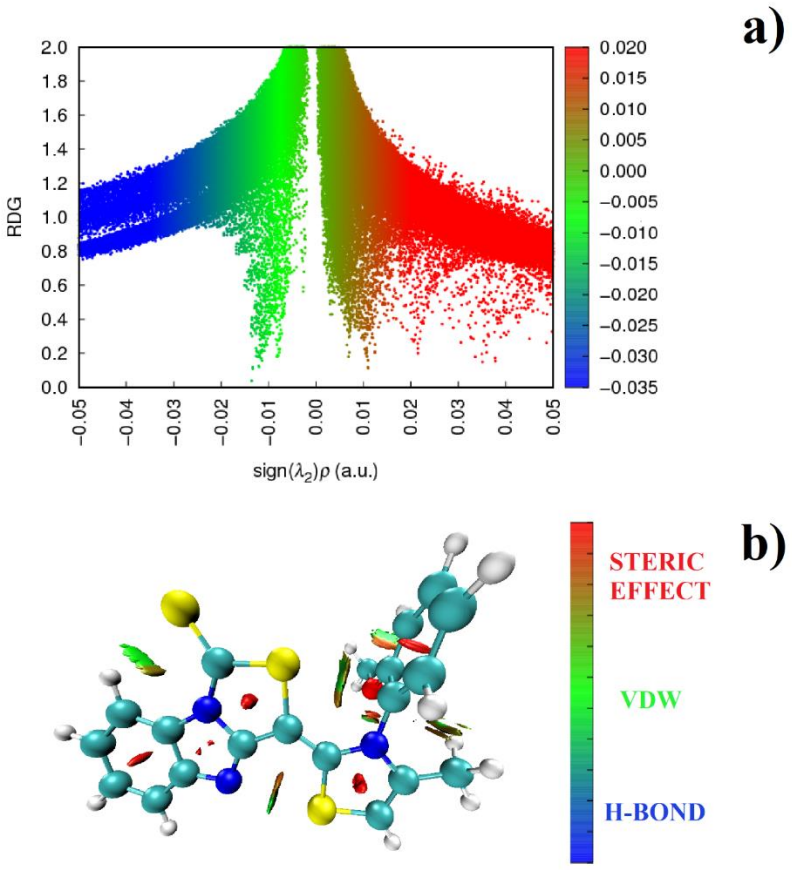

Fig.III.12 a)2scatter graph) 3d Reduced gradient density surface analysis.

III.6 Spectroscopic Analysis:

III.6.1 infrared spectra analysis:

The EMBIT molecule, consisting of 42 atoms, was analyzed for its vibrational properties. **Table III.9** presents the experimental and theoretical vibrational frequencies, potential energy distribution PED results, and **Fig.III.13** illustrates the infrared spectra. Theoretical frequencies were observed to be higher than experimental ones, which can be attributed to the neglect of anharmonic parameters in gas-phase calculations **[26].** To align the theoretical and experimental values, the calculated frequencies were scaled using a factor of 0.972 **[27].** The PED analysis was performed using the VEDA 4 program providing detailed insights into the vibrational modes **[28].** Aromatic C-H stretching vibrations, typically in the ranges 3100–3000 cm^{-1} asymmetric and 2990–2900 cm^{-1} symmetric**[29]**, showed little effect from substituents**[30]**, with absorption attributed to sp^2 hybridized C-H stretching in aromatic rings **[26]** These bands often overlap, resulting in higher absorption in this region**[31].** The 1375 cm^{-1} frequency was linked to symmetric and asymmetric CH_3 bending **[32],** The C-H bending vibration occurred

between 1500 and 500 cm-1, as confirmed in the literature [33,34]. while torsional vibrations were theoretically found to range from 965 to 729 cm^{-1}. C-C and C=C stretching vibrations were observed between 1650 and 1200 cm^{-1} [35], with the FT-IR attributing 1520 cm^{-1} to C=C stretching , The highest frequency mode is the C=C stretching vibration at 1635-1532 cm-1[36]. Theoretical calculations predicted the highest intensity mode at 1286 cm^{-1}, with 60% PED contribution from N-C stretching vibrations. Ring C-C bonds exhibit stretching vibrations at 950-1100 cm. The lower zone is described to be the stretching vibrations for the bonds that play an active part in the production of rings, whereas the deformation of the C-C ring occurs at around 876 cm-1 [33] C-O stretching bands, typically in the range 1260–1000 cm^{-1} [37], were observed at 1201 cm^{-1} in the FT-IR spectrum. DFT calculations identified intensities at 1269, 1253, and 1232 cm^{-1}, while in-plane and out-of-plane bending vibrations occurred at 566 cm^{-1} and 741–492 cm^{-1}, respectively [38]. N-C vibrations, expected in the 1200–1400 cm^{-1} range [39], were challenging to identify due to overlapping modes[40]. FT-IR assigned N-C vibrations to 1610 cm^{-1}, consistent with literature [41,42], while theoretical predictions included 1604, 1531, 1361, 1326, 1305, and 1223 cm^{-1}, with bending and torsional modes spanning 1079–428 cm^{-1},CN bending vibrations are EXPECTED to be around 400 cm^{-1} [43]. C=S stretching vibrations, typically within 730–660 cm^{-1} [44], were calculated at 798, 789, 529, and 437 cm^{-1}, while FT-IR analysis showed ν(C=S) at 1289 cm^{-1}. In cyclic thioamides, C=S stretching frequencies have been reported between 1050 and 1200 cm^{-1} [45], with N-C=S mixed vibrations appearing in the ranges 1260–1420 cm^{-1} and 940–1140 cm^{-1} [46]

.

Table III.9 FT-IR and computed vibrational frequencies of EMBIT

FT-IR (cm −1)	unscaled	B3LYP /6-311G++(d,p) Scaled freq(cm-1)	IR	Band assignement with PED > 10 %
-	3254	3162	3.3026	ν CH (99%) Ring 4
-	3222	3130	2.4938	ν CH (96%) Ring 1
-	3210	3119	3.9310	ν CH (86%) Ring 5
-	3200	3109	6.8426	ν CH (88%) Ring 5
-	3195	3104	14.950	ν CH (94%) Ring 1
-	3185	3094.81	6.2354	ν CH (71%) Ring 5+ ν CH_{asy} (19%)
-	3183	3093.38	17.4693	ν CH_{asy} (17%) Ring 1 + ν CH (81%) Ring 1
-	3176.00	3085.80	1.5974	ν CH_{asy} (20%) Ring 5+ ν CH (67%) Ring 5
-	3167.11	3077.16	5.0562	ν CH_{asy} (26%) Ring 1+ ν CH (66%) Ring 1
-	3146.07	3056.73	10.3782	ν CH (90%)
-	3125.17	3036.42	12.9860	ν CH (84%)
-	3085.12	2997.50	6.9034	ν CH (50)ν + CH_{asy} (50%)
-	3083.20	2995.63	22.7073	ν CH (56%) + ν CH_{asy} (43%)
-	3034.19	2948.02	28.1072	ν CH_{asy} (99%)
-	3017.05	2931.37	51.3395	ν CH (53%)
1610.70	1658.47	1611.37	19.9648	ν CC (61%) Ring 4
-	1650.99	1604.10	40.6072	ν NC_{asy} (11%) Ring 2 + ν CC_{asy} (19 %) Ring 4 + ν CC (21%) Ring 1
1594.21	1637.29	1590.79	40.2999	ν CC (41%) Ring 5 + ν CC_{asy} (27%) Ring 5
-	1621.30	1575.26	18.3973	ν CC (28%) Ring 5 + δ CCC (11%) Ring 1
-	1620.24	1574.22	3.0742	ν CC_{asy} (13%) Ring 5+ ν CC (22%) Ring1
-	1575.75	1531.00	372.053 3	ν NC_{asy} (46%) Ring 2 + ν CC (21%) Ring1
1520	1565.34	1520.88	1286.59 64	ν CC_{asy} (60%) + ν NC (12%) Ring 4
1516.39	1529.71	1486.27	128.110 5	δ HCC (35%) Ring 5

1495.04	1505.47	1462.71	31.8764	ν CC (16%) Ring 1+ ν CC asy (11%) Ring 1 + δ HCC $_{asy}$ (20%) Ring 1 + δ HCC (26%) Ring1
1462.65	1503.63	1460.93	49.2300	δ HCH $_{asy}$ (30%) + δ HCH (38%) + τ HCOC (12%)
-	1495.35	1452.88	6.0399	δ HCH $_{asy}$ (31%) + δ HCH (41%) + τ HCC $_{asy}$ (17%) Ring 5
-	1491.49	1449.13	13.2379	ν CC asy (10%) Ring 5 + δ HCC (32%) Ring 5+ δ HCH (16%)
-	1486.86	1444.64	4.6627	δ HCH (46%) + δ HCH $_{asy}$ (21%) + τ HCCN $_{asy}$ (12%)
1432.18	1476.63	1434.70	15.1718	δ HCH (43%) + δ HCH $_{asy}$ (30%) + τ HCCN (18%)
-	1470.94	1429.16	116.413 6	δ HCC (50%) Ring 1
-	1469.30	1427.57	17.9941	δ HCH (52%) + δ HCC $_{asy}$ (12%) Ring 5
1397.86	1421.56	1381.19	9.6531	δ HCH (92%)
-	1401.25	1361.46	306.640 2	ν NC $_{asy}$ (50%) Ring 3 + ν NC (21%) Ring 2
1338.47	1373.07	1334.08	67.2656	ν CC $_{asy}$ (41) Ring 1 + ν CC (11%) Ring 1 + δ HCC (16%) Ring 1
1320.64	1365.69	1326.90	95.0983	ν NC $_{asy}$ (30%) Ring 4 + ν NC (25%) 2
-	1343.89	1305.72	84.1396	ν NC $_{asy}$ (13%) Ring 2 + δ CNC (10%) Ring 4
1289	1330.03	1292.26	38.3830	ν CC (48%) Ring 5 + ν CC $_{asy}$ (27%) Ring 5
1284.61	1313.79	1276.48	35.1201	
-	1306.95	1269.83	58.5861	ν OC (16%) + δ HCC (21%) Ring 5
-	1289.85	1253.22	107.219 9	ν OC (14%)
1230.39	1268.70	1232.67	163.974 5	ν OC (13%) + δ HCC (11%) Ring 5
1201.85	1258.94	1223.18	143.993 9	ν CC $_{asy}$ (24%) + ν NC (33%) Ring 2
-	1208.33	1174.01	166.074 9	
-	1204.67	1170.46	43.9083	δ HCH (11%) + τ HCOC $_{asy}$ (21%) + τ HCOC (23%)
-	1196.78	1162.79	14.8889	δ HCS (23%) Ring 4
1145.86	1188.17	1154.42	12.5458	ν CC $_{asy}$ (10%) Ring 5 + δ HCC $_{asy}$ (24%) Ring 5 + δ HCC (49%) Ring 5
-	1173.25	1139.93	14.1524	ν CC (14%) Ring 1 + δ HCC $_{asy}$ (10%) Ring 1+ δ HCC (55%) Ring 1
-	1169.88	1136.65	0.4702	δ HCH (14%) Ring 5+ δ HCH $_{asy}$ (15%) + τ HCOC (38%) + τ HCOC $_{asy}$ (33%)
-	1154.12	1121.35	8.8470	ν CC (15%) Ring 5 + δ HCS (25%) Ring 4 + δ HCC $_{asy}$ (12%) Ring 5

-	1131.12	1098.99	17.2871	δ HCS (10%) Ring 4
1093.89	1128.35	1096.30	7.9429	ν CC $_{asy}$ (10%) Ring 1 + ν CC (13%) Ring 1 + δ HCC $_{asy}$ (12%) Ring 1+δ HCC (11%) Ring 1
-	1110.69	1079.15	32.9307	ν CC asy (12%) + δ NCC (10%) Ring 3
1039.07	1067.72	1037.40	20.7118	ν CC (46%) Ring 5 + δ HCC (22%) Ring 5
-	1061.39	1031.25	1.5489	δ HCH (12%) + δ HCH $_{asy}$ (12%) + τ HCCN $_{asy}$ (64%) Ring 4
-	1047.12	1017.38	46.6951	ν CC (55%) Ring 5 + δ CCC asy (12%) Ring 5
1010.07	1043.22	1013.59	69.8378	ν S=C $_{asy}$ (24%) + δ CCC (16%) Ring 1 + δ CCC $_{asy}$ (11%) Ring 1
-	1030.80	1001.52	13.4882	ν CC $_{asy}$ (19%) Ring 1 + δ HCC $_{asy}$ (21%) Ring 1
-	1021.44	992.43	2.3422	δ HCH (10%) + τ HCCN (42%) Ring 4
-	1010.56	981.86	1.2265	ν CC (11%) Ring 5 + δ CCC $_{asy}$ (11%) Ring 5
-	997.13	968.81	0.0163	τ HCCC $_{asy}$ (27%) Ring 5+ τ HCCC (41%) Ring 5+ τ CCCC $_{asy}$ (10%) Ring 5
-	973.14	945.51	0.0080	τ HCCC $_{asy}$ (10%) Ring 1 + τ HCCC (24%) Ring 1 + τ CCCC $_{asy}$ (17%) Ring 1
-	961.66	934.35	1.3432	τ HCCC $_{asy}$ (28%) Ring 5 + τ HCCC (47%) Ring 5
906.19	948.07	921.15	2.3235	τ HCCC (55%) Ring 1 + τ HCCC $_{asy}$ (36%) Ring 1
870.70	921.44	895.28	18.8346	δ CCC $_{asy}$ (32%) Ring 1 + δ CCC (13%) Ring 5
-	872.41	847.63	8.1872	τ HCCC (31%) Ring 5
-	866.05	841.46	0.4684	τ HCCC (54%) Ring 1 + τ CCCC (38%) Ring 1
830.24	857.33	832.98	19.2607	τ HCCC (34%) Ring5
816.69	842.43	818.51	11.7710	τ HCCC (14%) Ring 4 + δ CNC (11%) Ring 2
-	822.02	798.67	3.3043	ν SC (44%) Ring 4 + δ SCC $_{asy}$ (19%) Ring4
-	812.42	789.35	61.4978	ν SC (31%) Ring 3 + δ CCC $_{asy}$ (13%) Ring 1+ δ SCS $_{asy}$ (10%) Ring 3
-	800.22	777.49	6.0246	ν OC(16%) + δ CCC (27%) Ring 5
-	766.89	745.11	37.7188	τ CCCC $_{asy}$ (46%) Ring 1 + τ HCCC $_{asy}$ (23%) Ring 1 + τ CCCN $_{asy}$ (14%) Ring 2
-	766.48	744.71	62.7755	τ HCCC (74%) Ring 5 + γ OCCC $_{asy}$ (15%)
739.61	761.99	740.35	4.0661	τ HCCC (15%) Ring 1 + τ CCCC (21%) Ring 5 + γ OCCC $_{asy}$ (10%) + γ NCCC $_{asy}$ (12%) Ring 2
-	750.40	729.09	37.7604	τ HCCC (39%) Ring 1 + τ HCCC $_{asy}$ (26%) Ring 1+ γ NCCC $_{asy}$ (19%) Ring 2
-	735.78	714.89	30.3999	ν NC (10%) Ring 4 + δ CCC (10%) Ring 5
696.12	714.48	694.18	8.4424	τ HCSC (23%) Ring 4 + τ CCNC (16%) Ring 2 + τ CNCC (16%) Ring 2
-	705.72	685.68	19.0668	τ HCSC (69%) Ring 4
-	663.74	644.89	4.8443	δ CCC (10%) Ring 1
629.45	658.81	640.10	4.5972	δ CCC (25%) Ring 1
597.87	619.54	601.94	2.9717	δ NCC $_{asy}$ (11%) Ring 4 + τ CCNC asy (44%) Ring 4 + γ CCCN (12%) Ring 4

-	606.83	589.60	12.3467	δ CCC (14%) Ring 1 + δ CNC (10%) Ring 2
568.09	585.21	568.59	14.6240	δ OCC $_{asy}$ (14%) + τ CCCC $_{asy}$ (10%) Ring 5
-	583.67	567.09	0.0281	τ CCCC $_{asy}$ (21%) Ring 1 + τ CCC (25%) Ring 1 + τ CCCC 14 Ring1
-	576.18	559.81	1.8673	δ CCC (20%) Ring 1 + δ CCN $_{asy}$ (11%) Ring 2 + δ CNC (21%) Ring 2
555.42	570.13	553.94	9.1141	τ CCCC (28%) Ring 5
541.76	545.42	529.93	16.4571	ν CC (14%) Ring 1 + ν SC (27%) Ring 4 + δ SCC (30%) Ring 4
-	541.66	526.28	3.5456	τ CCNC (10%) Ring 2 + τ SCCN (23%) Ring 3 + γ SNSC (13%) Ring 3
-	520.53	505.74	2.1758	δ CCC (14%) Ring 5 + δ NCC (13%) Ring 4 + τ SCCN (12%) Ring 3 + γ CNCC (11%) Ring 2
-	512.55	497.99	0.5725	γ SNSC (52%) Ring 3
-	509.03	494.58	12.1893	δ CNC $_{asy}$ (12%) Ring 4 + τ CCCC $_{asy}$ (10%) Ring 5 + γ OCCC asy (26%)
-	449.91	437.13	0.9527	ν NC $_{asy}$ (14%) Ring 2 + ν SC $_{asy}$ (40%) Ring 3 + δ CCC $_{asy}$ (12%) Ring 1
-	443.08	430.49	3.9847	τ CCCC $_{asy}$ (25%) Ring 1 + τ CNCC (10%) Ring 2 + γ NCCC $_{asy}$ (19%) Ring 2
-	425.28	413.20	9.6004	δ CCC $_{asy}$ (13%) Ring 5+ δ SCN (32%) Ring 4
-	412.87	401.14	8.5968	δ CCC (17%) Ring 5+ δ SCN (18%) Ring 4

ν: stretching; sy : symmetric; asy : asymmetric; β : in-plane bending; γ : out of plane bending; ω : wagging; τ : twisting; δ : bending; ρ : rocking. Vibrational modes are based on potential energy distribution (PED). Scaled frequencies are given in cm–1. Ring 1:C1C2C3C4C5C6; ring 2:C1N1C8C6; ring 3:N1C7S2C9C8; ring 4:C10S3C11C12N3; ring 5:C14C15C16C17C1

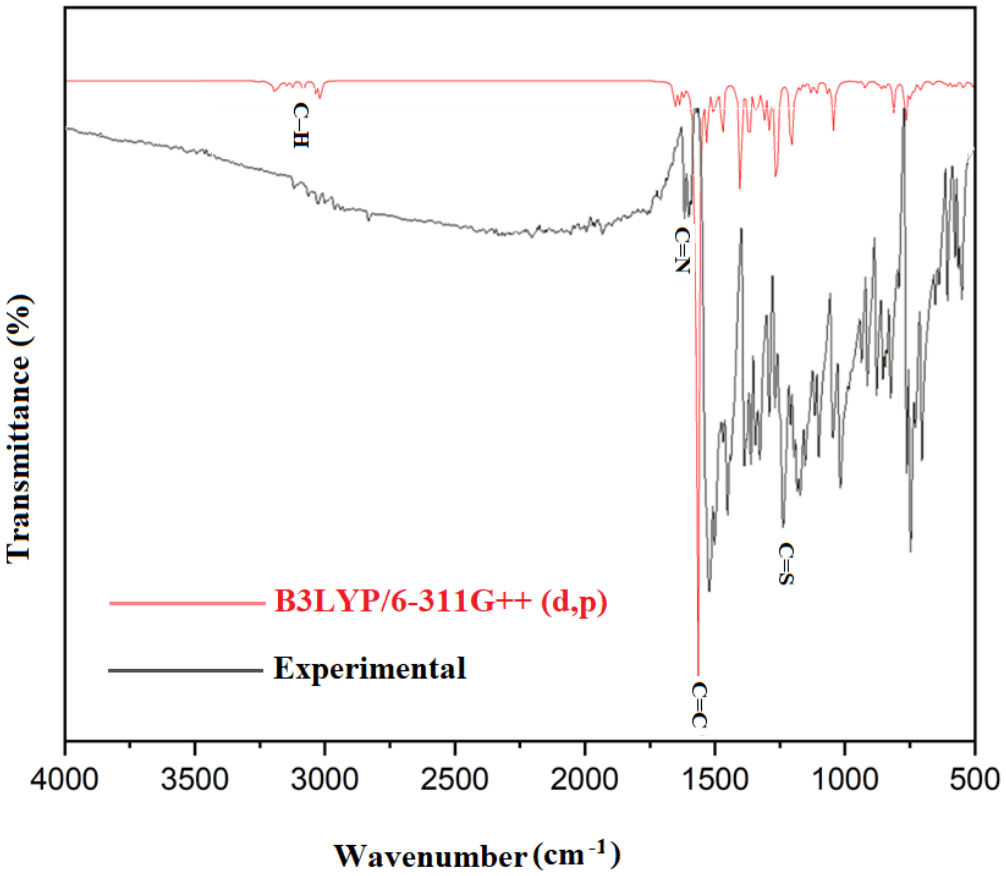

Fig.III.13 Theoretical and experimental infrared spectra of EMBIT

III.6.2 NMR Chemical Shifts

The nuclear magnetic resonance NMR method has been widely applied, particularly in determining the relative and, where feasible, absolute configurations of both natural and synthesized compounds [47]. In this study, TMS-calculated isotropic chemical shifts were used as a reference for calculations. Table III.10 presents a detailed summary of the experimental and calculated chemical shifts for the ^{1}H and ^{13}C NMR spectra of the EMBIT molecule. For ^{1}H NMR, the measured chemical shifts ranged from 1.9 to 8.65 ppm, while the calculated values extended from 2.38 to 9.45 ppm. The highest recorded ^{1}H NMR chemical shift values were observed for protons H2, H3, H4, H5, H15, H16, H17, and H18 within the benzene rings, consistent with theoretical predictions. These elevated chemical shift values are attributed to the strong deshielding effect of the benzene ring protons. In contrast, the methyl groups attached to C13 and C20 displayed the lowest chemical shift values, in agreement with both theoretical and experimental findings. This trend reflects the influence of the surrounding electronic environment: electron-withdrawing groups reduce shielding, causing an upfield shift (toward higher frequencies), whereas electron-donating groups increase shielding, leading to a downfield shift (toward lower frequencies) [48]. For ^{13}C NMR, chemical shifts were experimentally recorded between 14.01 and 181.53 ppm, while theoretical calculations spanned a wider range from 18.99 to 199.11 ppm. Notable peaks were observed for carbon atoms C6, C7, C8, C10, and C19, which showed significantly increased chemical shift values. This increase is attributed to the electronegativity of neighboring atoms, particularly nitrogen (N), sulfur (S), and oxygen (O), which induce deshielding and a shift toward higher ppm values. In contrast, the methyl group exhibited the lowest chemical shift, recorded theoretically at 18.99 ppm and experimentally at 14.01 ppm, reflecting substitution effects. The strong correlation between theoretical and experimental values underscores the role of electronegative elements in increasing chemical shift values and highlights the contrasting effects of substitution on methylene groups. Solvent effects also influence NMR chemical shifts, altering the molecule's averaged conformation. Additionally, variations in analysis conditions, such as concentration, temperature, and pH, may affect the observed shifts [49]. Despite employing advanced computational techniques, the average errors for calculated shifts can reach up to 0.4 ppm or more for ^{1}H and up to 10 ppm or more for ^{13}C [50,51]. Theoretical methods, including the use of B3LYP/6–311G(d,p), are known to slightly overestimate chemical shifts[52]. These results provide a comprehensive understanding of the factors influencing EMBIT's NMR spectra.

Table III.10 H^1 and C^{13} chemical shifts of EMBIT

	B3LYP/6-311G(d,p)	Experimental
H1		
H2	9.45	8.65
H3	7.94	7.12
H4	8.18	7.12
H5	8.47	7.17
H11	6.86	6.39
H13A	2.67	1.9
H13B	2.49	1.9
H13C	2.38	1.9
H15	8.29	7.34
H16	8.03	7.33
H17	8.39	7.34
H18	7.66	7.33
H20A	4.73	3.84
H20B	4.33	3.84
H20C	4.33	3.84
C13		
C1	140.47	125.95
C2	122.32	113.81
C3	129.81	121.97
C4	134.39	123.05
C5	127.39	118.50
C6	161.46	151.14
C7	199.11	181.53
C8	165.24	156.65
C9	96.20	98.06
C10	159.98	138.40
C11	115.97	102.41
C12	146.09	133.57
C13	18.99	14.01
C14	136.70	129.90
C15	142.66	130.92
C16	129.50	121.28
C17	140.86	130.82
C18	119.05	102.41
C19	170.26	170.53
C20	59.50	56.14

III.6.3 UV Vis

The electronic transitions of EMBIT were comprehensively studied through theoretical UV–Vis analysis. Theoretical wavelengths (λ), oscillator strengths, computed electronic transitions, and their major contributions are computed using gaussum [52] program and detailed in **Table III.11**, while the theoretical spectra are presented in **Fig.III.14**. The analysis

identified three significant electronic transitions in the absence of solvent: 437.45 nm, 336.65 nm, and 310.35 nm. These transitions predominantly involve the HOMO→LUMO excitation, with a contribution of 96%. The observed absorptions, which occur in the visible region, are attributed to n→π electron transitions [53]. The compound absorbs light in the violet region and reflects yellow, corresponding to its observed color [53]. Experimentally, however, the compound appears brown, likely due to solid-state effects that influence the perceived color

The UV–Vis spectrum of EMBIT was simulated under solvent-free conditions in the gaseous phase and in the presence of four distinct solvents: DMSO, ethanol, methanol, and chloroform using the CPCM model. The first spectral band remained consistent across all solvents, indicating an intrinsic electronic transition unaffected by solvation. However, the second band consistently exhibited a pronounced redshift, shifting toward longer wavelengths. This redshift emphasizes the notable effect of solvation on specific electronic transitions, resulting in the stabilization of the excited state in comparison to the ground state.This stabilization is corroborated by a slight narrowing of the energy gap under solvent conditions, with polar solvents providing the most pronounced effect [54].

These findings underscore the role of solvation in modulating the electronic properties of EMBIT, particularly through its influence on excited-state stability and transition energies.

Table III.11 Theoretical UV-vis analysis of EMBIT

solvent	Theoretical			B3LYP /6-311G++(d,p)
	λ (nm)	Energy (cm^{-1})	Osc. Strength	Major contributions
Gaseous state	437.45	22859	0.3722	HOMO->LUMO (96%)
	423.44	23616	0.0009	HOMO->LUMO+1 (99%)
	401.86	24883	0.0003	HOMO-1->LUMO (95%)
	358.06	27927	0.0875	HOMO->LUMO+2 (91%)
	336.65	29703	0.1055	HOMO-2->LUMO (14%), HOMO->LUMO+3 (80%)
	318.46	31400	0.0288	HOMO-3->LUMO (44%), HOMO-2->LUMO (40%)
	317.80	31466	0.0018	HOMO->LUMO+4 (83%)
	312.07	32043	0.0136	HOMO->LUMO+5 (33%), HOMO->LUMO+7 (11%), HOMO->LUMO+8 (38%)
	310.55	32200	0.1625	HOMO-3->LUMO (40%), HOMO-2->LUMO (29%), HOMO->LUMO+3 (11%)
	300.98	33223	0.0036	HOMO-1->LUMO+1 (96%)
	469.97	21277	0.4966	HOMO->LUMO (98%)
	381.68	26199	0.0003	HOMO-1->LUMO (90%)

DMSO	365.60	27352	0.0682	HOMO->LUMO+1 (74%), HOMO->LUMO+2 (24%)
	353.18	28313	0.1909	HOMO->LUMO+1 (21%), HOMO->LUMO+2 (72%)
	322.19	31037	0.0343	HOMO-3->LUMO (20%), HOMO-2->LUMO (67%)
	318.45	31401	0.1016	HOMO-3->LUMO (70%), HOMO-2->LUMO (16%)
	309.71	32288	0.1713	HOMO-4->LUMO (82%)
	306.98	32574	0.0036	HOMO->LUMO+4 (80%), HOMO->LUMO+5 (14%)
	301.87	33126	0.0279	HOMO->LUMO+3 (95%)
	282.46	35403	0.0001	HOMO->LUMO+4 (12%), HOMO->LUMO+5 (75%)
Ethanol	467.75	21378	0.4826	HOMO->LUMO (98%)
	382.14	26168	0.0002	HOMO-1->LUMO (91%)
	366.45	27288	0.0549	HOMO->LUMO+1 (73%), HOMO->LUMO+2 (24%)
	352.99	28328	0.1996	HOMO->LUMO+1 (21%), HOMO->LUMO+2 (72%)
	321.56	31097	0.0383	HOMO-3->LUMO (22%), HOMO-2->LUMO (65%)
	317.63	31482	0.0985	HOMO-3->LUMO (70%), HOMO-2->LUMO (17%)
	309.34	32326	0.1544	HOMO-4->LUMO (81%)
	306.98	32575	0.0043	HOMO->LUMO+4 (78%), HOMO->LUMO+5 (15%)
	302.71	33034	0.033	HOMO->LUMO+3 (94%)
	282.89	35348	0.0001	HOMO->LUMO+4 (14%), HOMO->LUMO+5 (73%)
Methanol	466.99	21413	0.4728	HOMO->LUMO (98%)
	381.78	26193	0.0002	HOMO-1->LUMO (91%)
	365.88	27331	0.0571	HOMO->LUMO+1 (72%), HOMO->LUMO+2 (26%)
	352.73	28349	0.196	HOMO->LUMO+1 (23%), HOMO->LUMO+2 (70%)
	321.71	31083	0.0344	HOMO-3->LUMO (25%), HOMO-2->LUMO (63%)
	317.82	31463	0.0901	HOMO-3->LUMO (67%), HOMO-2->LUMO (19%)
	309.22	32339	0.1612	HOMO-4->LUMO (79%), HOMO-2->LUMO (10%)
	306.95	32578	0.0047	HOMO->LUMO+4 (79%), HOMO->LUMO+5 (14%)
	302.25	33085	0.0318	HOMO->LUMO+3 (94%)
	282.63	35381	0.0001	HOMO->LUMO+4 (13%), HOMO->LUMO+5 (74%)
chloroform	465.89	21464	0.5128	HOMO->LUMO (98%)
	387.18	25827	0.0003	HOMO-1->LUMO (95%)
	376.51	26559	0.0194	HOMO->LUMO+1 (92%)
	353.75	28268	0.2267	HOMO->LUMO+2 (87%)
	321.15	31138	0.0805	HOMO-3->LUMO (15%), HOMO-2->LUMO (76%)
	314.41	31805	0.141	HOMO-3->LUMO (72%), HOMO->LUMO+3 (14%)
	310.19	32237	0.0937	HOMO->LUMO+3 (82%)
	307.33	32537	0.0006	HOMO->LUMO+4 (28%), HOMO->LUMO+5 (64%)

304.64	32824	0.028	HOMO-4->LUMO (94%)
287.89	34734	0.0001	HOMO->LUMO+4 (59%), HOMO->LUMO+5 (29%)

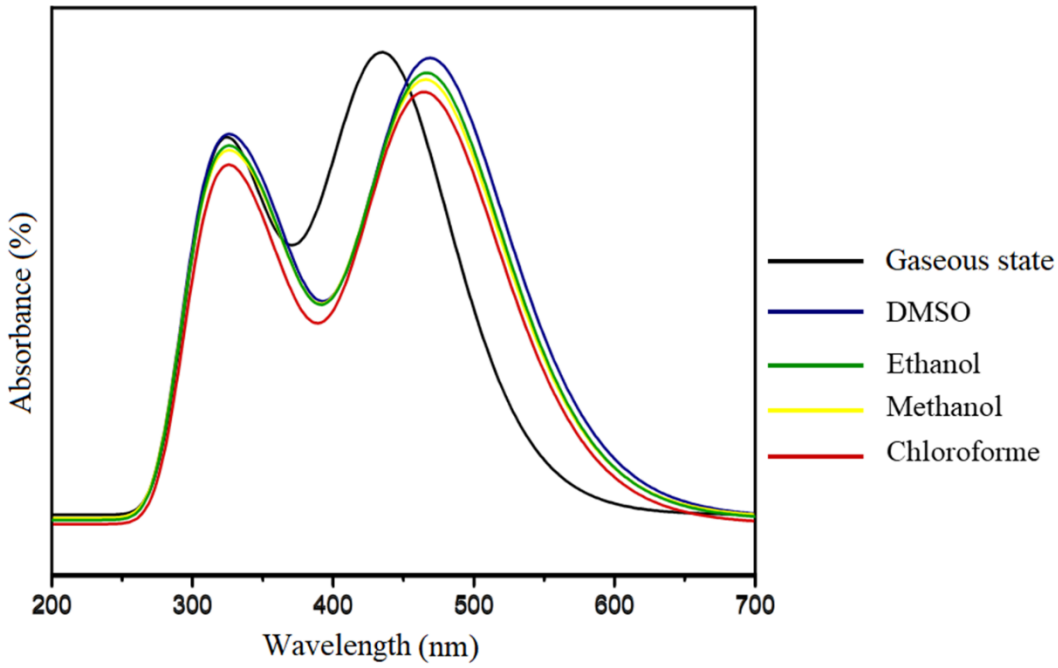

Fig.III.14 UVvis spectra of EMBIT

III.7. Conclusion:

In this chapter, the synthesis of EMBIT was meticulously detailed and later confirmed through a combination of X-ray analysis, computational modeling, and spectral analysis. EMBIT was synthesized under precise conditions to ensure optimal purity and yield and was later characterized through various analytical techniques. X-ray diffraction was employed to determine its three-dimensional crystal structure. The structure was determined using direct methods with the ShelXS program and refined using the ShelXL program, employing full matrix least-squares refinement based on F^2, via the WingX program. EMBIT crystallized in the monoclinic crystal system, with the space group P21/n. Infrared spectroscopy (IR) provided additional insight into the functional groups present in EMBIT, with distinct absorption bands corresponding to various chemical functionalities. NMR spectroscopy further detailed the chemical environment of the atoms in the compound. The optimized geometry obtained through Density Functional Theory (DFT) calculations was in good agreement with experimental findings, further validating the structural integrity and stability of EMBIT.

Computational modeling, including DFT, was used to predict NMR chemical shifts, UV-Vis spectra, and the optimized geometry of EMBIT. The predicted data closely matched the experimental results, confirming the accuracy of the computational models. The UV-Vis

analysis revealed significant electronic transitions and highlighted the effect of different solvents on the compound's absorption properties.

Overall, the synthesis of EMBIT, combined with its structural determination and spectral characterization, provided a comprehensive understanding of its molecular properties. This paves the way for further exploration of EMBIT's potential applications in fields such as materials science, electronics, and molecular design

References:

[1] L.J. Farrugia, WinGX suite for small-molecule single-crystal crystallography, *J. Appl. Crystallogr.* 32:837–838(1999). https://doi.org/10.1107/S0021889899006020.

[2] International Tables, Vol. A, (1999)

[3] G.M. Sheldrick, A short history of SHELX, *Acta Crystallogr. Sect. A Found. Crystallogr.*64:112–122(2008). https://doi.org/10.1107/S0108767307043930.

[4] C.F. Macrae, P.R. Edgington, P. McCabe, E. Pidcock, G.P. Shields, R. Taylor, M. Towler,J.van de Streek, Mercury: visualization and analysis of crystal structures, *J. Appl.Crystallogr*.39:453–457(2006). https://doi.org/10.1107/S002188980600731X.

[5] G.M. Sheldrick, Crystal structure refinement with SHELXL, *Acta Crystallogr. C Struct.Chem.* 71 (2015) 3–8, https://doi.org/10.1107/S2053229614024218.

[6] M.J. Frisch, G.W. Trucks, H.B. Schlegel, G.E. Scuseria, M.A. Robb, J.R. Cheeseman, G. Scalmani, V. Barone, B. Mennucci, G.A. Petersson, H. Nakatsuji, M. Caricato, X. Li, H.P. Hratchian, A.F. Izmaylov, J. Bloino, G. Zheng, J.L. Sonnenberg, M. Hada, M. Ehara, K. Toyota, R. Fukuda, J. Hasegawa, M. Ishida, T. Nakajima, Y. Honda, O. Kitao, H. Nakai, T. Vreven, J.A. Montgomery Jr., J.E. Peralta, F. Ogliaro, M. Bearpark, J.J. Heyd, E. Brothers, K.N. Kudin, V.N. Staroverov, R. Kobayashi,J. Normand, K. Raghavachari, A. Rendell, J.C. Burant, S.S. Iyengar, J. Tomasi, M. Cossi, N. Rega, J.M. Millam, M. Klene, J.E. Knox, J.B. Cross, V. Bakken, C. Adamo, J. Jaramillo, R. Gomperts, R.E. Stratmann, O. Yazyev, A.J. Austin,R. Cammi, C. Pomelli, J.W. Ochterski, R.L. Martin, K. Morokuma, V.G. Zakrzewski, G.A. Voth, P. Salvador, J.J. Dannenberg, S. Dapprich, A.D. Daniels, E.O. Farkas, J. B. Foresman, J.V. Ortiz, J. Cioslowski, D.J. Fox, Gaussian 09, Revision A.02, Gaussian Inc, Wallingford, CT, 2009.

[7] E.G. COX, Crystal Structure of Benzene, *Rev. Mod. Phys.* 30 (1) (1958) 159–162, https://doi.org/10.1103/RevModPhys.30.159.

[8] P.F. Lang, B.C. Smith, Electronegativity effects and single covalent bond lengths of molecules in the gas phase, *J. Chem. Society. Dalton Trans.* 43 (21) (2014)8016–8025, https://doi.org/10.1039/c4dt00807c.

[9] V. Schomaker and D.P. Stevenson, "Some revisions of the covalent radii and the additivity rule for the lengths of partially ionic single covalent bonds *," *J. Am.Chem. Soc.*, vol. 63, no. 1, pp. 37–40, 1941, https://doi.org/10.1021/ja01846a007.

[10] L.S. Higashi, M. Lundeen, K. Seff, Empirical relations between disulfide bond lengths, (nitrogen or carbon)-carbon-sulfur-sulfur torsion angles, and substituentsin aromatic disulfides. Crystal and molecular structure of 3,3'-dihydroxydi-2-pyridyl disulfide, *J. Am. Chem. Soc*. 100 (26) (1978) 8101–8106, https://doi.org/10.1021/ja00494a013

[11] A. Domenicano, P. Mazzeo, A. Vaciago, Substituent effects in the benzene series: A structural approach, Tetrahedron. Lett. 17 (13) (1976) 1029–1032, https://doi.org/10.1016/S0040-4039(00)77997-4.

[12] G. Schultz, T. Nagy, G. Portalone, F. Ramondo, I. Hargittai, A. Domenicano,Molecular structure of ethynylbenzene from electron diffraction and ab initio molecular orbital calculations, *Struct. Chem.* 4 (3) (1993) 183–190, https://doi.org/10.1007/BF00679344.

[13] Y. Maouche, G. Germain, M.C. Brianso, J.Y. Sanchez, P. Nicolet, M.J.M. Abadie,

T´etram´ethyl-1,1',3,3' biind`ene-1:1'-(±), C22H22, *Acta Crystallogr*. C 41 (1) (1985) 99–101, https://doi.org/10.1107/S0108270185002918.

[14] J. Jayabharathi, V. Thanikachalam, N. Srinivasan, M. Venkatesh Perumal,K. Jayamoorthy, Physicochemical studies of molecular hyperpolarizability of imidazole derivatives, *Spectrochim. Acta a Mol. Biomol. Spectrosc*. 79 (1) (2011)137–147, https://doi.org/10.1016/j.saa.2011.02.024.

[15]. M. Orio, D.A. Pantazis, F. Neese, Density functional theory, *Photosynth. Res.* 102(2) (2009) 443–453, https://doi.org/10.1007/s11120-009-9404-8.

[16] M. A Spackman, Turner, M. J., McKinnon, J. J., Wolff, S. K., Grimwood, D. J., Jayatilaka, D., & Spackman, P. R. (2021). CrystalExplorer: A program for Hirshfeld surface analysis, visualization and quantitative analysis of molecular crystals. Journal of Applied Crystallography, 54(3), 1006-1011. https://doi.org/10.1107/S160057672100379X

[17] F. Yuan, et al., Series of Ln-metal organic frameworks: Photocatalytic performance and Hirshfeld surface analyses, *J. Mol. Struct.* 1251 (2022) 131956, https://doi.org/10.1016/j.molstruc.2021.131956.

[18] M.A. Spackman, D. Jayatilaka, Hirshfeld surface analysis, *Cryst Eng Comm*. 11 (1)(2009) 19–32, https://doi.org/10.1039/B818330A.

[19] J.J. McKinnon, D. Jayatilaka, M.A. Spackman, Towards quantitative analysis of intermolecular interactions with Hirshfeld surfaces, *Chem. Commun.* (37) (2007) 3814–3816.

[20] C.F. Matta, J. Hern´andez-Trujillo, T. Tang, and R.F. W. Bader,Hydrogen–Hydrogen bonding: a stabilizing interaction in molecules and crystals,*Chem. A Eur. J.,* vol. 9, no. 9, pp. 1940–1951, 2003, https://doi.org/10.1002/chem.200204626.

[21] C.F. Matta, Hydrogen–Hydrogen Bonding: The Non-Electrostatic Limit of Closed-Shell Interaction Between Two Hydro, in Hydrogen Bonding—New Insights, *Springer Netherlands,* pp. 337–375. https://doi.org/10.1007/978-1-4020-4853-1_9.

[22] E.R. Johnson, S. Keinan, P. Mori-S´anchez, J. Contreras-García, A.J. Cohen, W. Yang, Revealing Noncovalent Interactions, *J. Am. Chem. Soc.* 132 (18) (2010) 6498–6506, https://doi.org/10.1021/ja100936w.

[23] Tian Lu, Feiwu Chen, Multiwfn: A Multifunctional Wavefunction Analyzer, J. Comput. Chem. 33, 580-592 (2012) DOI: 10.1002/jcc.22885

[24] W. Humphrey, A. Dalke, K. Schulten, VMD: Visual molecular dynamics, J. Mol. Graph. 14 (1) (1996) 33–38, https://doi.org/10.1016/0263-7855(96)00018-5.,

[25] Williams, T., & Kelley, C. (2023). Gnuplot 5.4: An Interactive Plotting Program [Computer software]. Retrieved from http://gnuplot.info

[26] N. Boukabcha, et al., Spectral investigation, TD-DFT study, Hirshfeld surface analysis, NCI-RDG, HOMO-LUMO, chemical reactivity and NLO properties of 1-(4-fluorobenzyl)-5-bromolindolin-2,3dione, *J. Mol. Struct.* 1285 (2023) 135492, https://doi.org/10.1016/j.molstruc.2023.135492.

[27] H. Arı, T. ¨Ozpozan, Y. Kabacalı, M. Saçmacı, Monomeric or dimeric? A theoretical and vibrational spectroscopic approach to the structural stability of 5-(4-metoxy benzoyl)-6-(4-metoxyphenyl)-3-methyl-2-thioxo-2,3-dihydropyrimidine-4(1H)-on, *J. Mol. Struct.* 1222 (2020) 128848, https://doi.org/10.1016/j.molstruc.2020.128848

[28] M. Jamr´oz, VEDA 4.0 Program: Vibrational Energy Distribution Analysis, *Drug Institute*, Warsaw, Poland, (2004).

[29] S. Gunasekaran, E. Sailatha, et al., FTIR, FT Raman spectra and molecular structural confirmation of isoniazid, Indian *J. Pure Appl. Phys.* 47:12-18(2009).

[30] E. Isac Paulraj, S. Muthu, Spectroscopic studies (FTIR, FT-Raman and UV), potential energy surface scan, normal coordinate analysis and NBO analysis of (2R,3R,4R,5S)-1-(2-hydroxyethyl)-2-(hydroxymethyl) piperidine-3,4,5-triol by DFT methods, *Spectrochim. Acta a Mol. Biomol. Spectrosc*. 108 (2013) 38–49, https://doi.org/10.1016/j.saa.2013.01.061.

[31] S. Muthu, J. Uma Maheswari, Quantum mechanical study and spectroscopic (FTIR, FT-Raman, 13C, 1H, UV) study, first order hyperpolarizability, NBO analysis,HOMO and LUMO analysis of 4-[(4-aminobenzene) sulfonyl] aniline by ab initio HF and density functional method, *Spectrochim. Acta a Mol. Biomol. Spectrosc*. 92 (2012) 154–163, https://doi.org/10.1016/j.saa.2012.02.056.

[32] S.M. Moosavinejad, M. Madhoushi, M. Vakili, D. Rasouli, Evaluation of degradation in chemical compounds of wood in historical buildings using FT-IR and FT-Raman vibrational spectroscopy, Maderas. Ciencia y tecnología (2019), https://doi.org/10.4067/S0718-221x2019005000310

[33] H.A.M. Salim, H.H. Abdallah, P. Ramasami, Stereoselectivity and Regioselectivity of the Cycloaddition Dimerization of allyl 3-(2-pyridyl) acrylate and allyl 3-(2-pyrryl) acrylate: DFT Calculations, IOP. *Conf. Ser. Mater. Sci. Eng.* 454 (2018) 012049, https://doi.org/10.1088/1757-899X/454/1/012049.

[34] V. Krishnakumar, G. Keresztury, T. Sundius, R. Ramasamy, Simulation of IR and Raman spectra based on scaled DFT force fields: a case study of 2-(methylthio) benzonitrile, with emphasis on band assignment, *J. Mol. Struct.* 702 (1–3) (2004) 9–21, https://doi.org/10.1016/j.molstruc.2004.06.004.

[35] S. Premkumar, et al., Vibrational Spectroscopic and Structural Investigations of 2-Amino 6-Methoxy-3-Nitropyridine: a DFT Approach, *Braz. J. Phys.* 45 (6) 621–632(2015), https://doi.org/10.1007/s13538-015-0365-4.

[36] K. Hasegawa, T. Ono, T. Noguchi, Vibrational Spectra and Ab Initio DFT Calculations of 4-Methylimidazole and Its Different Protonation Forms: Infrared and Raman Markers of the

Protonation State of a Histidine Side Chain, *J. Phys. Chem.* B 104 (17) (2000) 4253–4265, https://doi.org/10.1021/jp000157d.

[37] G. Varsanyi, Vibrational Spectra of Benzene Derivatives*, Academic Press*, NewYork, 1969".

[38] S. Sakthivel, T. Alagesan, S. Muthu, C.S. Abraham, E. Geetha, Quantum mechanical, spectroscopic study (FT-IR and FT - Raman), NBO analysis, HOMOLUMO, first order hyperpolarizability and docking studies of a non-steroidal anti-inflammatory compound, *J. Mol. Struct.* 1156 (2018) 645–656, https://doi.org/10.1016/j.molstruc.2017.12.024.

[39] P. Venkatesan, S. Thamotharan, A. Ilangovan, H. Liang, T. Sundius, Crystal structure, Hirshfeld surfaces and DFT computation of NLO active (2E)-2-(ethoxycarbonyl)-3-[(1-methoxy-1-oxo-3-phenylpropan-2-yl)amino] prop-2-enoic acid, *Spectrochim. Acta a Mol. Biomol. Spectrosc.* 153 (2016) 625–636, https://doi.org/10.1016/j.saa.2015.09.002.

[40] R.M. Silverstein, G.C. Basseler, T.C. Morrill, Spectrometric Identification of Organic Compounds, *Wiley*, New York,.

[41] A.T. Alphonsa, C. Loganathan, S.A.A. Anand, S. Kabilan, Molecular structure, NMR, UV–Visible, vibrational spectroscopic and HOMO, LUMO analysis of (E)-1-(2, 6-bis (4-methoxyphenyl)-3, 3-dimethylpiperidine-4-ylidene)-2-(3-(3, 5-dimethyl-1Hpyrazol-1-yl) pyrazin-2-yl) hydrazine by DFT method, *J. Mol. Struct.* 1106 (2016)277–285, https://doi.org/10.1016/j.molstruc.2015.11.005.

[42] N. Elangovan, B. Gangadharappa, R. Thomas, A. Irfan, Synthesis of a versatile Schiff base 4-((2-hydroxy-3,5-diiodobenzylidene)amino) benzenesulfonamide from 3,5-diiodosalicylaldehyde and sulfanilamide, structure, electronic properties, biological activity prediction and experimental antimicrobial properties, *J. Mol. Struct.* 1250 (2022) 131700, https://doi.org/10.1016/j.molstruc.2021.131700.

[43] F. Dahlmann, et al., Vibrational Predissociation Spectra of C 2 N □ and C 3 N □ : Bending and Stretching Vibrations, *Chem phys chem.* 24 (15) (2023), https://doi.org/10.1002/cphc.202300262.

[44] N.B. Colthup, L.H. Daly, S.E. Wiberley, Introduction to Infrared and Raman Spectroscopy, 3rd ed., *Academic Press Inc.*, New York, 1990.

[45] R. Mecke, R. Mecke, A. Luttringhaus, Chem. Ber. 90 (1957).

[46] C.N.R. Rao, R. Venkataraghavan, The C=S stretching frequency and the '□ N□ C=S bands' in the infrared, Spectrochim. Acta a 45 (1989) 299–305, https://doi.org/10.1016/S0584-8539(89)80280-6.

[47] G. Lauro, G. Bifulco, Elucidating the relative and absolute configuration of organic compounds by quantum mechanical approaches, *European. J. Org. Chem*. 2020 (26) (2020) 3929–3941, https://doi.org/10.1002/ejoc.201901878.

[48] K. Arici, D.E. Altınoz, M. Cavusoglu, S. Diken, Crystal structure, IR and NMR spectra of (E)-2methoxy-4-(2-morpholinovinyl) phenol molecule and its DFT calculations, *J. Mol. Struct.* 1275 (2023) 134669, https://doi.org/10.1016/j. molstruc.2022.134669.

[49] P.S. Achanta, et al., Quantum mechanical NMR full spin analysis in pharmaceutical identity testing and quality control, *J. Pharm. Biomed. Anal.* 192 (2021) 113601, **https://doi.org/10.1016/j.jpba.2020.113601.**

[50]. M.W. Lodewyk, M.R. Siebert, D.J. Tantillo, Computational prediction of 1H and 13C chemical shifts: a useful tool for natural product, mechanistic, and synthetic organic chemistry, *Chem. Rev.* 112 (3) (2012) 1839–1862, https://doi.org/10.1021/cr200106v.

[51] P. Cimino, L. Gomez-Paloma, D. Duca, R. Riccio, G. Bifulco, Comparison of different theory models and basis sets in the calculation of13C NMR chemical shifts of natural products, *Magn. Resonance Chem*. 42 (S1) (2004) S26–S33, https://doi.org/10.1002/mrc.1410.

[52] N.M. O'boyle, A.L. Tenderholt, K.M. Langner, cclib: A library for packageindependent computational chemistry algorithms, J. Comput. Chem. 29 (5) (2008) 839–845, https://doi.org/10.1002/jcc.20823

[53]. M.S.H. Akash, K. Rehman, Ultraviolet-Visible (UV-VIS) Spectroscopy. Essentials of Pharmaceutical Analysis, Springer Nature Singapore, Singapore, 2020, pp. 31–33, https://doi.org/10.1007/978-981-15-1547-7_3.

[54] S. Fleming, A. Mills, T. Tuttle, Predicting the UV–vis spectra of oxazine dyes, Beilstein. *J. Org. Chem*. 7 (2011) 432–441, https://doi.org/10.3762/bjoc.7.56.

Chapter IV

Electronic Properties

IV.1 Introduction:

The study of molecular properties is fundamental to understanding the behavior, stability, and reactivity of chemical compounds. By examining these properties, researchers can predict how molecules will interact with their environment and with other chemical species, enabling advancements in fields such as material science, pharmacology, and catalysis. This chapter explores the molecular properties of the EMBIT compound, focusing on its electronic structure and reactivity. A combination of computational and theoretical methods is employed to gain a deeper understanding of the molecule's geometry, charge distribution, and reactivity patterns. Key topics include the dipole moment, which highlights the molecule's polarity, and the molecular electrostatic potential (MEP), which maps regions of electrophilic and nucleophilic reactivity. Frontier molecular orbitals (HOMO and LUMO) are analyzed to assess electronic transitions and chemical stability, while reactivity descriptors offer quantitative insights into chemical behavior. Natural Bond Orbital (NBO) analysis and Fukui functions help identify bonding interactions and potential reactive sites. Furthermore, the Localized Orbital Locator (LOL) and Electron Localization Function (ELF) provide visual representations of these interactions and electron distribution. electron delocalization and bonding. Together, these analyses form a comprehensive framework for understanding the structural and chemical properties of the EMBIT compound.

IV.1 atomic charge:

Atomic charges are an essential component in quantum chemistry calculations, serving as a fundamental tool to describe the electron distribution within a molecular system. These charges provide valuable insights into the electron density of a molecule and are crucial for understanding its chemical reactivity, interactions with other molecules, and its overall behavior in different environments. In computational chemistry, two commonly used methods for evaluating atomic charges are Mulliken population analysis and Natural Population Analysis (NPA), each offering different approaches and insights into the electron distribution.

Mulliken charges [1] are derived from the overlap population of atomic orbitals, where the electron density is distributed among the atoms based on their atomic orbitals. This analysis is typically performed after optimizing the geometry of the molecule, which ensures that the electronic structure is accurately represented. While Mulliken charges provide a quick and straightforward way to assess charge distribution, they are often criticized for their dependence on the choice of basis set and the fact that they can lead to unrealistic charge assignments,

especially in highly polar or noncovalent systems. These charges are also known to sometimes assign high or nonphysical charges to atoms, particularly in cases of electron delocalization or when dealing with weak interactions. Nevertheless, Mulliken charges remain a popular tool for understanding general trends in charge distribution across molecules.

On the other hand, Natural Population Analysis (NPA) charges [2] are derived from the analysis of natural bonding orbitals (NBO), which are more chemically meaningful. NPA provides a more reliable depiction of charge distribution because it takes into account the inherent chemical bonding in the molecule, thus offering a more physically realistic picture of the electron density. NPA is particularly useful when dealing with complex molecular systems, where Mulliken charges may fail to provide an accurate representation of electron density, especially in the case of electron delocalization or charge transfer. By focusing on the natural bonding orbitals that best represent bonding interactions in the molecule, NPA is better suited for understanding the behavior of molecules in real-world environments, including solvent effects and molecular interactions.

In this study, the atomic charges of the EMBIT compound were computed using the B3LYP method with the 6-311G++(d,p) basis set. The B3LYP functional is commonly employed for its balanced description of electronic correlation and exchange effects, making it suitable for obtaining reliable charge distributions. The 6-311G++(d,p) basis set provides a high level of precision in the description of the molecular orbitals, allowing for a more accurate evaluation of the electronic structure. This combination of method and basis set ensures that the computed charges are both reliable and physically meaningful. **Table. IV.1** presents the Mulliken and Natural Population Analysis (NPA) charges for various atoms in the molecule computed by B3LYP/6-311G++(d,p) , revealing insights into its electron density distribution. For instance, oxygen O1 exhibits a slight negative charge in both Mulliken -0.037605 and NPA -0.53118 analyses, with the NPA charge being significantly more negative, suggesting a higher electron density around oxygen. Sulfur S3, on the other hand, shows a negative Mulliken charge -0.284540 but a positive NPA charge +0.46199, indicating that it is electron-deficient according to NPA. Nitrogen N1 presents contrasting charges: a positive Mulliken charge +0.489137 and a negative NPA charge -0.44764, reflecting the differing electron density distributions of each method. Carbon atoms like C6 and C14 display mild negative charges in Mulliken, with C6 also showing a more significant negative charge in NPA. The hydrogen atoms (H19, H2, etc.) exhibit smaller positive charges, typical for hydrogen when attached to electronegative atoms. Overall, the distribution of charges suggests significant polarization within the molecule, with

electron density accumulating in certain regions and being depleted in others, contributing to the molecule's dipole moment

Table. IV.1 Mulliken charges vs NPA by B3LYP/6-311G++(d,p)

	Mulliken charges:	NPA
O1	-0.037605	-0.53118
S3	-0.284540	0.46199
S2	0.099803	0.40522
S1	-0.565653	-0.09428
N2	0.096978	-0.51423
C9	-0.160140	-0.36415
C10	0.038197	0.09898
N1	0.489137	-0.44764
C8	-0.461906	0.41215
N3	1.098255	-0.45113
C1	0.274017	0.13039
C7	0.017840	-0.10235
C14	-0.897044	0.07596
C11	-0.231169	-0.41755
H11	0.257667	0.23379
C12	0.619494	0.18097
C6	0.164101	0.12869
C19	-0.165340	0.33561
C2	-0.187015	-0.21708
H2	0.134365	0.23791
C5	-0.252839	-0.20964
H5	0.166771	0.21377
C3	-0.360321	-0.21406
H3	0.174858	0.20436
C16	-0.348337	-0.22338
H16	0.189054	0.21477
C4	-0.268030	-0.20244
H4	0.160037	0.20294

C18	-0.244926	-0.27692
H18	0.203143	0.21820
C15	0.258715	-0.17021
H15	0.183647	0.22175
C20	-0.294296	-0.20578
H 20A	0.187023	0.19845
H 20B	0.158972	0.18013
H 20C	0.143662	0.17020
C13	-0.735408	-0.60090
H 13A	0.183421	0.22053
H 13B	0.165485	0.22305
H 13 C	0.184784	0.22230
C17	-0.332224	-0.15954
H17	0.177367	0.21095

IV.2 Dipole moment :

The dipole moment is a fundamental measure in molecular chemistry that reflects the distribution of electrical charges within a molecule [3]. This property, expressed in Debye (D), The dipole moment is represented as a three-dimensional vector, making it a valuable indicator of charge movement within a molecule. The orientation of the dipole moment vector is determined by the relative positions of the centers of positive and negative charge, The total dipole moment value is calculated using the equation IV.1:

$$\mu(D) = \sqrt{\mu_X^2 + \mu_Y^2 + \mu_Z^2} \qquad \text{IV.1}$$

The dipole moment of the molecule was calculated using the B3LYP/6-311G++(d,p) level of theory., The table enlists the components of the dipole moment along the x, y, and z axes as and we found that the components along the x and y axes are zero (μx = 0, μy = 0), while the z-component is μz = 3.39211 Debye. Consequently, the total dipole moment is μ = 3.39211 Debye, indicating that the dipole moment is entirely oriented along the z-axis. This result highlights the symmetry in the charge distribution within the x-y plane and a significant polarization along the z-axis. The Fig.IV.1 shows that the dipole moment is directed from the benzo[4,5]imidazo[1,2-c]thiazole-1(3H)-thione portion (the electron-deficient side) towards the 3-(3-(2-methoxyphenyl)-4-methylthiazol-2(3H)-ylidene part (the electron-rich side).

Table. IV.2 Calculated dipole moment component for EMBIT by B3LYP /6-311G++(d,p)

Parameters	B3LYP /6-311G++(d,p)
Dipole Moment	
μ_x=	0
μ_y=	0
μ_z=	3.39211
μ=	3.39211

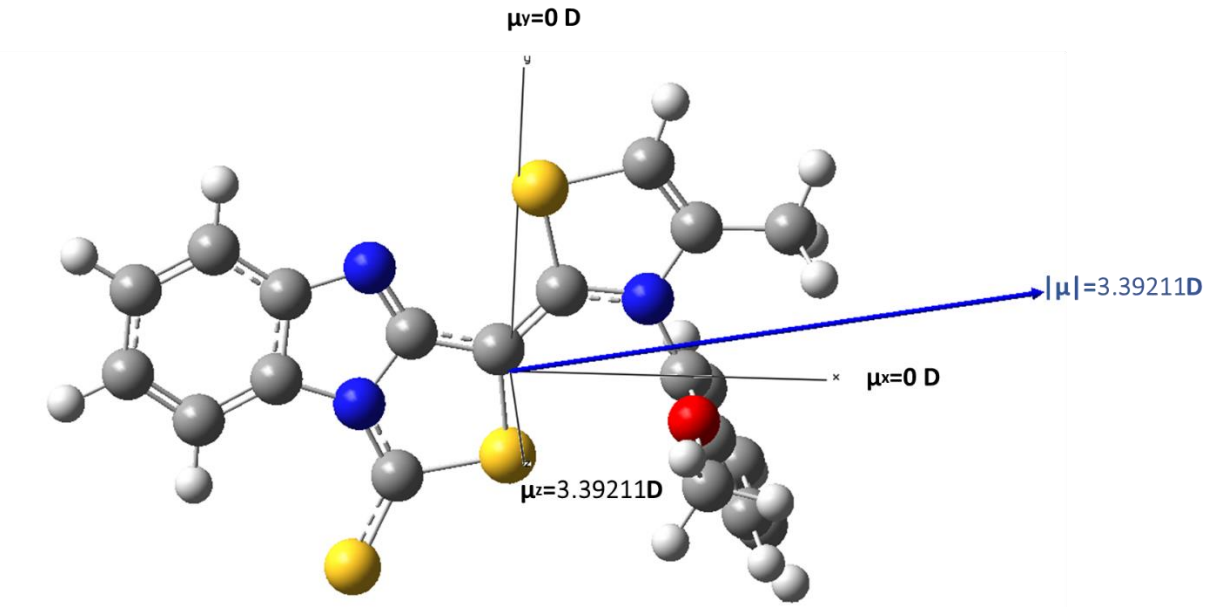

Fig.IV.1 dipole moment

IV.3 Natural bond orbitals NBO:

NBO analysis of the studied compound is conducted using the B3LYP method and the 6-31G(d,p) basis set to analyse intramolecular interactions. The NBO calculations were carried out using the NBO program [4]. Intramolecular charge transfer (ICT) can enhance the polarization of the molecule, and this ICT is likely responsible for the non-linear optical (NLO) properties of the compound. And predicts potential for future applications in non-linear optical materials [5]. The second-order Fock matrix is employed to assess the interaction between donor *(i)* and acceptor (j) orbitals in the NBO analysis [6–9]. This interaction results in a transfer of electron density from the occupied donor orbital in the idealized Lewis structure to an empty non-Lewis orbital. For each donor *(i)* and acceptor *(j)* pair, the stabilization energy $E^{(2)}$, which quantifies the delocalization from donor *i* to acceptor *j*, is given by the formula IV.2:

$$E^{(2)} = \Delta E_{ij} = q_i \frac{F(i,j)^2}{\varepsilon_J - \varepsilon_I}$$ IV.2

where q_i represents the occupancy of the donor orbital, ε_j are the diagonal elements of the Fock matrix, and *F(i,j)* is the off-diagonal Fock matrix element. A larger value of $E^{(2)}$ indicates a stronger interaction between the donor and acceptor orbitals, meaning a significant electron donation from the donor to the acceptor and an increased degree of conjugation within the system. The NBO analysis of EMBIT revealed key interactions include sigma bond contributions such as σ (S3–C10) →σ* (S2–C9) with $E^{(2)}$ =5.96 kcal/mol and notable π-π* delocalization like π (N2–C8) →π* (C1–C6 with $E^{(2)}$=19.20 kcal/mol . The intramolecular hyperconjugative interaction of the σ C 14 – C 15 bond is distributed to the σ* C 16– C 15 bond and to π*C 19 – C 18 resulting in stabilization energies of $E^{(2)}$ =11.05 kcal/mol $E^{(2)}$ = 29.09 kcal/mol respectively , Lone pair interactions also play a critical role, exemplified by LP (1) N1→π* (N2–C8) with $E^{(2)}$ =41.05 kcal/mol and LP (2) S2→π* (S1–C7) with E (2) =35.76 kcal/mol, the highest interaction energy was captured from LP (1)N to the antibonding π*(S 1 – C 7) with $E^{(2)}$ =72.48 kcal/mol reflecting strong electron delocalization and charge r distribution

Table. IV.3 Natural bond orbitals NBO B3LYP/6-311G++(d,p)

DONOR NBO (*I*)	Type	ED(e)	ACCEPTOR NBO (*J*)	type	ED(e)	E $^{(2)}$ KCAL/MO	E(J)– E(I) L A.U	F(I, J) A.U.
S3–C10	σ	1.96253	S2–C9	σ*	0.03355	5.96	0.84	0.063
S3–C10	σ		N3–C14	σ*	0.03987	4.52	1.02	0.061
S3–C11	σ	1.96913	C11–C12	π*	0.24457	6.97	0.66	0.064
S3– C11	σ		C16–C17	π*	0.32901	30.06	1.93	0.233
N2–C8	π	1.85543	C1– C6	π*	0.47565	19.20	0.34	0.079
C9–C10	σ	1.97726	C9–C8	σ*	0.03509	5.08	1.28	0.072
C9–C10	π	1.80580	N2– C8	π*	0.41815	22.02	0.31	0.078
C1–C6	π	1.59651	N2– C8	π*	0.41815	12.48	0.26	0.051
C14–C15	σ	1.97163	C16–C15	σ*	0.01463	11.05	1.26	0.106
C14 – C15	π	1.71484	C19 –C18	π*	0.38320	29.09	0.27	0.081
C19–C18	π	1.64219	C26–C17	π*	0.32901	15.26	1.51	0.136
C2 –C3	π	1.68876	C1–C6	π	0.47565	19.97	0.27	0.068
C5–C4	π	1.69840	C1–C 6	*	0.47565	20.79	0.28	0.071
C16–C17	σ	1.97932	C16–C17	π*	0.32901	40.89	1.97	0.275
C16–C17	π	1.66161	C14–C15	π*	0.37351	24.73	0.27	0.074
C16–C17	π		C19–C28	π*	0.38320	17.74	0.25	0.060
C18–C17	σ	1.97526	C18–C17	π*	0.32901	38.12	1.94	0.263
C18–C17	σ		C18–C17	π*	0.01447	14.82	2.73	0.180
LP (2) O1		1.83340	C19–C18	π*	0.38320	33.95	0.32	0.098
LP (2) S3		1.68477	C9–C10	π*	0.48165	26.87	0.24	0.075
LP (2) S3			C11–C12	π*	0.24457	22.88	0.21	0.062

LP (2) S2	1.72388	S1–C7	π^*	0.08360	35.76	0.18	0.075
LP (2) S 2		C9 –C10	π^*	0.48165	17.45	0.24	0.061
LP (2) S1	1.84978	S13–C7	σ^*	0.03355	14.56	0.37	0.067
LP (2) S1		N1–C7	σ^*	0.08360	13.59	0.60	0.082
LP (1) N2	1.90651	N1–C8	σ^*	0.05931	10.51	0.74	0.080
LP (1) N2		C1–C6	σ^*	0.03767	6.18	0.89	0.067
LP (1) N1	1.54620	S1–C7	π^*	0.08360	72.48	0.20	0.107
LP (1) N 1		N2–C8	π^*	0.41815	41.05	0.29	0.098
LP (1) N1		C1– C16	π^*	0.47565	27.67	0.30	0.082
LP (1) N3	1.62812	C9–C10	π^*	0.48165	48.21	0.27	0.105
LP (1) N3		C11–C12	π^*	0.24457	42.77	0.23	0.092

IV.4 Molecular Electrostatic Potential (MEP):

MEP maps depicted in Fig.IV.2, visualize a molecule's electron density in three dimensions, serves as crucial tools for identifying regions prone to nucleophilic and electrophilic attacks, as well as areas favorable for hydrogen bonding. These maps offer valuable insights into the chemical reactivity and behavior of the molecule by depicting the spatial distribution of electron density.By analyzing MEP maps, one can predict the molecule's tendency for nucleophilic or electrophilic interactions and its potential to form hydrogen bonds. The colors depicted on the MEP surfaces (see Fig. 10) correspond to different electrostatic potential values, ranging from blue (indicating the highest positive potential) to green, yellow, orange, and red (indicating the most negative potential). In the EMBIT molecule, red regions on the MEP map situated above the N2 and S2 atoms highlight areas of negative potential that are favorable for nucleophilic attacks. On the other hand, blue regions, primarily located above the methoxyphenyl and thiazole ring, represent electron-deficient areas with positive potential, making them susceptible to electrophilic attacks, MEP analysis provides a detailed understanding of the reactive regions in the EMBIT molecule. It identifies areas likely to participate in nucleophilic and electrophilic interactions [10], thereby shedding light on the compound's chemical reactivity and potential interaction sites.

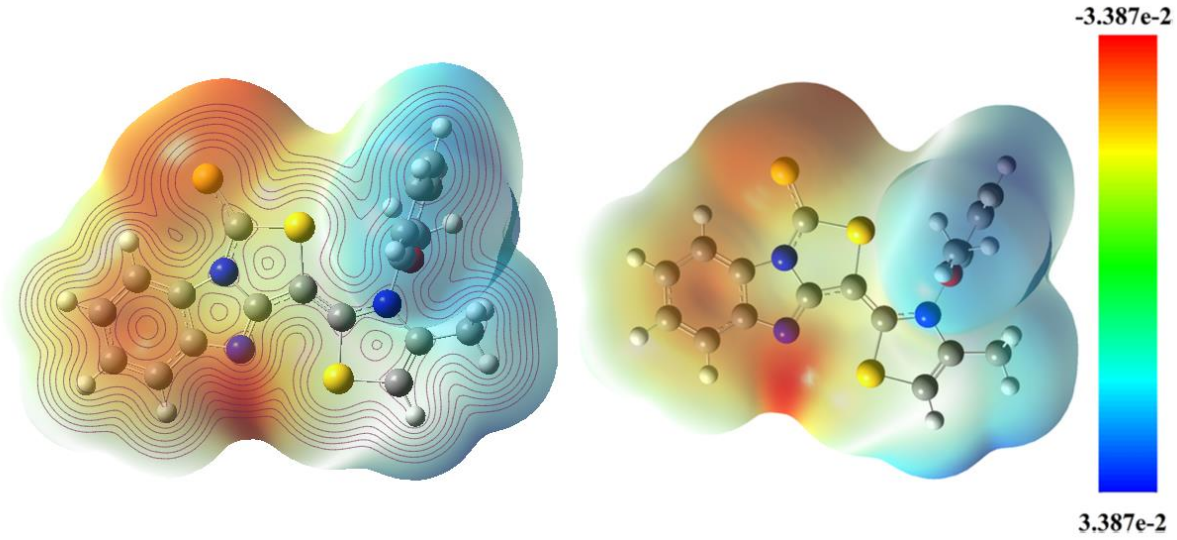

Fig.IV.2 Molecular electrostatic map of EMBIT

IV.5 Frontier molecular orbitals:

To provide deeper visualizations of the frontier molecular orbitals (FMOs) in the gaseous state are shown in Fig.IV.3, along with simulations in four different solvents. The highest occupied molecular orbital (HOMO) and the lowest unoccupied molecular orbital (LUMO) define the chemical reactivity and kinetic stability of the molecule through the HOMO-LUMO gap.Molecules with a wide HOMO termed hard, exhibiting low polarizability and reactivity, while a narrow gap characterizes soft molecules, making them more reactive and highly polarizable. The red and green regions in the FMO diagrams represent the positive and negative phases, respectively, illustrating charge transfer across the molecule. HOMO and LUMO orbitals span the entire molecule, indicating overall charge transfer, while HOMO-1 and LUMO+1 transitions highlight charge transfer from the sulfur group to the methoxyphenyl ring. The calculated band gap for EMBIT was approximately 3 eV, aligning with reported optical absorption edges for some biomaterials [11]. suggesting its potential use as a biomaterial. DOS (density of states) analysis, confirmed the calculated energy gap. High DOS intensities represent abundant potentially occupiable states, while the near-zero electron volt (eV) region indicates a lack of occupied states [12] The unoccupied orbitals are depicted by the red lines, whereas the green lines illustrate the occupied orbitals. the inclusion of solvents reduced the prediction energy discrepancies to less than 0.3 eV, with most deviations below 0.1 eV,

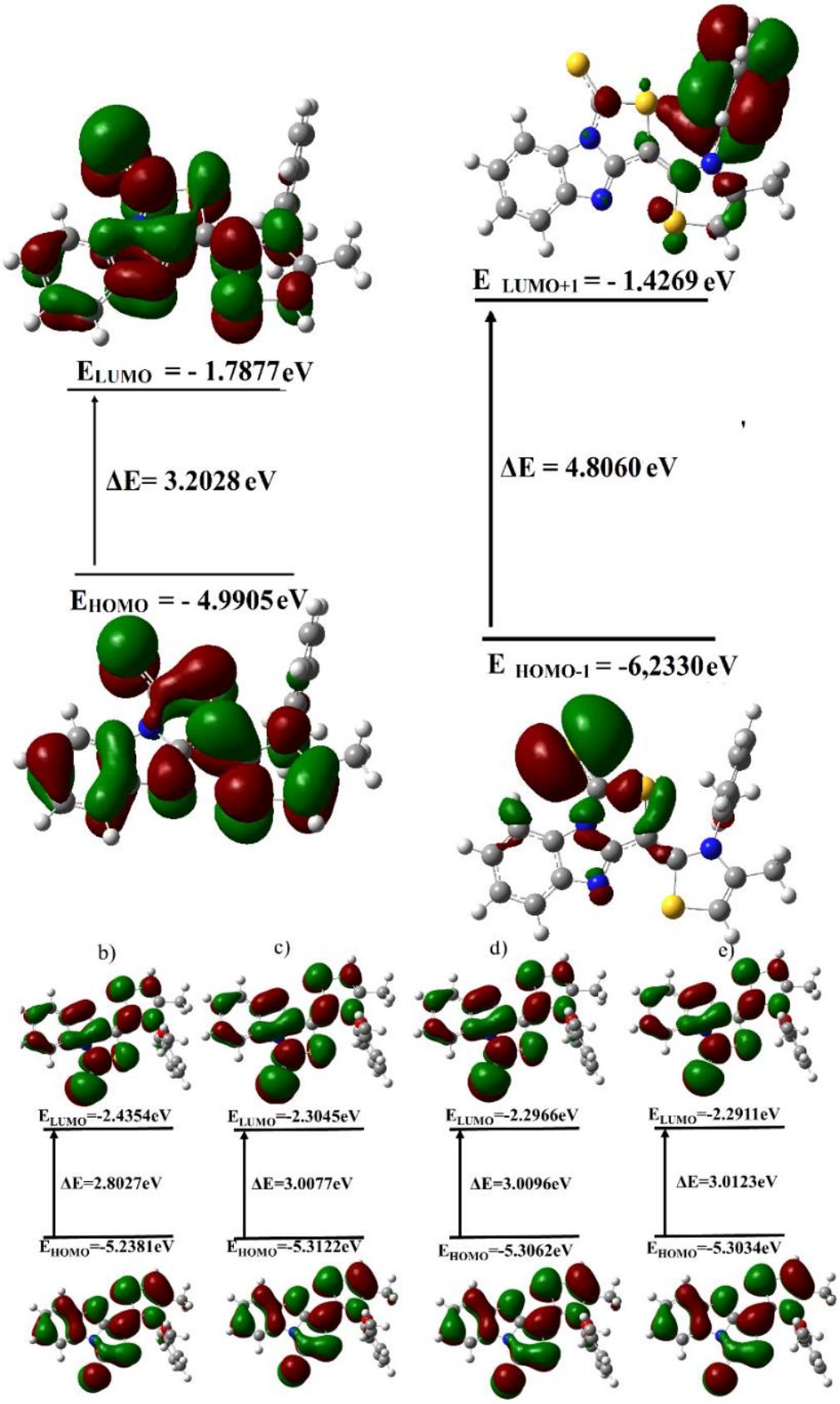

Fig.IV.3 EMBIT frontiers molecular orbitals in a) gas phase b) Chloroform, c) DMSO, d) Methanol, e) Ethanol

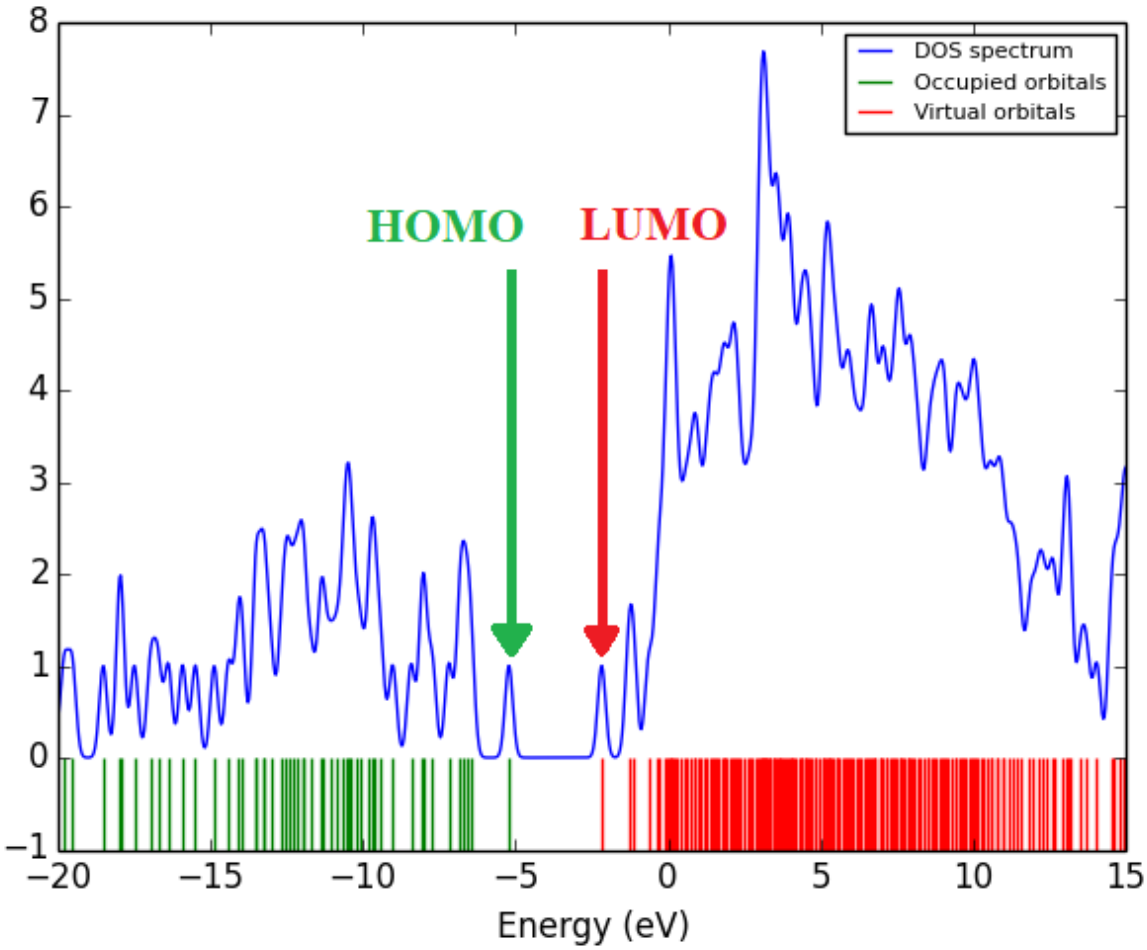

Fig.IV.4 EMBIT's Density of state spectra

IV.6 Global Chemical reactivity descriptors GCRD:

Global chemical reactivity descriptors have proven to be highly effective tools for predicting the reactivity of atoms and molecules, as well as determining reactive sites [13-15]. In this study, we explored the impact of solvents on global chemical reactivity descriptors by employing the CPCM model with four different solvents: DMSO, ethanol, methanol, and chloroform. The descriptors examined include chemical hardness (η) IV.3, chemical potential (μ) IV.4, chemical softness (s) IV.5, electron affinity (EA) IV.6, ionization potential (IP) IV.7, hyper-hardness (Γ) IV.8, electrophilicity index (ω) IV.9.and electronegativity (χ) IV. 10, These parameters were calculated using Koopman's theorem [16]. The results of the calculations are summarized in Table. IV.4

$$\eta = \frac{1}{2}(E_{LUMO} - E_{HOMO}) \quad \text{IV.3}$$

$$,\mu = \frac{1}{2}(E_{LUMO} + E_{HOMO}) \quad \text{IV.4}$$

$$S = \frac{1}{2}\eta \text{ , IV.5}$$

$$, E_A = -E_{LUMO} \text{ IV.6}$$

$$, I_P = -E_{HOMO} \text{ IV.7}$$

$$, \Gamma = E_{LUMO} - 2E_{HOMO} + E_{HOMO-1}\ \mu \text{ IV.8}$$

$$, \omega = \frac{\mu^2}{2\eta} \text{ IV.9}$$

$$\chi = -\frac{1}{2}(E_{LUMO} + E_{LUMO}) \text{ IV. 10}$$

The chemical potential represents the tendency of electrons to move away from equilibrium. [17]. electronegativity is defined as the ability of an atom to attract electron [14] Chemical hardness (η), a parameter linked to molecular stability, plays a significant role in various chemical and biological functions [13,16], while softness represents the inverse of hardness. The global electrophilicity index (ω), derived from thermodynamic properties, quantifies the favorable energy change associated with a chemical system reaching electron saturation. In simpler terms, it measures the energy reduction resulting from electron transfer between the donor (HOMO) and acceptor (LUMO) orbitals within a molecule, and is a critical factor in assessing chemical reactivity [18,19]. A system's stability is often associated with positive hyper-hardness values and electrophilicity index (ω) values greater than 1.5 Ev [20,21]. Additionally, the electrophilicity index is recognized as an effective descriptor for biological activity [22,23] and a predictor of toxicity [24]. Conversely, negative hyper-hardness values suggest higher reactivity [10]. A negative chemical potential (μ) also indicates stability, particularly when the electron affinity (EA) is lower than the ionization potential (IP), which corresponds to enhanced electron-donating capabilities and reduced electron-accepting tendencies. The data supports the conclusion that EMBIT is a stable compound. To deepen our understanding of the compound's reactivity, we analyzed the influence of different solvents on its global chemical reactivity descriptors (GCRD). Our analysis revealed a significant increase in electronegativity, electrophilicity index, and electron affinity under various solvent environments. Conversely, we observed a notable reduction in chemical potential, chemical hardness, chemical softness, and hyper-hardness in these conditions. Aprotic solvents like

DMSO, in particular, demonstrated a marked decrease in chemical potential and hardness, with minimal changes in their dielectric constants [23].in conclusion , In the gas phase, EMBIT exhibits relatively stable behavior with a moderate HOMO-LUMO gap and moderate chemical hardness, indicating a balanced reactivity. However, when placed in solvents, especially polar solvents like DMSO and chloroform, the molecule shows increased reactivity. This is reflected in the reduced HOMO-LUMO gap and lower chemical hardness, suggesting that EMBIT becomes more prone to undergoing chemical reactions in such environments. The increase in electrophilicity and the reduction in chemical hardness further indicate that the molecule in solution is more inclined to accept electrons and engage in chemical interactions. The solvent effect, particularly in aprotic solvents, enhances EMBIT's polarizability and reactivity, highlighting its potential for use in a wide range of chemical and biological applications.

Table. IV.4 Global chemical reactivity descriptors of EMBIT in Different Solvents Using B3LYP/6-311G++(d,p)

Parameters	B3LYP/6–311G++(d,p)				
	gaz	DMSO	Ethanol	methanol	chloroform
E_{HOMO} (eV)	-4.9905	-5.3122	-5.3034	-5.3062	-5.2381
E_{LUMO} (eV)	-1.7877	-2.3045	-2.2911	-2.2966	-2.4354
ΔE (eV)	3.2028	3.0077	3.0123	3.0096	2.8027
I_P (eV)	4.9905	5.3122	5.3034	5.3062	5.2381
E_A (eV)	1.7877	2.3045	2.2911	2.2966	2.4354
χ (eV)	3.3891	3.8083	3.7972	3.8014	3.8367
μ (eV)	-3.3891	-3.8083	-3.7972	-3.8014	-3.8367
η (eV)	1.6014	1.5038	1.5061	1.5048	1.4013
S (eV)	0.8007	0.7519	0.7530	0.7524	0.7006
ω (eV)	3.5862	4.8221	4.7867	4.8015	5.2523
Γ (eV)	1.9603	1.6923	1.7034	1.6953	1.5564

IV.7 The Electron Localization Function ELF and The Localized Orbital Locator LOL:

Topographical maps illustrate the electron environment surrounding each atom, providing a detailed view of the electron distribution. which highlight pronounced or diminished peaks. These maps provide valuable insights into the likelihood of locating electron pairs on the molecular surface, thereby revealing their spatial distribution and accessibility within the

molecular structure. The Electron Localization Function (ELF), denoted as τ(r), ranges from 0.0 to 1.0. Regions with higher values (between 0.5 and 1.0) correspond to areas containing both bonding and nonbonding localized electrons, whereas lower values (below 0.5) indicate regions with delocalized electrons [25]. As demonstrated in the ELF map (Fig. S1), the distribution of electron density in molecular bonds highlights notable differences. The degree of electron localization between carbon and oxygen is less pronounced compared to the carbon-nitrogen and carbon-carbon bonds.

The Localized Orbital Locator (LOL), represented by the Localization Index, η(r), similarly provides insights into electron behavior. High LOL values (> 0.5) indicate regions where electron density is strongly governed by localization [25]. In the LOL map, areas above hydrogen atoms are distinctly highlighted in red (when the value exceeds 0.5), with the covalent bonding regions exhibiting particularly high LOL values. Conversely, areas of electron depletion, which reflect contrasts between the valence and inner electron shells, are marked by characteristic blue circles [26].

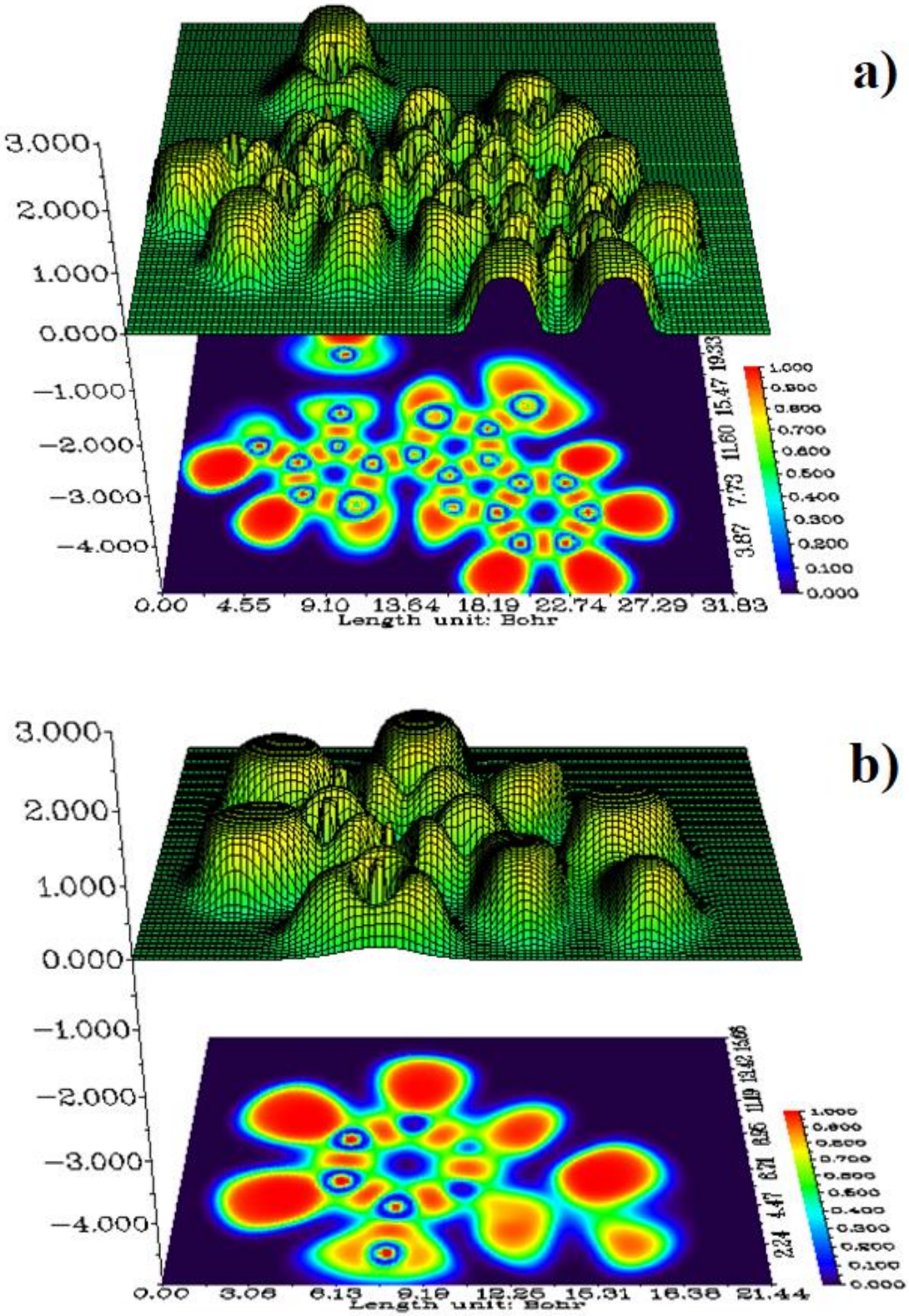

Fig.IV.5 Electron Localization Function of EMBIT a)x axis view b)z axis view

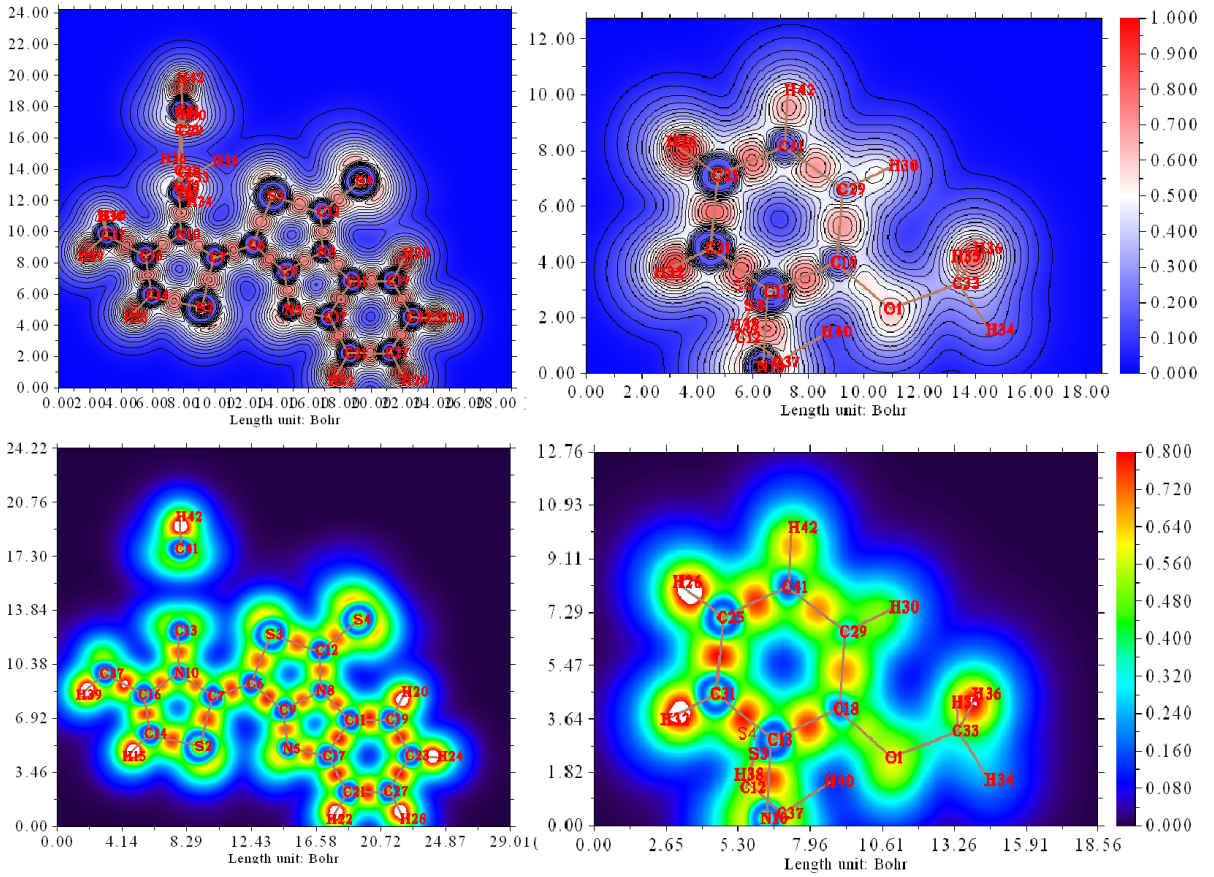

Fig.IV.6 localized orbital locator map of EMBIT

IV.8 Conclusion:

In this chapter in the main goal is studying the EMBIT proprieties, the computational analysis of the EMBIT compound provided valuable insights into its electronic structure, reactivity, and potential applications. The molecular charge distribution, calculated using methods, like Mulliken and Natural Population Analysis, revealed significant polarization, with regions such as oxygen and sulfur atoms displaying electron density accumulation and depletion, respectively. This polarization contributes to the molecule's dipole moment, oriented along the z-axis, highlighting areas of high reactivity. The NBO analysis emphasized the importance of intramolecular charge transfer and strong electron delocalization, which could enhance EMBIT's suitability for non-linear optical (NLO) materials. The Molecular Electrostatic Potential (MEP) maps further supported this by identifying electron-rich and electron-deficient regions prone to electrophilic and nucleophilic attacks. Additionally, global chemical reactivity descriptors such as chemical hardness, electronegativity, and electrophilicity index demonstrated that EMBIT is relatively stable, yet reactive under specific conditions, with solvent effects playing a significant role in effecting its reactivity. finally, all of the The Electron Localization Function (ELF) and Localized Orbital Locator (LOL) maps showed that EMBIT

exhibits both localized electron density in covalent bonds and delocalized electrons in other regions, contributing to its reactivity and polarizability. The HOMO-LUMO gap and Frontier Molecular Orbital (FMO) analysis further indicate that EMBIT is a soft molecule with high reactivity, making it a promising candidate for various applications, particularly in non-linear optics and biomaterials. Overall, EMBIT's combination of stability and reactivity, along with its electronic features, positions it as a versatile compound with significant potential in advanced material science and biotechnology.

References:

[1] R.S. Mulliken, Electronic Population Analysis on LCAO MO Molecular Wave Functions.I, *J. Chem. Phys.* 23 (1955) 1833 1840. https://doi.org/10.1063/1.1740588.

[2] A.E. Reed, R.B. Weinstock, F. Weinhold, Natural population analysis, *J. Chem. Phys.* 83 (1985) 735 746. https://doi.org/10.1063/1.449486.

[3] D. R. Lide, CRC Handbook of Chemistry and Physics 84th ed., CRC Press, 2004

[4] E. D. Glendening, A. E. Reed, J. E.Carpenter, F. Weinhold, NBO 3.1.ed.; *theoretical Chemestry Instituten,* University of Wisconsin, Madison, WI, 1996.

[5] N.Benhalima, N. Boukabcha, Ö. Tamer, A. Chouaih, D. Avcı, Y.Atalay , F. Hamzaoui , Solvent Effects on Molecular Structure, Vibrational Frequencies, and NLO Properties of N-(2,3-Dichlorophenyl)-2-Nitrobenzene–Sulfonamide: a Density Functional Theory Study *Braz. J. Phys*46: 371–383 (2016*)*. https://doi.org/10.1007/s13538-016-0419-2.

[6] M. Szafran, A. Komasa, E.B. Adamska, *J Mol Struct* (THEOCHEM) 827, 101 (2007)

[7] S. Sebastian, N. Sundaraganesan, Spectrochim Acta A 75, 941 (2010)

[8] Ö. Tamer, D. Avcı, Y. Atalay, *J Mol Struct* 1098, 12 (2015)

[9] S. Altürk, Ö. Tamer, D. Avcı, Y. Atalay, *J Organomet Chem* 797, 110 (2015)

[10] S. Sahin, N. Dege, (E)-N-(3-chlorophenyl)-1-(5-nitro-2-(piperidin-1-yl) phenyl) methanimine: X-Ray, DFT, ADMET, Boiled-Egg Model, Druggability, Bioavailabilty, and Human Cyclophilin D (CypD) Inhibitory Activity, *J. Mol. Struct*. 1250 (2022) 131744, https://doi.org/10.1016/j.molstruc.2021.131744.

[11] S. Fleming, A. Mills, T. Tuttle, Predicting the UV–vis spectra of oxazine dyes, Beilstein. *J. Org. Chem*. 7 (2011) 432–441, https://doi.org/10.3762/bjoc.7.56

[12] S. Gunasekaran, E. Sailatha, et al., FTIR, FT Raman spectra and molecular structural confirmation of isoniazid, *Indian J. Pure Appl. Phys.* 47 (2009) 12e18.

[13] P.P. Singh, H.K. Srivastava, F.A. Pasha, DFT-based QSAR study of testosterone and its derivatives, *Bioorg. Med. Chem.* 12 (1) (2004) 171–177, https://doi.org/ 10.1016/j.bmc.2003.11.002.

[14] L. Pauling, The Nature of the Chemical Bond, 3rd ed., Cornell University Press,Ithaca, New York, 1960.

[15] Parr, R.G.; Chattaraj, P.K. *J. Am. Chem. Soc*. 1991, 113,

[16] A.R. Guerroudj, N. Boukabcha, A. Benmohammed, N. Dege e, N. Belkafouf, N. Khelloul, A. Djafri, A. Chouaih, "Synthesis, crystal structure, vibrational spectral investigation, intermolecular interactions, chemical reactivity, NLO properties and molecular docking analysis on (E)-N-(4-nitrobenzylidene)-3-chlorobenzenamine: A combined experimental and theoretical study, *J. Mol. Struct.* 1240 (2021) 130589, https://doi.org/10.1016/j.molstruc.2021.130589.

[17] P. Jaque, A. Toro-Labb´e, Characterization of copper clusters through the use of density functional theory reactivity descriptors, *J. Chem. Phys.* 117 (7) (2002) 3208–3218, https://doi.org/10.1063/1.1493178.

[18] RG Parr, RG. Pearson, *J. Am. Chem. Soc.* 105 (1983) 7512.

[19] RG Parr, L Szentpaly, S Liu, *J. Am. Chem. Soc*. 121 (1999) 1922.

[20] C. Morell, A. Grand, A. Toro-Labb´e, H. Chermette, is hyper-hardness more chemically relevant than expected? *J. Mol. Model.* 19 (7) (2013) 2893–2900, https://doi.org/10.1007/s00894-013 -1778-z.

[21] L.R. Domingo, M.J. Aurell, P. P´erez, R. Contreras, Quantitative characterization of the global electrophilicity power of common diene/dienophile pairs in Diels–Alder reactions, *Tetrahedron.* 58 (22) (2002) 4417–4423, https://doi.org/10.1016/S0040-4020(02)00410-6.

[22] R. Parthasarathi, V. Subramanian, D.R. Roy, P.K. Chattaraj, Electrophilicity index as a possible descriptor of biological activity, *Bioorg. Med. Chem.* 12 (21) (2004) 5533–5543, https://doi.org/10.1016/j.bmc.2004.08.013.

[23] R. Kar, S. Pal, Effect of solvents having different dielectric constants on reactivity: A conceptual DFT approach, *Int. J. Quantum. Chem.* 110 (9) (2010) 1642–1647, https://doi.org/10.1002/qua.22333.

[24] D.R. Roy, Electrophilicity as a possible descriptor for toxicity prediction, *Bioorg.Med. Chem.* 13 (2005) 3405–3412, https://doi.org/10.1016/j.bmc.2005.03.011.

[25] "B. Silvi & A. Savin, Classification of chemical bonds based on topological analysis of electron localization functions *Nature.* 371, 683–686 (1994).

[26] S.Sangeetha Margreat, et al., Synthesis, spectroscopic, quantum computation, electronic, AIM, Wavefunction (ELF, LOL) and Molecular Docking investigation on(E)-1-(2,5-dichlorothiophen-3-yl)-3-(thiophen-2-yl)-2-propen-1-one, *Chem. Data Collect.* 33 (2021) 100701, https://doi.org/10.1016/j.cdc.2021.100701

Chapter V

Structure-Activity Relationship

V.1 Introduction:

This chapter delves into EMBIT's diverse potential by investigating its applications via a multidisciplinary approach. We examine the compound's nonlinear optical (NLO) characteristics, molecular docking interactions, and toxicity profile to determine its potential for technological and biological applications. This combination of research gives a comprehensive grasp of EMBIT's applicability.

Nonlinear optical properties have important implications in the design of materials for photonic and optoelectronic technologies such optical signal processing, telecommunications, and laser systems. This study examined EMBIT's NLO characteristics using quantum chemistry calculations, namely polarizability (α), first and second order hyperpolarizability (β). These properties are important indicators of a compound's capacity to interact with and affect light This chapter investigates EMBIT's potential uses as an efficient material for NLO application due to its promising band gap values assessed in the previous chapter.

a significant focus of this chapter is on EMBIT's potential biomedical applications, assessed through comprehensive molecular docking studies. These simulations were designed to investigate EMBIT's interactions with key biological targets, relevant to specific diseases. The docking analyses provided critical insights into the compound's binding affinities, interaction energies, and the molecular mechanisms underpinning its activity. To complement the evaluation of EMBIT's biological potential, toxicity prediction and ADMET (Absorption, Distribution, Metabolism, Excretion, and Toxicity) analyses were conducted to assess its pharmacokinetic and safety profiles. These analyses are essential in determining the viability of EMBIT as a candidate for therapeutic applications by addressing both its efficacy and safety.

V.2 Nonlinear Optical (NLO) Properties:

Theoretical predictions play a pivotal role in designing materials with specialized properties, particularly by elucidating the relationship between molecular structures and their associated behaviors. Nonlinear optical (NLO) properties, which are closely linked to electronic and vibrational structures, have garnered significant interest due to their critical role in practical applications. These applications include the development of advanced materials and devices, especially in optical technologies for data transmission and storage [1]. The NLO parameters were calculated using the following equations:

$$\mu = \sqrt{\mu_x^2+\mu_y^2+\mu_z^2}$$

$$a = \frac{1}{3} a_{xx} + a_{yy} + a_{zz}$$

$$\beta = [(\beta_{xxx} + \beta_{xyy} + \beta_{xzz})^2 + (\beta_{yyy} + \beta_{yzz} + \beta_{yxx})^2 + (\beta_{zzz} + \beta_{zww} + \beta_{zyy})^2]^{\frac{1}{2}}$$

Kleinman hypothesis [2]

$$\gamma = \frac{1}{5} (\gamma_{xxxx} + \gamma_{yyyy} + \gamma_{zzzz} + 2\gamma_{xxyy} + 2\gamma_{xxzz} + 2\gamma_{yyzz})$$

Table V.1 presents the calculated values for dipole moment, polarizability, and first- and second-order hyperpolarizabilities. The primary dipole moment is oriented along the Z-axis, with the highest magnitude, which provides valuable insights into the electric field's orientation from the acceptor to the donor **[3].** The computed polarizabilities are 219.00 au and 3.2457×10−23esu, with the most significant contribution attributed to α_{ZZ}

The EMBIT compound demonstrates a first-order hyperpolarizability approximately 70 times greater than that of urea, highlighting its strong potential for nonlinear optical (NLO) applications. It has been established that the first-order hyperpolarizability β is influenced by the energy gap, with narrower energy gaps correlating to higher β values, indicating enhanced NLO behavior **[2,4,5]**. The highest computed value for second-order hyperpolarizability was observed along the β_{ZZZ}

This molecule's nonlinear behavior is primarily driven by electron delocalization, as previously examined in the electron localization function studies **[6,7].** Additionally, the π -conjugated structure and non-centrosymmetric geometry of EMBIT contribute significantly further emphasizing its suitability for NLO activity.**[8].** The EMBIT compound also exhibits second-order hyperpolarizability γ of 85.67 esu, suggesting potential microscopic third-order nonlinear

Table V.1 Nonlinear Optical (NLO) Properties of EMBIT by B3LYP /6-311G++(d,p)

Parameters	**B3LYP /6-311G++(d,p)**
Dipole Moment	
μ_x=	0
μ_y=	0
μ_z=	3.39211
μ=	3.39211
Polarizability (0,0)	
α_{xx}=	236
α_{yy}=	360.89

α_{zz}=	489
α=(au)	219.00
α x 10^{-23} (esu)	3.2457
First Order Hyperpolarizability (0,0,0)	
β_{xxx}=	173.357
β_{yxx}=	-152.913
β_{xyy}=	119.698
β_{yyy}=	-357.367
β_{zxx}=	42.4962
β_{yxz}=	130.965
β_{zyy}=	152.339
β_{xzz}=	146.257
β_{yzz}=	493.156
β zzz=	1635.24
‹β›= a.u	1882.143327
‹β›x 10^{-29} (esu)	1.6260
Second Order Hyperpolarizability (0,0,0,0)	
γ_{xxxx}	29
γ_{xxyx}	-4.47735
γ_{xxyy}	14.0911
γ_{yxyy}	-3.76667
γ_{yyyy}	58.0324
γ_{xxzx}	7.07311
γ_{xxzy}	-1.84435
γ_{yxzy}	4.80328
γ_{yyzy}	6.69158
γ_{xxzz}	25.7173
γ_{yxzz}	-10.8184
γ_{yyzz}	45.1207
γ_{zxzz}	28.5918
γ_{zyzz}	-16.6478
γ_{zzzz}	171.398
‹γ›= esu	85.67944

V.3 biolgical activity :

V.3.1 Molecular Docking :

Glaucoma is a prevalent eye disease that, if undiagnosed or untreated, can lead to irreversible vision loss. It is primarily associated with increased intraocular pressure (IOP), which causes optic nerve damage and visual field loss. While elevated IOP is not always diagnostic of glaucoma, it is a major risk factor and a causal component in glaucomatous optic neuropathy [9]. Glaucoma ranks as the primary reason for vision impairment in the United States and other developed countries. [10,11].

Rho-associated protein kinase ROCK inhibitors have emerged as promising therapeutic agents for glaucoma due to their ability to reduce IOP, enhance ocular blood flow, suppress postoperative scarring, and promote retinal ganglion cell survival and axon regeneration [12]. Among these, the proteins ROCK1 and ROCK2 play crucial roles in cellular functions such as cytoskeletal structure maintenance, cell adhesion, and contractility regulation. Their dysfunction is linked to elevated IOP and subsequent optic nerve damage [13].

Using the Prediction of Activity Spectra of Substances (PASS) tool, we assessed the activity spectrum of EMBIT. Table V.2 highlights the PASS prediction results, indicating promising ophthalmic activity with a probable activity (Pa) score of 0.64. Based on these findings, molecular docking was conducted to investigate EMBIT's inhibition potential against ROCK1 and ROCK2. The receptor protein crystal structures were obtained from the RCSB database, with the corresponding PDB IDs referenced as 2ESM and 7JNT respectively [14]. Table V.4 provides a detailed summary of the binding interactions between the EMBIT ligand and both ROCK1 and ROCK2 proteins, including binding affinity and inhibition constants.

Rho kinase ROCK 1:

The binding interaction results enlisted in Table V.3 and visualized **in** Fig.V.1.a of EMBIT with ROCK1 reveals a binding energy of -7.4 kcal/mol and an inhibition constant (Ki) of 1.91 µM. the hydrogen bonding surface of ROCK 2 with EMBIT risidues is displayed in Fig.V.2.a Key molecular interactions include one conventional hydrogen bond between the ARG58 residue and the S1 atom at bond length of 3.06 Å and a carbon-hydrogen bond between the SER118 residue and the C20 carbon at a bond length of 3.56 Å. Additionally, electrostatic Pi-Anion interactions occur between the GLU24 residue and the C6H4 and C3N2 rings, with bond lengths of 4.28 Å and 4.65 Å, respectively. Hydrophobic interactions include multiple Pi-Pi Stacked bonds with the TRP122 residue, involving the C6H4 ring, C3N2 ring, and C3N1S1 groups, with bond lengths ranging from 3.63 Å to 5.62 Å. A Pi-Alkyl interaction is also observed between ARG58 and the C3N1S1H1 group at a bond length of 4.89 Å. These interactions highlight the moderate binding affinity of EMBIT with ROCK1, supported by detailed visualizations in Figures 11 and 12 and interaction characteristics in Table V.4

Rho kinase ROCK 2:

In contrast, EMBIT exhibits superior binding affinity with ROCK2, With a binding energy of -8.7 kcal/mol and a reduced inhibition constant (Ki) of 0.97 µM. This enhanced affinity is credited to two conventional hydrogen bonds: one between the LYS224 residue and the S1 atom (bond length: 2.86 Å), and another between the LYS229 residue and the O1 atom (bond length: 2.87 Å) the hydrogen bonding surface is displayed in **Fig.V.2. b.** Electrostatic Pi-Anion interactions are observed with the GLU170 residue, involving the C3N2 ring, C3S1N1 ring, and C3S1N1H1 group (bond lengths: 4.05 Å, 3.62 Å, and 4.10 Å, respectively). Hydrophobic interactions include a Pi-Sigma bond between LYS224 and the C6H4 group (bond length: 3.70 Å) and a Pi-Sulfur bond between PHE156 and the S3 group (bond length: 5.36 Å). A Pi-Donor is also present between HIS225 and the S1 atom (bond length: 4.10 Å). These interactions significantly contribute to the stronger inhibitory potential of EMBIT with ROCK2, as detailed in **Table V.4** and displayed in **Fig.V.1.b**

Table V.2 Pass activity prediction prediction of EMBIT

Pa	Pi	Activity
0,640	0,005	Ophthalmic drug
0,601	0,001	Prostaglandin-E2 synthase 1 inhibitor
0,568	0,004	Amyloid beta precursor protein antagonist
0,539	0,005	Antiglaucomic
0,536	0,039	Insulysin inhibitor
0,455	0,016	Rheumatoid arthritis treatment
0,432	0,005	Dual specificity phosphatase inhibitor
0,435	0,011	Mcl-1 antagonist
0,363	0,009	Calcium channel N-type blocker
0,377	0,028	PfA-M1 aminopeptidase inhibitor

Table V.3 Binding Affinity and Inhibition Constant of EMBIT Against ROCK1 and ROCK2

Compound	Binding affinity (kcal/mol)	Inhibition constant (µm)
ROCK1	-7.4	1.91
ROCK 2	-8.2	0.97

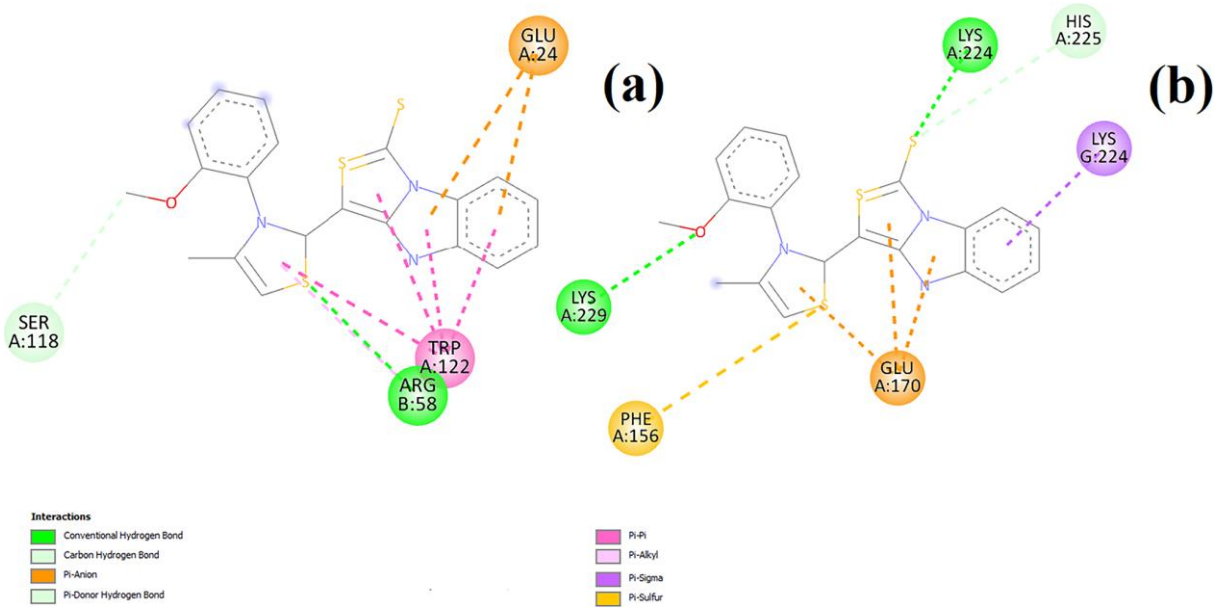

Fig.V.1 2D Diagrams Depicting Receptor-Ligand Interactionsa) Interaction with ROCK1b) Interaction with ROCK2

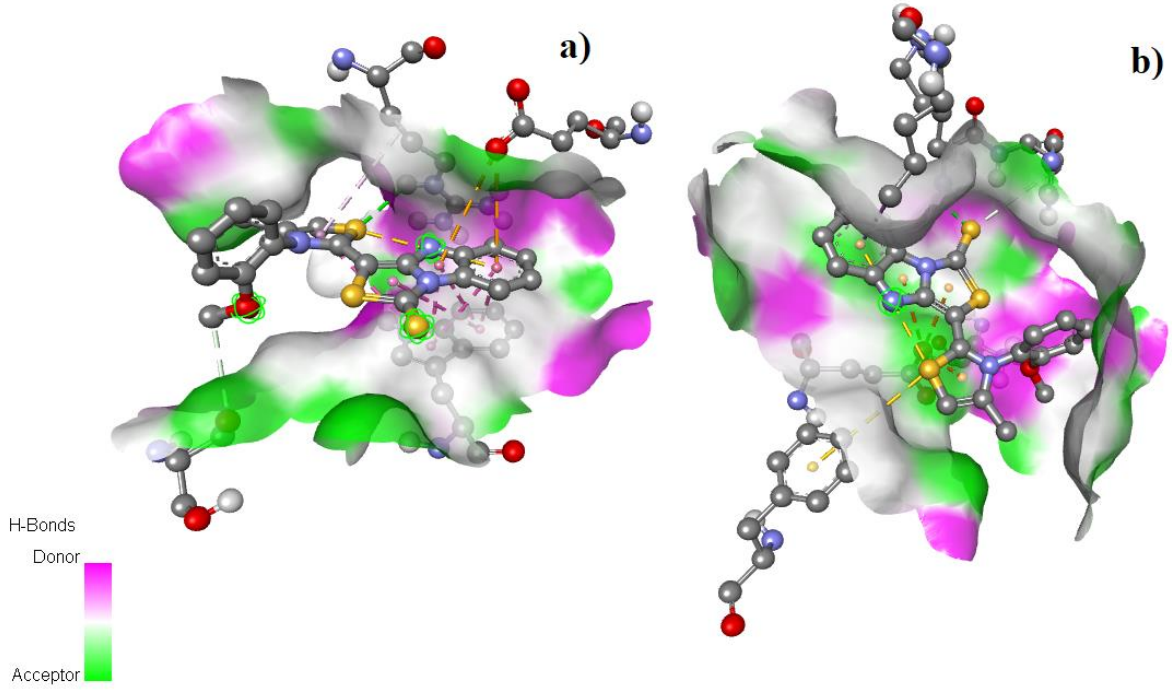

Fig .V.2 The hydrogen bonding interaction surface a) ROCK1 b)ROCK

Table V.4 Detailed Interaction Profile of EMBIT with ROCK1 and ROCK2 Proteins

Protein	Residue	Compound	Atom/group of compounds	Category	Types	Distance (Å)
ROCK 1	ARG58	(E)-3-(3-(2-methoxyphenyl)-4-methylthiazol-2(3H)-ylidene) benzo[4,5]imidazo[1,2-c]thiazole-1(3H)-thione	S1	Hydrogen Bond	Conventional Hydrogen Bond	3,06448
	SER118		C20	Hydrogen Bond	Carbon Hydrogen Bond	3,56487
	GLU24		C6H4 Ring	Electrostatic	Pi-Anion	4,2843
	GLU24		C3N2 Ring	Electrostatic	Pi-Anion	4,65708
	TRP122		C6H4 Ring	Hydrophobic	Pi-Pi Stacked	4,26705
	TRP122		C3N2 Ring	Hydrophobic	Pi-Pi Stacked	3,63532
	TRP122		C3N1S1	Hydrophobic	Pi-Pi Stacked	3,84114
	TRP122		C3N1S1H1	Hydrophobic	Pi-Pi Stacked	5,62537
	TRP122		C6H4 Ring	Hydrophobic	Pi-Pi Stacked	3,75098
	TRP122		C3N2 Ring	Hydrophobic	Pi-Pi Stacked	4,07374
	TRP122		C3N1S1	Hydrophobic	Pi-Pi Stacked	5,0854
	ARG58		C3N1S1H1	Hydrophobic	Pi-Alkyl	4,89729
ROCK 2	LYS224		S1	Hydrogen Bond	Conventional Hydrogen Bond	2,8648
	LYS229:		O1	Hydrogen Bond	Conventional Hydrogen Bond	2,87404
	GLU170		C3N2 Ring	Electrostatic	Pi-Anion	4,05017
	GLU170		C3S1N1 Ring	Electrostatic	Pi-Anion	3,62174
	GLU170		C3S1N1H1	Electrostatic	Pi-Anion	4,10376
	HIS225		S1	Hydrogen Bond	Pi-Donor Hydrogen Bond	4,10387
	LYS224		C6H4	Hydrophobic	Pi-Sigma	3,70175
	PHE156		S3	Other	Pi-Sulfur	5,36947

V.3.2 Toxicity prediction:

EMBIT with the formula $C_{20}H_{15}N_3OS_3$ and a molecular weight of 409.55 g/mol, underwent analysis using the SwissADME online tool, The compound adheres to Lipinski's rule of five, indicating potential oral bioavailability, and meets Veber and Egan criteria, supporting favorable pharmacokinetics, However, its classification as poorly soluble and low gastrointestinal absorption hinder its bioavailability. The compound is not blood-brain barrier permeant and is not a P-gp substrate, Additionally, EMBIT inhibits multiple cytochrome P450 enzymes (CYP1A2, CYP2C19, CYP2C9, and CYP3A4), indicating a high potential for drug-drug interactions. Despite a moderate bioavailability score (0.55), violations of Ghose and Muegge criteria due to molecular weight and lipophilicity highlight the need for structural optimization to enhance its drug-likeness and pharmacokinetic profile. The skin permeation of Embit, as indicated by the SwissADME analysis, is represented by a log Kp value of -5.05 cm/s, suggesting extremely low permeability through the skin. depicts the bioavailability radar and the BOILED-EGG model the position of EMBIT dot indicates negative blood-brain barrier (BBB) penetration and gastrointestinal (GI) absorption characteristics, and a negative P-GP.

Based on the ADMET investigation the EMBIT highlighted both promising drug-like characteristics and notable challenges and the need for further futur optimization of the compound so we further analysed F-EMBIT's fluorinated ($C_{20}H_{16}FN_3OS_2$) and Cl-EMBIT chlorinated ($C_{20}H_{16}ClN_3OS_2$) derivatives, the results highlight notable differences in their drug-like properties. While all three compounds exhibit poor solubility and low skin permeability, the derivatives show improved gastrointestinal absorption (classified as high) compared to EMBIT (low). Lipophilicity is reduced in the fluorinated (log $P_{o/w}$ 4.20) and chlorinated derivatives (4.31) relative to EMBIT (4.88), potentially enhancing their pharmacokinetics. All compounds satisfy Lipinski's rule of five and exhibit no PAINS alerts, but only the derivatives meet the Ghose criterion, reflecting better overall drug-like properties. However, the derivatives also display slightly reduced solubility and increased synthetic complexity compared to EMBIT. Additionally, all three compounds inhibit CYP1A2, CYP2C19, CYP2C9, and CYP3A4 enzymes, indicating a similar risk of drug-drug interactions. Overall, the derivatives appear to have advantages in absorption and lipophilicity, making them more suitable for further optimization, although their solubility remains a challenge. The excretion profile of EMBIT and its derivatives reveals notable differences. EMBIT exhibits low clearance 4.528 ml/min/ with an ultra-short half-life 0.459 hours indicating slower elimination and potential accumulation. In contrast, F-EMBIT and CL-EMBIT display moderate clearance 6.562 ml/min/kg and 6.156 ml/min/kg, respectively) and slightly shorter half-lives 0.306 and

0.359 hours suggesting faster excretion. Toxicity analysis shows that the derivatives have negligible eye corrosion potential 0.00 and lower eye irritation probability F-EMBIT: 0.256 Cl-EMBIT: 0.318 compared to EMBIT 0.508 indicating improved safety profiles.

In summary, the analysis of EMBIT and its derivatives (F-EMBIT and Cl-EMBIT) highlights promising drug-like properties alongside key challenges. While EMBIT meets basic drug-likeness criteria, its poor gastrointestinal absorption, low solubility, and CYP enzyme inhibition limit its potential. The derivatives show improved absorption, reduced lipophilicity, and better excretion profiles, with moderate clearance and shorter half-lives compared to EMBIT. Additionally, they exhibit lower eye irritation and corrosion risks, enhancing safety. However, poor solubility and persistent CYP inhibition remain obstacles, requiring further optimization to improve their pharmacokinetic and safety profiles.

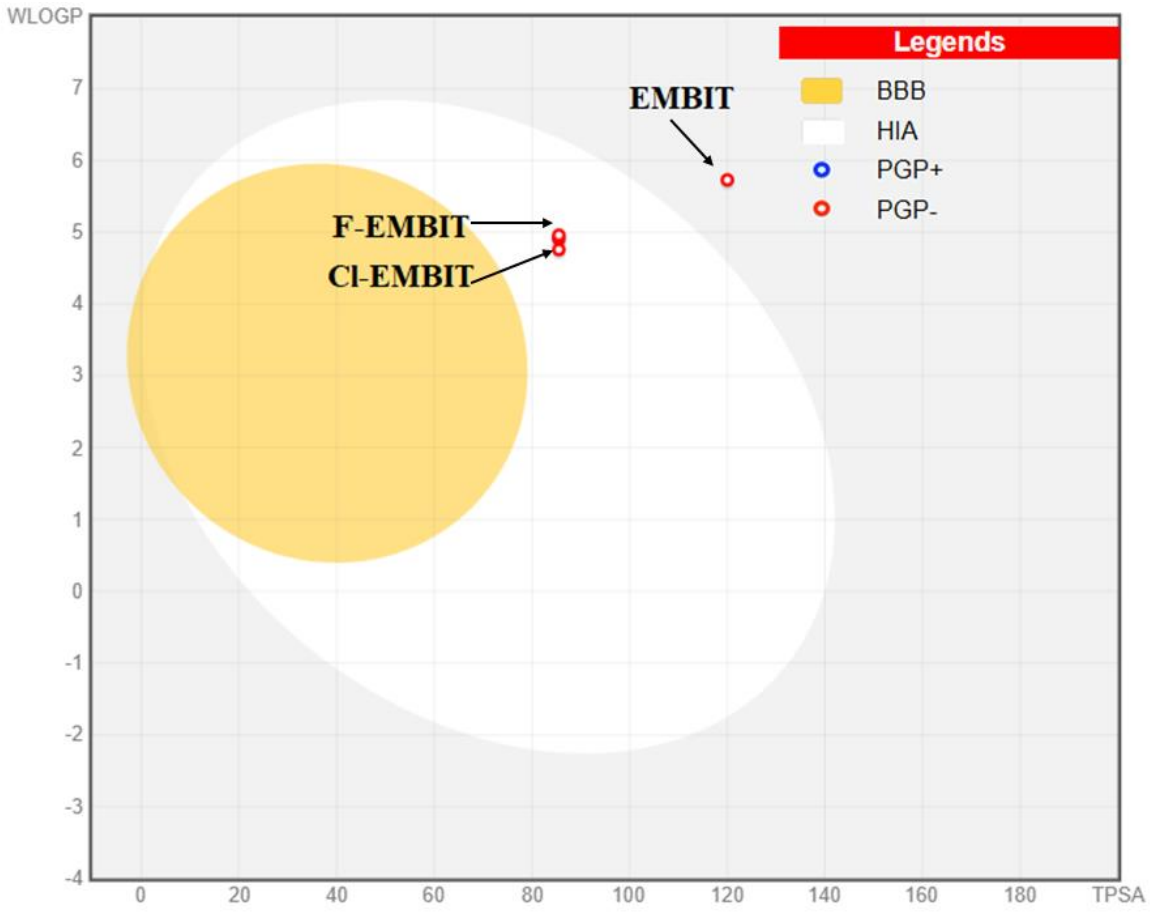

Fig.V.3 EMBIT and its derivated F-EMBIT and Cl-EMBIT BOILED-EGG Diagram

Table V.5 Comparative Radar View of Pharmacokinetics, Druglikeness, and Toxicity Profiles for EMBIT and Its Derivatives (Fluorinated and Chlorinated)

Radar view	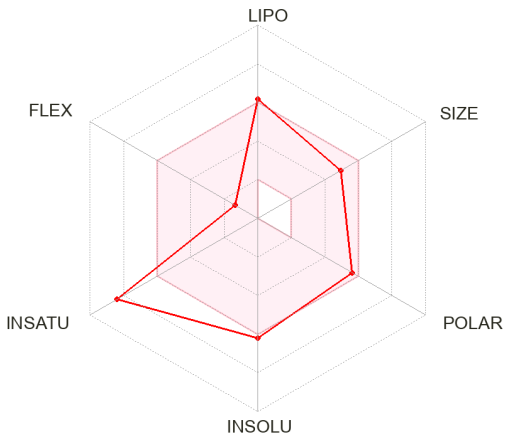	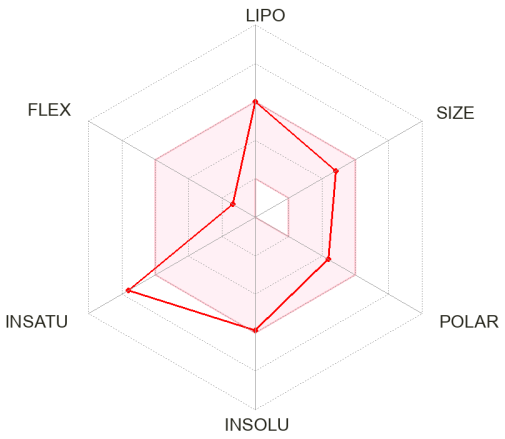	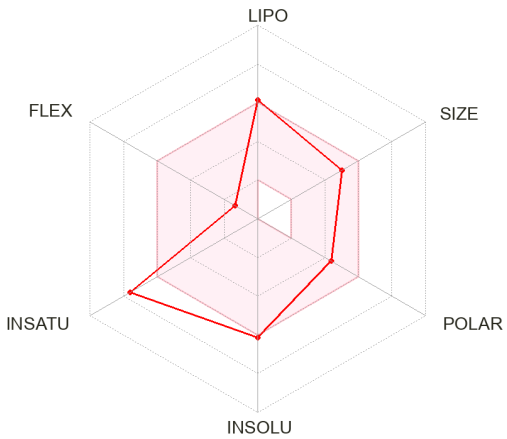
Structure	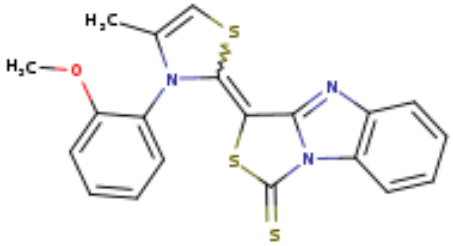	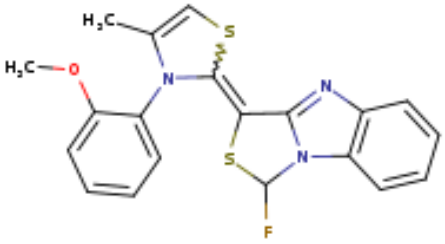	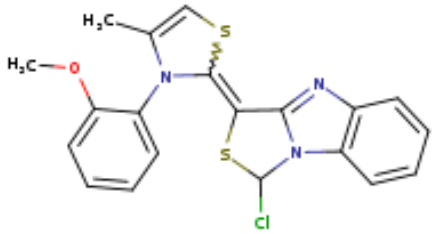
Formula	$C_{20}H_{15}N_3OS_3$	$C_{20}H_{16}FN_3OS_2$	$C_{20}H_{16}ClN_3OS_2$
Molecular weight	409.55 g/mol	397.49 g/mol	413.94 g/mol

Lipophilicity			
Consensus Log $P_{o/w}$	4.88	4.20	4.31
Solubility			
Log S	-6.20	-6.33	-6.65
Solubility	$2.56x10^{-4}$ mg/ml	1.86 x10-4 mg/ml	9.25 x10-4 mg/ml
Class	Poorly soluble	Poorly soluble	Poorly soluble
Pharmacokinetics			
Gastrointestinal absorption	Low	High	High
BBB permeant	No	No	No
P-gp substrate	No	no	no
CYP1A2 inhibitor	Yes	yes	yes
CYP2C19 inhibitor	Yes	yes	yes
CYP2C9 inhibitor	Yes	yes	yes
CYP2D6 inhibitor	No	no	no
CYP3A4 inhibitor	Yes	yes	yes
Log Kp (skin permeation)	-5.05 cm/s	-5.17 cm/s	-5.10 cm/s
Druglikeness			
lipinski	Yes	Yes	yes
Ghose	No	yes	yes

Veber	Yes	yes	yes
Egan	Yes	yes	yes
Muegge	No	No	no
Bioavailability Score	0.55	0.55	0.55
Medicinal Chemistry			
PAINS	0 alert	0 alert	0 alert
Brenk	1 alert: thiocarbonyl_group	0 alert	
Leadlikeness	No; 2 violations: MW>350, XLOGP3>3.5	No; 2 violations: MW>350, XLOGP3>3.5	No; 2 violations: MW>350, XLOGP3>3.5
Synthetic accessibility	3.73	4.47	4.44
exceretion			
CLplasma (ml/min/kg)	4.528 (low clearance)	6.562 (moderate clearance)	6.156(moderate clearance)
$T_{1/2}$ (hours)	0.459 (ultra-short half-life)	0.306 (ultra-short half-life)	0.359 (ultra-short half-life)
Toxicity			
Eye corrosion probability	0.001	0.0	0.0
eye irritation probability	0.508	0.256	0.318

V.4 Conclusion:

This chapter comprehensively explored the properties of EMBIT, focusing on its nonlinear optical (NLO) behavior, biological activity, and toxicity predictions. The NLO studies revealed EMBIT's strong potential for optical applications, driven by its electron delocalization and π-conjugated structure. The compound exhibited significant first- and second-order hyperpolarizabilities, highlighting its suitability for NLO-related devices.

Biologically, EMBIT demonstrated promising activity against key glaucoma-related targets, ROCK1 and ROCK2, based on molecular docking studies. The compound showed moderate binding affinity for ROCK1 and a stronger affinity for ROCK2, suggesting its potential as a therapeutic agent for glaucoma by inhibiting ROCK 2. These findings were further supported by a thorough study of EMBIT's bond interactions with the target. notably strong H-bonds which are crucial bonds in bioactivity.

Toxicity and pharmacokinetic predictions indicated some challenges for EMBIT in terms of solubility, gastrointestinal absorption, and skin permeability. While the compound adhered to Lipinski's rule and demonstrated favorable pharmacokinetic properties in some aspects, its limitations, such as low bioavailability and CYP enzyme inhibition, highlighted the need for structural optimization. The analysis of EMBIT derivatives fluorinated EMBIT: F-EMBIT and chlorinated EMBIT: Cl-EMBIT provided valuable insights, showing improved gastrointestinal absorption and reduced lipophilicity, thus enhancing their potential for further development further optimization to address its pharmacokinetic limitations. Structural modifications could improve solubility, absorption, and safety profiles, provide a valuable research contribution and pave the way for the development of more efficient therapeutic agents and advanced materials in optical technologies.

References:

[1] F.J. Luque, J.M. Lopez, M. Orozco, Perspective on "Electrostatic interactions of a solute with a continuum. A direct utilization of ab initio molecular potentials for the prevision of solvent effects, *Theor Chem. Acc.* 103 (2000) 343, https://doi.org/10.1007/s002149900013. [2] D.A. Kleinman, Nonlinear Dielectric Polarization in Optical Media, Physical Review 126 (6) (1962) 1977–1979, https://doi.org/10.1103/PhysRev.126.1977.

[3] N. Boukabcha, et al., Spectral investigation, TD-DFT study, Hirshfeld surface analysis, NCI-RDG, HOMO-LUMO, chemical reactivity and NLO properties of 1-(4-fluorobenzyl)-5-

bromolindolin-2,3dione, J. Mol. Struct. 1285 (2023) 135492 https://doi.org/10.1016/j.molstruc.2023.135492.

[4] M.G. Papadopoulos, A.J. Sadlej, J. Leszczynski (Eds.), Non-Linear Optical Properties of Matter, vol. 1, Springer Netherlands, *Dordrecht*:, 2006, https://doi.org/10.1007/1-4020-4850-5.

[5] N. Benhalima, et al., Solvent Effects on Molecular Structure, Vibrational Frequencies, and NLO Properties of N-(2,3-Dichlorophenyl)-2-Nitrobenzene–Sulfonamide: a Density Functional Theory Study, *Braz. J.* Phys. 46(4) (2016) 371–383, https://doi.org/10.1007/s13538-016-0419-2.

[6] S.M. Risser, D.N. Beratan, S.R. Marder, Structure-function relationships for .beta.,the first molecular hyperpolarizability, *J. Am. Chem. Soc.* 115 (17) (1993)7719–7728, https://doi.org/10.1021/ja00070a016.

[7] A. Mansour, et al., Experimental and theoretical spectroscopic characterization, Hirshfield surface analysis, TD-DFT calculation, and nonlinear optical properties of (E)-1-[(2,4,6tribromophenyl)diazenyl]-naphthalen-2-ol azo dye, *J. Mol. Struct.* 1261 (2022) 132887, https://doi.org/10.1016/j.molstruc.2022.132887.

[8] K.K. Jha, S. Dutta, P. Munshi, Concomitance, Reversibility, and Switching Ability of Centrosymmetric and Non-Centrosymmetric Crystal Forms: Polymorphism in an Organic Nonlinear Optical Material, *Cryst. Growth Des.* 18 (2) (2018) 1126–1135, https://doi.org/10.1021/acs.cgd.7b01560.

[9] D.A. Lee, E.J. Higginbotham, Glaucoma and its treatment: A review, Am. J. Health- Syst. Pharmacy 62 (7) (2005) 691–699, https://doi.org/10.1093/ajhp/62.7.691.

[10] U.S. Department of Health, Education, and Welfare. Statistics on Blindness in the Model Reporting area, 1969–70, Government Printing Office, Washington, D.C.: U. S, 1973. DHEW publication no. NIH 73-427.

[11] American Academy of Ophthalmology Quality of Care Committee Glaucoma Panel, Primary Open-Angle Glaucoma, American Academy of Ophthalmology, San Francisco, 1996, p. 2.

[12] R. Chang, S. Wang, An emerging treatment option for glaucoma: Rho kinase inhibitors, Clin. Ophthalmol. (2014) 883, https://doi.org/10.2147/OPTH.S41000.

[13] J. Wang, X. Liu, Y. Zhong, Rho/Rho-associated kinase pathway in glaucoma (Review), Int. J. Oncol. 43 (5) (2013) 1357–1367, https://doi.org/10.3892/ijo.2013.2100.

[14] Bodea, F.; Bungau, S.G.;Negru, A.P.; Radu, A.; Tarce, A.G.;Tit, D.M.; Bungau, A.F.; Bustea, C.;Behl, T.; Radu, A.-F. Exploring New Therapeutic Avenues for Ophthalmic Disorders: Glaucoma-Related Molecular Docking Evaluation and Bibliometric Analysis for Improved Management of Ocular Diseases.Bioengineering 2023, 10, 983. https://doi.org/10.3390/bioengineering10080983.

Conclusion

General conclusion

The examination of the noteworthy compound EMBIT, offers a comprehensive exploration of its synthesis, structural characterization, electronic properties, and potential applications in various fields, including nonlinear optics and biomedical research.

The foundational significance of thiazoles as a class of heterocyclic compounds was established, highlighting their versatile chemical and biological properties, including applications in NLO materials and pharmaceuticals, underscoring the relevance of compounds like EMBIT. Essential techniques for determining molecular structures, such as X-ray diffraction and computational methods like Density Functional Theory (DFT), provided the framework for accurately determining EMBIT's structure.

The synthesis and characterization of EMBIT were explored using techniques like X-ray diffraction, infrared and NMR spectroscopy, and DFT calculations. These analyses provided a detailed understanding of EMBIT's three-dimensional structure, validating its integrity and stability, which laid the groundwork for further exploration of its properties through theoretical molecular modeling that confirmed the experimental data.

The compound's electronic structure was examined, revealing significant polarization, intramolecular charge transfer, and reactivity. Studies of molecular electrostatic potential, frontier molecular orbitals, and other computational models suggested EMBIT's suitability for non-linear optical applications and highlighted its high reactivity, positioning it as a promising candidate for advanced material science and biotechnology.

Finally, the insights gained emphasized EMBIT's potential in NLO applications, its biological activity against glaucoma-related targets (ROCK1 and ROCK2), and its toxicity and pharmacokinetic profiles. While EMBIT showed promise as a therapeutic agent, its pharmacokinetic limitations, such as low bioavailability and solubility, suggested the need for structural optimization. The ADMET analysis of EMBIT derivatives, such as fluorinated and chlorinated EMBIT, offered a pathway for addressing these challenges, suggesting EMBIT's potential for future optimization for therapeutic applications.

Overall, this study presents EMBIT as a versatile compound with significant promise across multiple domains. Its combination of stability, reactivity, and unique electronic features makes it a valuable candidate for both pharmaceutical and materials research. Future work focusing on optimizing its pharmacokinetic properties and exploring its broader applications could pave

the way for the development of more efficient therapeutic agents and advanced materials in optical technologies.

Abstract:

This thesis investigates the synthesis, structural characterization, and potential applications of EMBIT (E)-3-(3-(2-Methoxyphenyl)-4-Methylthiazol-2(3H)-ylidene) Benzo[4,5]imidazole[1,2-c]thiazole-1(3H)-thione, a novel compound with promising nonlinear optical (NLO) and therapeutic properties. The research begins with a review of thiazole derivatives, emphasizing their role in pharmaceuticals, agrochemicals, and NLO materials, as well as their diverse biological activities. Experimental and theoretical techniques, particularly X-ray diffraction and quantum mechanical methods, were employed to determine the molecular structure of EMBIT. The synthesis of EMBIT was thoroughly characterized using X-ray diffraction, NMR, IR spectroscopy, and Density Functional Theory (DFT) calculations, confirming its molecular properties. Computational analysis revealed EMBIT's electronic structure, reactivity, and potential for NLO applications, highlighting its high polarizability and reactivity, making it a promising candidate for future material science and optical technologies. Further investigations into EMBIT's NLO behavior, biological activity against glaucoma-related targets, and pharmacokinetic predictions were conducted. The compound demonstrated significant first- and second-order hyperpolarizabilities and promising bioactivity, particularly in inhibiting ROCK2, suggesting its therapeutic potential. Despite pharmacokinetic challenges, EMBIT and its derivatives present a strong foundation for optimization, paving the way for future research in advanced materials and biotechnology.

Resumé:

Cette thèse porte sur la synthèse, la caractérisation structurelle et les applications potentielles de l'EMBIT (E)-3-(3-(2-méthoxyphényl) -4-méthylthiazol-2(3H)-ylidene) benzo[4,5]imidazole[1,2-c]thiazole-1(3H)-thione, un nouveau composé prometteur à optique non linéaire (NLO) et propriétés thérapeutiques. La recherche commence par un examen des dérivés thiazolés, en mettant l'accent sur leur rôle dans les produits pharmaceutiques, les produits agrochimiques et les matériaux NLO, ainsi que sur leurs diverses activités biologiques. Des techniques expérimentales et théoriques, en particulier la diffraction des rayons X et les méthodes de mécanique quantique, ont été utilisées pour déterminer la structure moléculaire d'EMBIT. La synthèse de l'EMBIT a été complètement caractérisée par diffraction aux rayons X, RMN, spectroscopie IR et calculs de théorie fonctionnelle de densité (DFT), confirmant ses propriétés moléculaires. L'analyse informatique a révélé la structure électronique, la réactivité et le potentiel d'EMBIT pour les applications NLO, mettant en évidence sa haute polarisabilité et réactivité, ce qui en fait un candidat prometteur pour les futures sciences des matériaux et

technologies optiques. D'autres investigations sur le comportement de NLO d'EMBIT, l'activité biologique contre les cibles liées au glaucome, et les prévisions pharmacocinétiques ont été menées. Le composé a démontré des capacités d'hyperpolarisation de premier et deuxième ordre significatives et une bioactivité prometteuse, en particulier dans l'inhibition de ROCK2, suggérant son potentiel thérapeutique. Malgré les défis pharmacocinétiques, EMBIT et ses dérivés constituent une base solide pour l'optimisation, ouvrant la voie à de futures recherches en matière de matériaux avancés et de biotechnologie.

ملخص

تستكشف هذه الأطروحة تخليق مركب-3)-3-(E) EMBIT (2-ميثوكسي فينيل)-4-ميثيل ثيازول-2-(3H)يلدين (بنزو[4,5]إيميدازول[1,2-c]ثيازول-1-(3H)ثيون، وهو مركب جديد ذو خصائص واعدة في البصريات غير الخطية (NLO)والنشاطات العلاجية. تبدأ الدراسة بمراجعة لمشتقات الثيازول، مع التركيز على دورها في الأدوية، والمبيدات الكيميائية، والمواد ذات البصريات غير الخطية، فضلاً عن أنشطتها البيولوجية المتنوعة. تم استخدام تقنيات تجريبية ونظرية، لا سيما حيود الأشعة السينية والطرق الميكانيكية الكمومية، لتحديد البنية الجزيئية لـ .EMBIT تم تخليق EMBIT وتحديده بعناية باستخدام حيود الأشعة السينية، والرنين المغناطيسي النووي(NMR) ، والأشعة تحت الحمراء(IR) ، وحسابات نظرية الكثافة الوظيفية(DFT) ، مما أكد خصائصه الجزيئية. كشفت التحليلات الحسابية عن البنية الإلكترونية لـEMBIT ، وتفاعليته، وإمكاناته في التطبيقات البصرية غير الخطية، مما يبرز قطبيته العالية وتفاعليته، مما يجعله مرشحاً واعداً للمواد العلمية المستقبلية وتقنيات البصريات. تم إجراء مزيد من التحقيقات في سلوك EMBIT في البصريات غير الخطية، والنشاط البيولوجي ضد أهداف مرتبطة بالجلوكوما، وتوقعات السمية والدوائية. أظهر المركب قابلية تفاعل من الدرجة الأولى والثانية كبيرة، ونشاطاً بيولوجياً واعداً، خاصة في تثبيطROCK2 ، مما يشير إلى إمكاناته العلاجية. على الرغم من التحديات في السمية والدوائية، فإن EMBIT ومشتقاته تمثل أساساً قوياً للتحسين، مما يمهد الطريق لمزيد من البحث في المواد المتقدمة وعلم الأحياء.

Journal of Molecular Structure 1318 (2024) 139157

Contents lists available at ScienceDirect

Journal of Molecular Structure

journal homepage: www.elsevier.com/locate/molstr

Synthesis, molecular structure, Hirshfeld surface analysis, NCI-RDG, spectral characterization analysis, nonlinear optical properties, and in silico molecular docking of (E)-3-(3-(2-methoxyphenyl)-4-methylthiazol-2 (3H)-ylidene) benzo[4,5] imidazo [1,2-c] thiazole-1(3H)-thione

Sabrina Smati [a], Ahmed Djafri [a,d], Karima Menad [a], Nourdine Boukabcha [a,e,*], Rachida Rahmani [a,g], Meriem Goudjil [h], Youcef Megrouss [a,e], Hafsa Khaldi [b,c], Necmi Dege [f], Abdelkader Chouaih [a], Ayada Djafri [b]

[a] Laboratory of Technology and Solid Properties (LTPS), Faculty of Sciences and Technology, Abdelhamid Ibn Badis University of Mostaganem, Mostaganem 27000, Algeria
[b] Laboratory of Organic Applied Synthesis (LSOA), Department of Chemistry, Faculty of Sciences, University of Oran 1, Ahmed Ben Bella 31000 Oran, Algeria
[c] Chemistry Department, Faculty of Exact Sciences and Informatics, Abdelhamid Ibn Badis University of Mostaganem, Mostaganem 27000, Algeria
[d] Centre de Recherche Scientifique et Technique en Analyses Physico-chimiques (CRAPC), BP 384 Bou-Ismail-RP 42004, Tipaza, Algeria
[e] Chemistry Department, Faculty of Exact Sciences and Informatics, Hassiba Benbouali University, Chlef 02000, Algeria
[f] Department of Physics, Ondokuz Mayis University Samsun, 54187, Samsun, Turkey
[g] Department of Process Engineering, Faculty of Sciences and Technology, Ahmed Zabana - University of Relizane, Relizane, Algeria
[h] Department of Earth Sciences, University of Florence, Via Giorgio La Pira 4, Florence 50121, FI, Italy

ARTICLE INFO

Keywords:
EMBIT
DFT
XRD
molecular docking
biological activity

ABSTRACT

(E)-3-(3-(2-methoxyphenyl)-4-methylthiazol-2(3H)-ylidene) benzo[4,5] imidazo [1,2-c] thiazole-1(3H)-thione (EMBIT) was synthesized and studied thoroughly by means of X-ray diffraction and molecular modeling. In this study, geometrical analysis together with FT-IR, NMR, and UV-Vis characterizations were performed. Using density functional theory and the B3LYP/6–311G++(d,p) set, geometric parameters accurately represent the structure, showing agreement between experimental and theoretical results. Various solvents were included in the calculations of the UV–Vis spectra, frontier molecular orbitals (FMOs), and global chemical reactivity descriptors (GCRD) calculations, revealing their potential for better prediction of energy gap values. The energy gap and some chemical descriptors analysis of the title compound indicated that it would be suitable for nonlinear optical properties and biological activity. Non-covalent bond interaction studies were conducted on EMBIT to investigate the intermolecular interactions. A deeper understanding of the electronic structure and chemical bonding patterns of the structure was gained by LOL and ELF studies.

The computed polarizabilities and hyperpolarizabilities indicated that the molecule has non-linear optical properties and assessed the influence of the energetic gap values and electron delocalization character on enhancing NLO proprieties. The predictions of EMBIT's biological activity suggested potential as a cure for glaucoma, and molecular docking revealed the various bonds involved against two potential critical glaucoma factors Rock1 and Rock2. Rock2 is found to have a superior binding affinity, as evidenced by its highest binding energy of -8.7 kcal/mol and a lower Ki inhibition constant of 0.97. The EMBIT ligand's effectiveness in inhibiting the Rock2 protein is highly likely, as suggested by this.

1. Introduction

Over the past decade, there has been a notable interest in heterocyclic compounds owing to their promising therapeutic applications. Among this class of compounds, thiazole derivatives have been regarded as particularly noteworthy [1–4], possessing a remarkable variety of biological functions [5]. These versatile compounds exhibit a wide spectrum of beneficial properties, demonstrating a proven efficiency as

* Corresponding author.
E-mail addresses: n.boukabcha@gmail.com (N. Boukabcha), meriem.goudjil@unifi.it (M. Goudjil).

https://doi.org/10.1016/j.molstruc.2024.139157
Received 31 March 2024; Received in revised form 8 June 2024; Accepted 26 June 2024
Available online 28 June 2024

antioxidants [6], antibacterials [7], anticancer agents [8], and anti-inflammatory [9].

Our current study highlights the significant therapeutic potential of the heterocyclic rings present in the compound under investigation, including thiazole [10], imidazole [11], and benzimidazole [12] moieties. The rising interest in these compounds further underscores their potential in medicinal chemistry. Notably, the biological activities of these compounds are greatly influenced by the synergistic effects of their diverse heterocyclic moieties, adding complexity and appeal to our research [5]. These novel combinations yield bioactive compounds with enhanced therapeutic potential. The exploration of thiazole based structures, especially in conjunction with diverse heterocyclic moieties, has opened up new avenues in drug discovery and development, contributing significantly to the ongoing efforts in the field of medicinal chemistry. Moreover, studies have demonstrated that asymmetrical thiazole derivatives can enhance non-linear optical properties (NLO), exhibiting significant second harmonic generation (SHG) values that make them suitable for technological and industrial applications in electronic and optical materials [13,14].

The newly created molecule, EMBIT, was first examined by means of single-crystal X-ray diffraction (SC-XRD). Followed by an experimental spectroscopic study from infrared spectroscopy (IR), and nuclear magnetic resonance (NMR) analysis. Further investigation was conducted into its properties through molecular docking simulations, local orbital locator (LOL), electron localization function (ELF), reduced density gradient (RDG), Hirshfeld surface analysis, and nonlinear optical (NLO) properties. The combined results provided a thorough summary of the intermolecular interactions, electrical structure, and chemical activity of EMBIT.

The experimental characterizations were complemented by a theoretical comparative study conducted using Density Functional Theory (DFT).

A comprehensive electronic structural analysis was conducted by use of frontier molecular orbitals, which comprise the Lowest Unoccupied Molecular Orbital (LUMO) and the Highest Occupied Molecular Orbital (HOMO). The compound's reactivity and stability were elucidated by the use of global chemical reactivity descriptors. To clarify the distribution of electron density within molecules and offer insights into their reactivity, stability, and molecular recognition processes, a molecular electrostatic potential (MEP) study was conducted.

The investigation into the NLO properties of EMBIT, and its potential for second harmonic generation (SHG), suggests that it is a promising candidate for applications requiring advanced optical materials.

The EMBIT molecule was subjected to molecular docking to study its potential as a glaucoma treatment agent. The aim of the study was to determine how EMBIT interacts with two proteins essential for the development of glaucoma: Rock1 and Rock2. We examined the binding mechanisms of EMBIT within the Rock1 and Rock2 binding sites at using computer simulations, and the results showed encouraging inhibitory effects. Further examination of ligand-protein interactions shed light on the processes underlying EMBIT's ability to regulate the activities of Rock1 and Rock2. These results make EMBIT a viable option for the development of additional treatments against glaucoma, provided that it is validated by experiments

2. Experimental and computational details

2.1. Synthesis of (E)-3-(3-(2-methoxyphenyl)-4-methylthiazol-2(3H)-ylidene) benzo[4,5] imidazo [1,2-c] thiazole-1(3H)-thione (EMBIT)

The synthetic route preparation of (E)-3-(3-(2-methoxyphenyl)-4-methylthiazol-2(3H)-ylidene) benzo[4,5]imidazo[1,2-c]thiazole-1(3H)-thione (4) is illustrated in Scheme 1. The thiazolium salt (2) was obtained by the condensation reaction of 3-(2-methoxyphenyl)-4-methylthiazole-2-thione (1) with methyl iodide in acetone at room temperature for 30 min. The title compound (4) was prepared by the reaction condensation of thiazolium salts (2) with thiazolo[3,4-a] benzimidazole-1-thione (3) in acetone under basic condition and at room temperature. The reaction was monitored by TLC (chloroform/ethanol: 8/2). After 24 hours, the product was filtered, washed with acetone, dried, and then recrystallized in ethanol to give a brown solid with a good yield.

2.2. Spectroscopic data

Brown solid, Yield 71 %, mp=260°C; IR (ν cm^{-1}):1289 (C=S), 1520 (C=C), 1610 (C=N). RMN ^{1}H (300 MHz, $CDCl_3$) δ(PPM) J(Hz):1,90 (s, 3H, CH_3thia); 3,84 (s, 3H, OMe); 6,39 (s, 1H, C-H, thia) ; 7,12 (q, 3H, benzimidazole, J=6,76, J=16,07) ; 7,34 (m, 2H, thia) ; 7,73 (m, 2H, thia) ; 8,65 (d, 1H, benzimidazole, J=7,46). RMN ^{13}C (75 MHz, $CDCl_3$):14,01 (CH_3); 56,14 (O-CH_3); 98,06 (C_{benzi}=C_{thia}); 102,41; 113,11; 113,81; 118,50 ; 121,28 ; 121,97 ; 123,05 ; 129,90 ; 130,82 ; 130,92 ; 133,57 ; 138,40 ; 151,14 ; 156,65 (C_{thia}=C_{benzi}) ; 170,53 (C-OMe) ; 181,53 (C=S).

2.3. Single-crystal X-ray data diffraction (SC-XRD)

Data collection was performed at 296 K on a STOE IPDS 2 diffractometer using a monochromatic graphite Mo-K_α (0.710731 Å) radiation. The structure was solved with the direct methods [15] using ShelXS program. Refinement was subsequently performed using the ShelXL program [16], employing the complete matrix least-squares based on F^2 through the WingX program [17]. The compound crystallizes in the monoclinic crystal system, with the space group $P2_1/n$. Table 1 provides a summary of the crystallographic data and the refinement parameters.

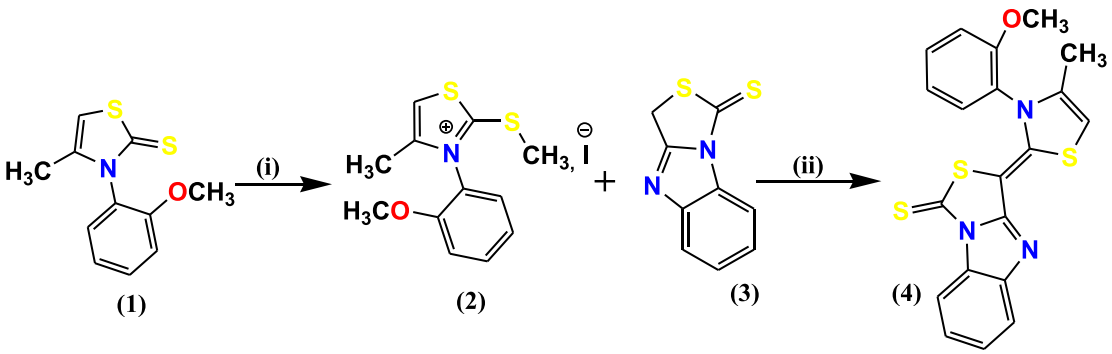

Condition and reagent: (i)CH_3I, Acetone, 25°C; **(ii)**Acetone, 25°C

Scheme 1. Synthesis pathway of EMBIT.

Table 1
Crystallographic data, selected data collection and refinement parameters for EMBIT.

Crystal data	
Chemical formula	$C_{20}H_{15}N_3O_1S_3$
Mr	409.53
Temperature (K)	293(2)
Crystal system, Space Group	Monoclinic, $P2_1/n$
Radiation type, wavelength (λ)	Mo K_α, 0.71073
a (Å)	10.6516(4)
b (Å)	13.4438(6)
c (Å)	13.0539(5)
α (°)	90.00
β (°)	95.581(3)
γ (°)	90.00
V (Å^3)	1860.38(13)
Z	4
ρ (g/cm^3)	1.462
μ (mm^{-1})	0.414
Data collection	
Diffractometer	STOE IPDS 2
Absorption integration and correction	X-RED32; Stoe & Cie, 2002
F(000)	848
$2\theta_{min}$-θ_{max}	4.36-60.0
hkl index range	$-8 \leq h \leq 15$ $-19 \leq k \leq 19$ $-18 \leq l \leq 18$
N°. of measured reflections	12728
N°. of independent reflections	5309
N°. of observed reflections with $[I > 2\sigma(I)]$	3143
R_{int}, R_σ	0.0489, 0.0592
Refinement	
Data/restraints/parameters	5309/0/246
R $[I > 2\sigma(I)]$, *wR*, *S*	0.039, 0.085, 0.888
$\Delta\rho$max, $\Delta\rho$ min (e-.Å^{-3})	0.43, -0.32
CCDC no.	1898125

2.4. Materials and Instrumentations

Experimental techniques, including Fourier-transform infrared spectroscopy (FT-IR), nuclear magnetic resonance NMR spectroscopy for both proton ^{1}H and carbon ^{13}C nuclei were employed to characterize EMBIT. The FT-IR spectrum was recorded using a Perkin-Elmer spectrometer with wavenumbers reported in cm^{-1}. NMR spectra were obtained in chloroform solvent using a Bruker AC-500 MHz spectrometer, with chemical shifts reported as δ (ppm) relative to tetramethyl silane TMS.

2.5. Computational details

Determining the molecular properties and identifying the structure of the chemical requires the use of theoretical calculation methods. The computations were performed using the Gaussian 09 program [18], the 6–311 G ++ (d,p) basis set, and the B3LYP functional. The computed vibrational frequencies are scaled by a factor of 0.9716 [19]. To produce the potential energy distribution assignment, the VEDA 4 program was utilized (PED) [20]. The program uses the potential energy distribution (PED) calculation to determine the vibrational modes [20,21] UV–Vis spectra and solvent effect simulation were calculated using time-dependent TD-DFT with CPCM model. The Gauss-sum tool was used to generate the group contributions of FMO's and DOS spectra [22]. Protons and carbon's nuclear magnetic resonance chemical shifts were calculated using the GIAO method. Gauss View 06 has been utilized to display all of the optimized molecular geometry details, vibrational wavenumbers and NMR spectra, MEP surface, and FMO's [23]. Multiwfn program [24] to compute all of NCI-RDG, LOL, and ELF maps, VMD program for visualization [25], molecular docking was performed using Autodock tools [26] and Autodock Vina [27]. Discovery studio to visualize protein-ligand interactions [28].

3. Results and discussion

3.1. Structure description

The experimental and theoretical structures are shown in Fig. 1. Table 2 lists the X-ray and calculated bond lengths, bond, and torsion angles. The experimental and theoretical C−C bond lengths of the two benzene rings were close to the values cited in the literature [29]. However, certain bond lengths observed in the X-ray experiments were marginally shorter, the shortest bond lengths for the C−C bond were attributed to C1−C2 equal to 1.375 Å and 1.388 Å for experimental and DFT calculations respectively. the following bonds: N1−C1, N3−C10, and N2−C8 presented shorter bond distances than the average aromatic C−C bonds, This can be explained by the fact that in the gaseous state, both electronegativity and atom size influence the probability of ionic versus covalent bonding. A bond between a large atom and a much smaller atom is more likely to have ionic character than a bond between two atoms of similar size, as the smaller atom can attract the bonding electrons closer to itself [30,31].. Average observed C−S bond lengths for both the experimental and computed values were approximately equal to 1.75 Å, which is in very good agreement with the reported values in the literature [32], the largest deviations that occurred in bond angles involved Nitrogen atoms and were underestimated by the DFT approach by about two degrees. The first benzene ring experimental and calculated bond angles were mostly 2° differentiated from the ideal 120° value this is probably due to the substitution of the imidazole ring [33, 34,35].On the other hand, the second benzene ring presented fewer variations than the ideal value. Furthermore, to understand the 3-dimensional behavior of our compound we analyzed the experimental and theoretical dihedral angles, The torsion angles of the bridge between first and second fragments S2−C9−C10−N3 and C8−C9−C10−S3 are equal to 0.4° and −0.8° respectively which is almost planar, C12−N3−C14−C15 and C10−N3−C14−C19 are equal to 93.4° and 95.6° respectively indicating that the second benzene is perpendicular on the whole molecule. The majority of the optimized bond lengths, bond angles, and dihedral angles were found to be slightly larger than those observed in the XRD results, according to the theoretical values. The optimized structures obtained by DFT generally match closely with the X-ray diffraction (XRD) data [36]. These variations can be attributed to the theoretical calculations focusing on the isolated molecule in the gaseous phase, whereas the XRD data pertain to the molecule in the solid state [37].

3.2. Intermolecular contacts, HS and fingerprints

Intermolecular contacts provide valuable insights into the way molecules interact with each other in various environments. In our research, we employed various analytical techniques to investigate intermolecular contacts. Specifically, we used X-ray analysis to examine the spatial arrangement of atoms within molecules and their interactions with neighboring molecules. Additionally, we utilized Hirshfeld surface analysis to visualize the distribution of intermolecular interactions across crystal structures. Furthermore, we generated fingerprint plots to characterize and quantify these interactions, providing comprehensive insights into molecular packing and bonding patterns. Table 3. Displays the probable hydrogen bonds of EMBIT obtained by X-ray diffraction. Based on the obtained results, it can be inferred that certain carbon atoms C2, C2, C15, and C17 exhibit donor behavior, whereas S2, S3, N2, and H2 have acceptor characteristics, and the crystal packing of EMBIT lattice is displayed in Fig. 2. Hirschfeld surface analysis was conducted with Crystal Explorer provides detailed visualizations of the molecule's surface and its interactions. This includes features such as d_{norm}, d_i, d_e, curvedness, fragment patches, and shape index, as displayed in Fig. 4. These features offer valuable insights into the molecular structure and

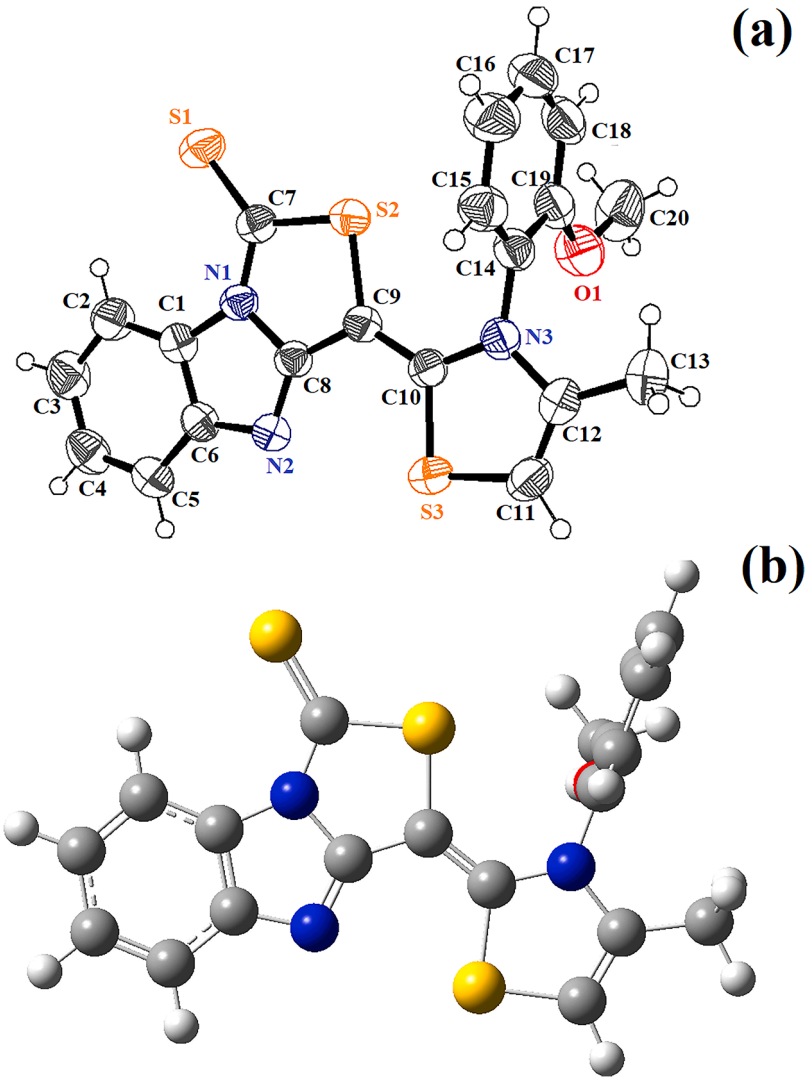

Fig. 1. a) X-ray structure, b) optimized structure of (E)-3-(3-(2-methoxyphenyl)-4-methylthiazol-2(3H)-ylidene) benzo [4,5] imidazo [1,2-c] thiazole-1(3H)-thione.

bonding of the studied compound. The shape index surface is used to identify complementary cavities (red), characterized by a shape index of 0, and bumps (blue), with a shape index greater than 0, where two molecular surfaces interact. Meanwhile, curvedness maps often show large patches of green (relatively flat) interrupted by dark blue edges (high positive curvature) [38,39]. d_i refers to the distance from the Hirshfeld surface to the closest nucleus within the surface, and d_e to the closest nucleus outside the surface. d_{norm} , which incorporates both d_e and d_i , displays intermolecular interactions with distances less than, equal to, or greater than van der Waals radii by red, white, and blue specks, respectively.

Fingerprint analysis has been done to further understanding of the different molecular interaction contributions of the EMBIT to the Hirschfeld surface. Displayed in Fig. 5, the fingerprints are plotted as *di* and *de* combined in the form of a 2D fingerprint diagram to give a more informed usage of these values. The interaction is shown as a pair of spikes at the bottom left of the diagram (short *di* and *de*, the top one related to the donor atom, the lower one with the acceptor) [40]. The hydrogen-hydrogen (H-H) bond of the EMBIT stands out with the highest contribution to the Hirshfeld surface analysis with 33.3% this type of bond is stated to contribute to a significant stabilization of crystal structures [40,41]. The EMBIT d_{norm} mapped surface analysis shown in Fig. 3 revealed apparent red patches highlighting molecular bonding in the compound under investigation. Among this intermolecular interaction the shortest happened to be between N2···H14/H14···N2 equal to 1.69 Å suggesting a strong bonding between the two entities the nitrogen-proton bond contributed 6.6% to the total HS surface according to the fingerprints diagram with two distinct spikes *de* and di at 1.4 Å each, followed by S2···H3/H3···S2 at 2.67 Å still indicating a significant interaction between sulfur and hydrogen especially with the high percentage to the contribution of the sulfur-hydrogen bond to the Hirschfeld surface equal to 26.4%. Meanwhile, the broadest generated intermolecular interactions, S3···H2/H2···S3 at 3.46 Å, suggesting a weaker yet notable bond. Furthermore, the weakest interactions less than 5% were H···O/O···H ,C···C ,C···S/S···C ,C···N/N···C , S···S , and N···N as shown in Fig. 6.

3.3. NCI – RDG analysis

Johnson et al [42] established the RDG technique, which is based on the electron density and its first derivative. According to the following equation:

$$RDG\ (r) = \frac{1|\nabla\rho(\mathrm{r})|}{2(3\pi 2)^{1/3}\rho(\mathrm{r})^{4/3}}$$

Where 1 denotes electron density and r denotes coordinate vector established the noncovalent interaction (NCI) approach.

Lambda 2 values, depicted in the 2D scatter graph in Fig. 7.a, serve as

Table 2
Experimental and DFT geometrical data of EMBIT.

Parameters	X-ray	DFT/6–311 G ++(d,p) B3LYP
Bond lengths Å		
S2–C7	1.740 (2)	1.776
S2–C9	1.7652 (17)	1.792
S3–C11	1.728 (2)	1.756
S3–C10	1.7337 (17)	1.766
S1–C7	1.639 (2)	1.651
N1–C7	1.367 (2)	1.370
N1–C8	1.391 (2)	1.409
N1–C1	1.398 (2)	1.402
N3–C10	1.365 (2)	1.382
N3–C12	1.398 (2)	1.407
N3–C14	1.441 (2)	1.435
N2–C8	1.315 (2)	1.309
N2–C6	1.396 (2)	1.393
O1–C19	1.361 (3)	1.353
O1–C20	1.441 (3)	1.427
C8–C9	1.419 (2)	1.422
C9–C10	1.370 (2)	1.378
C1–C2	1.375 (3)	1.388
C1–C6	1.397 (3)	1.418
C6–C5	1.399 (2)	1.395
C14–C15	1.379 (3)	1.391
C14–C19	1.393 (3)	1.408
C12–C11	1.335 (3)	1.342
C12–C13	1.487 (3)	1.494
C2–C3	1.384 (3)	1.395
C15–C16	1.373 (3)	1.392
C5–C4	1.375 (3)	1.392
C4–C3	1.385 (3)	1.402
C19–C18	1.385 (3)	1.397
C18–C17	1.373 (4)	1.394
C16–C17	1.376 (4)	1.391
Bond angles		
C7–S2–C9	94.05 (8)	93.58
C11–S3–C10	90.59 (9)	90.36
C7–N1–C8	117.90 (15)	117.76
C7–N1–C1	135.48 (16)	136.05
C8–N1–C1	106.62 (13)	106.18
C10–N3–C12	114.99 (15)	114.75
C16–C15–C14	119.6 (2)	120.45
C4–C5–C6	117.88 (19)	118.13
C10–N3–C14	121.63 (15)	123.18
C12–N3–C14	123.30 (15)	121.91
C8–N2–C6	103.78 (14)	104.75
C19–O1–C20	118.1 (2)	118.84
N2–C8–N1	113.43 (15)	113.40
N2–C8–C9	134.60 (16)	133.77
N1–C8–C9	111.97 (14)	112.81
C10–C9–C8	124.14 (15)	123.37
C10–C9–S2	127.65 (13)	128.66
C8–C9–S2	108.20 (12)	107.95
N3–C10–C9	128.20 (15)	128.37
N3–C10–S3	109.78 (13)	109.57
C9–C10–S3	122.01 (13)	122.05
C2–C1–C6	123.60 (16)	122.82
C2–C1–N1	132.43 (17)	133.02
C6–C1–N1	103.97 (16)	104.14
N2–C6–C1	112.20 (14)	111.51
N2–C6–C5	129.03 (18)	129.02
C1–C6–C5	118.77 (18)	119.45
N1–C7–S1	127.28 (15)	128.37
N1–C7–S2	107.88 (13)	107.86
S1–C7–S2	124.82 (11)	123.76
C15–C14–C19	121.26 (18)	120.43
C15–C14–N3	119.16 (16)	120.17
C19–C14–N3	119.56 (17)	119.38
C11–C12–N3	111.36 (17)	112.42
C11–C12–C13	128.91 (19)	127.28
N3–C12–C13	119.72 (17)	120.28
C1–C2–C3	116.44 (19)	116.67
C12–C11–S3	113.27 (15)	112.86
C5–C4–C3	122.08 (19)	121.52
O1–C19–C18	125.53 (19)	124.93
O1–C19–C14	116.25 (17)	116.16
C18–C19–C14	118.2 (2)	118.90
C17–C18–C19	120.1 (2)	119.98
C2–C3–C4	121.2 (2)	121.37
C15–C16–C17	119.5 (2)	119.15
C18–C17–C16	121.2 (2)	121.05
Torsion angles		
S2–C9–C10–N3	0.4 (3)	0.54
C8–C9–C10–S3	−0.8 (2)	-0.77
C10–N3–C14–C15	−83.2 (2)	94.53
C12–N3–C14–C15	93.4 (2)	-90.05
C10–N3–C14–C19	95.6 (2)	-86.48
C12–N3–C14–C19	−87.8 (2)	88.92

Table 3
Potential hydrogen bonds of EMBIT.

D–H···A	D–H (Å)	H···A(Å)	D···A(Å)	D–H···A (°)
C2–H2*A*···S3^{i}	0.93	2.89	3.65	140
C3 H3···S2^{ii}	0.93	2.97	3.89	171
C15–H15···N2^{iii}	0.93	2.59	3.44	154
C17 H17···H2^{iv}	0.93	2.84	3.28	111

Symmetry codes : (i) x-1/2,-y+1/2, +z+1/2, (ii) -x+1/2,+y+1/2,-z+1/2+1 (iii) -x+1,-y,-z+1 (iv) -x+1/2+1,+y-1/2,-z+1/2+1

crucial indicators of the underlying molecular interactions. These values offer insights into the nature of intermolecular forces. When lambda 2 is greater than zero, it signifies a pronounced repulsion effect between the molecules, suggesting that they are actively pushing each other apart. Conversely, when lambda 2 falls below zero, it is an indication of a substantial attraction between the molecules, signifying their strong affinity to each other. The region around zero on the lambda 2 scale is where the Van der Waals effect becomes prominent. This means that molecules in this region experience relatively weak, non-covalent forces, and they tend to interact through the attractive Van der Waals forces, often described as dispersion forces, dipole-dipole interactions, and hydrogen bonding.

Reduced Density Gradient (RDG) analysis was employed to gain a deeper understanding of the intrinsic molecular interactions within the EMBIT compound. This analysis involved the utilization of an isosurface with a threshold of 0.5, helping to visualize and quantify the electron density within the molecule. The results obtained from both the 2D (Fig. 7.a) scatter graph and the 3D (Fig. 7.b) isosurface rendering consistently pointed to the absence of strong hydrogen bonds in the compound's structure. Instead, they revealed the presence of multiple red patches, indicating a strong steric effect. These red patches are localized in the central regions of the aromatic rings within the molecule, signifying that there is significant electronic density in these areas, which contributes to steric repulsion. Additionally, the analysis demonstrated the occurrence of Van der Waals interactions in various regions of the compound. These Van der Waals forces were observed between specific pairs of atoms within the molecule, namely H2 and S1, N2 and S3, O1 and N3, H15 and H13, and also between H17 and H20. Furthermore, such interactions were identified between S2 and H12, highlighting the presence of Van der Waals forces between these atom pairs as well. In summary, the lambda 2 values offer valuable insights into the nature of molecular interactions, while the RDG analysis using the 0.5-ISO surface threshold unveiled the lack of strong hydrogen bonds and the presence of pronounced steric effects localized within the aromatic rings of the molecule. Simultaneously, Van der Waals forces were shown to be at play among various atom pairs, emphasizing the complexity of intermolecular forces within the compound.

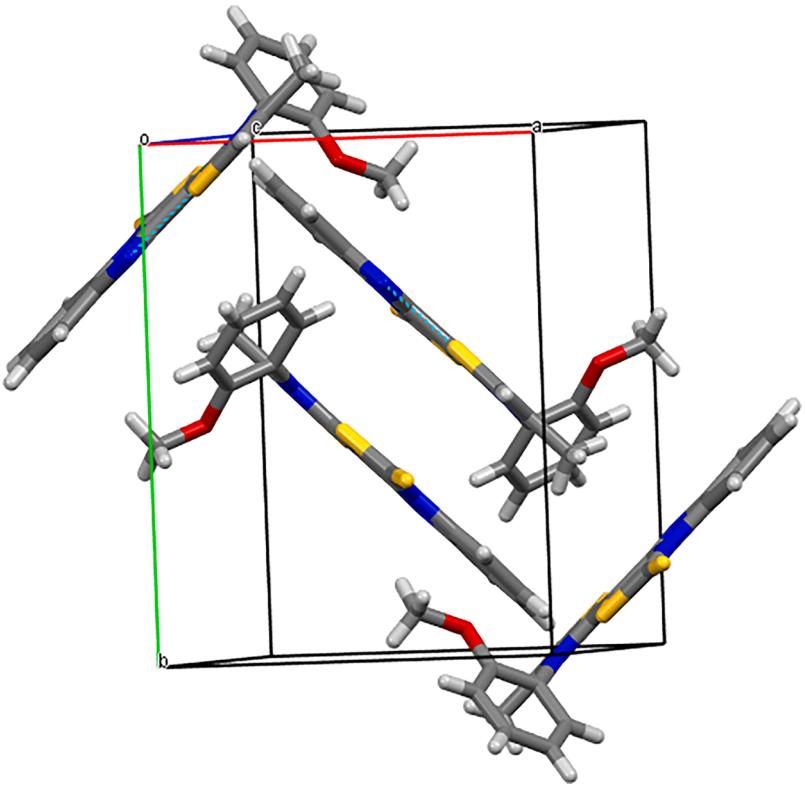

Fig. 2. Crystal packing of EMBIT.

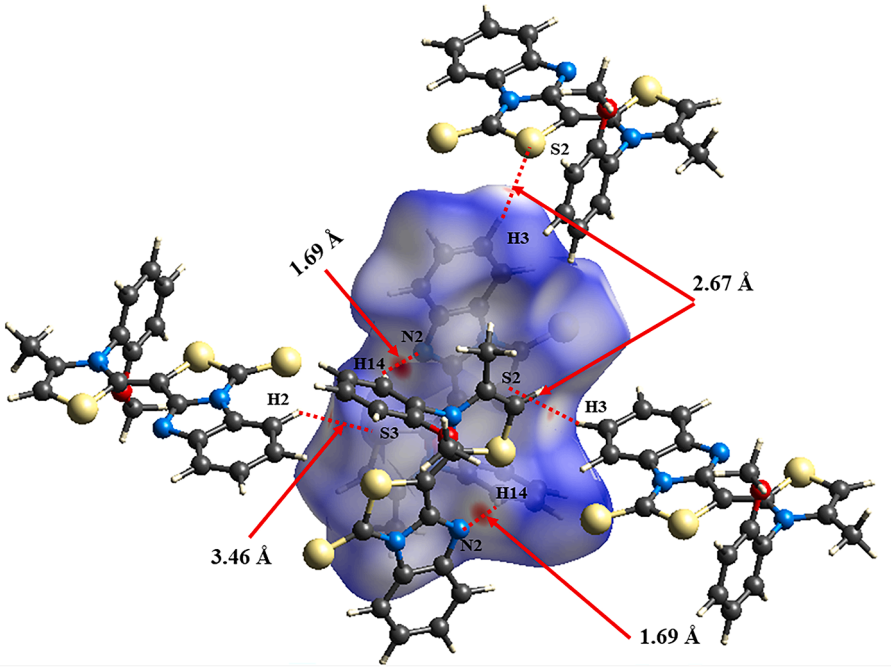

Fig. 3. Hirshfeld surfaces mapped with d_{norm} surface of EMBIT.

3.4. LOL and ELF

The electron environment around each atom is characterized by prominent or diminished peaks on a topographical map. Such maps reveal the significant likelihood of locating an electron pair on the molecular surface, offering insights into the spatial distribution and accessibility of electron pairs within the molecular framework. The Electron Localization Function (ELF), τ(r), exhibits a range from 0.0 to 1.0 in its values. Regions with relatively large values within the interval of 0.5 to 1.0 signify areas containing both bonding and nonbonding localized electrons. In contrast, smaller values, below 0.5, characterize regions where electrons are anticipated to be delocalized [43]. As revealed by the elf map Fig. S1. which provides insights into the distribution of electron density in molecular bonds, it is noteworthy that

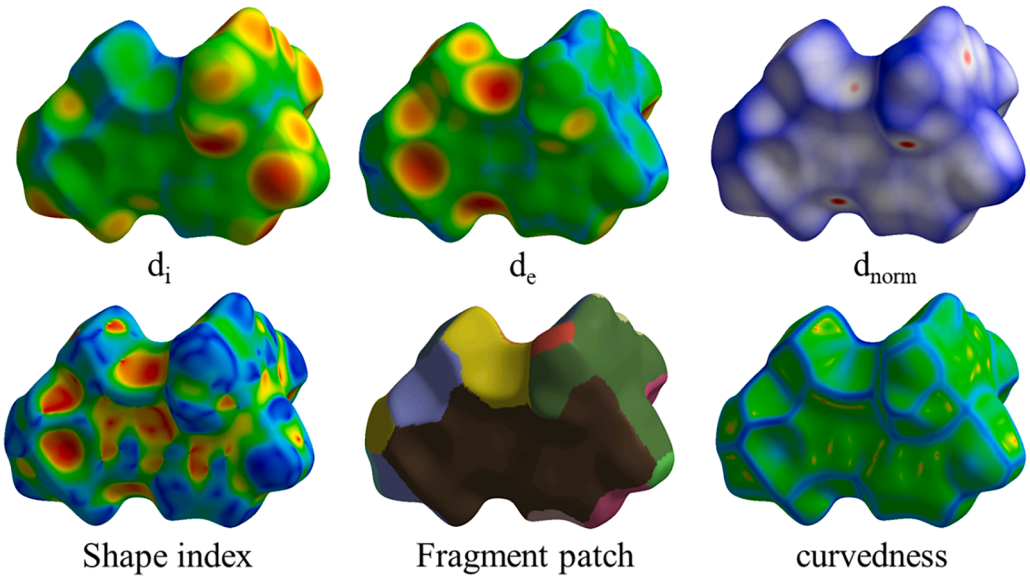

Fig. 4. Hirshfeld surface analysis of the EMBIT compound with d_{norm}, d_i, d_e, shape index, and curvedness.

the degree of electron localization between carbon and oxygen is not as prominent as is observed in the context of carbon-nitrogen and carbon-carbon bonds. The localized orbital locator (LOL), Localization Index, η(r), achieves elevated values (> 0.5) in areas where the electron density is primarily controlled by electron localization [39]. In the LOL map (see Fig. S2), regions over hydrogen atoms are visually accentuated with red coloring (when the value is > 0.5). Remarkably, the covalent region stands out with an elevated LOL value. Conversely, the presence of electron depletion, signifying a contrast between the valence shell and inner shell, is represented by a distinctive blue circle [44].

3.5. Vibrational spectra

The EMBIT molecule consists of 42 atoms. Table 4. Displays the Experimental and theoretical vibrational frequencies as well as potential energy distribution results, as well as infrared spectra in Fig. 7. The theoretical frequencies were found to be higher than the experimental ones which can be attributed to the neglect of the anharmonic parameters in gaseous phase calculation [45]. To align the theoretical and experimental values the calculated frequencies were scaled by 0.972 [19].

C-H Vibrations:

Aromatic CH stretching vibrations usually lie in the range 3100–3000 cm^{-1} for asymmetric (and 2990–2900 cm^{-1} for symmetric stretching types of vibration [46]. The type of substituent has little effect on the bands in this range [47] . CH stretching vibrations were observed in the reported plage and appeared on the IR spectrum as small peaks. These bands are rarely effective since they overlap, leading to higher absorption in this region [48]. This region's absorption is prompted by sp^2-hybridized C-H (= C-H) stretching in aromatic rings [45]. The 1375 cm^{-1} frequency is attributed to symmetric and asymmetric CH_3 group bending [49]. The C-H bending vibration showed up between 1500 and 500 cm^{-1} as mentioned in the literature [50,51], the highest CH bending frequency intensity 116 cm^{-1} in the first benzene ring. And the highest CH stretching frequency intensity is equal to 51 attributed to the methyl group. The torsional vibrations were found theoretically from 965 to 729 cm^{-1}.

C-C and C=C Aromatic Ring CC stretching vibrations usually occur in the 1650 and 1200 cm^{-1} range [52]. The computed frequencies were assigned were found in the reported region The FT-IR analysis attributed 1520 cm^{-1} to C=C stretching. The highest frequency mode is the C=C stretching vibration, which occurs at 1635–1532 cm^{-1} and [53] which is in good agreement with both the theoretical and experimental findings for the EMBIT molecule which the highest intensity equal was 1286 assigned to 152 and 1520 cm^{-1} for FT-IR and calculations respectively and 60 % potential energy distribution in mix mode with NC stretching vibration. The stretching vibration of the ring C-C bonds also appears in the 950–1100 cm^{-1} lower zone were explained to be the stretching vibrations for the bonds that play an active role in the formation of rings, meanwhile, the deformation of the C-C ring takes place at approximately 876 cm^{-1} [50]. the calculated torsion and bending vibration of C-C the bond appeared in the 891–400 cm^{-1} zone. Mostly occurring in the first benzene ring according to PED analysis.

C-O:

C-O bands are typically detected in the 1260–1000 cm^{-1} range [54]. CO was observed at 1201 by the FT-IR spectrum for the title compound. The intensities at 1269, 1253 and 1232 cm^{-1} are assigned to C-O by DFT calculations and at 1230 cm^{-1} experimentally, the highest CO stretching calculated vibration intensity was equal to 163 cm^{-1}. The in-plane and out-of-plane bending modes of C-O are usually recorded in the 725±95 and 595±120 cm^{-1} ranges, respectively [55]. PED analysis assigned 741, 737, and 492 cm^{-1} to CO out-of-plane bending and 566 cm^{-1} to in-plane bending.

N-C:

N-C vibrations are expected to appear in the 1200–1400 cm^{-1} region [56]. Due to various vibrations that that may be occurring in this region, identifying the C-N vibration is a difficult process according to *Silverstein et al* [57]. FT-IR analysis predicted N-C vibration 1610 cm^{-1} as reported in the literature [58,59] theoretical calculation predicted 1604, 1531, 1361, 1326, 1305 and 1223 cm^{-1} for N-C stretching vibration. CN bending vibrations are predicted to be around 400 cm^{-1} [60]. The following calculated vibrations 1079, 818, 601, 589, 505, and 494 cm^{-1} are attributed to NC in-plane bending meanwhile740, 729, 505, and 430 cm^{-1} have been assigned to out-of-plane bending. NC torsion vibrations happened in the range of 691- 428 cm^{-1} according to calculations.

C=S

Usually, C=S stretching vibrations are in the range of 730 to 660 cm^{-1} [61]. The theoretical C=S stretching vibrations of the title compound were in the reported area at 798, 789, 529, and 437cm^{-1} meanwhile FT-IR analysis showed ν(C=S) at 1289 cm^{-1}, in several cyclic thioamides, the C=S stretching frequency has been assigned to the fields 1050–1200 cm^{-1} by *Mecke et al* [62]. Many SC bending vibrations have been assigned at the range of 800–400 cm^{-1}. The bands appearing in the areas of 1260–1420 cm^{-1}, and 940–1140 cm^{-1} in these

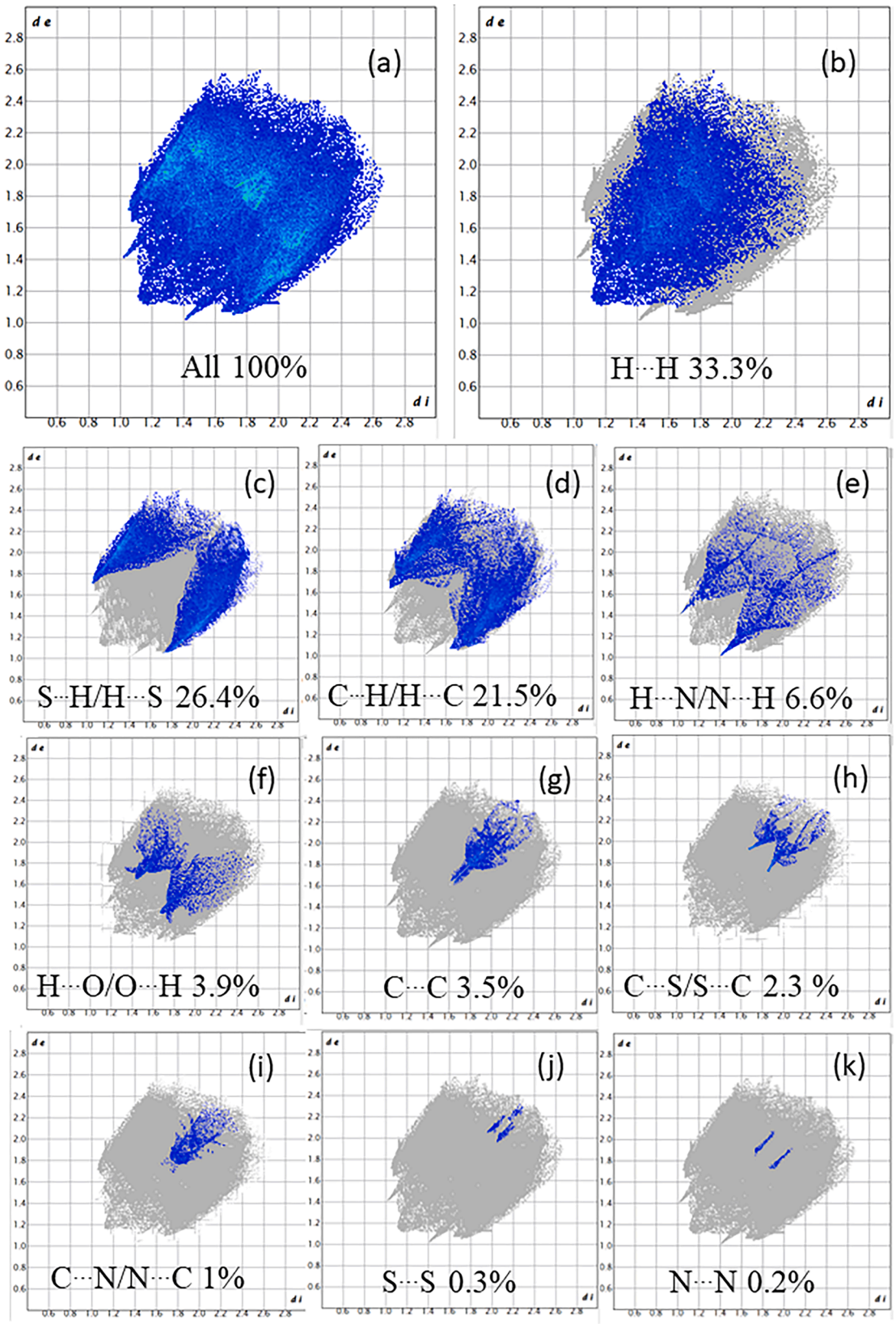

Fig. 5. 2D Fingerprint plots of bond contribution of EMBIT.

nitrogen-containing derivatives are possibly referred to as the N-C=S due to the mixed vibrations [63]

3.6. NMR spectral analysis

The combined Quantum mechanical/NMR method has been used in a wide range of applications, most notably in outlining the relative and,

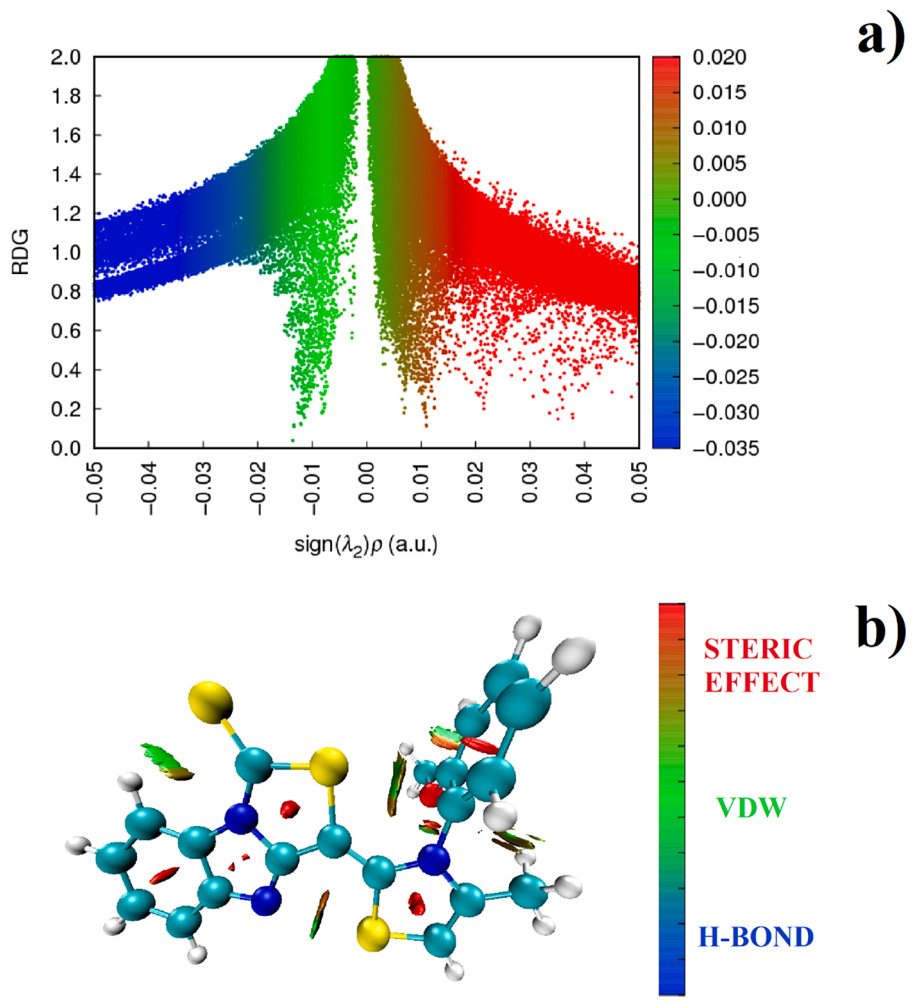

Fig. 6. a) 2D scatter graph, b) Reduced gradient density surface analysis.

where possible, absolute configurations of natural and synthesized substances [64]. TMS-calculated isotropic chemical shifts were used as a reference for the calculations.

In Table 5, The ^{1}H and ^{13}C NMR experiment is described, as well as the calculated chemical shifts for the title compound. The measured ^{1}H chemical shifts for the title EMBIT ranged from 2.38 to 9.45 ppm for the calculated values, and from 1.9 to 8.65 ppm for the experimental values. Protons H2, H3, H4, H5, H15, H16, H17, and H18 were the highest recorded proton ^{1}H NMR chemical shift values in the benzene rings. Theoretical predictions and experimental results support this finding. Chemical shift values are caused by the strong deshielding of the benzene ring protons. The methyl groups attached to C13 and C20 exhibited the lowest recorded chemical shift values.

This observation holds in both theoretical predictions and experimental data. The explanation is that chemical proton displacements in organic compounds are strongly affected by the surrounding electrical environment. When an atom or group bonded to hydrogen attracts electrons, the shielding around the hydrogen is reduced, resulting in an upfield shift or a shift to higher frequencies. In contrast, when hydrogen is bound to an electron-donating group, shielding increases, resulting in a downward shift of the field or to lower frequencies [65].

The ^{13}C chemical shifts of EMBIT have been carefully recorded in the range of 14.01 to 181.53 ppm and computationally evaluated over the broadest range of 18.99 to 199.11 ppm. Notably, chemical shift peaks are clearly observed at carbon atoms C6, C7, C8, C10, and C19. The significant increase in chemical shift values is attributed to the electronegativity of neighboring atoms, particularly nitrogen (N), sulfur (S), and oxygen (O).

The high chemical shifts in carbon atoms C6, C7, C8, C10, and C19 can be theoretically and experimentally correlated with the electronegative properties exhibited by the surrounding nitrogen, sulfur, and oxygen atoms. The influence of these electronegative elements leads to an increase in the chemical shift values, showing a shift towards higher ppm values in the recorded spectra. In contrast, the lowest chemical shift of the methyl group is accurately recorded, theoretically at 18.99 ppm and experimentally at 14.01 ppm. The observed decrease in chemical shifts can be attributed to substitution effects. The theoretical and experimental values agree well and provide a comprehensive understanding of the subtle complexities that influence EMBIT chemical shifts. In summary, EMBIT chemical shifts detected between 14.01 and 181.53 ppm and analyzed computationally over a wider range from 18.99 to 199.11 ppm show remarkable diversity. The increased chemical shifts of certain carbon atoms arising from the electronegativity of the surrounding nitrogen, sulfur, and oxygen atoms contrast sharply with the low chemical shifts exhibited by the methylene groups due to substitution effects.

Solvents also impact NMR chemical shifts due to changes in the molecule's averaged conformation. Additionally, chemical shifts might also vary depending on the analysis concentration, temperature variances, and pH [66]. Theoretically, even when employing the most advanced computational methods, the average errors reach up to 0.4 ppm or greater for ^{1}H shifts and up to 10 ppm or more for ^{13}C shifts [67]. The use of B3LYP/6–311 G (d, p) has been reported to overestimate chemical shifts [68]

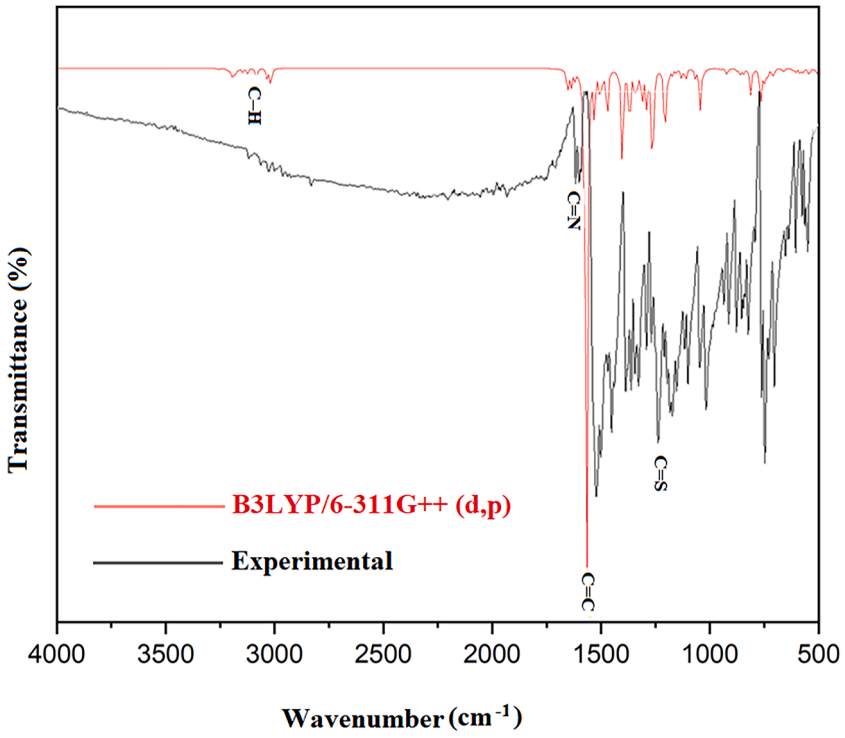

Fig. 7. The comparison of FT-IR and computed IR spectra for EMBIT.

3.7. UV–Vis spectra, FMOs and reactivity's descriptor's

The EMBIT's electronic transitions were thoroughly explored using a theoretical UV–Vis study. All of the theoretical wavelength (λ), oscillator strength and the computed electronic transitions and major contributions were enlisted in Table S1. And theoretical spectra have been displayed in Fig. 8. The EMBIT theoretical UV–Vis analysis revealed three significant electronic transitions at 437.45 nm, 336.65 nm, and 310.35 nm in the absence of solvent, with a predominant contribution of 96% from the HOMO to LUMO transition. The following absorptions occurred in the visible region. These absorptions may be assigned to n → π*electron transitions [69]. The EMBIT absorbs light in the violet region and reflects yellow color which corresponds to the compound's color [69]. The UV spectrum of EMBIT was simulated in gaseous state in solvent-free conditions and with four distinct solvents using the CPCM model including DMSO, Ethanol, methanol, and chloroform. While the first spectral band remains consistent across all solvents, indicating an inherent electronic transition unaffected by solvation, the second band consistently displays a notable redshift. This shift, toward longer wavelengths, suggests a significant influence of solvation on specific electronic transitions, resulting in a stabilization of the excited state relative to the ground state, which is confirmed by the slight narrowing of the energy gap when considering the solvent effect this stability is provided by polar solvents [70].

Visual representations of the frontier molecular orbitals in gaseous state are provided for a better understanding Fig. 9. Additionally, the visualization of simulated frontier molecular orbitals in four different solvents, displayed in Fig. S3. HOMO stands for highest occupied molecular orbital and LUMO for lowest unoccupied molecular orbital. The energy gap, often referred to as the HOMO-LUMO gap, plays a pivotal role in determining a molecule's chemical reactivity and kinetic stability [71]. When a molecule possesses a substantial HOMO-LUMO gap, it is characterized as a "hard" molecule, exhibiting minimal polarizability and being relatively unreactive. Conversely, "soft" systems feature a narrow HOMO-LUMO gap, making them highly polarizable and reactive. The red color represents the positive phase, while the green color represents the negative phase. The figure demonstrates that the HOMO and LUMO orbitals are distributed throughout the entire molecule, indicating the occurrence of charge transfer within the molecule. In contrast, the HOMO-1 and LUMO +1 indicate charge transfer from the sulfur group to the methoxyphenyl ring. The band gap was equal to 3 eV which makes the molecule probable as a biomaterial the literature reported the optical absorption edge of some biomaterials is around 3 eV [72]-Furthermore, the performed DOS analysis confirms the energy gap calculated in the study Fig. S4. The abundance of potentially occupiable states is indicated in the DOS spectra by elevated intensities, whereas in the vicinity of zero electron volts (eV) signifies the lack of occupied states [46]. The non-occupied orbitals are represented by the red lines, while the green lines represent the occupied orbitals. The incorporation of a solvent diminishes the discrepancy in the forecasted excitation energy to less than 0.3 electron volts (eV), with the majority of instances showing a reduction to below 0.1 eV [70].

Global chemical reactivity descriptors have been reported to be highly effective when forecasting atom and molecule reactivity along with site selection. [73,74,75]. We investigated the solvent effect on global chemical reactivity descriptors using four solvents DMSO, Ethanol, methanol, and chloroform using the CPCM model, The global reactivity descriptors: Electron affinity (E_A), ionization potential (I_P), chemical potential (μ), electronegativity (χ), chemical hardness (η), chemical softness (s), hyper hardness (Γ), and electrophilicity index (ω) are calculated by the following equations using Koopman's theorem [76]The obtained results are gathered in Table 6:

$$\eta = \frac{1}{2}(E_{LUMO} - E_{HOMO}),\ \mu = \frac{1}{2}(E_{LUMO} + E_{HOMO}),\ S = \frac{1}{2}\eta,\ \chi = -\frac{1}{2}(E_{LUMO} + E_{LUMO})$$

$$EA = -ELUMO\ ,\ I_P = -E_{HOMO},\ \Gamma = E_{LUMO} - 2E_{HOMO} + E_{HOMO-1},\ \omega = \frac{\mu^2}{2\eta}$$

The chemical potential describes the tendency of electrons to escape from equilibrium [77]. *Pauling* [74] described electronegativity as an

Table 4
FT-IR and computed vibrational frequencies of EMBIT.

FT-IR (cm −1)	B3LYP /6–311G++(d,p) Band assignement with PED > 10 %			
	Unscaled	Scaled freq(cm-1)	IR	
-	3254	3162	3.3026	ν CH (99%) Ring 4
-	3222	3130	2.4938	ν CH (96%) Ring 1
-	3210	3119	3.9310	ν CH (86%) Ring 5
-	3200	3109	6.8426	ν CH (88%) Ring 5
-	3195	3104	14.950	ν CH (94%) Ring 1
-	3185	3094	6.2354	ν CH (71%) Ring 5+ ν CH $_{asy}$ (19%)
-	3183	3093	17.4693	ν CH $_{asy}$ (17%) Ring 1 + ν CH (81%) Ring 1
-	3176	3085	1.5974	ν CH $_{asy}$ (20%) Ring 5+ ν CH (67%) Ring 5
-	3167	3077	5.0562	ν CH $_{asy}$ (26%) Ring 1+ ν CH (66%) Ring 1
-	3146	3056	10.3782	ν CH (90%)
-	3125	3036	12.9860	ν CH (84%)
-	3085	2997	6.9034	ν CH (50)ν + CH $_{asy}$ (50%)
-	3083	2995	22.7073	ν CH (56%) + ν CH $_{asy}$ (43%)
-	3034	2948	28.1072	ν CH $_{asy}$ (99%)
-	3017	2931	51.3395	ν CH (53%)
-	1658	1611	19.9648	ν CC (61%) Ring 4
1610	1650	1604	40.6072	ν NC $_{asy}$ (11%) Ring 2 + ν CC $_{asy}$ (19 %) Ring 4 + ν CC (21%) Ring 1
1594	1637	1590	40.2999	ν CC (41%) Ring 5 + ν CC $_{asy}$ (27%) Ring 5
-	1621	1575	18.3973	ν CC (28%) Ring 5 + δ CCC (11%) Ring 1
-	1620	1574	3.0742	ν CC $_{asy}$ (13%) Ring 5+ ν CC (22%) Ring1
-	1575	1531	372.0533	ν NC $_{asy}$ (46%) Ring 2 + ν CC (21%) Ring1
1520	1565	1520	1286.5964	ν CC $_{asy}$ (60%) + ν NC (12%) Ring 4
1516	1529	1486	128.1105	δ HCC (35%) Ring 5
1495	1505	1462	31.8764	ν CC (16%) Ring 1+ ν CC asy (11%) Ring 1 + δ HCC $_{asy}$ (20%) Ring 1 + δ HCC (26%) Ring1
1462	1503	1460	49.2300	δ HCH $_{asy}$ (30%) + δ HCH (38%) + τ HCOC (12%)
-	1495	1452	6.0399	δ HCH $_{asy}$ (31%) + δ HCH (41%) + τ HCC $_{asy}$ (17%) Ring 5
-	1491	1449	13.2379	ν CC asy (10%) Ring 5 + δ HCC (32%) Ring 5+ δ HCH (16%)
-	1486	1444	4.6627	δ HCH (46%) + δ HCH $_{asy}$ (21%) + τ HCCN $_{asy}$ (12%)
1432	1476	1434	15.1718	δ HCH (43%) + δ HCH $_{asy}$ (30%) + τ HCCN (18%)
-	1470	1429	116.4136	δ HCC (50%) Ring 1
-	1469	1427	17.9941	δ HCH (52%) + δ HCC $_{asy}$ (12%) Ring 5
1397	1421	1381	9.6531	δ HCH (92%)
-	1401	1361	306.6402	ν NC $_{asy}$ (50%) Ring 3 + ν NC (21%) Ring 2
1338	1373	1334	67.2656	ν CC $_{asy}$ (41) Ring 1 + ν CC (11%) Ring 1 + δ HCC (16%) Ring 1
1320	1365	1326	95.0983	ν NC $_{asy}$ (30%) Ring 4 + ν NC (25%) 2
-	1343	1305	84.1396	ν NC $_{asy}$ (13%) Ring 2 + δ CNC (10%) Ring 4
1289	1330	1292	38.3830	ν CC (48%) Ring 5 + ν CC $_{asy}$ (27%) Ring 5
1284.	1313	1276	35.1201	
-	1306	1269	58.5861	ν OC (16%) + δ HCC (21%) Ring 5
-	1289	1253	107.2199	ν OC (14%)
1230	1268	1232	163.9745	ν OC (13%) + δ HCC (11%) Ring 5
1201	1258	1223	143.9939	ν CC $_{asy}$ (24%) + ν NC (33%) Ring 2
-	1208	1174	166.0749	
-	1204	1170	43.9083	δ HCH (11%) + τ HCOC $_{asy}$ (21%) + τ HCOC (23%)
-	1196	1162	14.8889	δ HCS (23%) Ring 4
1145	1188	1154	12.5458	ν CC $_{asy}$ (10%) Ring 5 + δ HCC $_{asy}$ (24%) Ring 5 + δ HCC (49%) Ring 5
-	1173	1139	14.1524	ν CC (14%) Ring 1 + δ HCC $_{asy}$ (10%) Ring 1+ δ HCC (55%) Ring 1
-	1169	1136	0.4702	δ HCH (14%) Ring 5+ δ HCH $_{asy}$ (15%) + τ HCOC (38%) + τ HCOC $_{asy}$ (33%)
-	1154	1121	8.8470	ν CC (15%) Ring 5 + δ HCS (25%) Ring 4 + δ HCC $_{asy}$ (12%) Ring 5
-	1131	1098	17.2871	δ HCS (10%) Ring 4
1093	1128	1096	7.9429	ν CC $_{asy}$ (10%) Ring 1 + ν CC (13%) Ring 1 + δ HCC $_{asy}$ (12%) Ring 1+δ HCC (11%) Ring 1
-	1110	1079	32.9307	ν CC asy (12%) + δ NCC (10%) Ring 3
1039	1067	1037	20.7118	ν CC (46%) Ring 5 + δ HCC (22%) Ring 5
-	1061	1031	1.5489	δ HCH (12%) + δ HCH $_{asy}$ (12%) + τ HCCN $_{asy}$ (64%) Ring 4
-	1047	1017	46.6951	ν CC (55%) Ring 5 + δ CCC asy (12%) Ring 5
1010	1043	1013	69.8378	ν S=C $_{asy}$ (24%) + δ CCC (16%) Ring 1 + δ CCC $_{asy}$ (11%) Ring 1
-	1030	1001	13.4882	ν CC $_{asy}$ (19%) Ring 1 + δ HCC $_{asy}$ (21%) Ring 1
-	1021	992	2.3422	δ HCH (10%) + τ HCCN (42%) Ring 4
-	1010	981	1.2265	ν CC (11%) Ring 5 + δ CCC $_{asy}$ (11%) Ring 5
-	997	968	0.0163	τ HCCC $_{asy}$ (27%) Ring 5+ τ HCCC (41%) Ring 5+ τ CCCC $_{asy}$ (10%) Ring 5
-	973	945	0.0080	τ HCCC $_{asy}$ (10%) Ring 1 + τ HCCC (24%) Ring 1 + τ CCCC $_{asy}$ (17%) Ring 1
-	961	934	1.3432	τ HCCC $_{asy}$ (28%) Ring 5 + τ HCCC (47%) Ring 5
906	948	921	2.3235	τ HCCC (55%) Ring 1 + τ HCCC $_{asy}$ (36%) Ring 1
870	921	895	18.8346	δ CCC $_{asy}$ (32%) Ring 1 + δ CCC (13%) Ring 5
-	872	847	8.1872	τ HCCC (31%) Ring 5
-	866	841	0.4684	τ HCCC (54%) Ring 1 + τ CCCC (38%) Ring 1
830	857	832	19.2607	τ HCCC (34%) Ring5
816	842	818	11.7710	τ HCCC (14%) Ring 4 + δ CNC (11%) Ring 2
-	822	798	3.3043	ν SC (44%) Ring 4 + δ SCC $_{asy}$ (19%) Ring4
-	812	789	61.4978	ν SC (31%) Ring 3 + δ CCC $_{asy}$ (13%) Ring 1+ δ SCS $_{asy}$ (10%) Ring 3
-	800	777	6.0246	ν OC(16%) + δ CCC (27%) Ring 5
-	766	745	37.7188	τ CCCC $_{asy}$ (46%) Ring 1 + τ HCCC $_{asy}$ (23%) Ring 1 + τ CCCN $_{asy}$ (14%) Ring 2
-	766	744	62.7755	τ HCCC (74%) Ring 5 + γ OCCC $_{asy}$ (15%)

(*continued on next page*)

Table 4 (*continued*)

FT-IR (cm −1)		B3LYP /6–311G++(d,p) Band assignement with PED > 10 %		
	Unscaled	Scaled freq(cm-1)	IR	
739	761	740	4.0661	τ HCCC (15%) Ring 1 + τ CCCC (21%) Ring 5 + γ OCCC $_{asy}$ (10%) + γ NCCC $_{asy}$ (12%) Ring 2
-	750	729	37.7604	τ HCCC (39%) Ring 1 + τ HCCC $_{asy}$ (26%) Ring 1+ γ NCCC $_{asy}$ (19%) Ring 2
-	735	714	30.3999	ν NC (10%) Ring 4 + δ CCC (10%) Ring 5
696	714	694	8.4424	τ HCSC (23%) Ring 4 + τ CCNC (16%) Ring 2 + τ CNCC (16%) Ring 2
-	705	685	19.0668	τ HCSC (69%) Ring 4
-	663	644	4.8443	δ CCC (10%) Ring 1
629	658	640	4.5972	δ CCC (25%) Ring 1
597	619	601	2.9717	δ NCC $_{asy}$ (11%) Ring 4 + τ CCNC asy (44%) Ring 4 + γ CCCN (12%) Ring 4
-	606	589	12.3467	δ CCC (14%) Ring 1 + δ CNC (10%) Ring 2
568	585	568	14.6240	δ OCC $_{asy}$ (14%) + τ CCCC $_{asy}$ (10%) Ring 5
-	583	567	0.0281	τ CCCC $_{asy}$ (21%) Ring 1 + τ CCC (25%) Ring 1 + τ CCCC 14 Ring1
-	576	559	1.8673	δ CCC (20%) Ring 1 + δ CCN $_{asy}$ (11%) Ring 2 + δ CNC (21%) Ring 2
555	570	553	9.1141	τ CCCC (28%) Ring 5
541	545	529	16.4571	ν CC (14%) Ring 1 + ν SC (27%) Ring 4 + δ SCC (30%) Ring 4
-	541	526	3.5456	τ CCNC (10%) Ring 2 + τ SCCN (23%) Ring 3 + γ SNSC (13%) Ring 3
-	520	505	2.1758	δ CCC (14%) Ring 5 + δ NCC (13%) Ring 4 + τ SCCN (12%) Ring 3 + γ CNCC (11%) Ring 2
-	512	497	0.5725	γ SNSC (52%) Ring 3
-	509	494	12.1893	δ CNC $_{asy}$ (12%) Ring 4 + τ CCCC $_{asy}$ (10%) Ring 5 + γ OCCC asy (26%)
-	449	437	0.9527	ν NC $_{asy}$ (14%) Ring 2 + ν SC $_{asy}$ (40%) Ring 3 + δ CCC $_{asy}$ (12%) Ring 1
-	443	430	3.9847	τ CCCC $_{asy}$ (25%) Ring 1 + τ CNCC (10%) Ring 2 + γ NCCC $_{asy}$ (19%) Ring 2
-	425	413	9.6004	δ CCC $_{asy}$ (13%) Ring 5+ δ SCN (32%) Ring 4
-	412	401	8.5968	δ CCC (17%) Ring 5+ δ SCN (18%) Ring 4

ν: stretching; sy : symmetric; asy : asymmetric; β : in-plane bending; γ : out of plane bending; ω : wagging; τ : twisting; δ : bending; ρ : rocking. Vibrational modes are based on potential energy distribution (PED). Scaled frequencies are given in cm–1. Ring 1:C1C2C3C4C5C6; ring 2:C1N1C8C6; ring 3:N1C7S2C9C8; ring 4:C10S3C11C12N3; ring 5:C14C15C16C17C1

atom's ability to attract electrons to itself. Many chemical, biological functions are connected to chemical hardness η [73], which represents the stability of molecules [76]. Softness is the opposite of hardness. The global electrophilicity index (ω) is grounded in thermodynamic properties, it quantifies the beneficial energy change occurring when a chemical system reaches electron saturation. To put it simply, it represents the energy decrease resulting from the electron flow between the donor (HOMO) and acceptor (LUMO) within molecules. Furthermore, it plays a pivotal role in determining a system's chemical reactivity [78, 79]. Systems exhibiting positive hyperhardness values and

Table 5
^{1}H and ^{13}C theoretical and experimental NMR shifts of EMBIT.

	B3LYP/6–311G(d,p)	Experimental
^{1}H		
H2	9.45	8.65
H3	7.94	7.12
H4	8.18	7.12
H5	8.47	7.17
H11	6.86	6.39
H13A	2.67	1.9
H13B	2.49	1.9
H13C	2.38	1.9
H15	8.29	7.34
H16	8.03	7.33
H17	8.39	7.34
H18	7.66	7.33
H20A	4.73	3.84
H20B	4.33	3.84
H20C	4.33	3.84
^{13}C		
C1	140.47	125.95
C2	122.32	113.81
C3	129.81	121.97
C4	134.39	123.05
C5	127.39	118.50
C6	161.46	151.14
C7	199.11	181.53
C8	165.24	156.65
C9	96.20	98.06
C10	159.98	138.40
C11	115.97	102.41
C12	146.09	133.57
C13	18.99	14.01
C14	136.70	129.90
C15	142.66	130.92
C16	129.50	121.28
C17	140.86	130.82
C18	119.05	102.41
C19	170.26	170.53
C20	59.50	56.14

electrophilicity index (ω) values exceeding 1.5 eV indicate stability [80, 81]. It also has been stated that the electrophilicity index is an appropriate descriptor for biological activity [82,83], and a toxicity predicting tool [84]. Whereas negative hyperhardness values suggest reactivity [85]. Moreover, a negative chemical potential (μ) further signifies a stable system when the Electron affinity (E_A), is smaller than the ionization potential (I_P), which implies enhanced electron donor capabilities and reduced electron acceptor capacities The data confirms that EMBIT is a stable compound.

To further investigate the reactivity of the compound, we conducted an in-depth analysis on how different solvents affect its computed GCRD properties. Our findings unveiled a substantial increase in the values of electronegativity, electrophilicity index, and electron affinity when subjected to various solvent environments. Conversely, we noted a discernible decrease in the values of chemical potential, chemical hardness, chemical softness, and hyper hardness across these solvent conditions. It has been noted that aprotic solvents such as DMSO exhibit a substantial decrease in chemical potential and hardness with only minor alterations in their dielectric constants [83].

3.8. Molecular Electrostatic Potential

MEP maps, visualizing a molecule's electron density in three dimensions, are essential descriptors for identifying nucleophilic and electrophilic attack regions as well as sites favorable for hydrogen bonding interactions. These maps play a vital role in understanding the reactivity and chemical behavior of molecules by offering insights into the distribution of electron density. MEP maps aid in predicting and assessing a molecule's susceptibility to nucleophilic or electrophilic reactions and its likelihood to engage in hydrogen bonding interactions

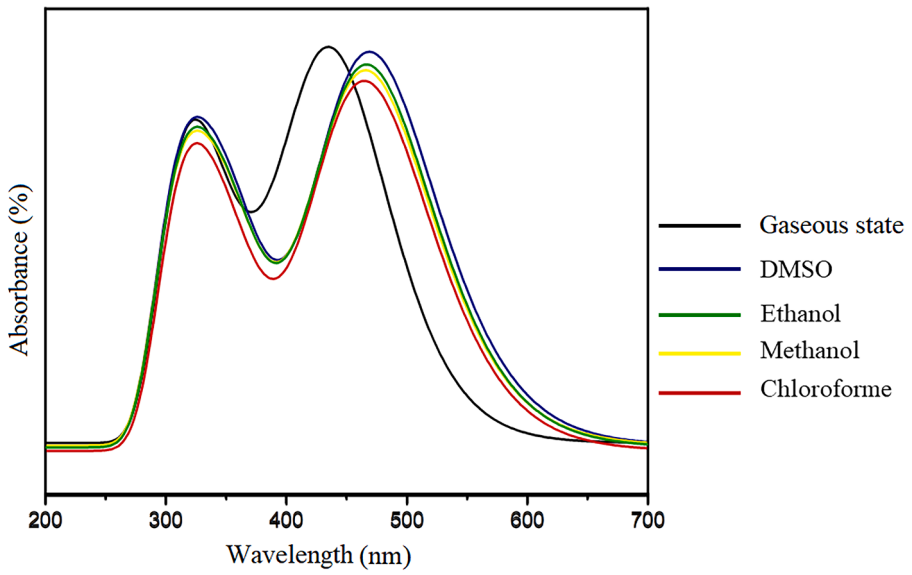

Fig. 8. UV–vis spectra of EMBIT.

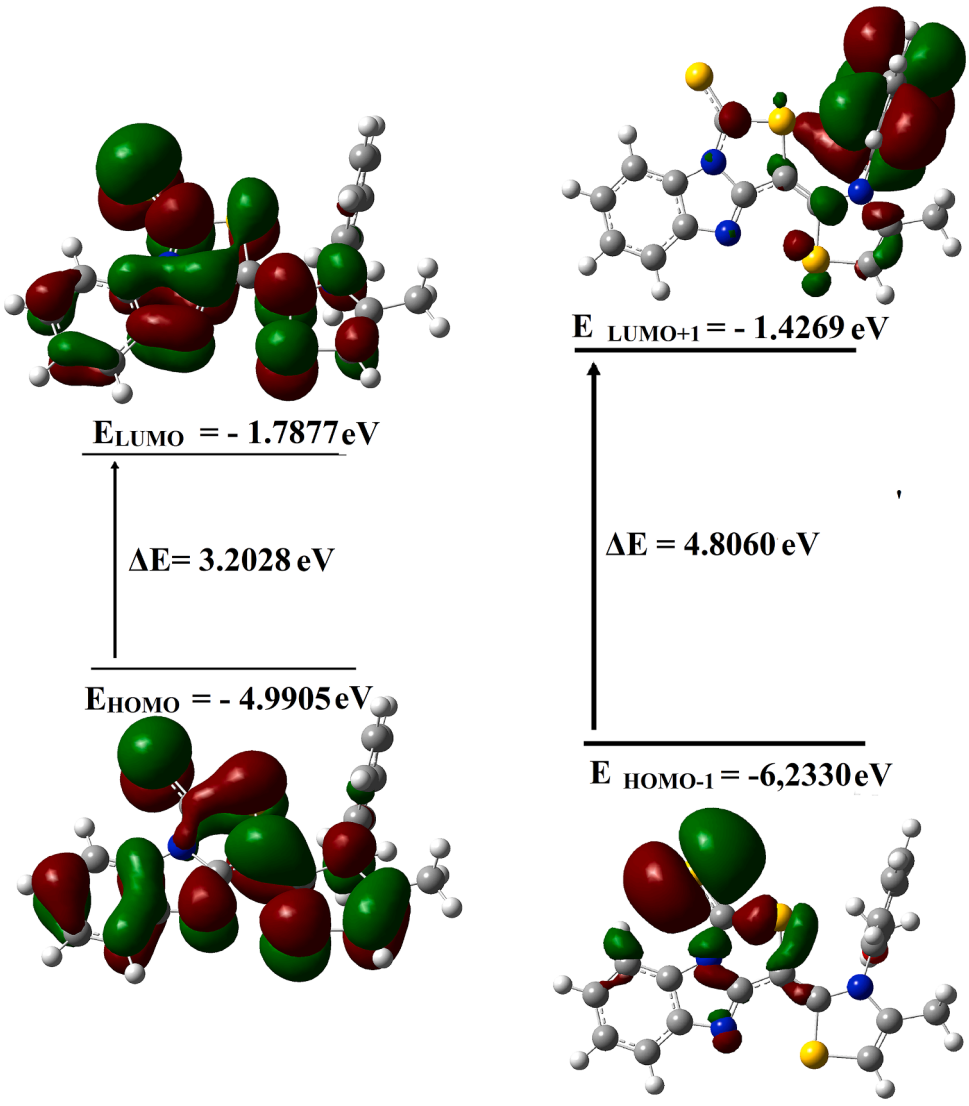

Fig. 9. Frontiers molecular orbitals of EMBIT.

Table 6
Calculated global chemical reactivity descriptors of the EMBIT molecule.

Parameters	B3LYP/6–311G(d,p)				
	Gaz	DMSO	Ethanol	Methanol	Chloroform
E_{HOMO} (eV)	-4.9905	-5.3122	-5.3034	-5.3062	-5.2381
E_{LUMO} (eV)	-1.7877	-2.3045	-2.2911	-2.2966	-2.4354
ΔE (eV)	3.2028	3.0077	3.0123	3.0096	2.8027
I_P (eV)	4.9905	5.3122	5.3034	5.3062	5.2381
E_A (eV)	1.7877	2.3045	2.2911	2.2966	2.4354
χ (eV)	3.3891	3.8083	3.7972	3.8014	3.8367
μ (eV)	-3.3891	-3.8083	-3.7972	-3.8014	-3.8367
η (eV)	1.6014	1.5038	1.5061	1.5048	1.4013
S (eV)	0.8007	0.7519	0.7530	0.7524	0.7006
ω (eV)	3.5862	4.8221	4.7867	4.8015	5.2523
Γ (eV)	1.9603	1.6923	1.7034	1.6953	1.5564

[85]. The various colors displayed on the MEP surfaces, see Fig. 10. Indicate distinct electrostatic potential values, with a decreasing order of potential values from blue to green, yellow, orange, and finally red. The red region on the MEP map corresponds to the negative portion above the N2 and S2 atoms in the EMBIT molecule, signifying a region favorable for nucleophilic attack. Conversely, the blue regions concentrate above the methoxyphenyl and thiazole ring, representing an electron-rich area with a positive charge, making it suitable for electrophilic attack. In conclusion, MEP analysis provided valuable insights into the reactive sites of the EMBIT molecule, highlighting areas conducive to nucleophilic and electrophilic interactions, and enhancing our understanding of its reactivity.

3.9. Nonlinear optical (NLO) properties

Theoretical predictions significantly impact the design of materials with unique characteristics, particularly in understanding molecular structures and their connection to desired properties. NLO properties, such as their relation to electronic and vibrational structures, have gained considerable attention. These properties are crucial for practical applications, including the design of materials and devices, notably in optical technologies for data transfer and storage [86]. The NLO parameters were determined by applying the following equations:

$$\mu = \sqrt{\mu_x^2 + \mu_y^2 + \mu_z^2}$$

$$a = \frac{1}{3} a_{xx} + a_{yy} + a_{zz}$$

$$\beta = \left[\left(\beta_{xxx} + \beta_{xyy} + \beta_{xzz} \right)^2 + \left(\beta_{yyy} + \beta_{yzz} + \beta_{yxx} \right)^2 + \left(\beta_{zzz} + \beta_{zww} + \beta_{zyy} \right)^2 \right]^{\frac{1}{2}}$$

Kleinman hypothesis [88]

$$\gamma = \frac{1}{5} \left(\gamma_{xxxx} + \gamma_{yyyy} + \gamma_{zzzz} + 2\gamma_{xxyy} + 2\gamma_{xxzz} + 2\gamma_{yyzz} \right)$$

Table 7 presents the computed values for dipole moment, polarizability, and first and second-order hyperpolarizability. The primary dipole moment is observed along the Z-axis, with the highest magnitude providing insights into the orientation of the electric field from the acceptor to the donor [45]. The calculated polarizabilities are equal to 219.00 au and 3. 2457 × 10^{-23} esu, with the most significant contribution from α_{ZZ}. The EMBIT compound exhibits a first-order hyperpolarizability approximately 70 times greater than that of urea, making it highly suitable for nonlinear optical (NLO) applications. It has been reported that the first oder hyperpolarlizaby is related to the energy gap , a narrower energy gap tends to yield a higher β value, indicative of enhanced nonlinear optical behavior [87–89]. The highest computed value for second-order hyperpolarizability are observed along the β_{zzz} axis .The nonlinear behavior in this molecule is a result of electron delocalization previously studied in electron localization function [90, 91]. The π-conjugated character and non-centrosymmetric forms of EMBIT also contributed to ability to generate second harmonic generation SHG effects making it a suitable compound for NLO activity [92]. The EMBIT generated second order hyperpolarizabilities γ was equal to 85.67 esu suggesting that title compound might possess microscopic third order nonlinear behavior [93] .

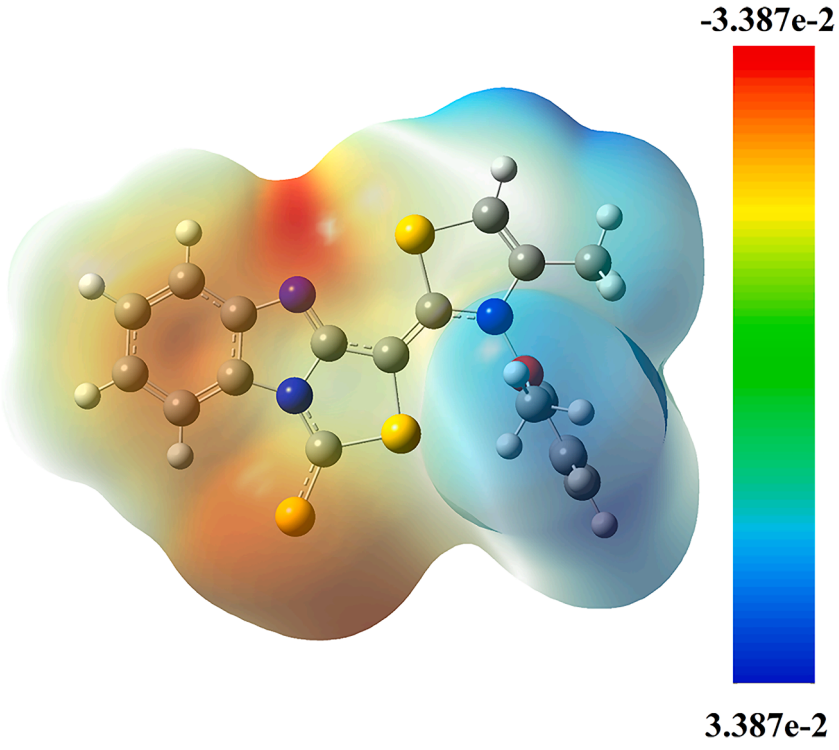

Fig. 10. Molecular electrostatic potential map of EMBIT.

Table 7
Computed Dipole Moment (μ), Polarizability (α), First order hyperpolarizability (β), and second order hyperpolarizability (γ) of EMBIT.

Parameters	B3LYP /6–311G++(d,p)
Dipole Moment	
μ_x=	0
μ_y=	0
μ_z=	3
μ=	3.39211
Polarizability	
α_{xx}=	236
α_{yy}=	360.89
α_{zz}=	489
α=(au)	219.00
α x 10^{-23} (esu)	3.2457
First Order Hyperpolarizability	
β_{xxx}=	173.357
β_{yxx}=	-152.913
β_{xyy}=	119.698
β_{yyy}=	-357.367
β_{zxx}=	42.4962
β_{yxz}=	130.965
β_{zyy}=	152.339
β_{xzz}=	146.257
β_{yzz}=	493.156
β zzz=	1635.24
⟨β⟩= a.u	1882.143327
⟨β⟩x 10^{-29} (esu)	1.6260
Second Order Hyperpolarizability	
γ_{xxxx}	29
γ_{xxyx}	-4.47735
γ_{xxyy}	14.0911
γ_{yxyy}	-3.76667
γ_{yyyy}	58.0324
γ_{xxzx}	7.07311
γ_{xxzy}	-1.84435
γ_{yxzy}	4.80328
γ_{yyzy}	6.69158
γ_{xxzz}	25.7173
γ_{yxzz}	-10.8184
γ_{yyzz}	45.1207
γ_{zxzz}	28.5918
γ_{zyzz}	-16.6478
γ_{zzzz}	171.398
⟨γ⟩= esu	85.67944

3.10. Molecular Docking

Glaucoma is a widespread eye illness that, if left misdiagnosed and untreated, can result in irreparable sight loss. Glaucoma is defined by an increase in intraocular pressure (IOP), which causes optic nerve injury and visual field loss. Although increased intraocular pressure (IOP) is not always diagnostic of glaucoma, it is a primary risk factor and a causal component in glaucomatous optic neuropathy [94]., and it is the most common cause of vision loss in the US and other industrial nations [95, 96].

Rock inhibitors have been shown to have at least four separate uses in the treatment of glaucoma, including considerable IOP reduction, increased ocular blood flow, suppression of postoperative scarring, and stimulation of retinal ganglion cell survival and axon regeneration [97]. Rock1 and Rock2, key proteins, have been pinpointed as essential elements in the development of glaucoma. They play vital roles in the multiple cellular functions, such as influencing cell contractility, maintaining the structure of the cytoskeleton, and regulating cell adhesion. In the case of glaucoma, their malfunctioning is linked to the rise in intraocular pressure (IOP), ultimately resulting in damage to the optic nerve [98]..

The table shows the results of predicting a substance's activity spectrum using the Prediction of Activity Spectra of Substances (PASS) tool. The results of PASS prediction highlight the expected activity spectrum's probable activity (Pa) and inactivity (Pi) for the EMBIT enlisted in Table 9, the studied molecule has promising activity as an ophthalmic medication with 0.64 according to the findings of the PASS research given in Table 8, we molecular docking to investigated the inhibition activity of the EMBIT on Rock1 and Rock2. Furthermore, the literature supports our choice, The PDB ID for the receptor protein crystal structure, which was obtained from the RCSB database.

Table S2. provides a comprehensive overview of the binding characteristics between the EMBIT ligand and both Rock1 and Rock2 proteins, incorporating information on binding affinity and inhibition constants. Notably, the data reveals that Rock2 exhibits superior binding affinity, reflected in the highest recorded binding energy of -8.7 kcal/mol and a smaller Ki inhibition constant of 0.97 μm. Compared to a lower binding affinity of -7.4 kcal/mol and a greater inhibition constant of 1.91 μm towards Rock1. This suggests a higher likelihood of effective inhibition for the EMBIT ligand against the Rock2 protein.

Fig. 11 and Fig. 12 provide 2D and 3D displays of examination of the molecular interactions. Table 9 enlists all the characteristics of the interactions between EMBIT and the two targets. The results revealed that Rock1 forms a single conventional hydrogen bond. This interaction occurs between the ARG58 residue and the S1 atom, with a bond length of 3.06 angstroms. Additionally, a carbon-hydrogen bond is established between the SER118 residue and the C20 carbon, spanning a distance of 3.56 angstroms. Conversely, Rock2 demonstrates a more intricate bonding pattern, engaging in two conventional hydrogen bonds with the EMBIT ligand. The first bond forms between the Rock2 protein and the S1 atom, measuring a remarkably close distance of 2.36 Å. The second conventional hydrogen bond occurs between Rock2 and the O1 atom, with a slightly longer but still significant distance of 2.87 Å. These findings underscore the molecular basis for the heightened binding affinity observed in Rock2, emphasizing the importance of multiple, closely spaced hydrogen bonds for enhanced biological activity.

In summary, the detailed analysis of the molecular interactions between the EMBIT ligand and Rock1/Rock2 proteins reveals a superior binding affinity for Rock2, attributed to the formation of multiple, strategically positioned hydrogen bonds (see Fig. 6). This insight enhances our understanding of the EMBIT ligand's potential inhibitory effects on Rock2 and underscores its promising potential in biological activities, see Table 8.

4. Conclusion

In summary, the thorough investigation into the novel synthesized compound EMBIT has unveiled its promising potential as a multifunctional compound for both optical and biological applications. The investigation of solvent effects revealed a stabilizing influence by comprehensive experimental and computational analyses, including FT-IR, NMR, and UV-Vis analysis using density functional theory. This narrowed the band gap and produced more precise computed gap values. The MEP surface visualizes the potential locations for electrophilic and nucleophilic attacks. In addition to studies like Hirshfeld surface and Reduced Gradient Density, which revealed possible bond interactions of EMBIT, investigations using LOL and ELF provided valuable insights into the electronic configuration and chemical bonding

Table 8
PASS online prediction of EMBIT biological activity.

Pa	Pi	Activity
0,640	0,005	Ophthalmic drug
0,601	0,001	Prostaglandin-E2 synthase 1 inhibitor
0,568	0,004	Amyloid beta precursor protein antagonist
0,539	0,005	Antiglaucomic
0,536	0,039	Insulysin inhibitor
0,455	0,016	Rheumatoid arthritis treatment
0,432	0,005	Dual specificity phosphatase inhibitor
0,435	0,011	Mcl-1 antagonist
0,363	0,009	Calcium channel N-type blocker
0,377	0,028	PfA-M1 aminopeptidase inhibitor

Table 9
Distances types and location of intermolecular interactions formed from the residues of the Rock1 and Rock2 and the molecule EMBIT.

Protein	Residue	Compound	Atom/group of compounds	Category	Types	Distance (Å)
Rock1	ARG58	(E)-3-(3-(2-methoxyphenyl)-4-methylthiazol-2(3H)-ylidene) benzo [4,5]imidazo[1,2-c]thiazole-1(3H)-thione	S1	Hydrogen Bond	Conventional Hydrogen Bond	3,06448
	SER118		C20	Hydrogen Bond	Carbon Hydrogen Bond	3,56,487
	GLU24		C6H4 Ring	Electrostatic	Pi-Anion	4,2843
	GLU24		C3N2 Ring	Electrostatic	Pi-Anion	4,65,708
	TRP122		C6H4 Ring	Hydrophobic	Pi-Pi Stacked	4,26,705
	TRP122		C3N2 Ring	Hydrophobic	Pi-Pi Stacked	3,63,532
	TRP122		C3N1S1	Hydrophobic	Pi-Pi Stacked	3,84,114
	TRP122		C3N1S1H1	Hydrophobic	Pi-Pi Stacked	5,62,537
	TRP122		C6H4 Ring	Hydrophobic	Pi-Pi Stacked	3,75,098
	TRP122		C3N2 Ring	Hydrophobic	Pi-Pi Stacked	4,07374
	TRP122		C3N1S1	Hydrophobic	Pi-Pi Stacked	5,0854
	ARG58		C3N1S1H1	Hydrophobic	Pi-Alkyl	4,89,729
Rock2	LYS224		S1	Hydrogen Bond	Conventional Hydrogen Bond	2,8648
	LYS229:		O1	Hydrogen Bond	Conventional Hydrogen Bond	2,87,404
	GLU170		C3N2 Ring	Electrostatic	Pi-Anion	4,05017
	GLU170		C3S1N1 Ring	Electrostatic	Pi-Anion	3,62,174
	GLU170		C3S1N1H1	Electrostatic	Pi-Anion	4,10,376
	HIS225		S1	Hydrogen Bond	Pi-Donor Hydrogen Bond	4,10,387
	LYS224		C6H4	Hydrophobic	Pi-Sigma	3,70,175
	PHE156		S3	Other	Pi-Sulfur	5,36,947

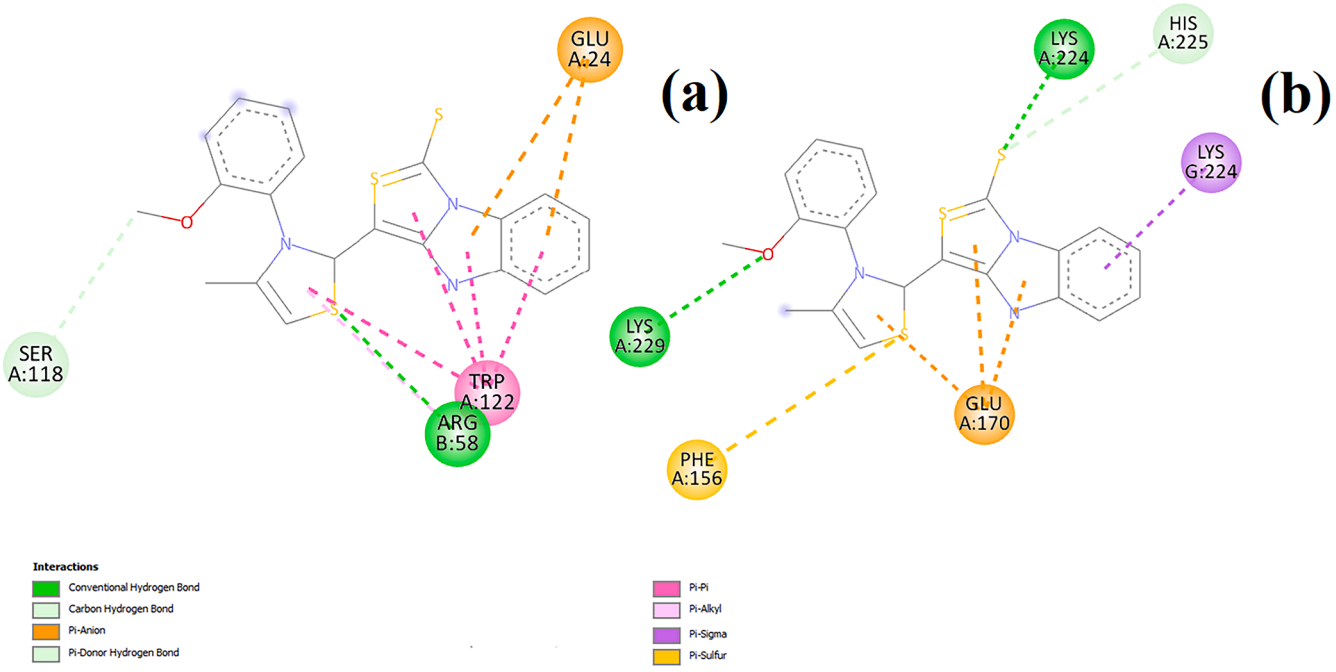

Fig. 11. 2D receptor-ligand interaction diagram a) Rock1 b) Rock2.

characteristics of EMBIT, the least localized carbon-oxygen bond, might influence NLO properties of EMBIT. Predictions of its biological activity against glaucoma, particularly its high inhibition constants towards Rho-associated protein kinases Rock1 and Rock2 key factors in this eye disease, indicated its potential inhibition efficacy towards Rock2 with higher binding affinity and lower Ki, further exploration, including clinical studies, is necessary to validate these findings and evaluate EMBIT's efficacy in both optical and biological contexts. The results presented herein could lead to the development of new treatments for glaucoma and advancements in NLO technologies. In particular, the NLO studies suggest its suitability for second harmonic generation (SHG) and other NLO applications including microscopic third-order nonlinear behavior.

CRediT authorship contribution statement

Sabrina Smati: Writing – original draft. **Ahmed Djafri:** Writing – original draft, Investigation, Data curation. **Karima Menad:** Writing – original draft, Formal analysis. **Nourdine Boukabcha:** Writing – review & editing, Software, Methodology, Investigation, Formal analysis. **Rachida Rahmani:** Formal analysis, Writing – review & editing. **Meriem Goudjil:** Formal analysis, Methodology. **Youcef Megrouss:** Formal analysis. **Hafsa Khaldi:** Investigation, Methodology. **Necmi Dege:** Investigation, Methodology, Formal analysis. **Abdelkader Chouaih:**

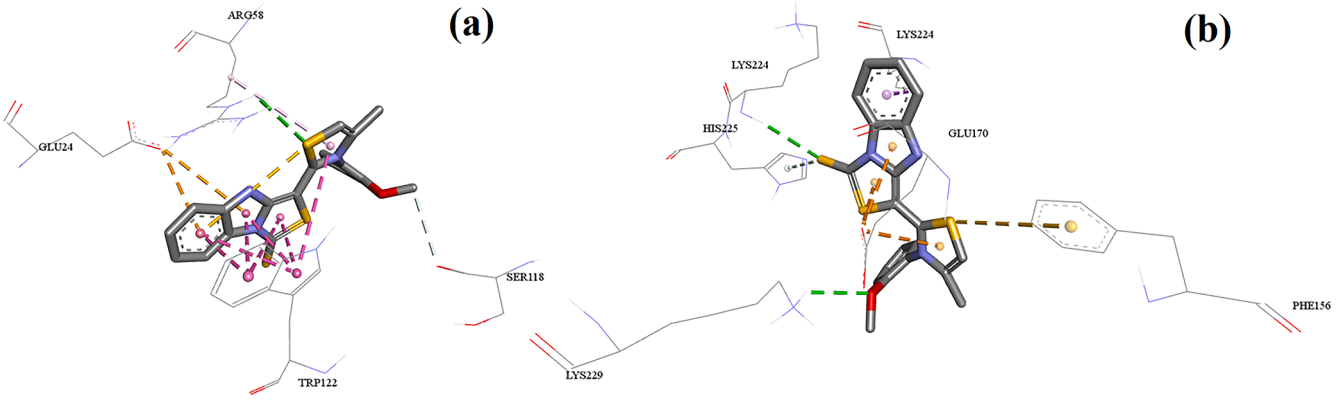

Fig. 12. 3D receptor-ligand interaction a) Rock1, b) Rock2.

Investigation, Methodology, Software, Formal analysis. **Ayada Djafri:** Formal analysis, Investigation, Methodology.

Declaration of competing interest

The authors declare no conflict of interest.

Data availability

The data that has been used can be made available upon request to the authors.

Acknowledgments

The authors thank the Algerian Ministry of Higher Education and Scientific Research, the General Directorate of Scientific Research and Technological Development (DGRSDT) and the Hassiba Benbouali Chlef University for supporting the PRFU project number B00L01UN020120230006.

Supplementary materials

Supplementary material associated with this article can be found, in the online version, at doi:10.1016/j.molstruc.2024.139157.

References

[1] Y. Megrouss, F. Triki Baara, N. Boukabcha, A. Chouaih, A. Hatzidimitriou, A. Djafri, F. Hamzaoui, "Synthesis, X-Ray Structure Determination and Related Physical Properties of Thiazolidinone Derivative by DFT Quantum Chemical Method, Acta Chim. Slov. 66 (2) (2019) 490–500, https://doi.org/10.17344/acsi.2019.5066.

[2] Y. Megrouss, S. Yahiaoui, N. Boukabcha, Charge Density Study, DFT Calculations, Hirshfield Surface Analysis and Molecular Docking of (Z)-3-N-(Ethyl)-2-N '-(3-methoxyphenyl imino) thiazolidine-4-one, Russ. J. Phys. Chem. A 97 (8) (2023) 1731–1745, https://doi.org/10.1134/S0036024423080319.

[3] A. Benmohammed, et al., Insight into (Z)-ethyl-2-(2-((E)-2,4-dinitro benzylidene amino)-4-oxo-3-phenylthiazolidin-5-ylidene) acetate in-silico anti-SARS-CoV-2 performance: Synthesis, structural-spectral characterizations and DFT computations, J. Mol. Struct. 1295 (2024) 136696, https://doi.org/10.1016/j.molstruc.2023.136696.

[4] A. Chebli, A. Djafri, N. Boukabcha, Y. Megrouss, M. Drissi, M.H.M. Belhachemi, S. Yahiaoui, A.R. Guerroudj, A. Chouaih, A. Djafri, Synthesis, crystal structure, DFT calculations, NBO, Fukui function, NCI-RDG, Hirshfeld surface analysis, NLO properties and molecular docking analysis on (E)-N'-(3-methoxybenzylidene)-2-(quinolin-8-yloxy) acetohydrazide, J. Mol. Struct. 1310 (2024) 138287, https://doi.org/10.1016/j.molstruc.2024.138287.

[5] A. Petrou, M. Fesatidou, A. Geronikaki, Thiazole Ring—A Biologically Active Scaffold, Molecules. 26 (11) (2021) 3166, https://doi.org/10.3390/molecules26113166.

[6] M.A. Shalaby, A.M. Fahim, S.A. Rizk, Microwave-assisted synthesis, antioxidant activity, docking simulation, and DFT analysis of different heterocyclic compounds, Sci. Rep. 13 (2023) 4999, https://doi.org/10.1038/s41598-023-31995-w.

[7] K. Ahmed, M.I. Choudhary b, R.S.Z. Saleem, Heterocyclic pyrimidine derivatives as promising antibacterial agents, Eur J Med Che 259 (2023) 1157015, https://doi.org/10.1016/j.ejmech.2023.115701.

[8] M.H.A Al-Jumaili, et al., Comprehensive review on the Bis–heterocyclic compounds and their anticancer efficacy, J. Mol. Struct. 1271 (2023) 133970, https://doi.org/10.1016/j.molstruc.2022.133970.

[9] S Nataliia, et al , " Sulfones of Pyridinyloxy-Substituted Imidazo[2,1-b][1,3] thiazines: Synthesis, Anti-Inflammatory Activity Evaluation In Vivo and Docking Studies, Lett. Drug Des. Discov.", vol 20 , pp. 1867–1875, novembre 2023 doi:10.2174/1570180819666220812144409.

[10] A. Andleeb, Pharmacological Significance of Synthetic Bioactive Thiazole Derivatives, Curr. Bioact. Compd. 18 (2022) 77–89, 15734072186662203031005O1.

[11] M. d. Badrul Islam, et al., Recent Advances in Pyridine Scaffold: Focus on Chemistry, Synthesis, and Antibacterial Activities, Biomed. Res. Int. 2023 (2023) 15, https://doi.org/10.1155/2023/9967591, mai.

[12] R. Shah, P.K. Verma, Therapeutic importance of synthetic thiophene, Chem. Cent. J. 23 (2018) 137, https://doi.org/10.1186/s13065-018-0511-5.

[13] C.W. Dirk, H.E. Katz, M.L. Schilling, L.A. King, Use of thiazole rings to enhance molecular second-order nonlinear optical susceptibilities, Chemistry of Materials 2 (6) (1990) 700–705, https://doi.org/10.1021/cm00012a020.

[14] E.M. Breitung, C.F. Shu, R.J. McMahon, Thiazole and thiophene analogues of donor-acceptor stilbenes: Molecular hyperpolarizabilities and structure-property relationships, J. Am. Chem. Soc. 122 (6) (2000) 1154–1160, https://doi.org/10.1021/ja9930364.

[15] "G.M. Sheldrick, A short history of SHELX, Acta Crystallogr. A Found. Crystallogr. 64 (2008) 112–122, https://doi.org/10.1107/S0108767307043930.

[16] "G.M. Sheldrick, Crystal structure refinement with SHELXL, Acta Crystallogr. C Struct. Chem. 71 (2015) 3–8, https://doi.org/10.1107/S2053229614024218.

[17] L.J. Farrugia, WinGX suite for small-molecule single-crystal crystallography, J. Appl. Crystallogr. 32 (4) (1999) 837–838, https://doi.org/10.1107/S0021889899006020.

[18] M.J. Frisch, G.W. Trucks, H.B. Schlegel, G.E. Scuseria, M.A. Robb, J.R. Cheeseman, G. Scalmani, V. Barone, B. Mennucci, G.A. Petersson, H. Nakatsuji, M. Caricato, X. Li, H.P. Hratchian, A.F. Izmaylov, J. Bloino, G. Zheng, J.L. Sonnenberg, M. Hada, M. Ehara, K. Toyota, R. Fukuda, J. Hasegawa, M. Ishida, T. Nakajima, Y. Honda, O. Kitao, H. Nakai, T. Vreven, J.A. Montgomery Jr., J.E. Peralta, F. Ogliaro, M. Bearpark, J.J. Heyd, E. Brothers, K.N. Kudin, V.N. Staroverov, R. Kobayashi, J. Normand, K. Raghavachari, A. Rendell, J.C. Burant, S.S. Iyengar, J. Tomasi, M. Cossi, N. Rega, J.M. Millam, M. Klene, J.E. Knox, J.B. Cross, V. Bakken, C. Adamo, J. Jaramillo, R. Gomperts, R.E. Stratmann, O. Yazyev, A.J. Austin, R. Cammi, C. Pomelli, J.W. Ochterski, R.L. Martin, K. Morokuma, V.G. Zakrzewski, G.A. Voth, P. Salvador, J.J. Dannenberg, S. Dapprich, A.D. Daniels, E.O. Farkas, J. B. Foresman, J.V. Ortiz, J. Cioslowski, D.J. Fox, Gaussian 09, Revision A.02, Gaussian Inc, Wallingford, CT, 2009.

[19] H. Arı, T. Özpozan, Y. Kabacalı, M. Saçmacı, Monomeric or dimeric? A theoretical and vibrational spectroscopic approach to the structural stability of 5-(4-metoxy benzoyl)-6-(4-metoxyphenyl)-3-methyl-2-thioxo-2,3-dihydropyrimidine-4(1H)-on, J. Mol. Struct. 1222 (2020) 128848, https://doi.org/10.1016/j.molstruc.2020.128848.

[20] M. Jamróz, VEDA 4.0 Program: Vibrational Energy Distribution Analysis, Drug Institute, Warsaw, Poland, 2004.

[21] A. Pekparlak, D. Avcı, Y. Atalay, K. Esmer, Theoretical studies of molecular structure and vibrational spectra of melaminium salt: 2,4,6-triamino-1,3,5-triazin-1,3-ium Tartrate monohydrate, Arab. J. Sci. Eng. 37 (1) (2012) 171–181, https://doi.org/10.1007/s13369-011-0151-8.

[22] N.M. O'boyle, A.L. Tenderholt, K.M. Langner, cclib: A library for package-independent computational chemistry algorithms, J. Comput. Chem. 29 (5) (2008) 839–845, https://doi.org/10.1002/jcc.20823.

[23] "R.D.T.K.J. Millam, Shawnee Mission KS. GaussView, Semichem Inc. (2009).".

[24] T. Lu, F. Chen, Multiwfn: A multifunctional wavefunction analyzer, J. Comput. Chem. 33 (5) (2012) 580–592, https://doi.org/10.1002/jcc.22885.

[25] W. Humphrey, A. Dalke, K. Schulten, VMD: Visual molecular dynamics, J. Mol. Graph. 14 (1) (1996) 33–38, https://doi.org/10.1016/0263-7855(96)00018-5.
[26] G.M. Morris, et al., AutoDock4 and AutoDockTools4: Automated docking with selective receptor flexibility, J. Comput. Chem. 30 (16) (2009) 2785–2791, https://doi.org/10.1002/jcc.21256.
[27] O. Trott, A.J. Olson, AutoDock Vina: Improving the speed and accuracy of docking with a new scoring function, efficient optimization, and multithreading, J. Comput. Chem. 31 (2) (2010) 455–461, https://doi.org/10.1002/jcc.21334.
[28] Life Sciences and Material Sciences, BIOVIA, Dassault Systems (2023). https://www.3ds.com/products-services/biovia/.
[29] E.G. COX, Crystal Structure of Benzene, Rev. Mod. Phys. 30 (1) (1958) 159–162, https://doi.org/10.1103/RevModPhys.30.159.
[30] P.F. Lang, B.C. Smith, Electronegativity effects and single covalent bond lengths of molecules in the gas phase, J. Chem. Society. Dalton Trans. 43 (21) (2014) 8016–8025, https://doi.org/10.1039/c4dt00807c.
[31] V. Schomaker and D.P. Stevenson, "Some revisions of the covalent radii and the additivity rule for the lengths of partially ionic single covalent bonds *," *J. Am. Chem. Soc.*, vol. 63, no. 1, pp. 37–40, 1941, doi: 10.1021/ja01846a007.
[32] L.S. Higashi, M. Lundeen, K. Seff, Empirical relations between disulfide bond lengths, (nitrogen or carbon)-carbon-sulfur-sulfur torsion angles, and substituents in aromatic disulfides. Crystal and molecular structure of 3,3'-dihydroxydi-2-pyridyl disulfide, J. Am. Chem. Soc. 100 (26) (1978) 8101–8106, https://doi.org/10.1021/ja00494a013.
[33] A. Domenicano, P. Mazzeo, A. Vaciago, Substituent effects in the benzene series: A structural approach, Tetrahedron. Lett. 17 (13) (1976) 1029–1032, https://doi.org/10.1016/S0040-4039(00)77997-4.
[34] G. Schultz, T. Nagy, G. Portalone, F. Ramondo, I. Hargittai, A. Domenicano, Molecular structure of ethynylbenzene from electron diffraction and ab initio molecular orbital calculations, Struct. Chem. 4 (3) (1993) 183–190, https://doi.org/10.1007/BF00679344.
[35] Y. Maouche, G. Germain, M.C. Brianso, J.Y. Sanchez, P. Nicolet, M.J.M. Abadie, Tétraméthyl-1,1',3,3' biindène-1:1'-(±), C22H22, Acta Crystallogr. C 41 (1) (1985) 99–101, https://doi.org/10.1107/S0108270185002918.
[36] M. Orio, D.A. Pantazis, F. Neese, Density functional theory, Photosynth. Res. 102 (2) (2009) 443–453, https://doi.org/10.1007/s11120-009-9404-8.
[37] J. Jayabharathi, V. Thanikachalam, N. Srinivasan, M. Venkatesh Perumal, K. Jayamoorthy, Physicochemical studies of molecular hyperpolarizability of imidazole derivatives, Spectrochim. Acta a Mol. Biomol. Spectrosc. 79 (1) (2011) 137–147, https://doi.org/10.1016/j.saa.2011.02.024.
[38] F. Yuan, et al., Series of Ln-metal organic frameworks: Photocatalytic performance and Hirshfeld surface analyses, J. Mol. Struct. 1251 (2022) 131956, https://doi.org/10.1016/j.molstruc.2021.131956.
[39] M.A. Spackman, D. Jayatilaka, Hirshfeld surface analysis, CrystEngComm. 11 (1) (2009) 19–32, https://doi.org/10.1039/B818330A.
[40] C.F. Matta, J. Hernández-Trujillo, T. Tang, and R.F. W. Bader, "Hydrogen–Hydrogen bonding: a stabilizing interaction in molecules and crystals," *Chem. A Eur. J.*, vol. 9, no. 9, pp. 1940–1951, 2003, doi: 10.1002/chem.200204626.
[41] C.F. Matta, "Hydrogen–Hydrogen Bonding: The Non-Electrostatic Limit of Closed-Shell Interaction Between Two Hydro," in *Hydrogen Bonding—New Insights*, Springer Netherlands, pp. 337–375. doi: 10.1007/978-1-4020-4853-1_9.
[42] E.R. Johnson, S. Keinan, P. Mori-Sánchez, J. Contreras-García, A.J. Cohen, W. Yang, Revealing Noncovalent Interactions, J. Am. Chem. Soc. 132 (18) (2010) 6498–6506, https://doi.org/10.1021/ja100936w.
[43] "B. Silvi & A. Savin ,Classification of chemical bonds based on topological analysis of electron localization functions Nature. 371, 683–686 (1994)".
[44] S.Sangeetha Margreat, et al., Synthesis, spectroscopic, quantum computation, electronic, AIM, Wavefunction (ELF, LOL) and Molecular Docking investigation on (E)-1-(2,5-dichlorothiophen-3-yl)-3-(thiophen-2-yl)-2-propen-1-one, Chem. Data Collect. 33 (2021) 100701, https://doi.org/10.1016/j.cdc.2021.100701.
[45] N. Boukabcha, et al., Spectral investigation, TD-DFT study, Hirshfeld surface analysis, NCI-RDG, HOMO-LUMO, chemical reactivity and NLO properties of 1-(4-fluorobenzyl)-5-bromolindolin-2,3dione, J. Mol. Struct. 1285 (2023) 135492, https://doi.org/10.1016/j.molstruc.2023.135492.
[46] S. Gunasekaran, E. Sailatha, et al., FTIR, FT Raman spectra and molecular structural confirmation of isoniazid, Indian J. Pure Appl. Phys. 47 (2009) 12e18.
[47] E. Isac Paulraj, S. Muthu, Spectroscopic studies (FTIR, FT-Raman and UV), potential energy surface scan, normal coordinate analysis and NBO analysis of (2R,3R,4R,5S)-1-(2-hydroxyethyl)-2-(hydroxymethyl) piperidine-3,4,5-triol by DFT methods, Spectrochim. Acta a Mol. Biomol. Spectrosc. 108 (2013) 38–49, https://doi.org/10.1016/j.saa.2013.01.061.
[48] S. Muthu, J. Uma Maheswari, Quantum mechanical study and spectroscopic (FT-IR, FT-Raman, 13C, 1H, UV) study, first order hyperpolarizability, NBO analysis, HOMO and LUMO analysis of 4-[(4-aminobenzene) sulfonyl] aniline by ab initio HF and density functional method, Spectrochim. Acta a Mol. Biomol. Spectrosc. 92 (2012) 154–163, https://doi.org/10.1016/j.saa.2012.02.056.
[49] S.M. Moosavinejad, M. Madhoushi, M. Vakili, D. Rasouli, Evaluation of degradation in chemical compounds of wood in historical buildings using FT-IR and FT-Raman vibrational spectroscopy, Maderas. Ciencia y tecnología (2019), https://doi.org/10.4067/S0718-221x2019005000310 no. ahead, pp. 0–0.
[50] H.A.M. Salim, H.H. Abdallah, P. Ramasami, Stereoselectivity and Regioselectivity of the Cycloaddition Dimerization of allyl 3-(2-pyridyl) acrylate and allyl 3-(2-pyrryl) acrylate: DFT Calculations, IOP. Conf. Ser. Mater. Sci. Eng. 454 (2018) 012049, https://doi.org/10.1088/1757-899X/454/1/012049.
[51] V. Krishnakumar, G. Keresztury, T. Sundius, R. Ramasamy, Simulation of IR and Raman spectra based on scaled DFT force fields: a case study of 2-(methylthio) benzonitrile, with emphasis on band assignment, J. Mol. Struct. 702 (1–3) (2004) 9–21, https://doi.org/10.1016/j.molstruc.2004.06.004.
[52] S. Premkumar, et al., Vibrational Spectroscopic and Structural Investigations of 2-Amino-6-Methoxy-3-Nitropyridine: a DFT Approach, Braz. J. Phys. 45 (6) (Dec. 2015) 621–632, https://doi.org/10.1007/s13538-015-0365-4.
[53] K. Hasegawa, T. Ono, T. Noguchi, Vibrational Spectra and Ab Initio DFT Calculations of 4-Methylimidazole and Its Different Protonation Forms: Infrared and Raman Markers of the Protonation State of a Histidine Side Chain, J. Phys. Chem. B 104 (17) (2000) 4253–4265, https://doi.org/10.1021/jp000157d.
[54] "G. Varsanyi, Vibrational Spectra of Benzene Derivatives, Academic Press, NewYork, 1969".
[55] S. Sakthivel, T. Alagesan, S. Muthu, C.S. Abraham, E. Geetha, Quantum mechanical, spectroscopic study (FT-IR and FT - Raman), NBO analysis, HOMO-LUMO, first order hyperpolarizability and docking studies of a non-steroidal anti-inflammatory compound, J. Mol. Struct. 1156 (2018) 645–656, https://doi.org/10.1016/j.molstruc.2017.12.024.
[56] P. Venkatesan, S. Thamotharan, A. Ilangovan, H. Liang, T. Sundius, Crystal structure, Hirshfeld surfaces and DFT computation of NLO active (2E)-2-(ethoxycarbonyl)-3-[(1-methoxy-1-oxo-3-phenylpropan-2-yl)amino] prop-2-enoic acid, Spectrochim. Acta a Mol. Biomol. Spectrosc. 153 (2016) 625–636, https://doi.org/10.1016/j.saa.2015.09.002.
[57] "R.M. Silverstein, G.C. Basseler, T.C. Morrill, Spectrometric Identification of Organic Compounds, Wiley, New York,.
[58] A.T. Alphonsa, C. Loganathan, S.A.A. Anand, S. Kabilan, Molecular structure, NMR, UV–Visible, vibrational spectroscopic and HOMO, LUMO analysis of (E)-1-(2, 6-bis (4-methoxyphenyl)-3, 3-dimethylpiperidine-4-ylidene)-2-(3-(3, 5-dimethyl-1H-pyrazol-1-yl) pyrazin-2-yl) hydrazine by DFT method, J. Mol. Struct. 1106 (2016) 277–285, https://doi.org/10.1016/j.molstruc.2015.11.005.
[59] N. Elangovan, B. Gangadharappa, R. Thomas, A. Irfan, Synthesis of a versatile Schiff base 4-((2-hydroxy-3,5-diiodobenzylidene)amino) benzenesulfonamide from 3,5-diiodosalicylaldehyde and sulfanilamide, structure, electronic properties, biological activity prediction and experimental antimicrobial properties, J. Mol. Struct. 1250 (2022) 131700, https://doi.org/10.1016/j.molstruc.2021.131700.
[60] F. Dahlmann, et al., Vibrational Predissociation Spectra of C_2N^- and C_3N^-: Bending and Stretching Vibrations, Chemphyschem. 24 (15) (2023), https://doi.org/10.1002/cphc.202300262.
[61] N.B. Colthup, L.H. Daly, S.E. Wiberley, Introduction to Infrared and Raman Spectroscopy, 3rd ed., Academic Press Inc., New York, 1990.
[62] "R. Mecke, R. Mecke, A. Luttringhaus, Chem. Ber. 90 (1957).
[63] C.N.R. Rao, R. Venkataraghavan, The C=S stretching frequency and the '−N−C=S bands' in the infrared, Spectrochim. Acta a 45 (1989) 299–305, https://doi.org/10.1016/S0584-8539(89)80280-6.
[64] G. Lauro, G. Bifulco, Elucidating the relative and absolute configuration of organic compounds by quantum mechanical approaches, European. J. Org. Chem. 2020 (26) (2020) 3929–3941, https://doi.org/10.1002/ejoc.201901878.
[65] K. Arici, D.E. Altınoz, M. Cavusoglu, S. Diken, Crystal structure, IR and NMR spectra of (E)-2methoxy-4-(2-morpholinovinyl)phenol molecule and its DFT calculations, J. Mol. Struct. 1275 (2023) 134669, https://doi.org/10.1016/j.molstruc.2022.134669.
[66] P.S. Achanta, et al., Quantum mechanical NMR full spin analysis in pharmaceutical identity testing and quality control, J. Pharm. Biomed. Anal. 192 (2021) 113601, https://doi.org/10.1016/j.jpba.2020.113601.
[67] M.W. Lodewyk, M.R. Siebert, D.J. Tantillo, Computational prediction of ^{1}H and ^{13}C chemical shifts: a useful tool for natural product, mechanistic, and synthetic organic chemistry, Chem. Rev. 112 (3) (2012) 1839–1862, https://doi.org/10.1021/cr200106v.
[68] P. Cimino, L. Gomez-Paloma, D. Duca, R. Riccio, G. Bifulco, Comparison of different theory models and basis sets in the calculation of13C NMR chemical shifts of natural products, Magn. Resonance Chem. 42 (S1) (2004) S26–S33, https://doi.org/10.1002/mrc.1410.
[69] M.S.H. Akash, K. Rehman, Ultraviolet-Visible (UV-VIS) Spectroscopy. Essentials of Pharmaceutical Analysis, Springer Nature Singapore, Singapore, 2020, pp. 31–33, https://doi.org/10.1007/978-981-15-1547-7_3.
[70] S. Fleming, A. Mills, T. Tuttle, Predicting the UV–vis spectra of oxazine dyes, Beilstein. J. Org. Chem. 7 (2011) 432–441, https://doi.org/10.3762/bjoc.7.56.
[71] B. Kosar, C. Albayrak, Spectroscopic investigations and quantum chemical computational study of (E)-4-methoxy-2-[(p-tolylimino)methyl]phenol, Spectrochim. Acta a Mol. Biomol. Spectrosc. 78 (1) (2011) 160–167, https://doi.org/10.1016/j.saa.2010.09.016.
[72] A. Shafiee, E. Ghadiri, J. Kassis, D. Williams, A. Atala, Energy band gap investigation of biomaterials: a comprehensive material approach for biocompatibility of medical electronic devices, Micromachines. (Basel) 11 (1) (2020) 105, https://doi.org/10.3390/mi11010105.
[73] P.P. Singh, H.K. Srivastava, F.A. Pasha, DFT-based QSAR study of testosterone and its derivatives, Bioorg. Med. Chem. 12 (1) (2004) 171–177, https://doi.org/10.1016/j.bmc.2003.11.002.
[74] L. Pauling, The Nature of the Chemical Bond, 3rd ed., Cornell University Press, Ithaca, New York, 1960.
[75] " Parr, R.G.; Chattaraj, P.K. J. Am. Chem. Soc. 1991, 113,.
[76] A.R. Guerroudj, N. Boukabcha, A. Benmohammed, N. Dege e, N. Belkafouf, N. Khelloul, A. Djafri, A. Chouaih, "Synthesis, crystal structure, vibrational spectral investigation, intermolecular interactions, chemical reactivity, NLO properties and molecular docking analysis on (E)-N-(4-nitrobenzylidene)-3-chlorobenzenamine: A combined experimental and theoretical study, J. Mol. Struct. 1240 (2021) 130589, https://doi.org/10.1016/j.molstruc.2021.130589.

[77] P. Jaque, A. Toro-Labbé, Characterization of copper clusters through the use of density functional theory reactivity descriptors, J. Chem. Phys. 117 (7) (2002) 3208–3218, https://doi.org/10.1063/1.1493178.
[78] RG Parr, RG. Pearson, J. Am. Chem. Soc. 105 (1983) 7512.
[79] RG Parr, L Szentpaly, S Liu, J. Am. Chem. Soc. 121 (1999) 1922.
[80] C. Morell, A. Grand, A. Toro-Labbé, H. Chermette, Is hyper-hardness more chemically relevant than expected? J. Mol. Model. 19 (7) (2013) 2893–2900, https://doi.org/10.1007/s00894-013-1778-z.
[81] L.R. Domingo, M.J. Aurell, P. Pérez, R. Contreras, Quantitative characterization of the global electrophilicity power of common diene/dienophile pairs in Diels–Alder reactions, Tetrahedron. 58 (22) (2002) 4417–4423, https://doi.org/10.1016/S0040-4020(02)00410-6.
[82] R. Parthasarathi, V. Subramanian, D.R. Roy, P.K. Chattaraj, Electrophilicity index as a possible descriptor of biological activity, Bioorg. Med. Chem. 12 (21) (2004) 5533–5543, https://doi.org/10.1016/j.bmc.2004.08.013.
[83] R. Kar, S. Pal, Effect of solvents having different dielectric constants on reactivity: A conceptual DFT approach, Int. J. Quantum. Chem. 110 (9) (2010) 1642–1647, https://doi.org/10.1002/qua.22333.
[84] D.R. Roy, Electrophilicity as a possible descriptor for toxicity prediction, Bioorg. Med. Chem. 13 (2005) 3405–3412, https://doi.org/10.1016/j.bmc.2005.03.011. Page.
[85] S. Şahin, N. Dege, (E)-N-(3-chlorophenyl)-1-(5-nitro-2-(piperidin-1-yl)phenyl) methanimine: X-Ray, DFT, ADMET, Boiled-Egg Model, Druggability, Bioavailabilty, and Human Cyclophilin D (CypD) Inhibitory Activity, J. Mol. Struct. 1250 (2022) 131744, https://doi.org/10.1016/j.molstruc.2021.131744.
[86] F.J. Luque, J.M. Lopez, M. Orozco, Perspective on "Electrostatic interactions of a solute with a continuum. A direct utilization of ab initio molecular potentials for the prevision of solvent effects, Theor Chem. Acc. 103 (2000) 343, https://doi.org/10.1007/s002149900013.
[87] M.G. Papadopoulos, A.J. Sadlej, J. Leszczynski (Eds.), *Non-Linear Optical Properties of Matter*, vol. 1, Springer Netherlands, Dordrecht:, 2006, https://doi.org/10.1007/1-4020-4850-5.
[88] D.A. Kleinman, Nonlinear Dielectric Polarization in Optical Media, Physical Review 126 (6) (1962) 1977–1979, https://doi.org/10.1103/PhysRev.126.1977.
[89] N. Benhalima, et al., Solvent Effects on Molecular Structure, Vibrational Frequencies, and NLO Properties of N-(2,3-Dichlorophenyl)-2-Nitrobenzene–Sulfonamide: a Density Functional Theory Study, Braz. J. Phys. 46 (4) (2016) 371–383, https://doi.org/10.1007/s13538-016-0419-2.
[90] S.M. Risser, D.N. Beratan, S.R. Marder, Structure-function relationships for .beta., the first molecular hyperpolarizability, J. Am. Chem. Soc. 115 (17) (1993) 7719–7728, https://doi.org/10.1021/ja00070a016.
[91] A. Mansour, et al., Experimental and theoretical spectroscopic characterization, Hirshfield surface analysis, TD-DFT calculation, and nonlinear optical properties of (E)-1-[(2,4,6tribromophenyl)diazenyl]-naphthalen-2-ol azo dye, J. Mol. Struct. 1261 (2022) 132887, https://doi.org/10.1016/j.molstruc.2022.132887.
[92] K.K. Jha, S. Dutta, P. Munshi, Concomitance, Reversibility, and Switching Ability of Centrosymmetric and Non-Centrosymmetric Crystal Forms: Polymorphism in an Organic Nonlinear Optical Material, Cryst. Growth Des. 18 (2) (2018) 1126–1135, https://doi.org/10.1021/acs.cgd.7b01560.
[93] A. Karakaş, H. Ünver, A. Elmali, Synthesis, structure, linear and third-order nonlinear optical behavior of N-(3-hydroxybenzalidene)4-bromoaniline, J. Mol. Struct. 877 (1–3) (2008) 152–157, https://doi.org/10.1016/j.molstruc.2007.07.030.
[94] D.A. Lee, E.J. Higginbotham, Glaucoma and its treatment: A review, Am. J. Health-Syst. Pharmacy 62 (7) (2005) 691–699, https://doi.org/10.1093/ajhp/62.7.691.
[95] U.S. Department of Health, Education, and Welfare. Statistics on Blindness in the Model Reporting area, 1969–70, Government Printing Office, Washington, D.C.: U. S, 1973. DHEW publication no. NIH 73-427.
[96] American Academy of Ophthalmology Quality of Care Committee Glaucoma Panel, Primary Open-Angle Glaucoma, American Academy of Ophthalmology, San Francisco, 1996, p. 2.
[97] R. Chang, S. Wang, An emerging treatment option for glaucoma: Rho kinase inhibitors, Clin. Ophthalmol. (2014) 883, https://doi.org/10.2147/OPTH.S41000.
[98] J. Wang, X. Liu, Y. Zhong, Rho/Rho-associated kinase pathway in glaucoma (Review), Int. J. Oncol. 43 (5) (2013) 1357–1367, https://doi.org/10.3892/ijo.2013.2100.